Ionic liquids under one-dimensional nanometric confinement

Filippo Ferdeghini

UPMC
SORBONNE UNIVERSITÉS

THÈSE DE DOCTORAT
DE L'UNIVERSITÉ PIERRE ET MARIE CURIE

Spécialité : Physique

École doctorale : « Physique en Île-de-France »

réalisée au

Laboratoire Léon Brillouin (CEA-CNRS)
CEA Saclay, France

présentée par

Filippo FERDEGHINI

pour obtenir le grade de :

DOCTEUR DE L'UNIVERSITÉ PIERRE ET MARIE CURIE

Sujet de la thèse :

Liquides ioniques sous confinement nanométrique unidimensionnel

soutenue le 20 octobre 2015

devant le jury composé de :

Prof.	Jean Le Bideau	Université de Nantes	Rapporteur
Dr.	Arnaud Desmedt	Université de Bordeaux 1	Rapporteur
Prof.	Aleksandar Matic	Chalmers University of Technology	Examinateur
Dr.	Denis Morineau	Université de Rennes 1	Examinateur
Dr.	Anne-Laure Rollet	Université Pierre et Marie Curie	Présidente
Dr.	Patrick Judeinstein	CEA Saclay	Invité
Dr.	Jean-Marc Zanotti	CEA Saclay	Directeur de thèse

Acknowledgements

This PhD work has taken place at the Laboratoire Léon Brillouin of CEA of Saclay. I would like to thank the laboratory director Christiane Alba-Simionesco and the deputy directors Jean-Paul Visticot and Eric Eliot for welcoming me to the laboratory and guaranteeing me excellent work conditions during these three years.

I am very thankful to Jean Le Bideau and Arnaud Desmedt for accepting to be the referees of my work and to Denis Morineau, Anne-Laure Rollet and Aleksandar Matic for accepting to be my thesis examiners.

I would like to express all my gratitude to my two supervisors Jean-Marc Zanotti and Patrick Judeinstein, who have followed me during these three years. I thank them for their support and patience they always showed me during my PhD and for the confidence in me. Furthermore I have particularly appreciated their pleasantness and their continuous helpfulness which made my stay at the LLB a very good experience.

I would like to thank also the other members of the "Ionic Liquids Dream Team".

First of all I thank Quentin Berrod, who has always showed me his availability, support and enthusiasm during all phases of my doctorate (from the measurements to the defense). I am grateful for the time he spent discussing all topics stretching from the QENS data analysis to the French grammar (I would try not to forget his lessons).

I also thank Kuldeep Panesar, who helped me to settle in the laboratory (and in Paris) and introduced me to the world of ionic liquids.

The results obtained during these years have been possible thanks to collaboration and the advice of several people that I met during my PhD and I would like to thank all of them: the group of LITEN of Grenoble composed by Jean Dijon, Adeline Fournier , Hélène Le Poche and Raphael Ramos for the synthesis of the carbon nanotubes; Jacques Ollivier, local contact of IN5 (ILL); Stéphane Rols, local contact of IN4 (ILL); Peter Fouquet and Orsolya Czakkel local contacts of IN11 (ILL); Victoria Garcia-Sakai, local contact of IRIS (ISIS); Ralf Gilles, local contact of SANS-1 (MLZ); Stéphane Longeville, local contact of MUSE (LLB)

and Alain Lapp local contact of PAXY (LLB); Daniela Russo who allowed me to perform some tests on IN16; Fernando Formisano (ILL), Sandrine Lyonnard (INAC) and Stefano Mossa (INAC) for their time spent to discuss about my results of my QENS study and their precious advices; Marie Plazanet (LIPHY) for the tests of transient grating spectroscopy; Cristina Iojoiu (LEPMI) for the PFG-NMR measurements. Benoît Coasne (PSM) for the useful advice concerning the developed model for the neutron data analysis; Doru Constantin (LPS) for the measurements on MOMAC and the help for data analysis; Dimitrios Sakellariou (LSDRM) and Angelo Guiga (LSDRM) for their help in the NMR tomography measurements; Patrick Bonnaillie (SLIC) for the SEM measurements; Emanuelle Dubois (PHENIX) for her advice about the colloidal solution in the ionic liquids; Sanat Kumar (Columbia University) for his advice on the development of model and the DSC measurements.

I would like to thank all LLB members, who have always shown their openness to discussion and the availability to give a helping hand whenever needed. In particular I would like to thank: José Teixeira for spending his time helping me with data interpretation and for introducing me to the small angle neutron scattering; Didier Lairez and Giulia Fadda for their help during voltage clamp and dynamic light scattering tests; Fabrice Cousin for his support in the SANS data reduction; Stéphane Longeville for his several explications concerning the neutrons spin-echo.

Then I would like to thank all the students and postdocs for all the everyday life that we have shared and has been very nice: Philipp, Quentin, Marc-Antoine, Kuldeep, Nicolas, Adrien, Zineb, Antoine, Émilie, Maïva, Sumeyye, Eva, Alexandre, Yann, Simone, Albane, Mikkel and Grâce.

In conclusion I thank my family, my parents and Giulia for their continuous support and patience.

Contents

Introduction

Why this thesis?

Batteries designed for hybrid electric vehicles should be able to provide both high energy and power densities. In comparison to other electrochemical storage systems Lithium (Li)-ion batteries are known to deliver very high energy densities (150 Wh/kg). This property is associated with faradic reactions that take place within the volume of active grains by simultaneous ions and electrons uptake/removal. However, the amplitude of such reactions being large with respect to the amount of ions available in the porosity of electrodes, power performance (1-3 kW/kg) are usually frustrated by slow ionic "refuelling" from the electrolyte. The opposite holds for supercapacitors that provide relatively high power densities (10 kW/kg) at the expense of energy (5 Wh/kg) because storing reactions (capacitive ions adsorption and pseudocapacitive surface redox reactions) are confined to the surface. Accordingly, a gap appears in the Ragone Power/Energy plot because no system fulfils both power and energy requirements (Figure 1).

To fill this gap (shown in red on Figure 1), constant and regular progresses are obtained by improving the capabilities of each elements of the battery: chemical composition and structure of the positive and negative electrodes, nature of the electrolytes. But these incremental step by step improvements of the order of 10% each time are far from being able to challenge the logarithmic scale gap shown in red on the Ragone plot Figure 1.

The ambition of this thesis is to identify a possible route for a gain of one order of magnitude in the instant power of lithium batteries.

Ionic Liquids: a safe electrolyte, but not efficient enough

Ionic Liquids (ILs) are organic cations based molten salts, with a melting points below 100°C. Thanks to their unique properties these liquids seem to be very promising for a wide applications set, which stretches from the catalysis to the electro-chemistry, involving very current topics such as nuclear fuel recycling and energy storage. Among all their particular features, ILs show a broad electro-

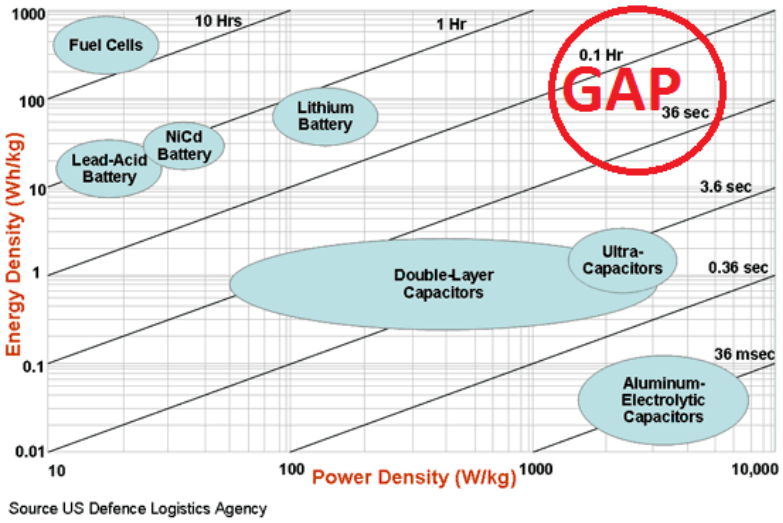

Figure 1: This so-called Ragone plot compares the performance of electro-chemical devices. While capacitors can deliver high power, their storage capacity is very limited. At the opposite, Fuel Cells can store large amounts of energy but offer low power output. The diagonal solid black lines on the plot indicate the relative time to charge/discharge of generic devices. The dynamic performances of capacitors and fuel cells/lithium batteries are opposite. Increasing the power of lithium batteries is a major challenge of modern applied electrochemistry. From USDLA and http://www.mpoweruk.com

chemical window and nearly null volatility and flammability, which make them very promising as electrolytes in electrochemical devices such as lithium accumulators.

As evidenced by a pre-peak measured by X-rays diffraction in the 0.2-0.4 Å^{-1} region (Fig.2) [4], most of ILs are characterized by a nanometric structuration. As it generates density fluctuations within the liquid that reduces the ionic mobility, this propensity to self-assembly in transient nanoscopic domains represents an unfavourable condition for the ionic conductivity.

A promising route for better conductivity: nanometric confinement

In numerous real life situations, molecular systems are not found in bulk but instead trapped in limited volumes of nanometric size: this is nanometric confinement. The complex interplay of the confinement topology, dimensionality (3D to 1D) and surface/volume ratio significantly affects the physical properties of the

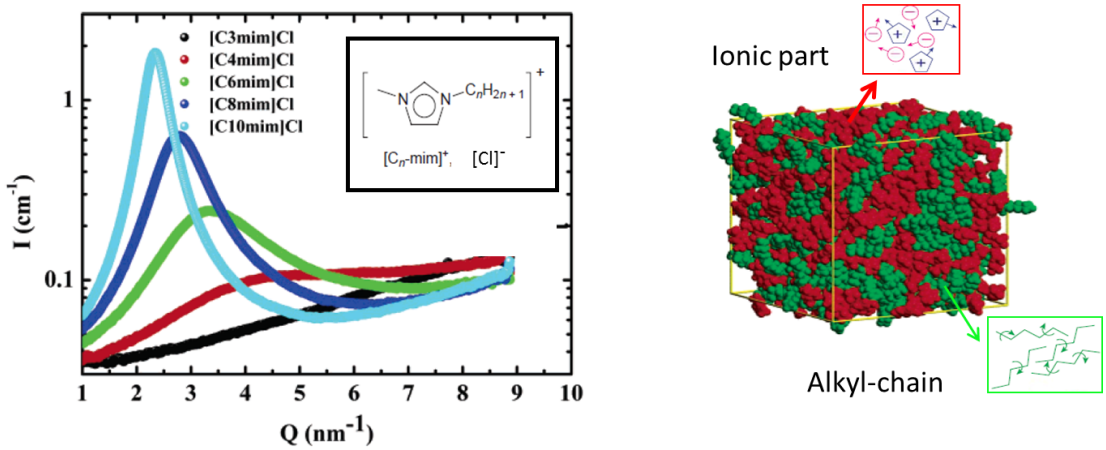

Figure 2: In the left: Example of the pre-peak measured by X-rays diffraction on 1-alkyl-3-methyl imidazolium chloride. In the insert example of an IL cation/anion couple. The index n mark the number of CH_2 composing the cationic side alkyl-chain. This figure is modified by the references [4] and [5]. In the right: molecular dynamics snapshots (size of the box 6*6*6 nm^3) of the nanometric structuration of the OMIM-PF_6 inducing the prepeak in the structure factor shown in the left (after [6]).

confined material. Water confined inside a 1.4 nm diameter CNT is a perfect example of the unexpected effect induced by nanometric confinement. As shown by Kolesnikov et al. [7] such a strong confinement drives a very specific organization of the water molecules. As a consequence, at the macroscopic scale, when forced inside a CNT membrane, water is found to flow-up three orders of magnitude faster than predicted by the continuum hydrodynamics picture [8].

A recent patch-clamp study has demonstrated that an IL confined in a nanometric pore ($\oslash \approx 20$ nm) shows an ionic conductivity one order of magnitude higher than its bulk analogue [9]. Depending on the ionic liquid, the transport of charge carriers is strongly facilitated or jammed. This higher conductivity is ascribed to a cooperative effect of ions motions in confined geometry. These results suggest that the confinement in a space whose dimension is comparable to the size of the characteristic fluctuation of the systems, could induce considerable changes in the IL transport properties. Confinement therefore seems to be a route to significantly increase the ionic conductivity of IL.

Confinement of ionic liquids within nano-pipes

Confinement of molecular liquids is a notorious way to obtain thermodynamical deviations from the regular bulk properties. It can for example be used to tune

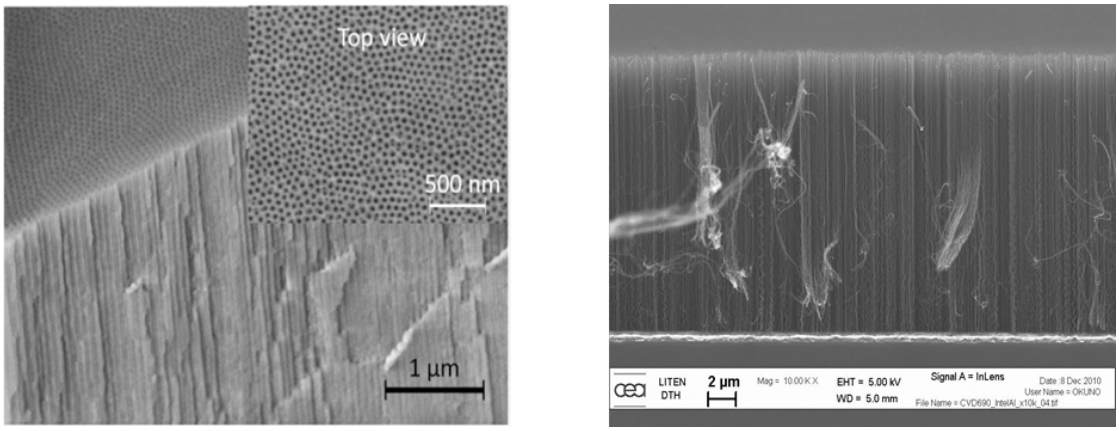

Figure 3: Real samples showing both nanometric porous structure and macroscopic orientation. Left) Anodic Aluminum Oxide (AAO) membrane. The parallel pore network starting on the top and going down the bulk of the membrane is clearly visible. Right) Carbon NanoTube (CNT) forest produced at LITEN/DTNM/LCRE. While AAO samples naturally come as membranes, specific treatments of the CNT forest is needed to turn them in CNT membranes.

very significant temperature depression of the melting point. It is nevertheless important to keep in mind that such thermodynamic upheavals are only the direct visible consequences of significant structural changes that, in turn, induce specific dynamical behaviours.

Even in the recent past, confinement was achieved in media with no macroscopic orientation: "powders" in the crystallographic sense of this word. This had two consequences when probing the physical properties of confined fluids:

- first, all the retrieved structural and dynamical information was blurred by isotropic average: key points like for example the relative directions of the motion of a molecule by respect to the pore (radial or longitudinal) are basically lost.

- at a second level, the tortuosity (imposed by the pore morphology and/or the random spatial arrangement of the powder grains) was making it extremely challenging to link the local (few Å or nm) transport properties, like the self-diffusion coefficient, to the macroscopic transport flow of the material.

But, following recent progress in inorganic chemistry, porous media with pores showing macroscopic orientation are now available (Figure 3). Such nano-pipes made of oriented tens of micrometer-long pores with diameters down to 1-10 nm have come to reality. Lifting the "powder average" limitation can therefore be easily achieved by orienting the porous sample in a measuring device (confocal

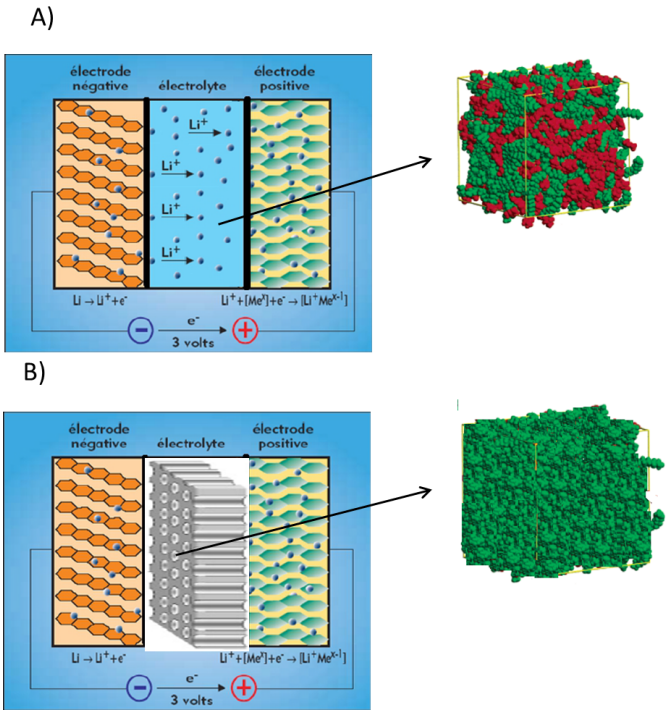

Figure 4: A) Sketch of lithium battery using an IL as electrolyte. The self-organisation produces the density fluctuations (shown on the right), which reduce the ionic mobility. B) Sketch of lithium battery using a confined IL as electrolyte. In this case the liquid confined in a porous matrix, whose pores show a 1D anisotropy along a direction perpendicular to the electrodes. In the confined state we expect that the self-organisation could be reduced and the ionic motion enhanced along the pores axis.

microscope, spectrometers: NMR, IR, Neutron...). It is then relatively easy to firmly disentangle dynamical phenomena in the parallel or radial direction to the pore axis. We argue below that taking advantage of the enhanced flow in one dimension has a prime technological relevance.

On this basis, the goal of this work is the study of the 1D nanometric confinement effect on the ionic liquids transport properties. Our idea is to frustrate the formation of the IL nanometric domains using confinement within macroscopically oriented controlled porous structure membranes.

As confinement matrix, we have used Anodised Aluminium Oxide (AAO) porous membranes. In this systems it is possible to tune the pores size between 20 and 300 nm, without modifying the matrix topology. This enables to develop a study of the ILs properties as a function of the confinement size. On decreasing the

pore size, we expect that the pre-peak will vanish and therefore i) to be able to estimate the characteristic size of the IL domains ii) to develop a full characterization of the confined "desegregated" IL transport properties.

As it imposes a ionic diffusion alongside a preferential direction, the use confinement space with an axial anisotropy (1D confinement) could give a further benefit to the ion conductivity, and could represent a remarkable benefit for the ILs use in batteries (see figure 4).

Nevertheless, 10 nm is the minimal pore diameter achievable with AAO. This confining material therefore does not allow to probe confinement size under severe confinement conditions i.e. of the order of the size of few IL molecules. Moreover the AAO pores surface are covered by hydroxyl groups which can interact with the liquid ions and induce detrimental surface effects. These limitations are easily overtaken by the carbon nanotubes (CNTs), which have diameter of few nm and smooth and inert walls. This feature allows to observe the effects due to the tight confinement with limited interaction with the confining surface.

This manuscript is composed of three chapters. In the first one we propose a study on the ionic liquids bulk properties. The goal of this section is to understand the implication of the self-organisation in the liquids dynamical properties. For this purpose we have divided this analysis in two section. The first one consists in a diffraction study performed in order to quantify the degree of the organisation of the liquids and the main parameters which characterize this phenomenon. The second is related to the dynamical features of these systems. In this study we demonstrate the limit of a classical phenomenological analysis, and we develop a multiscale approach([1 ps-2000 ps] and [0.1 $Å^{-1}$ -3 $Å^{-1}$]) based on several Quasi Elastic Neutron Scattering (QENS) techniques. This physical appealing model can both qualitatively and quantitatively describe the role of the self-organisation on the dynamical quantities. The robustness of this model is confirmed by QENS experiments on a specifically deuterated sample. An achievement of this new analysis is to be able to disantangle the complex dynamic interplay of the cation side-chains to assess the pure long range translational diffusion coefficient of the cation center of mass. This is a critical quantity as, through the Nernst-Einstein relation, it drives the key information at stake for batteries electrolytes: ionic conductivity.
This original model of the IL dynamics at the local scale (few nm and ns) is then used to probe the dynamics of IL under confinement, first in AAO membranes (large pores and strong surface effects), then in CNT membranes (narrow pores and no or limited surface effects).
The second chapter of this manuscript focuses on the ionic liquids properties when they are confined in alumina membranes. A first part is dedicated to the AAO confinement effects on phase transition temperatures. The goal of this section

is to demonstrate the importance of both the surface effects and the pores size for determination of the thermophysical properties of these systems. The most important part of this study is however dedicated to the confined liquids properties at the molecular level. The main goals of this analysis is to quantify the confinement effects on the liquids self-organisation and the impact of the eventual structural modifications on the dynamical properties. By a diffraction study we develop a quantitative analysis of the changes induced by the confinement on the self-organisation. We show also that our model of the IL dynamics holds under AAO confinement.

In a third chapter, we then use the model that we have developed to discriminate the radial and the axial dynamics of IL in macroscopically oriented narrow pores of CNT membranes. We extend this analysis by PFG-NMR and impedance spectroscopy measurements to probe the transport properties at the mesoscopic scale (μm and ms).

Chapter 1

Ionic liquids in the bulk state

This chapter is dedicated to the study of the bulk ILs properties. It is a first fundamental step for the understanding of the confinement effects observed in the different systems overviewed in this work.

The first part of this section is about the ILs self-organization behaviour. We will show how the cation hydrocarbon chain length plays a key role in the formation of the structural heterogeneities.

In the second part of this chapter we will focus on the liquids dynamics. The goal of this part is to demonstrate the influence of the self-organization on the ionic dynamics. For this purpose we choose to use the quasi-elastic neutrons scattering (QENS) for studying the liquids dynamics at the molecular the scale. We will begin to analyse the experimental data using firstly a phenomenological model and then we will develop a more accurate multi-scale approach. At the end of this section we will show the coherence between the obtained results by this approach and those observed by the study of the structural ILs properties.

1.1 Historical hints

The origin of ILs dates back to the beginning of 20^{th} century. The first IL was discovered by Walden in 1914, with his study on ethylammonium nitrate formed by the neutralisation of ethylamine with nitric acid [10]. In this report Walden defines this liquid as: "an organic molten salt with a melting point lower than 100°C". This first definition survived in the years and it has become the classical definition of IL which is still used nowadays. Another important feature, highlighted by the author in this report, is the presence in the liquid of an "ions association" which is, even now, a topic of debate.

The Walden's results defined thus the basis for the development of new class of materials. Before the ILs discovery, the study of molten salts was limited by the

necessity of very high temperatures for reaching the compound melting point (mp) (e.g. for the NaCl the mp is around 804° C). With the ILs advent this condition is no more necessary, because it is possible to work at relatively low temperatures for obtaining the salt melting. This first discovery gave the access to a new kind of compounds which show some unique properties. The ILs are systems in the liquid phase composed at 100% by charged elements. These particular properties aroused the interest of the international community, who began soon to perform several studies about the features and the possible application fields of these salts.

The first ILs based application was found in the 1930s. In 1934 an US patent demonstrated that these liquids can be used for treating the cellulose [11]. It has been shown that ILs can break the cellulose molecules and reducing this biopolymer in a more reactive form, that can be used later in other chemical reactions. From this first discovery, the use of IL for the cellulose dissolving processes was more and more improved and, nowadays, these liquids are still used in several industrial applications concerning the cellulose treatment [11].

The other field, where ILs seemed to be very promising, was that of the electrochemical applications. Their intrinsic ionic nature made these compounds very good candidates for being used as liquid electrolytes in electrochemical devices, such as the batteries. However, for developing this topic, it has been necessary to obtain compounds with mp below the room temperature. An intensive work was thus performed during the second half of 20^{th} century, in order to synthesise new salts which were liquid at room temperature (called *room temperature ionic liquids* (RTILs)). A first approach was tried using mixture aluminium chloride salts with different cation such as 1-butylpyridinium [12] and 1-alkyl-3-methylimidazolium [13]. These methods produced ILs which have mp below 0°C under some specific conditions. However the stability of liquids showed a great sensitivity to environment moisture. This represented a big limit in the ILs application because it obliged to work in the inert atmosphere box.

The big change in the ILs field was achieved with the advent of the "air and water stable ILs" [14]. With this discovery the ILs became finally a kind of system which was easy to handle. This generates an increase of interest from the international community who began to invest big amount of energy and money on the study of the properties of these salts. An effect of this interest growth is shown in figure 1.1, which shows the exponential boost of patents and publications about ILs in these last years.

The increase of the results about ILs causes also an augmentation of the amount of ILs easily available. For giving an example, in 2007 it was estimated there are at least 1 million of ILs which can be synthesised [11]. This number can give the idea about the increasing interest on ILs that, in the last twenty years, has captured the attention of the scientific and industrial communities.

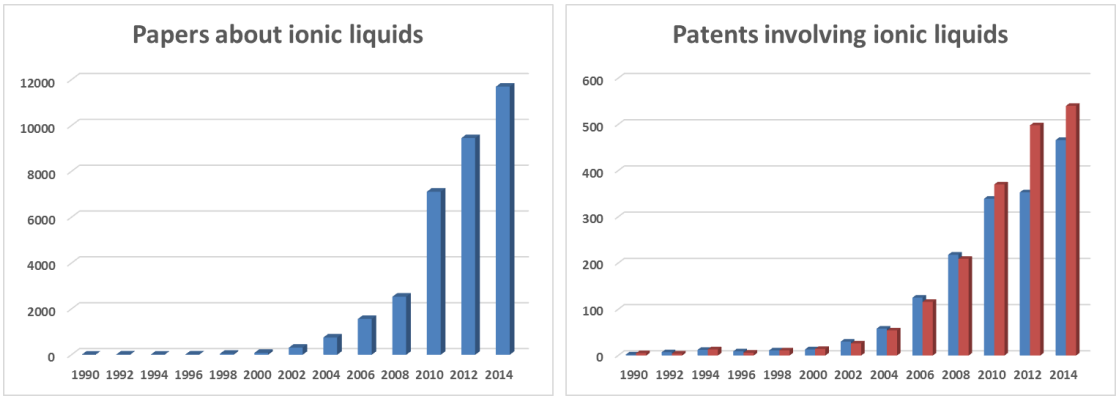

Figure 1.1: Left: number of the published papers about ILs between the 1990 and 2014. The research was done searching the words "ionic liquids" in the web of knowledge data bases. Right: number of the filed patents about ILs between the 1990 and 2014 (for courtesy of Marco Campani). The values was obtained by the data bases "patent scope" and "espacenet". In both cases we can observe an exponential growth of the scientific production.

1.2 Self-organization at the mesoscale

1.2.1 State of the art

1.2.1.1 Ions ordering

One of the crucial features about ILs is the ions arrangement inside the liquid. It is known that in the liquid state it is impossible to observe an extended order as in the crystalline phase, however we will show that the electrostatic interaction between the ions can influence the ions disposition at local scale (few Å).

The first study in this context was performed on 1,3-dimethylimidazolium chloride (DMIM-Cl) [15]. In this work it was measured the neutron diffraction pattern of the protonated and deuterated liquid in order to extract the pair correlation functions ($g(r)$) of the couple cation-anion and cation-cation. An example of the obtained pair correlation functions is shown in figure 1.2.

From this plot we can notice that, both pair correlation functions show an oscillating trend with at least two principle maxima. At each peak corresponds thus the presence of ions shell which is formed around the cation. The shift of the two g(r)s maxima shows, furthermore, that two shells of the same ion are separated by another one composed by the other ionic specie. However the diminution of the peaks intensity with the increase of the distance demonstrates that this correlation has a limited range of few Å.

A similar behaviour was also observed on other DMIM based ILs having bigger

anions such as hexafluorophosphate (PF_6) [16] and bis(trifluoromethyl)sulfonylamide (TFSI) [17], suggesting that this ordering is common for all ILs. Moreover it was also observed an expansions of the ions packing proportional to anions size which seems to increase of the number of anions populating the first shell [17].

1.2.1.2 Self-organisation at the mesoscale

Another particular feature about the ILs structural properties is their self-organisation at the nanometer length scale.

In the ILs cation has a general complex structure composed by a polar (the charged zone) and a-polar (the alkyl-chain(s)) part. This complexity generates thus the presence of multiple intermolecular interactions which differentiates the ILs from the simple inorganic salts. In these latter the only interaction between the ions is due to electrostatic force. In the ILs, instead, the presence of the a-polar moieties introduces in these systems other interactions such as Van de Waals and inductive interactions which contrast the Coulomb forces between the charges. This complex interplay generates thus a sort of segregation at the nanoscopic scale between the polar and a-polar part of the liquid.

One of the first studies which pointed out this aspect was the molecular dy-

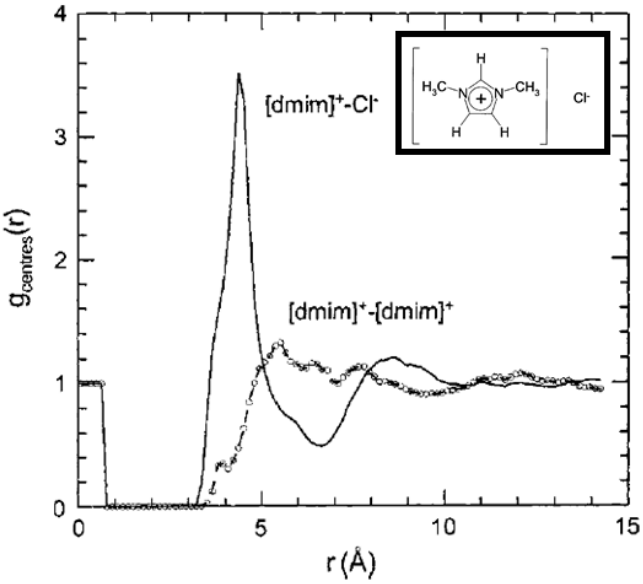

Figure 1.2: Pair correlation function of the cation-cation (solid line) and cation-anion distribution (circles+lines) obtained from the neutron diffraction data on DMIM-Cl. In the insert the cation-anion couple is shown. This picture is taken by the reference [15].

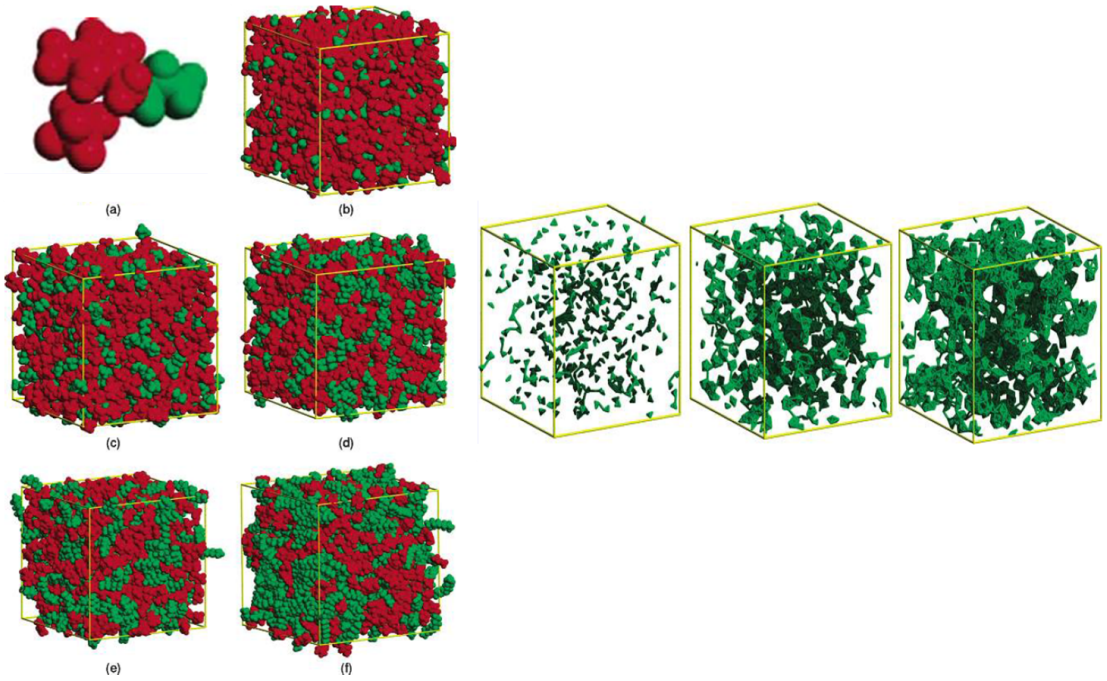

Figure 1.3: Left part: Frame (a) ionic couple explaining the color code used during the MD simulation: green part represents the a-polar tail of the cation while the red one refers to the charged parts of the system (the imidazolium heads+the anions). Frame (b-f) snapshots of the simulation boxes of the different simulated liquids, the box size is in the parentheses :the C_2MIM-PF_6 (b), the C_4MIM-PF_6 (l_{box}=49.8 Å) (c), the C_6MIM-PF_6 (l_{box}=52.8 Å) (d), the C_8MIM-PF_6 (l_{box}=54.8 Å) (e) and the C_{12}MIM-PF_6 (l_{box}=59.1 Å) (f). Right part: topology of the a-polar domains for the C_2MIM-PF_6 (left), C_4MIM-PF_6 (middle) and the C_6MIM-PF_6 (right). We can notice that when the chains grow the a-polar domains size increases and they begin to form a sort of continuous phase. This picture is modified by the reference [6].

namics (MD) approach of Padua et al. [6]. In this work the authors studied the structural organisation of the ILs C_nMIM-PF_6 series using the force field MD technique. The results of their analysis are summarized in figure 1.3.

Let's begin to consider the left part of this figure. The color code is explained in the frame (a), where it is shown an example of ionic couple considered in this study. The green spots represent the a-polar tails of the cations whereas the red ones refer to the charged parts of the system (i.e. the imidazolium heads+the anions). The other frames show instead the snapshots of the simulation boxes of the different studied liquids in this work: the C_2MIM-PF_6 (b), the C_4MIM-PF_6 (c), the C_6MIM-PF_6 (d), the C_8MIM-PF_6 (e) and the C_{12}MIM-PF_6 (f). If we observe the pictures we can notice that the charged part of the liquids develops

a 3D polar network surrounded by a-polar domains formed by the cations tails. If we consider the simulation boxes dimension (reported in the figure 1.3 caption) we can ascertain that these domains have a nanometric size. Furthermore we can also notice that the liquid structure changes as a function of the chain length. For the ILs with short cationic tails the charged network shows a good continuity in the space, which is locally interrupted by the presence of the a-polar domains. On the other hand, when the chains grow, we can observe that the charge symmetry is always more and more disrupted as the a-polar domains raise. They begin to be a continuous phase forming a sort of "Bicontinuous microphase" for very long chains. For a better clarity, the growth of tails domains in function of the chain length is highlighted in the right part of figure 1.3 where it is shown that for long chains the domains are interconnected and they forms a spongelike structure.

From the MD simulations Padua et al. calculated the ILs structure factor, predicting the presence of a peak in the Q region, between 0.2 and 0.5 $Å^{-1}$, due to distance between two polar (or a-polar) zones [6].

The first experimental evidence of the ILs self-organisation was produced by Triolo and co-workers [4]. In their work the authors measured by small angle X-ray scattering (SAXS) the structure factor of two ILs series: the alkyl-imidazolium tetrafluoroborate C_nMIM-BF_4 and the alkyl-imidazolium chloride C_nMIM-Cl. From these measurements it was shown the existence of the first sharp diffraction peak (FSDP) at low Q region as it was predicted by Padua's simulations (see example in figure 1.4). Due to it particular position, which is for wave vector values much smaller than those of the classic liquids FSDP, this peak was called *pre-peak*. This name was then used in literature as the typical name for defining this self-organisation signature.

In this study Triolo's and al. defined thus an IL self-organisation correlation length associated to the pre-peak position by the simple relation L= $2\pi/Q_P$. It was demonstrated that this latter shows a linear relation with the alkyl-chain length [4] (see insert Fig.1.4). This result confirmed thus the Padua's theory of the a-polar tails segregation. Furthermore, it was also observed the liquid organisation is strongly temperature dependent, suggesting that the IL ordering is perturbed by the ions dynamics [4].

After the Triolo's group analysis, several studies, based on diffraction techniques, were performed on other different imadazolium based ILs having bigger anions such as the PF_6 [18], or the TFSI [19, 20] and even on ILs having different cations [21], confirming the presence of the ILs self-organisation. It was also observed that in the case of cation with very long chain (more than twelve CH_2 groups) the IL shows a more ordered organisation consisting in a smectic phase at room temperature [5, 22].

Recently the work of Zheng et al. has demonstrated that the pre-peak proper-

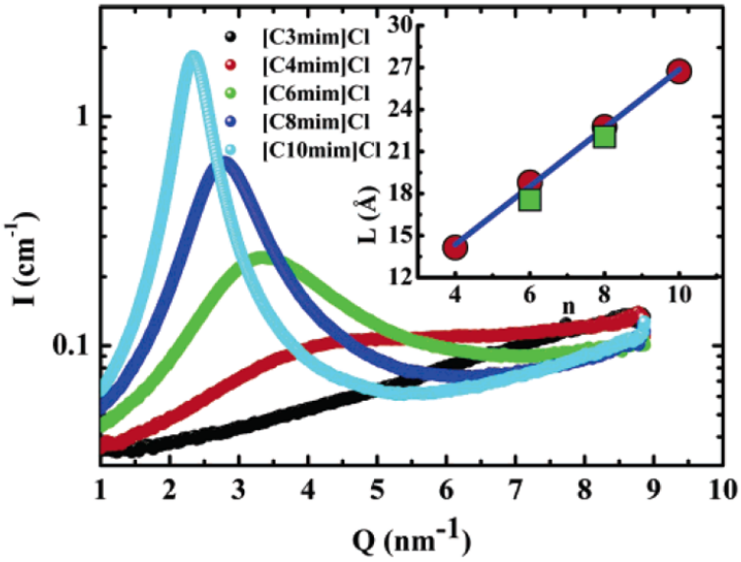

Figure 1.4: Diffraction patterns of $C_n$mim-Cl with n=3,4,...,10 at room temperature. We can observe the pre-peak appearance at n=4 indicating a correlation at the nanometer scale. In the insert the plot of correlation length L, calculated as L= $2\pi/Q_P$ (Q_P is the postion of the pre-peak), in function of the cation alkyl-chain length for the $C_n$mim-Cl (circles) and $C_n$mim-BF_4 (squares). This picture is taken by the reference [4].

ties are influenced also by the cation symmetry [23].

In parallel of these experimental works, the Padua's MD approach was reclaimed and applied on other systems [24–26] in order to complement the information given by the diffraction measurements. The recent work of Annapureddy at al. has finally demonstrated that the pre-peak position is related to the typical distance between two adjacent cations charged heads separated by an apolar domain [25].

In conclusion a consensus seems to emerge about the existence of a common ILs self-organisation due to the segregation of the a-polar tails. However there is still an open debate about the morphology of this ordering. These days we have no proof of experimental or simulation technique which could affirm definitely which shape is adopted by the ions aggregates. For the moment there are some different theories, which suppose different possible morphologies. Some authors affirm that the segregation is just a deformation of the solvatation shell due to the asymmetric shape of the cation [27], while others propose that the self-organisation acquires some specific morphology such as alkyl-chains channels [6], micelle [18] or lamellar structure [28] (see figure 1.5).

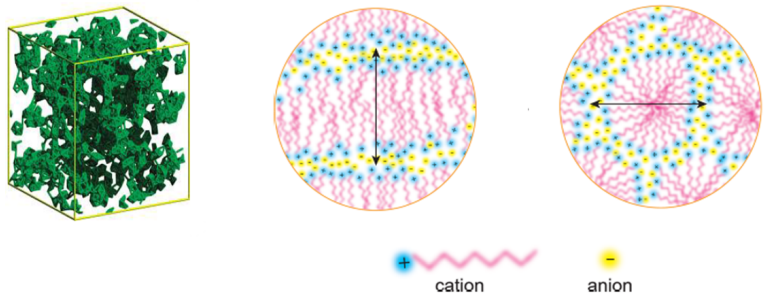

Figure 1.5: Various examples of possible IL self-organisation morphologies. From left to right: alkyl-chain channel (the green parts are the tails domains while the empty ones are polar zones), the micelle like and the lamellar structure. This picture is taken by the references [6] and [28].

1.2.2 Self-organization: a SANS analysis

The goal of this section is the study of this particular property especially in relation with the couple cation-anion present in the liquid. The purpose of this analysis is to demonstrate that the key-parameter driving the structuration is the length of the cation a-polar alkyl-chain.

In fact in the ILs the ions electrostatic interactions are in competition with the attractive Van der Waals forces between the cationic a-polar parts. When the alkyl-chain is long enough (i.e. for four or more methanediyl groups [4]) the interplay between these interactions produces an organisation at the nanoscale of the ILs ions. Molecular dynamics simulations show that the charged parts of the ions (i.e. the anions and polar head of cations) organise them-selves in nano-aggregates which are surrounded by a-polar network constituted by the cationic alkyl-chains (see Fig.1.6A) [6]. It was shown that this segregation is sharper with longer chain owing to the augmentation of the Van der Waals forces. This organisation produces a peak in the ILs structure factor in the low Q region (between 0.2 and 0.5 $Å^{-1}$). This so-called "pre-peak" has been observed experimentally on different ILs [4, 20, 28] (Fig.1.6B). It was shown that the position of the peak (Q_P) is defined by the relation [18]:

$$Q_P = \frac{2\pi}{L_D} \tag{1.1}$$

where L_D is the distance between the center of mass (c.o.m.) of two aggregates (see the set of the Fig.1.6B). Thus measuring the structure factor of these liquids, we can observe directly the physical signature of the ILs organisation at the nanoscale.

In this work we have chosen to use the Small Angle Neutron Scattering (SANS)

technique to assess the structural organization of these systems. This technique measures the elastic scattering intensity of a monochromatic neutrons beam occurring at small scattering angles. This allows to determine the static correlation of the sample, taking place at distance much longer than the typical interatomic distance.

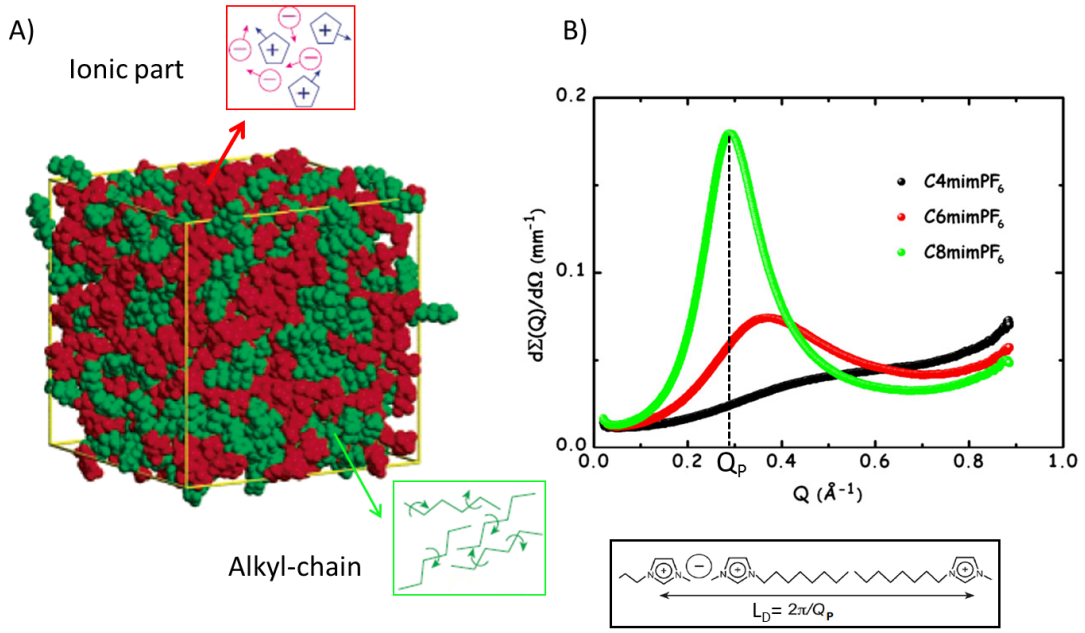

Figure 1.6: A) Simulation box taken by the reference [6], which shows the self-organization in the IL OMIM-PF_6 (adapted by the references [6, 29]). The red parts represent the charged part of ions (anions and imidazole head), while the green ones are constituted by the a-polar cationic alkyl-chains. B) Structure factor measured on different $C_nMIM-PF_6$ (adapted by the reference [18]). We can note that for long alkyl chain we can distinguish the pre-peak due to self-organization. The inset explains how the pre-peak position Q_P is linked to the distance between two aggregates c.o.m. L_D (adapted by the reference [28]).

In our study, in order to decorrelate the effects of the cation and of the anion on the ILs self-organization we have chosen four samples of molten salts with different couples of ions:

- 1-Butyl-3-methylimidazolium bis(trifluoromethanesulfonyl)imide (BMIM-TFSI),
- 1-Methyl-3-octylimidazolium bis(trifluoromethanesulfonyl)imide (OMIM-TFSI),
- 1-Methyl-3-octylimidazolium tetrafluoroborate (OMIM-BF_4),

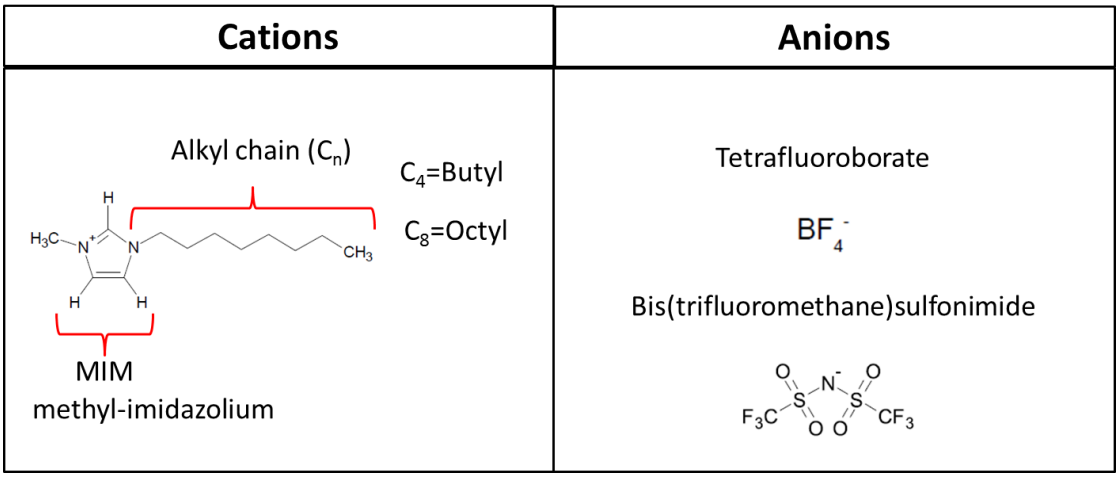

Figure 1.7: Cations and anions couples studied by SANS. In the four cases we considered imidazolium based RTILs, with the two possible cations having two different hydrocarbon chain length.

- 1-Butyl-3-methylimidazolium tetrafluoroborate (BMIM-BF_4).

All of these samples are imidazolium based RTILs. The cation (see Fig.1.7) is an organic molecule composed by a charged head of imidazole plus an a-polar alkyl-chain. In this work we have opted for two kinds of cation: one with a long alkyl-chain composed by eight CH_2 groups (octyl-chain) and a second one with a shorter chain composed by only four methanediyl groups (butyl-chain). On the other hand we have picked as counterion bis(trifluoromethanesulfonyl)imide (TFSI) and tetrafluoroborate (BF_4), which have different sizes and properties.

The SANS measurements were done on the spectrometer PAXY [30] of Léon Brillouin Laboratory (CEA-CNRS) of the C.E.A. of Saclay. Since we were interested to determine the ILs correlation at the nanometer scale, we could narrow the observed Q range for values bigger than 0.1 $Å^{-1}$.

In order to observe the Q range from 0.1 and 0.7 $Å^{-1}$, each ILs spectrum was measured at room temperature with an incident wavelength λ =3.5 Å and a detector distance D=1.2 m.

The four ILs measured spectra, after an isotropic grouping, are shown in Figure 1.8A and 1.8B.

The first feature that we can observe comparing the spectra is that in the case of the OMIM based ILs the pre-peak is well defined. For the OMIM-BF_4 and the OMIM-TFSI we found a diffraction peak respectively nearby to 0.3 and 0.35 $Å^{-1}$. These values correspond to a distance between two aggregates c.o.m. (equation 1.1) of around 2.1 nm for the OMIM-BF_4 and of 1.8 nm for the OMIM-TFSI. On the other hand we can notice that for BMIM based ILs a broad bad-defined peak

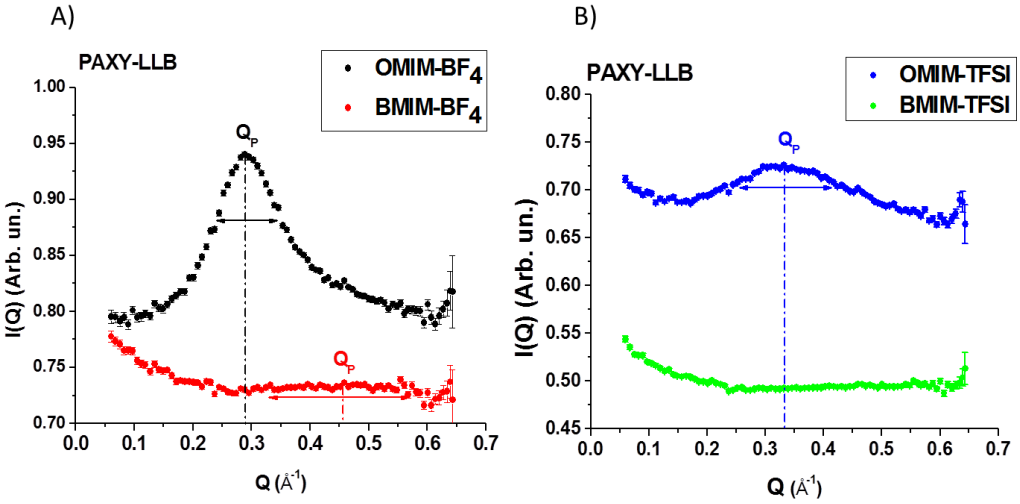

Figure 1.8: Measured structure factor of the four samples: A) spectra of ILs with BF_4 as anion, B) spectra of ILs with TFSI as anion. We can observe in the case of OMIM based liquids the presence of well defined peak due to the self-organization, while for the BMIM ILs we can notice a broad structure for the BMIM-BF_4. The dotted lines point the values of the position of peak maximum Q_P, while the arrows show the peak width. All of them are only eye guides.

is observable at Q=0.4 $Å^{-1}$ for the BMIM-BF_4 ($L_D \approx 1.4$ nm), while no peak is detected for the BMIM-TFSI. Many works in literature, based on simulation or experimental measures, show the presence of a pre-peak for the BMIM based liquids [4, 6, 18, 20, 26], however cause of the low organisation of the liquid the pre-peak has a shoulder shape. This feature requires a very good experimental resolution for detecting it, condition that is not assured by a SANS spectrometer in this range of Q ($\frac{\delta Q}{Q} \approx 15\%$). In addition at high wave vector the contribution of incoherent scattering begins to be not negligible and it can affect the quality of signal. We can then suppose that in the case of the BMIM-TFSI the limitations of the experimental technique don't allow to observe the peak. In conclusion this first comparison suggests that the cation side chains length is the key parameter for the formation of self-organization in the ILs. This result is coherent with the results present in the literature [4, 6, 20], where it was shown that the correlation peak tends to disappear with short alkyl-chains.

The other consideration that we can do is that the anion nature has no effect on the self-organization formation. We can notice, however, that it influences the features of the structural heterogeneities. In fact if we compare the pre-peak of OMIM-TFSI and OMIM-BF_4, we can notice that it position and it width are slightly different in the two cases. These differences suggest the anion influences

the average distance and the dispersion of the structural heterogeneities. This could be due to the difference of ion size or ion charge delocalisation between the TFSI and the BF_4. It was shown by Yamamuro et al. [28], that for more compact anion the peak doesn't change shape, while for bigger ions, as the TFSI, it features are slightly modified. We can conclude then the anion size could modify lightly the correlation properties of the ILs.

1.3 Dynamical properties of bulk ILs probed by QENS measurements

1.3.1 State of the art

When we try to characterize the elementary steps of the molecular motion in these systems, we find that the ionic dynamical behaviour is composed by a combination roto-translational relaxations [31]. The long alkyl-chain contributes in the dynamics of the cation introducing in the system dynamical spectrum all the moieties re-orientation dynamics. This feature makes very difficult to separate the part due the translational properties to the rest.

On other hand we can overcome this problem using techniques with spatial and temporal resolution larger than molecular ones, i.e. $R_s \gg 1$ nm and $R_t \gg 1$ ps. In this way the re-orientation dynamics is no more visible, because it is constituted by very localised and fast motions, and we have directly access to the ions translational motion. However, with these techniques, we can no more observe the elementary steps of the ionic diffusion, but we obtain only a global information averaged on thousands elementary steps.

The goal of this section is thus to illustrate the state of art of these two different experimental approaches. We have divided our explanation in two parts.

In the first one we will focus on the existent studies of ILs dynamics at the molecular scale. Since in this thesis we will focus particularly our attention on this topic, this part we will more exhaustive in order to give the means for understanding the studies developed in this work.

On other hand the second one is dedicated to the experimental approach which uses less resolute techniques for studying the ionic translational motion.

1.3.1.1 ILs dynamic at the molecular scale

One of the aptest experimental methods for probing the elementary steps of the ions motions is probably the quasi elastic neutron scattering (QENS). The techniques based on this process allow in fact to probe the sample dynamics at a very local scale (i.e. at the Ångström length scale and at the pico/nanosecond

time scale), giving simultaneously spatial and temporal information about the dynamical relaxations occurring in the system. Due to the large incoherent neutron scattering cross-section of the ^{1}H nucleus and the abundance of this element in ILs, QENS techniques give a global view of the IL dynamics as sensed via the averaged individual motions of its hydrogen atoms. This means the information extracted from these measurements involves the cation dynamics.

One of the first approach which used QENS for probing the ILs dynamics was that of Triolo and co-workers [32]. In this work the authors studied the 1-n-butyl-3-methylimidazolium hexafluorophosphate (BMIM-PF_6) dynamics in function of the temperature. From this analysis they pointed out the existence of two different relaxations in the liquid dynamical spectrum occurring in time range between 0.4 and 25 ps. In was shown that the time dependence of the faster one, called *β-relaxation*, followed a classical Debye relaxation:

$$I_\beta(t) \propto e^{-\frac{t}{\tau_\beta}} \tag{1.2}$$

where τ_β is of order of picosecond.

On the other hand it was observed that the slower one, defined as *α-relaxation*, showed a trend which was strongly non-exponential. The authors described it with the phenomenological Kohlrausch-Williams-Watts (KWW) function, which introduces the stretching parameter β ($0 \leq \beta \leq 1$) for describing the non-exponential behaviour:

$$I_\alpha(t) \propto e^{-\left(\frac{t}{\tau_\alpha}\right)^\beta} \tag{1.3}$$

where τ_α is the order of hundreds of picoseconds.

From this study Triolo's group observed that typical time constants of the two relaxations show a different temperature and space dependence, as it is shown in figure 1.9.

For the β-relaxation it was observed that τ_β changes weakly as a function of the temperature and wave vector. This result was interpreted as the signature of a very localised motion with a very low energy activation, that authors defines as "motion inside a cage whose spatial extent is approximately 0.7 Å" [32].

On the other hand the α-process seemed to be strongly temperature dependent showing a non-Arrenhius behaviour, which is a typical feature of many glass-formers [32]. The non-exponential trend is thus explained by the authors as a reminiscence of a cooperativity typical of the glass phase. Furthermore the presence of this latter together with the dispersive dependence of τ_α by Q, drove the authors to suppose that this relaxation is the print of the cation diffusion inside the liquid.

The innovative results given by the Triolo's group QENS study were thus the point of departure of several studies about the ILs dynamics.

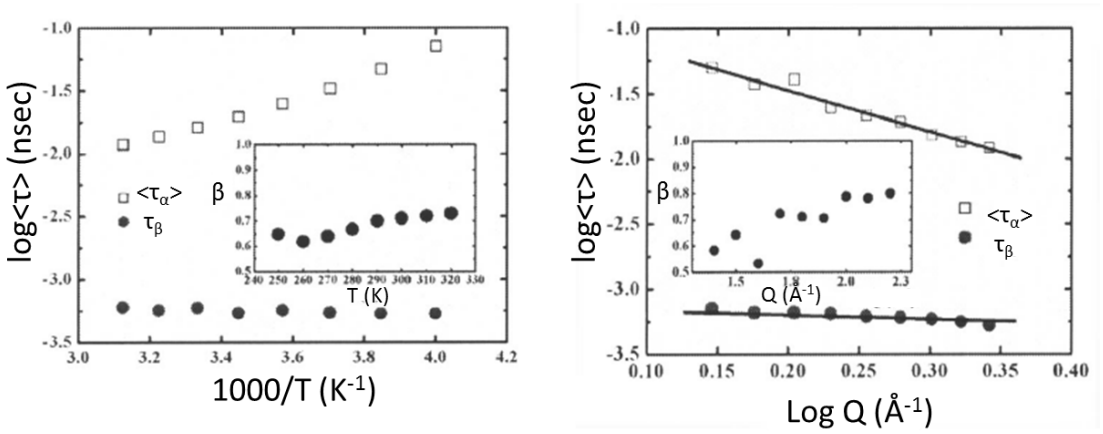

Figure 1.9: Left: Plot of τ_β and of the average τ_α measured at Q=2.0 Å^{-1} in function of the temperature. In the inset the value of the stretching parameter β measured at the same configuration. Right: Plot of τ_β and of the average τ_α measured at T= 300 K in function of the wave vector Q. In the inset the value of the stretching parameter β measured at the same configuration. We can notice that τ_α seems to be weakly dependent on these parameters while τ_β is strongly Q and T dependent. These plots were taken by the reference [32].

It was necessary making light on some features which were not clarified by this first approach. For example one open question was the molecular origin of the localised motion. A later study of Triolo's group justified the presence of this relaxation as the superimposition of multiple localised relaxations due to the cation re-orientation dynamics [33]. Similar excitations were observed by other more recent works [28, 34], underling the importance of the cation a-polar part in the cationic dynamics .

The origin of a localised motion was called into the question again with the discovery of the ILs self-organisation. Hu et al. showed by MD simulation that the BMIM-PF_6 ions show an heterogeneous translational dynamics [35]. The results of their simulations are summarized in figure 1.10, where is shown the cation mean squared displacement (MSD) at 400 K.

We can notice that the ion MSD shows three different regions: a ballistic behaviour (slope=2) for very short times (t< 1 ps), a plateau region (slope$\approx$ 0) and a diffusional behaviour (slope=1) for a longer times (t> 100 ps). These results show then that the cations see the effect of cage, produced by the presence of other ions, during their translational motions which is at the same time range where it was observed the IL β-relaxation [32]. Furthermore the MD simulation demonstrated that the ions could be divided in two ensembles, where one seems to move slower than a classic diffusional (or Fickian) process and the other faster

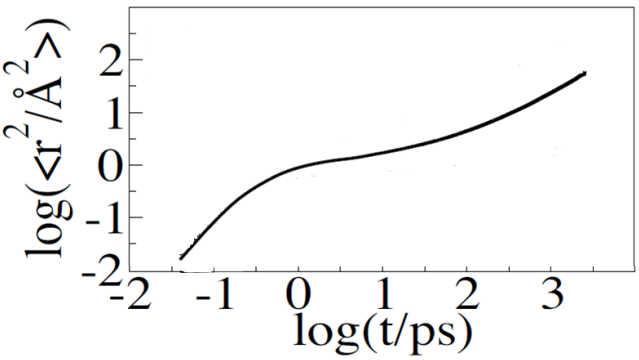

Figure 1.10: Cation MSD in the liquid BMIM-PF_6 at T=400 K determined by MD simulation. We can distinguish three main trends as a function of the time. A ballistic one (slope=2) for sub-picoseconds times, followed by an intermediate region where the ion is a subjected to a cage effect (slope≈0) and a Fickian diffusion (slope=1) for the long times. This plot is taken from the reference [35].

and the two groups seem have a spatial correlation between them. These results pointed out so, that the translational motion in the ILs can not represents by a simple diffusive behaviour, but it is composed by different processes. Moreover the founded spatial correlation suggested that the dynamical behaviour seems to be influenced by the structural organisation of the systems.

These conclusions gave another push for developing more sophisticated approaches for characterizing the ILs dynamics at the molecular level. Nowadays there are reports of numerous QENS studies, performed in order to characterize the re-orientational and translational contribution of the cation dynamics and the effect of self-organisation on the dynamical features of the ILs [28, 29, 34, 36–40].

Between them we want to cite the recent works of Embs and co-workers, which studied the dynamics of pyridinium based ILs by QENS [34, 38–40]. In these references the authors demonstrated that the cation diffusional motion is constituted by two main process, whose sketch is shown figure 1.11.

The first one is a fast diffusional motion, to which we can associate a self-diffusion coefficient called D_{loc}. This is a single particle excitation (i.e. each hydrogen is decorrelated from the others), where each nucleus moves inside a confined space (of size 2σ), which could have different size in function of which hydrogen atoms we are considering.

On the other hand there are another diffusional process, much slower than the first one, at which we can associate a self-diffusion coefficient called D_{tr}. This is, instead, a collective excitation which represents a global diffusion of the entire cation [38].

In conclusion QENS based studies has demonstrated that the ILs dynamics any-

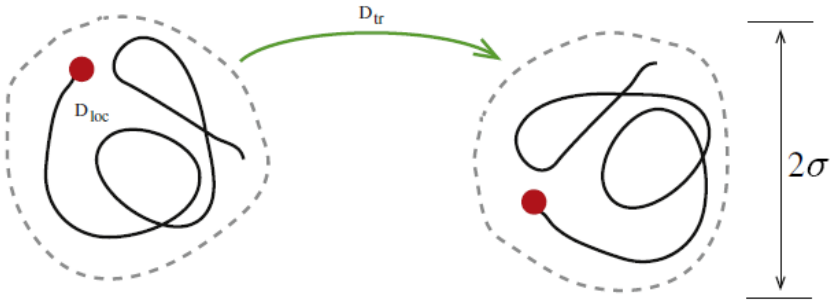

Figure 1.11: Sketch of cationic translational motion hypothesized by Embs et al. Each hydrogen nucleus (red sphere) has a rapid diffusion confined a space of size (2σ), at which a self-diffusion coefficient D_{loc} is associated. This consists of a single particle relaxation so each hydrogen diffusion is decorrelated from the diffusion of the other atoms. On the other hand there is another slower diffusional process, with a self-diffusion coefficient D_{tr}, which consists of a translational motion of the entire cation. This figure is taken from the reference [40].

thing but simple. Cause of the structural ion complexity the dynamical spectrum of these systems is a combination of the re-orientational and translation motion. Furthermore this latter seems to be influenced to the liquid self-organisation and it shows a spatial heterogeneity.

1.3.1.2 Ion diffusion at the microscopic scale

As we have already mentioned at the beginning of this section, it is possible to observe the translational motion with techniques which have lower resolution. The most used is the Pulsed Field Gradient Nuclear Magnetic Resonance (PFG-NMR). This technique has typical resolution of about 100 nm as length scale and 1 ms as time scale. This implies that we can't observe the elementary motion of ions (occurring at length of few Å and times of few ps), because the re-orientation contribution of molecules moieties is no more in the observed dynamical range, then we have directly access to the diffusional dynamics of ions. Another advantage of the NMR techniques is the possibility to choose the atomic specie to probe. This allows then to observe the diffusion of the cation and anion which is not possible with QENS on the hydrogenated samples.

In this context the most complete study on the ILs dynamical properties is that of Tokuda et al. [41–43]. In these references the authors measured the self-diffusion coefficient of different families of ILs.

In particular they coupled the macroscopic measure of liquid viscosity with the value of the self-diffusion coefficient. From this comparison they discovered

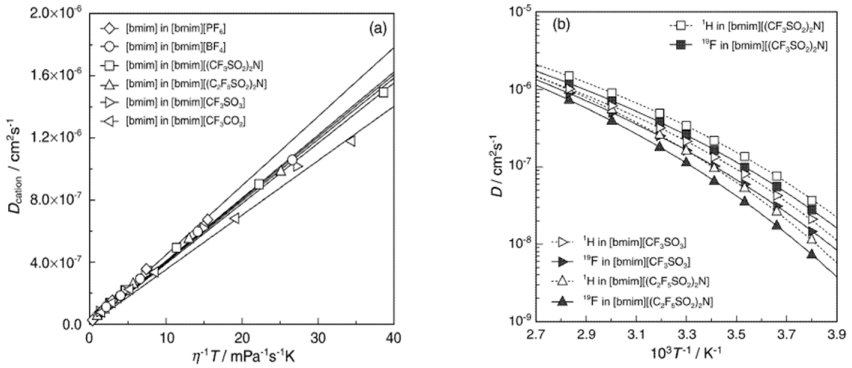

Figure 1.12: (a) Cation self-diffusion coefficient of different ILs as a function the variable T/η measured by PFG-NMR. The symbols are the experimental data while the solid lines are fit using the Stokes-Einstein equation (eq.1.4).(b) Cation self-diffusion coefficient of different ILs as a function of the temperature measured by PFG-NMR. The symbols are the experimental data while the solid lines are fit using the Vogel-Fulcher-Tammann equation (eq.1.5). These plots are taken from the reference [41].

the self-diffusion coefficient follows the Stokes-Einstein equation [41,42] (see figure 1.12 A):

$$D = \frac{k_B T}{\pi X \eta r} \tag{1.4}$$

where k_B is Boltzmann constant, T is the liquid temperature, η it viscosity, r the ion hydrodynamic radius and X a factor included between 4 and 6 which takes in account the hydrodynamic boundary condition between the ion and the rest of the medium.

The other important results coming from this analysis is the relation between the self-diffusion coefficient and the liquid temperature. In fact the trend of this quantity, in the ILs, doesn't follow the classic exponential Arrhenius behaviour, but it can be described by the Vogel-Fulcher-Tammann (VFT) equation (see figure 1.12 B):

$$D = D_0 e^{-\frac{B}{T-T_0}} \tag{1.5}$$

The parameter T_0 in the equation 1.5 represents the temperature at which the self-diffusion coefficient is null. It was observed that experimentally T_0 is 30-60 K below the glass temperature (T_g) measured by calorimetry [31]. We can then conclude that the dynamical properties of the ILs are influenced by the glass properties of the system. These results seem to be consistent with the non-exponential behaviour observed at the molecular length scale.

1.3.2 Experimental part

1.3.2.1 Choice of experimental techniques

For determining the correlation between the self-organisation and the ILs dynamics, we need to probe a very local scale. For this purpose we opted for the quasi-elastic neutrons scattering (QENS) techniques because they allow to observe, at the same time, the dynamics in function of time and space at the molecular scale (i.e. spatial range 1-10 Å and time range 1-1000 ps).

For a more deepened explanation of theory neutrons scattering we refer the reader to the appendix A. In this section we will only show the basic concepts of neutron scattering spectroscopy and explain the reasons that why we choose these techniques.

The methods based on the inelastic neutron scattering are spectroscopic techniques which measure the change of energy and momentum of a neutrons beam after its interaction with the sample. These particles are particularly good probes because they have no electric charge, thus they interact directly with the sample nuclei and they have a penetration length deeper than X-rays. Moreover their wavelength is particularly appropriate for studying the condensed matter, because it has the same order of magnitude of the inter-atomic distance. Furthermore the neutrons kinetic energy are near the those of typical molecular excitations; this makes them very good candidates for studying the condensed matter dynamics.

Especially the QENS is a very apt method for this genre of analysis because it allows to observe the dynamical events which occur at very low energies such as the self-diffusion or the molecular re-orientation.

In this work we selected three different QENS techniques:

- the time of flight (ToF),
- the neutron back-scattering (BS),
- the neutrons spin-echo (NSE).

The length and the time scale and the relative experimental resolution of the three techniques are shown in Table 1.1.

The ToF and the BS probe a faster dynamics occurring at a time scale between 0.1 and tens of ps. These methods allow to observe the faster dynamical mode such as the molecular orientations.

On the other hand the NSE can probe slower dynamics because it observes characteristic times included between 10 ps and 1 ns.

With these techniques, especially in the ToF and BS case, we can observe practically only the incoherent contribution coming from the hydrogen because it has

Technique	Time range (ps)	Length range (Å)	Energy Resolution (μeV)
ToF	0.1- 10	4 - 125	81
BS	1 - 30	6 - 13	17.5
NSE	10 - 1000	6 - 21	0.001

Table 1.1: Probed ranges and experimental resolution of the QENS techniques used in the study of ILs dynamics

an incoherent scattering cross section which is much bigger than other scattering cross section of other elements in the samples [44]. This implies that we could determine only the self-part of van Hove correlation function, so we could probe only the individual part of hydrogen nuclei dynamics [45]. Moreover since the hydrogen is present only in the cation, with the QENS techniques we could obtain information only about the cationic dynamics.

1.3.2.2 The measurements

The goal of this section is the description of experimental part performed for the study of the ILs dynamics. For an accurate explication of the QENS techniques we refer the reader to the appendix B and C. In this part we will focus on the description of the instrument configurations and the basic treatment of the raw data adopted for each measurements.

1.3.2.2.1 The Time of Flight experiments on IN5

Part of the ToF measurement were performed on the spectrometer IN5B (ILL-Grenoble) [46]. Each sample has been measured at T=293 K with a wavelength of 8 Å, using a cylindrical cell of thickness of 0.2 mm. This configuration allowed to probe the dynamics with an energy resolution around 10 μeV on a wave vector range going from 0.005 to 1.45 $Å^{-1}$. This means that, with this spectrometer configuration, we could observe characteristic times included between 0.7 and 65 ps.

At each raw spectrum was firstly subtracted the contribution of the empty cell. Then each signal was normalized to the spectrum of a cylindrical vanadium reference sample (measured in the same spectrometer configuration) for correcting the efficiency variation of the different detectors. Finally it was applied a Q grouping for improving the signal statistics and energy rebinning with a step of 0.01 meV.

1.3.2.2.2 The Time of Flight experiments on LET

For improving the characterization of the cationic faster dynamics we performed some ToF measurements on the spectrometer LET (ISIS-Didcot) [47].

For this series of measures we used three different instrument configuration, that are shown in the table 1.2.

E_i (meV)	λ (Å)	Measured resolution (μeV)	Energy range (meV)	Q range (Å^{-1})
3.00	0.8	81	-1.6 - 1.00	0.05-1.65
1.27	1.3	22	-1 - 0.5	0.05-1.05
0.70	1.7	13	-0.5 - 0.2	0.05-0.75

Table 1.2: LET configurations used during the ToF measurements.

For the characterization of the faster modes we opted for a configuration with a low energy resolution (δE $\approx$ 80 μeV), which had a wide observation energy range, while we choose other two configurations at high resolution (δE $\approx$ 20 μeV and δE $\approx$ 13 μeV), for the observation of the slower excitations.

At each spectrum was treated with the standard procedure explained in the section 1.3.2.2.1

1.3.2.2.3 The Backscattering measurements on IRIS

To probe the cationic dynamic occurring at tens of picoseconds time scale, we performed some measurements on the ToF spectrometer IRIS (ISIS-Didcot) [48].

We setted the instrument in a back-scattering (BS) configuration. This allowed to achieve a better energy resolution ($\delta_E \approx 17.5\ \mu eV$) than a classic ToF machine. We choose a wavelength equal to 1.1 Å which allowed to probe an energy range included between -0.5 and 0.5 meV and Q range coming from 0.48 to 1.07 Å^{-1}. All acquisitions were done at room temperature. Each spectra was normalized to the signal of vanadium sample for the correction of the efficiency of the detector. After that the spectra were subjected to Q-grouping for increasing the signal statistic.

1.3.2.2.4 The neutron spin-echo measurements on IN11

The spin-echo measurements were performed on the spectrometer IN11C (ILL-Grenoble) [49].

For these measures we used a wavelength of 5.5 Å and an angle between the two procession coils equal to 20° and 50°. This apparatus has a energy resolution much higher than a typical ToF machine ($\delta_E \approx 1\ neV$), which allowed us to probe

a time scale coming from 10 to 1000 ps and the Q range included between 0.1 to 1.2 $Å^{-1}$.

We acquired each IL spectra at room temperature (T= 300 K). For correcting the signal for the spectrometer resolution (see section C.5), we divided the room temperature spectra for those measured on the sample at low temperature (T=2 K).

It is important to notice that with NSE we don't measure the dynamical structure factor $S(\mathbf{Q},\omega)$ as ToF or BS. In fact because of the specific characteristics of the technique (see appendix C), with NSE the measured quantity is the intermediate scattering function $I(\mathbf{Q},t)$ which is the Time Fourier Transform of $S(\mathbf{Q},\omega)$ [1]:

$$I(\mathbf{Q},t) = \int_{-\infty}^{+\infty} S(\mathbf{Q},\omega) e^{-i\omega t}\, d\omega \tag{1.6}$$

So in this case, the observed correlation function is defined in the space of the time and the wave vector.

Before acquiring the sample scattering function, we performed a polarisation analysis for choosing which Q values to probe.

In fact, how it is explained in section C, by NSE the sample scattering function is obtained measuring the polarisation of neutron beam after it interaction with the sample. So the presence of polarisation after the scattering event is a necessary condition for detecting a signal. Seen that the sample is not magnetic, the polarised neutrons may interact in two different ways with nuclei: they can scatter coherently or incoherently. The first scattering doesn't cause a neutron spin-flip while the second one does. So this latter can be a detrimental effect because it could decrease the polarisation of the beam. Being the incoherent scattering an isotropic event, a $\frac{1}{3}$ of total amount of incoherently scattered neutrons will go through a spin reversal which doesn't change the spin direction. So if we define as *SF* the number of scattered neutrons which had a spin-flip, while with *NSF* the number of those which didn't had it, these quantities will be given by the equations:

$$NSF = N_{coh}(\mathbf{Q}) + \frac{1}{3} N_{inc}(\mathbf{Q}) \tag{1.7}$$

$$SF = \frac{2}{3} N_{inc}(\mathbf{Q}) \tag{1.8}$$

where $N_{coh}(\mathbf{Q})$ and $N_{inc}(\mathbf{Q})$ are respectively the number of scattered neutrons in the coherent and incoherent way at a given $\mathbf{Q}$ value. With the quantities shown in the relations 1.7 and 1.8 we can define the measured polarisation P as:

$$P = \frac{NSF - SF}{NSF + SF} = I_{coh}(\mathbf{Q}) - \frac{1}{3} I_{inc}(\mathbf{Q}) \tag{1.9}$$

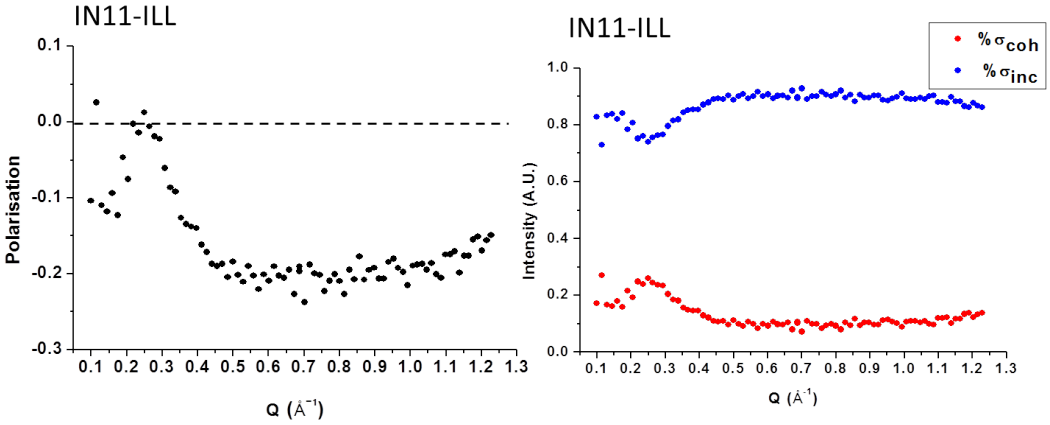

Figure 1.13: Polarisation analysis performed on the spectrometer IN11C (ILL) on the sample OMIM-BF_4. A) Measured polarisation in function of the wave vector. B) Percentage of coherent (red) and incoherent (blue) scattering in function of **Q**. These quantities were calculated using the equations 1.10 and 1.11.

where $I_{coh}(\mathbf{Q})$ ($I_{inc}(\mathbf{Q})$) is the number of scattered neutrons in the coherent (incoherent) way at given **Q** value divided by the number of all scattered neutrons $N_{tot}(\mathbf{Q}) = N_{coh}(\mathbf{Q}) + N_{inc}(\mathbf{Q})$.

Furthermore the polarisation analysis allows also to quantify the percentage of coherent and incoherent scattering occurring in the experiment (evaluation not possible with ToF measurements). Using the relation 1.9 and the definition of N_{tot} we can demonstrate that the percentages of the coherent and incoherent scattering are given by the equations:

$$\%\sigma_{coh} = \frac{(3P+1)}{4} \tag{1.10}$$

$$\%\sigma_{inc} = \frac{(3-3P)}{4} \tag{1.11}$$

As example, the results of this analysis on the OMIM-BF_4 are shown in Figure 1.13.

We normalized the measured values of P for those one measured on a sample of TiZr where the scattering is 100% coherent. This procedure allows to consider the real efficacy of he spectrometer components. As we can see from the plot, the polarisation at low Q is quite low ($P \approx$- 0.1). From 0.15 Å^{-1} it grows reaching the zero at Q=0.25 Å^{-1} and then it decreases again to negative values until Q=0.45 Å^{-1} where it remains stable to -0.2. Due to low values of P for low Q, we choose to measure the spectra for Q bigger than 0.45Å^{-1}, where the polarisation is higher.

If now we consider the percentages of coherent and incoherent scattering in the sample (Fig.1.13B), we can notice that the scattering is mainly incoherent ($\%\sigma_{inc} \gg \%\sigma_{coh}$). This is due to the large amount of hydrogen nuclei (23 atoms for each cation) present in the sample. Only for low Q, in the region between 0.15 and 0.45 Å^{-1}, there is an augmentation of the coherent contribution. This is caused by the pre-peak of the static structure factor, that was observed in this Q range (see section 1.2).

1.3.3 Effects of the cation-anion couple on ILs dynamics

The first step of this work was the determination of the influence of the ionic couple on the ILs dynamics. We will show that the anion nature seems to have an important role on the ion dynamics at the local level.

For this purpose we studied the same four ILs that we have analysed by SANS.

An example of the measured spectra (normalized to the sample mass) is shown in figure 1.14, where the samples are grouped by the cation. From the plot we can notice that for the same cation the spectra have the same intensity for null energy transfer $S(Q, \omega = 0)$. This latter is proportional to the sample scattering cross section (see appendix A), which, in the case of protonated samples can be approximated to its incoherent part. Since in the samples considered in this study the hydrogen is only in the cation, the incoherent cross section is approximated to the cationic one. This means that the systems with the same cation have the same cross section. When we consider the quasi-elastic signal ($S(Q, \omega)$ with $\omega \neq 0$) for the liquids in the same groups, it seems to have different width. This difference suggests the cation is not a key parameter to define the dynamical features of the samples.

Another feature that we can observe from the comparison of the spectra in the figure 1.14, is that the width of the quasi-elastic signal seems to be narrower in the case of ILs which have the BF_4 as anion. Since the characteristic time of the dynamics is proportional to the width of the quasi-elastic signal, we can conclude that for this latter group of liquids the dynamics is slower. This effect could be explained by delocalisation of the TFSI electric charge which causes a weakening of the coupling anion-cation inducing greater freedom to the cationic dynamics. This effect seems to agree with the results obtained by different NMR measurements performed on the same liquids. In fact if we use the values reported in the works of Tokuda [41,42] and Harris [50] for calculating the cation self-diffusion coefficient at T=293 K we find the following cationic self-diffusion coefficient: $D_{OMIM-TFSI} = 9\ 10^{-8}$ cm^2/s, $D_{BMIM-TFSI} = 2.2\ 10^{-7}$ cm^2/s, $D_{OMIM-BF_4} = 2.6\ 10^{-8}$ cm^2/s and $D_{BMIM-BF_4} = 1.1\ 10^{-7}$ cm^2/s, which show the same trend observed by our neutron study.

On the other hand if we group the samples by the anion we obtain spectra with

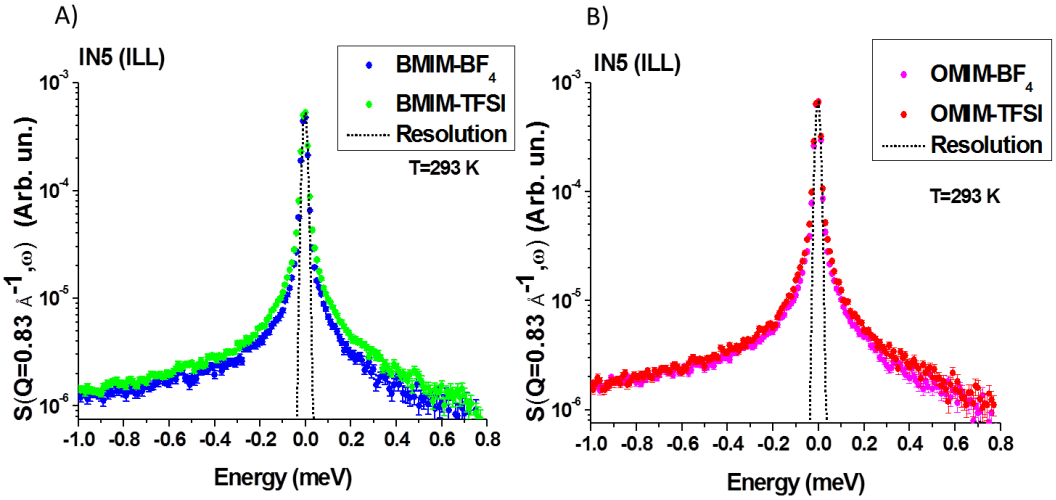

Figure 1.14: Dynamical structure factors,normalized to the sample mass, of the four ILs measured at Q=0.83 $Å^{-1}$ grouped by cation (the dotted line shows experimental resolution measured on a cylindrical sample of Vanadium). We can note that for the same cation the elastic intensity is the same, however the quasi elastic signal is different. A) Dynamical structure factor of BMIM based ILs. B) Dynamical structure factor of OMIM based ILs.

different intensity at $\omega = 0$ where it is difficult to do a qualitative comparison. However if we perform a normalisation to the elastic signal, we observe that in this case the spectra are perfectly superposed in all energy range, as it is shown in figure 1.15. This superimposition is observed for all probed Q range.

This superimposition suggests that the anion has an important role on the dynamics at the local level. We can conclude thus that, for liquids with the same anion, the dynamics of the cation is the same in the range between 1-65 ps.

This result doesn't follow the trend shown by the previous NMR study. If we take the results obtained by Tokuda on the OMIM-TFSI and BMIM-TFSI [42], it was shown that the BMIM at 293 K has a self-diffusion coefficient which is two times bigger than the OMIM one in agreement with the measurement of the liquids macroscopic viscosity. Consequently this discrepancy between the QENS and NMR study shows that the cation dynamics at the picosecond and Ångström scale is not influenced by the macroscopic properties of the system such as the viscosity.

The spectra superimposition demonstrates also that, in the observed dynamical range, the dynamics seems to be insensitive to the self-organization of the system (determined by the cation).

In conclusion since the localisation of the charge on the cation is the same for

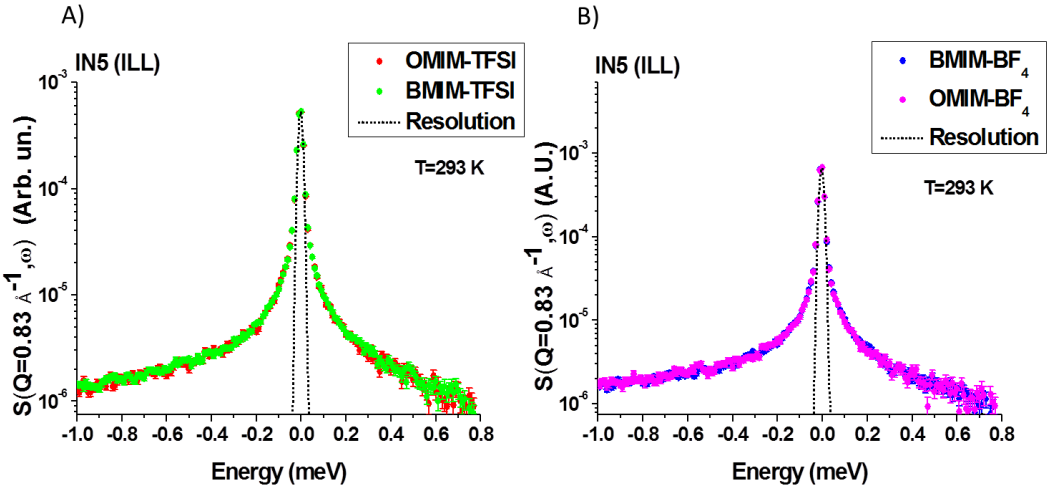

Figure 1.15: Dynamical structure factors, normalized to the sample mass and to elastic peak, of the four ILs measured at Q=0.83 $Å^{-1}$ grouped by anion (the dotted line shows experimental resolution measured on a cylindrical sample of Vanadium). We can note that for all the cases the quasi-elastic signal are superimposed. A) Dynamical structure factor of TFSI based ILs. B) Dynamical structure factor of BF_4 based ILs.

the four samples, we can conclude that the cation dynamics in the time region between 1 and 60 ps is strictly dependent on the strength of the coupling of the ionic couple. It was shown that the characteristic time of the cation dynamics increases with the the delocalisation of the anion charge, which suggests a low coupling between the cation and anion.

1.3.4 Study of the cationic diffusion OMIM-BF_4 at the molecular scale: a phenomenological approach

In order to examine in depth the ILs dynamics we choose to focus on an unique liquid as model system. For this study we choose as reference the OMIM-BF_4. We did this choice because we want consider a liquid where the self-organisation is strong, (see section1.2). In this way it is possible to verify if the self-organisation has any effects on the ions dynamics at the local scale.

For all neutrons measurements we used the OMIM-BF_4 produced by Sigma-Aldrich.

We started our study probing the dynamics between 10 and 1000 ps following as reference the study already performed on similar systems [28, 29, 32].

We choose this dynamical range because we are mainly interested to the cation

diffusion that occurs on time scale longer than few picoseconds. So in this part we will present the results coming from BS and NSE measurements on the OMIM-BF_4 analysed using a phenomenological approach.

The goal of this section is to show the complexity of the ILs dynamical behaviour. We will illustrate that the dynamics of these systems is composed by multiple relaxations occurring at different time scale. Concerning the study of the ionic diffusion we will demonstrate the cation doesn't exhibit a classical Brownian motion.

If we compare the spectra acquired by BS and NSE on the OMIM-BF_4 (in figure 1.16), we can observe some differences.

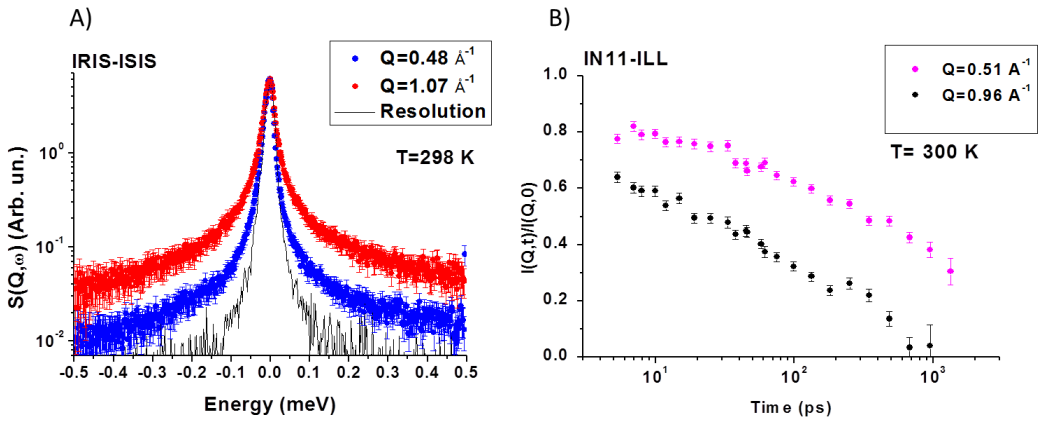

Figure 1.16: A) Dynamic structure factors of OMIM-BF_4 at Q=0.48 $Å^{-1}$ (in blue) and at Q=1.07 $Å^{-1}$ (in red) at room temperature measured on spectrometer IRIS (ISIS). The measured resolution (measured on an anodized aluminium oxide membrane (AAO)) is also represented in black. All the spectra are normalised to the elastic peak. B) OMIM-BF_4 intermediate scattering function measured at Q=0.51 $Å^{-1}$ (in magenta) and at Q=0.96 $Å^{-1}$ (in black) on the NSE spectrometer IN11C (ILL).

Concerning the BS data (figure 1.16 A), if we compare the sample spectra acquired at two different Q values, we can notice two main features. There is a very narrow signal in the region between -0.1 and 0.1 meV which doesn't change width in function of Q. This must be a dynamical relaxation, occurring at very low energy (i.e. at times longer than 30 picoseconds) that is not resolved with this spectrometer configuration. Besides this narrow peak there is also a broader relaxation with a width of order of meV (fraction of ps) which goes out of the observation window.

On the other hand when we observe the intermediate scattering functions measured by NSE (figure 1.16B), they show a monotonic decay, which suggests the

presence of a unique relaxation occurring at the scale of tens of picoseconds. This has to be the narrow peak observed by the BS measurements. We can notice also that for different Q values each scattering function doesn't tend to 1 for short time. This means the presence of a loss of correlation due to a liquid dynamical relaxation taking place a times shorter than 10 ps, which is not observable with this techniques. We can suppose that this should be the broad relaxation observed on IRIS.

Owing to the narrowness of the observation window in the BS data, we couldn't fit the spectra. The broad relaxation goes out of the energy window, so it wasn't possible estimate its width properly. This constraint forced us to consider the BS and NSE simultaneously in order to perform a more in-depth data analysis.

For this purpose it was necessary to merge the two series of spectra.

For realizing this procedure, we needed to have the scattering functions defined in the same space. Thus a numerical Fast Fourier Transform (FFT) of the dynamic structure factor $S(\mathbf{Q}, \omega)$ was performed using the equation 1.6. For this calculation it was used as resolution the sample dynamic structure factor measured at low temperature on IRIS. After the FFT, the transformed ToF spectra were merged to the NSE ones measured at the same Q value.

These latter were multiplied by scale factor for assuring the good curves merging (the factors used are reported in the table 1.3). We can justify this last operation considering that the NSE analyser has a finite efficiency, so we can correct the acquired signal for considering this limitation.

Q (Å^{-1})	Scale Factor
0.51	1.05
0.63	1.15
0.74	1.2
0.85	1.2
0.96	1.2
1.07	1.3

Table 1.3: Factor scale for merging the NSE intermediate scattering function with the ToF ones.

The obtained curves are shown in figure 1.17.

We can notice that each function shows two relaxations: one occurring in the 10 picoseconds region and a slower one visible at longer times.

For analysing the experimental data we firstly use a phenomenological model. We assumed the presence of two distinct loss of correlation using the function:

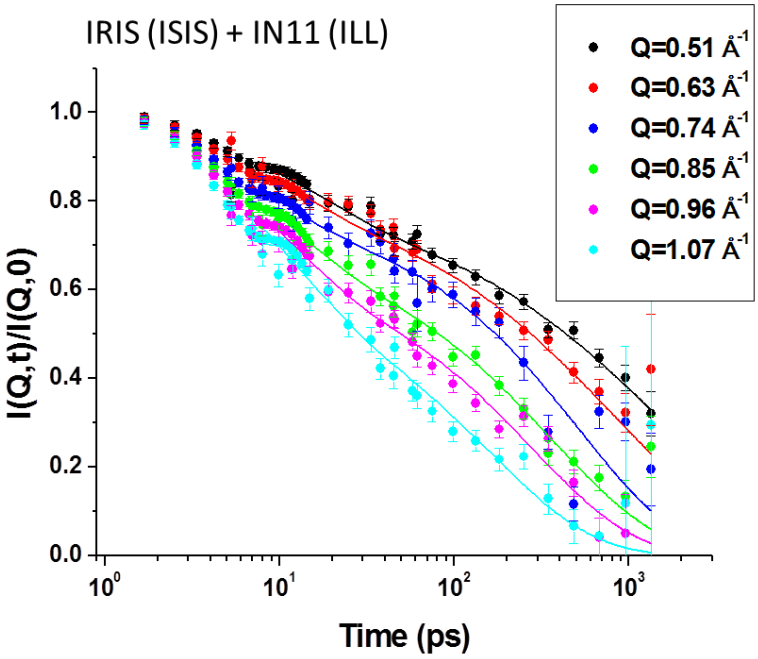

Figure 1.17: OMIM-BF_4 intermediate scattering function obtained after the merging procedure (see the text for more explications). The point are measured value while the continuous are the fit function obtained using the relation 1.12.

$$I(\mathbf{Q},t) = Ae^{-\frac{t}{\tau_\beta(\mathbf{Q})}} + (1-A)e^{-\left(\frac{t}{\tau_\alpha(\mathbf{Q})}\right)^\beta} \tag{1.12}$$

The first fast relaxation (called "β-relaxation") is represented as a simple exponential, while the second one (called "α-relaxation") is represented as a stretched exponential (Kohlrausch-Williams-Watts (KWW) function). This latter has been intensively used in QENS studies for representing the heterogeneous dynamics of different systems such as super-cooled liquids [51] or of glass formers (among which ILs) [28,29,32,52]. The stretching parameter β could be vary between 0 and 1 and it represents the deviation of the relaxation from the exponential behaviour. It has been shown that it is linked to the degree of cooperativity of the dynamical relaxation [32]. Combining the values of β and τ_α it is possible to obtain information about the typology of the dynamics as it will be shown in this section.

The obtained parameters values by the curves fitting are shown in figures 1.18 and 1.19.

We can observe the relaxations parameters have very different behaviour in function of the wave-vector.

In the β-relaxation the characteristic time changes weakly with Q, while its amplitude does. Similar studies in literature have demonstrated that in different

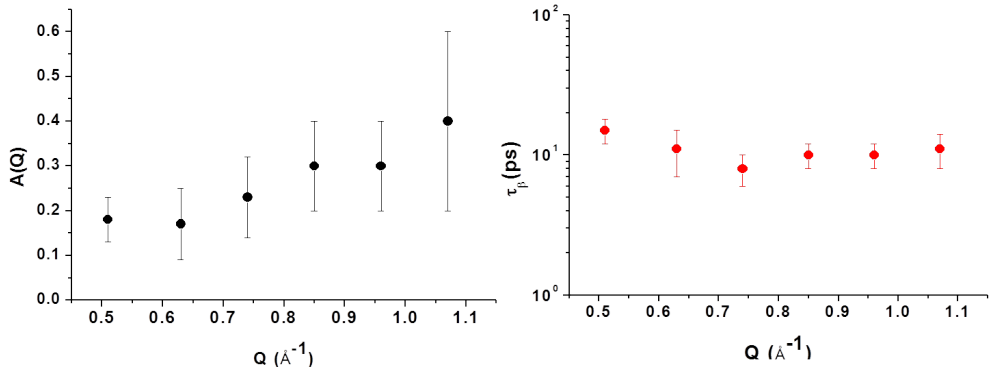

Figure 1.18: Values of β-relaxation parameter obtained by the curves fitting. We can notice that its amplitude $A(Q)$ changes with the wave-vector while the time constant τ_β is weakly dependent on Q.

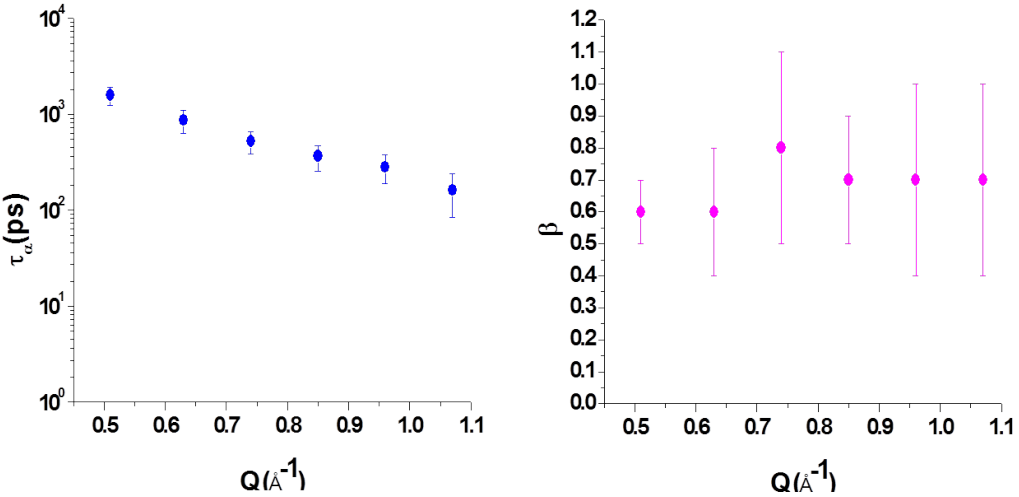

Figure 1.19: Values of α-relaxation parameter obtained by the curves fitting. We can notice that in this relaxation the time constant τ_α is strongly dependent on Q.

ILs this relaxation is weakly dependent on the temperature [28, 29, 32] and anion size [28]. For this reason, this relaxation could be attributed to a fast motion of the hydrogen atoms which has an activation energy very low.

From the parameter $A(Q)$ it is possible to extract information about vibrational properties of cation hydrogen nuclei. They vibrate around their equilibrium position cause of thermal excitation. This dynamics, produces a factor in the scattering function called Debye-Waller factor, DWF, which is given by the equation [2]:

$$DWF = e^{-\frac{1}{3}Q^2u^2} \tag{1.13}$$

where u is the mean-squared displacement of the vibration, which depends by the temperature [2]. We found that the quantity *(1-A)* follows the law 1.13 as it is shown by the fit in figure 1.20. The fit of the experimental points gives that the hydrogen nuclei vibration amplitude at room temperature is equal to 1.2 ± 0.1 Å.

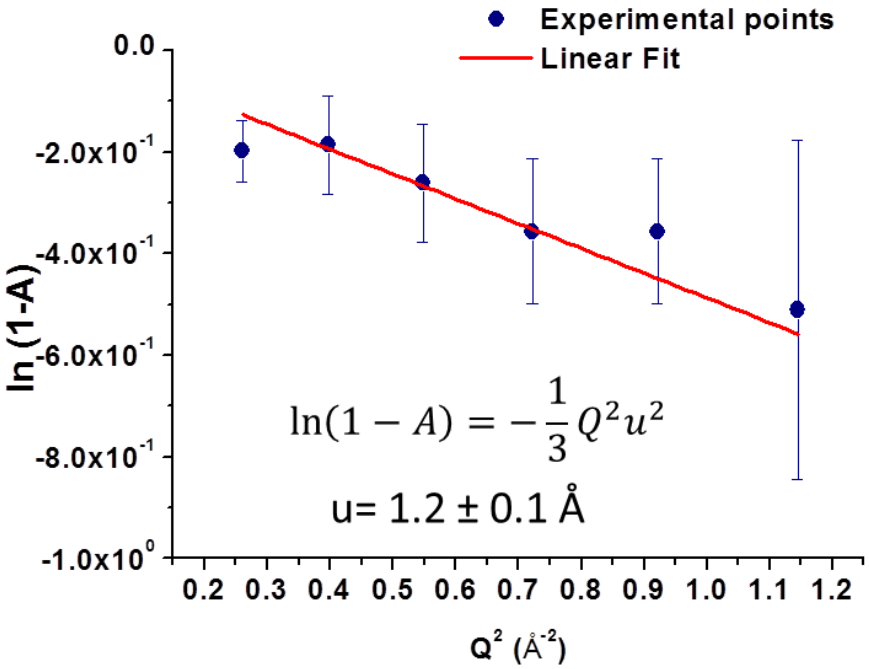

Figure 1.20: Linear fit of the quantity ln(1-A) (eq. 1.13). We found a libration amplitude of 1.2Å.

If we consider the α-relaxation, in this case the time constant τ_α is strongly dependent on Q. Moreover we can notice that the values assumed by the stretching parameter β are far from 1. This deviation form the exponential behaviour suggests an high degree of cooperativity. Moreover from further studies it was shown that in this case τ_α depends also by the size of anion and by the temperature [28,29,32].

Given these particular features, we correlate this relaxation to the cation diffusive motion. We studied the nature of this relaxation using the approach developed by Richter et al. in their QENS study on the glass-former systems dynamics [52]. In this reference the authors demonstrate that the KWW function can invoke two different dynamical scenarios. The first one is called "heterogeneous scenario" which is typical for the supercooled liquids [51]. In this case all molecules have a Brownian diffusion so their mean-squared displacement is linear with time ($< R^2 > (t) \propto$ t). This means each molecule has an exponential relaxation:

$$I_{mol}(\mathbf{Q},t) = e^{-\frac{t}{\tau}} \tag{1.14}$$

with

$$\tau = \frac{1}{DQ^2} \tag{1.15}$$

where D is the molecule self-diffusion coefficient. However in the system there is a distribution of the relaxation time, so the measured scattering function is a KWW function generated by the weighted super-imposition of each molecular relaxation:

$$I(\mathbf{Q},t) = \int_{-\infty}^{+\infty} g(ln(\tau))e^{-\frac{t}{\tau}}\, d(\tau) = e^{-\left(\frac{t}{\tau_w}\right)^{\beta}} \tag{1.16}$$

where g is the time distribution and τ_w is the KWW function time constant. In this scenario τ_w follows the law:

$$\tau_w = \tau_0 Q^{-2} \tag{1.17}$$

where τ_0 is a constant.

On the other hand there is "homogeneous scenario", which is typical of the glass formers such as the polymers [52]. In this case all molecules have the same relaxation, but they have sub-diffusive behaviour, i.e. their mean-squared displacement, $< r^2 >$, has sublinear relation with the time ($< r^2 > (t) \propto t^{\beta}$ with β <1). So also in this case, the scattering function is given by a KWW function:

$$I(\mathbf{Q},t) = e^{-Q^2 \mathscr{D} t^{\beta}} = e^{-\left(\frac{t}{\tau_w}\right)^{\beta}} \tag{1.18}$$

where $\mathscr{D}$ is the proportionality factor between the mean-squared displacement and the time. In this scenario the relaxation time of the KWW function follows the power law:

$$\tau_w = \tau_0 Q^{-\frac{2}{\beta}} \tag{1.19}$$

Thus checking the dependence of τ_α by Q, we can determine which scenario fits better the dynamical behaviour of OMIM diffusion.

The performed fit of KWW function constant time, for the OMIM-BF_4, is shown in in the figure 1.21. For this operation we used as fitting function the law τ_α=τ_0 Q^{-n}.

The fit procedure gives as exponent of power law n=2.9. If we consider the average value of the stretched parameter ($< \beta > \approx 0.66$), we can note that the relation $n = -\frac{2}{\beta}$ is verified so τ_α follows the law 1.19. We can conclude the cation

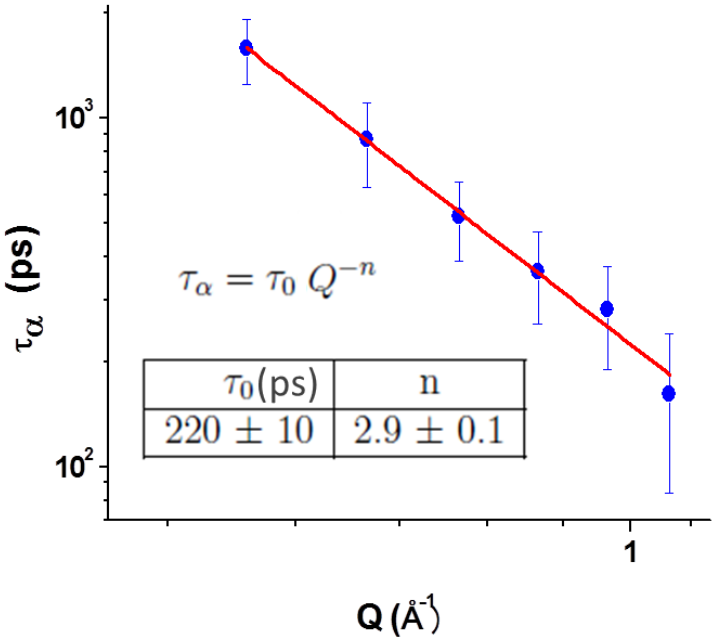

Figure 1.21: Fit of values of τ_α with the equation τ_α=$\tau_0\ Q^{-n}$.

diffusion at the Å and ps time scale can be associated to the homogeneous scenario, so it translational motion couldn't be considered as Brownian.

The results obtained in this study are consistent with the previous study performed on other ILs using the similar approach [28, 29, 32].

From the results deduced by this analysis we can affirm that the model proposed in this section fits well the experimental data and it is able to show the complexity of dynamical behaviour of ionic liquids. However there are some evident limitations. For example the use KWW function doesn't allow to investigate deeply the physical properties the anomalous diffusional behaviour of the cation. The stretched exponential can highlight the presence of a cooperativity in the dynamics, but it is not able to give any geometrical information about the motion. Furthermore the representation of the fast dynamics as an exponential β-relaxation is an oversimplified model function which doesn't give a microscopical origin of the motion. Some authors attribute this fast relaxation to the alkyl-chain re-orientation [28, 29], whereas others affirm that is due to a localised molecular motion in a "cage" [32]. From these considerations is thus clear the necessity of a more quantitative model which explains the complex dynamics of this system. For this purpose a further characterization of the dynamics in the picoseconds scale is required for probing properly the dynamical modes occurring at shorter times.

1.3.5 Characterization of the cationic dynamics at the molecular scale using a combination of QENS techniques: the case of the OMIM-BF_4

1.3.5.1 Point of the departure: the dynamics at the picoseconds scale probed by ToF spectroscopy

For improving the study of the ILs dynamics at the molecular scale we performed some ToF measurements on the spectrometer LET as it has been described in the section 1.3.2.2. The new features shown by these spectra represent the point of the departure of the development of a new model for the data analysis.

We want to underline that LET has access also at a wider range of Q than IRIS, which has allowed to probe also scale length bigger that the typical correlation-length of the OMIM-BF_4 ($\approx$ 2 nm).

An example of a measured spectrum, acquired at the configuration with E_i =3 meV, is shown in figure 1.22.

As we can see from this plot, with a broader scan in energy we can observe three different components, which have different features:

- a first narrow relaxation with a width less than 10 μeV (t > 66 ps),
- a second one with a width of order of tens of μeV (t $\approx$ 10 ps),
- a third very broad excitation around 1 meV (t $\approx$ 0.6 ps).

We can notice that the wider scan in energy, accessible by the ToF machine, not only has permitted to observe properly the broad excitation, but it has also enabled to distinguish two different relaxations in the interval of small energy exchange that were indistinguishable in the BS configuration. The presence of these three dynamical mechanisms is the point of departure for the development of new model of ILs dynamics.

1.3.5.2 A new multi-components model

The goal of this part is to describe the model developed for interpreting the QENS data. This section is divided in three main parts. After a short introduction, which explains the physical origin of each relaxation, there will be a part dedicated to components due to the cation translational motion and another talking about the contribution of the molecular re-orientation. After that the last part will show how the different components were put together for forming the model used during the fit.

This new model is based on two fundamental considerations.

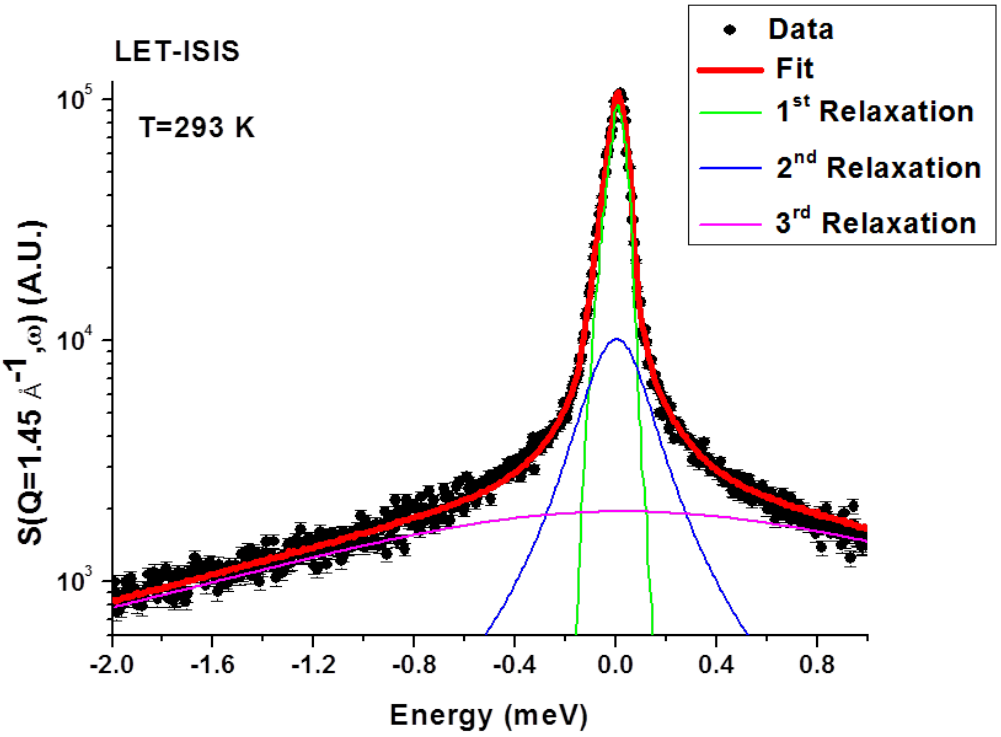

Figure 1.22: Example of a spectrum of OMIM-BF_4 measured on LET at $E_i = 3$ meV and Q= 1.45 $Å^{-1}$. We can distinguish three relaxations (represented respectively in green, blue and magenta) occurring at three different dynamical scales. The solid red line is the sum of three relaxations.

The first one is the heterogeneity of the system at the local level. It was observed that the IL shows a self-organisation at the local level (see section 1.2). This results in a formation of density fluctuations at the nanoscale. We can sketch these fluctuations as energy barriers for the ions long range diffusion. Thus we can see each hydrogen as trapped within an aggregate where it has a diffusive motion. However we can imagine these heterogeneities as soft barriers, so sometimes the particle could escape from one aggregate and jump into another one. This behaviour generates thus two relaxations in the IL spectrum as it explained graphically in figure 1.23.

The second basic consideration is the complexity of the cation structure. The OMIM is composed by a charged part plus a long octyl-chain. Seeing that the majority of hydrogen nuclei are on the alkyl-chain (17/23), we conclude that the relaxations of a-polar chain are not negligible in the QENS spectrum. We can then

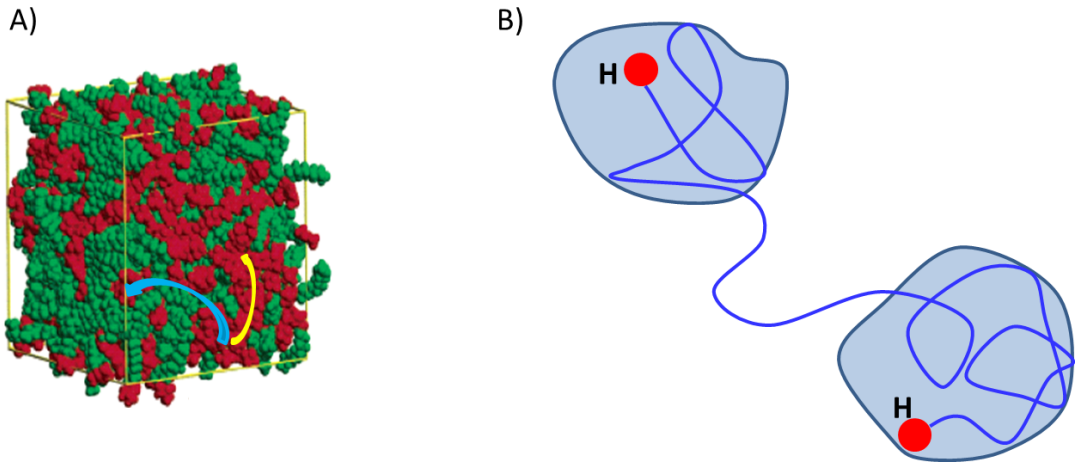

Figure 1.23: Figurative representation of the self-organization effects on the ion diffusion. The domains act like energy barriers, which trap the ions. However the walls of these cages are not impermeable so the particle can jump out the domains. This interpretation supposes thus two kinds of diffusion: one confined inside the aggregates and another one between them. A) Explanation of the model using the simulation box of the reference [6]. In this picture the confined diffusion is represented by the yellow arrow, while the long range diffusion between two aggregates is represented by the blue arrow. B) Schematic representation of the model, where the hydrogen (we are observing the sample incoherent scattering) is the red circle while it displacement is the blue line.

suppose that this dynamics causes at least one relaxation in the IL correlation function.

Let pass now to explain how we can sketch the different relaxations. For developing the model we need to use the formalism described in the appendix A. We remind that we are studying a hydrogenated sample. This means that we are measuring the self part of the correlation function, so the probed dynamics is that of the single hydrogen nucleus decorrelated by the rest of the cation atoms.

1.3.5.2.1 Modelling of the cation diffusion: the generalised Gaussian model

This model consider two kinds of diffusion: one inside the aggregates and the other one between them.

For modelling this dynamics we used the so called generalised Gaussian model proposed by Volino et al. [53, 54], which describes the translational motion of particles confined in space with soft boundary.

Let's consider the diffusion inside the aggregate. In this case the dynamics

is not ergodic since the hydrogen can't explore all the phase space because it is confined in a finite space. So the relative self-correlation function at infinite time $G_s(\mathbf{r}, t = +\infty)$ is not null. This implies that it dynamic structure factor will have an elastic component [1]. This quantity is called Elastic Incoherent Structure Factor (EISF). It represents the form factor of the confinement space of the nucleus, being the Space Fourier Transform of $G_s(\mathbf{r}, t = +\infty)$ [1].

In order to take into account this confined diffusion Volino's model supposes that the molecules of the sample are not caged in a impermeable well (such as the model of a particle confined in an impermeable spheric space [55]), but in a softer well of Gaussian shape.

This means that, if we consider, for example, an 1D system, the proton displacement along the x-axis u_x follows the a Gaussian statistics with variance σ^2. So under this assumption the proton dynamics is localized in a space of dimension of 2σ. In this model, the self-correlation function of the hydrogen displacement is defined as [53]:

$$< u_x(t)u_x(0) >= \sigma^2\rho(t) \tag{1.20}$$

where $\rho(t)$ is a function which describes how the proton loses the memory about its initial position as a function of time. This model hypothesizes that there is a full correlation for t=0 ($\rho(t = 0) = 1$), while at infinite time the two displacements are totally decorrelated ($\rho(t = +\infty) = 0$). Extending the model in three dimensions and in an isotropic space, it is possible demonstrate that the proton intermediate scattering function is given by the relation [53]:

$$I(Q, t) = e^{-Q^2\sigma^2(1-\rho(t))} \tag{1.21}$$

The simplest function to use for describing the loss of correlation is the exponential form $\rho(t) = e^{-\frac{t}{\tau_0}}$, where τ_0 is the characteristic time needed by the particle for exploring all the confined space.

If we consider now the limit at high Q ($Q \to \infty$) of the expression 1.21, we notice that the scattering function has significant values for $\frac{t}{\tau_0} \ll 1$. In this case we find the relation of the classical Brownian motion:

$$I(Q, t) = e^{-Q^2 D_{loc}^2 t} \tag{1.22}$$

With

$$D_{loc} = \frac{\sigma^2}{\tau_0} \tag{1.23}$$

which is the particle self-diffusion coefficient.

However when we move to finite values of Q we have to consider the "granularity" of the medium. In reality the proton hops between two sites at distance δ with characteristic time τ_{mi}. This implies that the effective particle self-diffusion coefficient follows jump diffusion law:

$$D_{eff} = \frac{D_{loc}}{1 + 2D_{loc}Q^2\tau_{mi}} \tag{1.24}$$

Using this last relation the correlation function becomes:

$$\rho(t) = e^{-\frac{D_{eff}t}{\sigma^2}} \tag{1.25}$$

Thus we obtain the scattering function:

$$I(Q,t) = e^{-Q^2\sigma^2(1-e^{\frac{-D_{loc}t}{\sigma^2(1+2D_{loc}Q^2\tau_{mi})}})} \tag{1.26}$$

It was shown that the function 1.26 could be adjusted as an exponential function plus a factor independent by the time [56]:

$$I(\mathbf{Q},t) \approx A_{Gauss}(\mathbf{Q}) + (1 - A_{Gauss}(\mathbf{Q}))\, e^{-\frac{t}{\tau(\mathbf{Q})}} \tag{1.27}$$

So when we perform the frequency Fourier Transform of the intermediate scattering function we obtain the dynamical structure factor:

$$S(\mathbf{Q},\omega)_{Gauss} = A_{Gauss}(\mathbf{Q})\,\delta(\omega) + L_{Gauss}(\mathbf{Q},\omega) \tag{1.28}$$

where the $L_{Gauss}(\mathbf{Q},\omega)$ is a Lorentzian function defined by the equation:

$$L(\mathbf{Q},\omega) = \frac{1}{\pi}\frac{\Gamma(\mathbf{Q})}{\Gamma^2(\mathbf{Q}) + \omega^2} \tag{1.29}$$

where $\Gamma(\mathbf{Q})$ is it half width at half maximum (HWHM).
The quantity $A_{Gauss}(\mathbf{Q})$ is the EISF. This latter is given by the equation:

$$A_{Gauss}(\mathbf{Q}) = e^{-Q^2\sigma^2} \tag{1.30}$$

Whereas for the HWHM of the Lorentzian in the relation 1.28 doesn't exist a precise formula, however its trend has two main features:

- $\Gamma_{Gauss}(Q \to 0) = \frac{\hbar D_{loc}}{\sigma^2}$,
- $\Gamma_{Gauss}(Q \to \infty) = \frac{\hbar}{\tau_{mi}}$

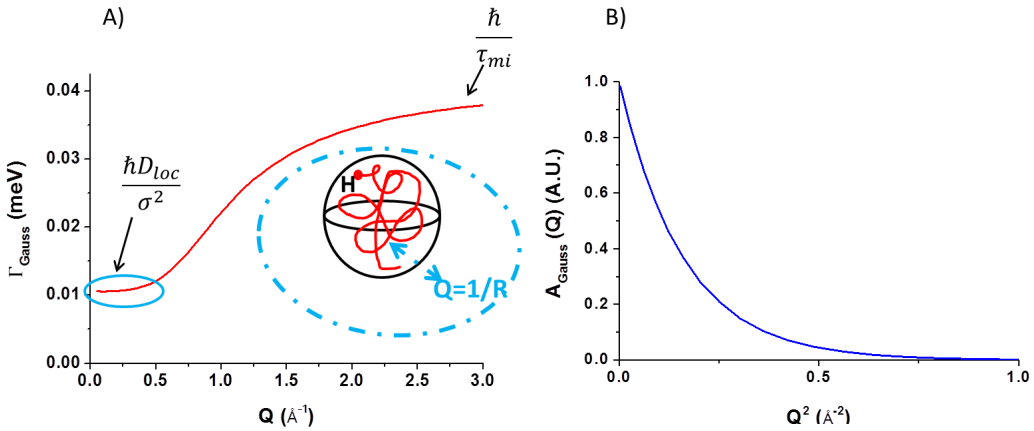

Figure 1.24: A) Simulated trend of $\Gamma_{Gauss}(\mathbf{Q})$ versus Q for σ =2.5 Å, $D_{loc} = 10^{-5}$ cm^2/s and $\tau_{mi} = 8$ ps. The inset explains the meaning of plateau observed at low Q. This is due to impossibility to observe a loss of correlation when we are probing a length scale bigger than the space of confinement (black sphere). B) Simulated trend of $A_{Gauss}(\mathbf{Q})$ versus Q^2 for σ =2.5 Å.

An example of Γ versus Q and A_{Gauss} versus Q^2 is shown in figure 1.24.

As we can see for low Q the Lorentzian width tends to a plateau equal to $\frac{\hbar D_{loc}}{\sigma^2}$, while for bigger Q it follows the law of the jump diffusion until the saturation at the value $\hbar/\tau_{mi}$. The plateau at small Q is a typical feature of diffusion on a confined space. It reveals that we are probing a length scale which is larger than confinement space of the particle, so we can't observe a loss of correlation due to diffusion (see inset figure 1.24 A).

When we observe the trend of the EISF (figure 1.24 B), we notice that it has a Gaussian form in Q.

In conclusion in our model we sketch the component due to the hydrogen diffusion inside the aggregates, defined as $S(\mathbf{Q},\omega)_{loc}$, using the form 1.28, so we can write:

$$S(\mathbf{Q},\omega)_{loc} = S(\mathbf{Q},\omega)_{Gauss} \tag{1.31}$$

On the other hand the diffusion between the aggregates (that we call long range (lr) diffusion) is supposed to be a free diffusion. In this case the dynamics is ergodic so there is no the elastic contribution. The dynamical structure factor which represents this relaxation is a simple Lorentzian function [1]:

$$S(\mathbf{Q},\omega)_{lr} = L_{lr}(\mathbf{Q},\omega) \tag{1.32}$$

where it HWHM follows the law:

$$\Gamma_{lr} = D_{lr} Q^2 \tag{1.33}$$

where D_{lr} is the self diffusion coefficient associated to this kind of diffusion.

Supposing that these two diffusional dynamics are not correlated, $S(\mathbf{Q},\omega)_{diff}$, the dynamical structure factor standing for the totality of the diffusion processes is the convolution of the two elemental (local and long range) mechanisms:

$$\begin{aligned} S(\mathbf{Q},\omega)_{diff} &= S(\mathbf{Q},\omega)_{loc} \otimes S(\mathbf{Q},\omega)_{lr} \\ &= A_{loc}(\mathbf{Q}) L_{lr}(\mathbf{Q},\omega) + (1 - A_{loc}(\mathbf{Q})) L_{lr+loc}(\mathbf{Q},\omega) \end{aligned} \tag{1.34}$$

where the subscript "lr+loc" means that the HWHM of the Lorentzian function is equal $\Gamma_{lr} + \Gamma_{loc}$.

In conclusion the dynamical structure factor sketching the ionic dynamics is composed by two Lorentzians which have as intensity two functions of the EISF due to the local diffusion.

1.3.5.2.2 Modelling the molecular re-orientation.

Owing to the OMIM structural complexity, it is evident that we can expect many degrees of freedom concerning the molecular re-orientation. In the cation there are different functional groups, such as the methyl and CH_2 groups, which have their own dynamics. In each moiety the hydrogen nuclei will have their typical rotational dynamics. Furthermore we can imagine that existence of more complex re-orientation modes which involve more (or all) functional groups.

The development of a model which considers the totality of these modes is difficult and not meaningful to confront to the experimental data. We can suppose that most of them have characteristic dynamical times which are near enough between each other to be indistinguishable experimentally. With this hypothesis we can approximate the re-orientation dynamics as unique relaxation. Also in this case the protons can't explore all the space, thus in the dynamical structure factor there will be an elastic component. The van Hove function due to relaxation will be given by the equation:

$$S(\mathbf{Q},\omega)_{orient} = A_{orient}(\mathbf{Q}) \delta(\omega) + (1 - A_{orient}(\mathbf{Q})) L_{orient}(\mathbf{Q},\omega) \tag{1.35}$$

where $A_{orient}(\mathbf{Q})$ is the EISF of the relaxation, while $L_{orient}(\mathbf{Q},\omega)$ is a Lorentzian function of HWHM Γ_{orient}.

Generally for this kind of dynamics the characteristic time depends weakly on the wave-vector [1]. We can so approximate Γ_{orient} as a constant.

1.3.5.2.3 The total dynamical structure factor

In order to determine the scattering function which reproduces the total of the IL dynamics, we have to consider the structure of the cation (see Fig. 1.7). Seeing the position of each hydrogen nucleus we can affirm that all the atoms can participate to the cation diffusional motion. On other hand not all of them are concerned to the re-orientation dynamics. In fact it is clear that the hydrogen bounded to the carbon atoms of the imidazolium ring are excluded to this kind of relaxation. In conclusion if we call p the fraction of hydrogen nuclei which could participate both to diffusional and re-orientational dynamics, the incoherent dynamical structure factor of the cation will be given the relation:

$$\begin{aligned} S(\mathbf{Q},\omega)_{inc}^{cation} &= p\left(S(\mathbf{Q},\omega)_{diff} \otimes S(\mathbf{Q},\omega)_{orient}\right) + (1-p)\, S(\mathbf{Q},\omega)_{diff} \\ &= I_A(\mathbf{Q})\, L_{lr}(\mathbf{Q},\omega) + I_B(\mathbf{Q})\, L_{lr+loc}(\mathbf{Q},\omega) \\ &+ I_C(\mathbf{Q})\, L_{lr+orient}(\mathbf{Q},\omega) + I_D(\mathbf{Q})\, L_{lr+loc+orient}(\mathbf{Q},\omega) \end{aligned} \tag{1.36}$$

With

$$I_A(\mathbf{Q}) = pA_{loc}(\mathbf{Q})\, A_{orient}(\mathbf{Q}) + (1-p)\, A_{loc}(\mathbf{Q}) \tag{1.37}$$

$$I_B(\mathbf{Q}) = pA_{orient}(\mathbf{Q})\,(1 - A_{loc}(\mathbf{Q})) + (1-p)\,(1 - A_{loc}(\mathbf{Q})) \tag{1.38}$$

$$I_C(\mathbf{Q}) = pA_{loc}(\mathbf{Q})\,(1 - A_{orient}(\mathbf{Q})) \tag{1.39}$$

$$I_D(\mathbf{Q}) = p\,(1 - A_{orient}(\mathbf{Q}))\,(1 - A_{loc}(\mathbf{Q})) \tag{1.40}$$

Reminding the results shown in the section 1.3.5.1, we can further simplify the equation 1.36. In fact the three relaxations take place in three different dynamical scales. Generally the modes due to the re-orientation are faster than other so we can associate it Lorentzian to the broader relaxation. Furthermore we can suppose that the local diffusion is faster than that one of long range, thus we can associate this latter to the narrower relaxation of the QENS spectrum. These considerations imply that $\Gamma_{orient} \gg \Gamma_{loc} \gg \Gamma_{lr}$. This takes to write to approximate the incoherent structure factor as:

$$S(\mathbf{Q},\omega)_{inc}^{cation} \approx I_1(\mathbf{Q})\, L_{lr}(\mathbf{Q},\omega) + I_2(\mathbf{Q})\, L_{loc}(\mathbf{Q},\omega) + I_3(\mathbf{Q})\, L_{orient}(\mathbf{Q},\omega) \tag{1.41}$$

With

$$I_1(\mathbf{Q}) = pA_{loc}(\mathbf{Q})\, A_{orient}(\mathbf{Q}) + (1-p)\, A_{loc}(\mathbf{Q}) \tag{1.42}$$

$$I_2(\mathbf{Q}) = pA_{orient}(\mathbf{Q})\,(1 - A_{loc}(\mathbf{Q})) + (1-p)\,(1 - A_{loc}(\mathbf{Q})) \tag{1.43}$$

$$I_3(\mathbf{Q}) = p\,(1 - A_{orient}(\mathbf{Q})) \tag{1.44}$$

In conclusion the dynamical structure factor proposed by this model is composed by three Lorentzian relaxations whose each HWHM are linked to a unique dynamical mode while the intensities are combination of the different EISF.

1.3.5.3 Analysis procedure

To estimate the dynamical quantities of the OMIM-BF_4, we performed the fit of the spectra of the ToF and the NSE measurements using the model that we have developed. In this section we will explain the analysis procedure that we have followed.

We started with the characterization of the faster dynamics. For this purpose we started fitting the ToF data, acquired at the three resolutions on LET, using the function 1.41.

Before to perform any fit we divided each dynamical structure factor for it integral in energy, which corresponds to the static structure factor of the system:

$$S(\mathbf{Q}) \approx \int_{E_{min}}^{E_{max}} S(\mathbf{Q}, \omega)\, d\omega \tag{1.45}$$

This operation permitted to eliminate eventual coherent contribution present in the signal.

Since the excitation due to the lr diffusion seems to have a HWHM comparable or smaller than the instrumental resolution (see figure 1.22), we had to impose Γ_{lr} as a fixed parameter using the law 1.33. In a first phase we chose as self-diffusion coefficient that one found by the NMR studies at T=293 K (D = 2.8 10^{-8} cm^2/s [50]).

We began to fit the data acquired at E_i =3 meV in order to estimate the HWHM of the cation re-orientation dynamics. For this purpose we chose as fit parameters I_1, I_2, I_3, Γ_{loc} and Γ_{orient}.

The result obtained on Γ_{orient} is shown in figure 1.25 A. We can notice that the it has a weak dependence by Q except for low wave vector.

The drop of the parameter for $Q \to 0$ is a consequence of the narrow cinematic window observable by the spectrometer at low wave vector (see the spectra in figure 1.25 B), that doesn't allow to observe properly this fast relaxation. We then considered only the values where this effect is absent (i.e. Q $\geq$0.45 $Å^{-1}$) and we calculated an average, weighted on the estimated incertitude, of the Γ_{orient} values given by the fit at the different Qs. The obtained average was then used as fix parameter for the Γ_{orient} in the following steps.

After that we performed the fit of all three resolutions using as fit parameters I_1, I_2, I_3 and Γ_{loc}.

From the values of the intensities the two EISF were calculated inverting the equations 1.42,1.43 and 1.44:

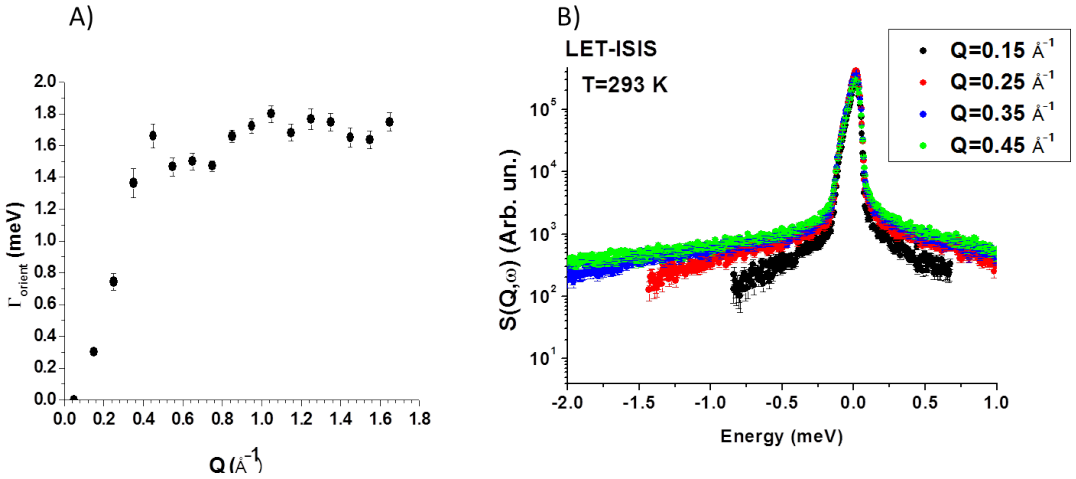

Figure 1.25: A) Trend of Γ_{orient} versus Q obtained by the fit of the data acquired with the LET configuration at E_i =3 meV on the OMIM-BF_4. It shows a weak dependence by Q except for low wave vector. This effect is due to the little energy window observable at low Q which doesn't allow to determine the Lorentzian HWHM properly. B) Different dynamical structure factors of the OMIM-BF_4 acquired at different Q. We can notice that for small wave vectors the cinematic window of the spectrometer is reduced.

$$A_{loc}(\mathbf{Q}) = 1 - \frac{I_2(\mathbf{Q})}{1 - I_3(\mathbf{Q})} \tag{1.46}$$

$$A_{orient}(\mathbf{Q}) = 1 - \frac{I_3(\mathbf{Q})}{p} \tag{1.47}$$

The comparison of the results obtained on the three resolutions showed a discrepancy on the trend of Γ_{loc}, that is shown in figure 1.26.

The three series of values show a similar trend in function of Q. However at low Q the curves seem to assume very different value especially for of low resolution curve (labelled as E_i =3 meV). We can notice that in this case the values assumed by Γ_{loc} never descends down from the experimental resolution (represented as a dotted line in the figure 1.26). We suppose that the discrepancy must be due to the too low resolution (δE $\approx$ 80 μeV) which can't resolve the real width of the relaxation in the low Q region.

So we fitted another time all resolutions imposing Γ_{loc} as fixed parameter. We tried to impose the values of Γ_{loc} found from the fits of data acquired at E_i =0.70 meV and E_i =1.27 meV and we found that this latter series fits better the data at low resolution. Thus we decided to use these values for fixing Γ_{loc}.

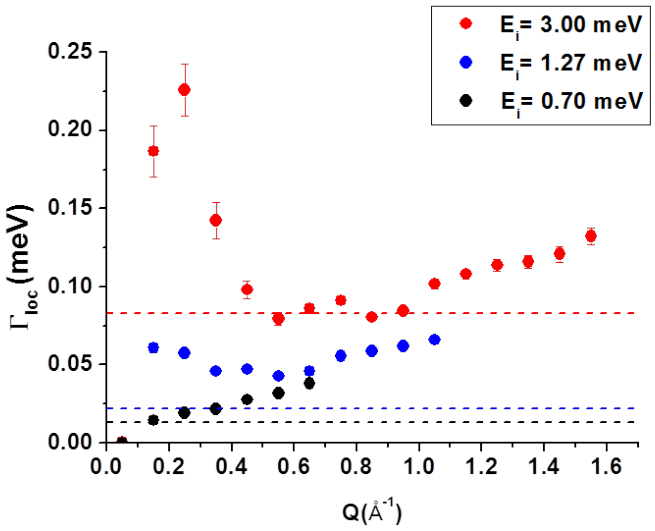

Figure 1.26: Trend of Γ_{loc} versus Q obtained by the fit of the data acquired at the three LET configurations on the OMIM-BF_4. The dotted line of the same color of the points represent the energy resolution of each configuration where the data were acquired (see table 1.2).

For fitting the spectra acquired at low resolution in the Q range not covered by the high resolution configuration (Q> 1.05 $Å^{-1}$), we imposed to Γ_{loc} the law of the jump diffusion [1]:

$$\Gamma(\mathbf{Q}) = \frac{DQ^2}{1 + DQ^2\tau} \tag{1.48}$$

where D is the self-diffusion coefficient while τ is the residence time of the proton between two jumps. We adjusted the value of D of equation 1.48 in order that the HWHM followed trend of Γ_{loc} founded at high resolution for low Q. We chose the value of τ so that the curve tends, for high Q, to the values found by the fit of the data at low resolution when Γ_{loc} was used as a free parameter (figure 1.26).

In this way we found a good agreement between the three resolutions.

After that we passed to characterize the slower diffusion with the fit of the NSE data.

In the space of time the function 1.41 becomes:

$$I(\mathbf{Q},t)_{inc}^{cation} = I_1(\mathbf{Q})\, e^{-\frac{t}{\tau_{lr}(\mathbf{Q})}} + I_2(\mathbf{Q})\, e^{-\frac{t}{\tau_{loc}(\mathbf{Q})}} + I_3(\mathbf{Q})\, e^{-\frac{t}{\tau_{orient}(\mathbf{Q})}} \tag{1.49}$$

where $\tau_i = \frac{\hbar}{\Gamma_i}$ with i=loc,orient and $\tau_{lr} = \frac{1}{D_{lr}Q^2}$.

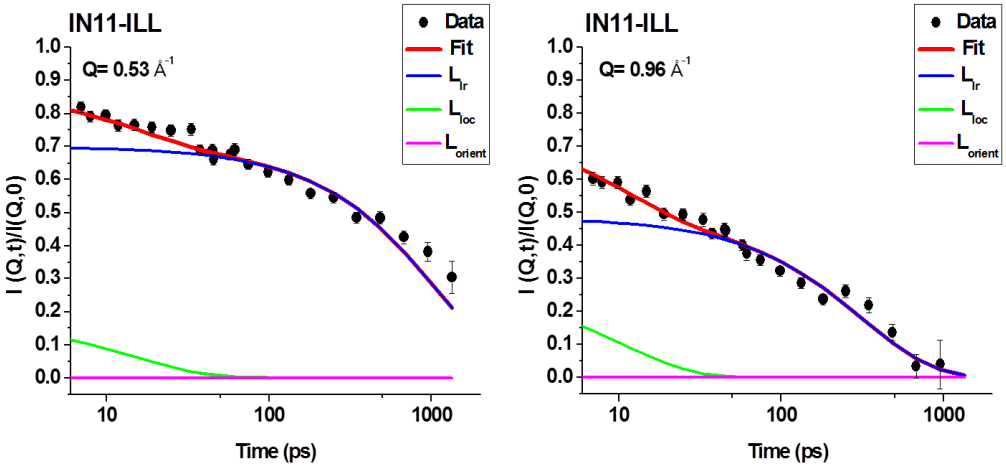

Figure 1.27: OMIM-BF_4 NSE spectra fit using function 1.49.

For these fits we imposed as fixed parameters the values of τ_{loc} and τ_{lr} founded by the ToF analysis and we let as free parameters the three intensity and D_{lr}. In this way we could characterize the diffusion at long range that was unresolved in ToF data (Fig.1.27).

Finally we performed again the fit of ToF data, following the procedure shown antecedently, imposing the D_{lr} founded by the NSE fit in order to verify if there were further changes in the faster dynamics (Fig.1.28).

1.3.5.4 Results and discussion

In this section we show the results obtained by the analysis procedure explained in section 1.3.5.3. It is divided in three parts. Each of them is dedicated to one of the dynamical relaxations observed during the QENS experiments.

1.3.5.4.1 Re-orientation dynamics

In the OMIM there are 23 atoms of hydrogen (see inset figure 1.29). As we already pointed out the three hydrogen bounded to the carbon atoms of the imidazolium ring are not concerned to the re-orientational motion, so the fraction p of hydrogen atoms which participate to rotational motion will be equal to $20/23 \approx 0.87$. We used this value to deduce the EISF by the equation 1.47, which is showed in figure 1.29. As we can notice from the plot, there is a good agreement between the three ToF resolutions.

We tried to fit the trend of $A_{orient}(\mathbf{Q})$ using different functions. We found that the best agreement is given by the EISF of a rotation on three equivalent sites [1]:

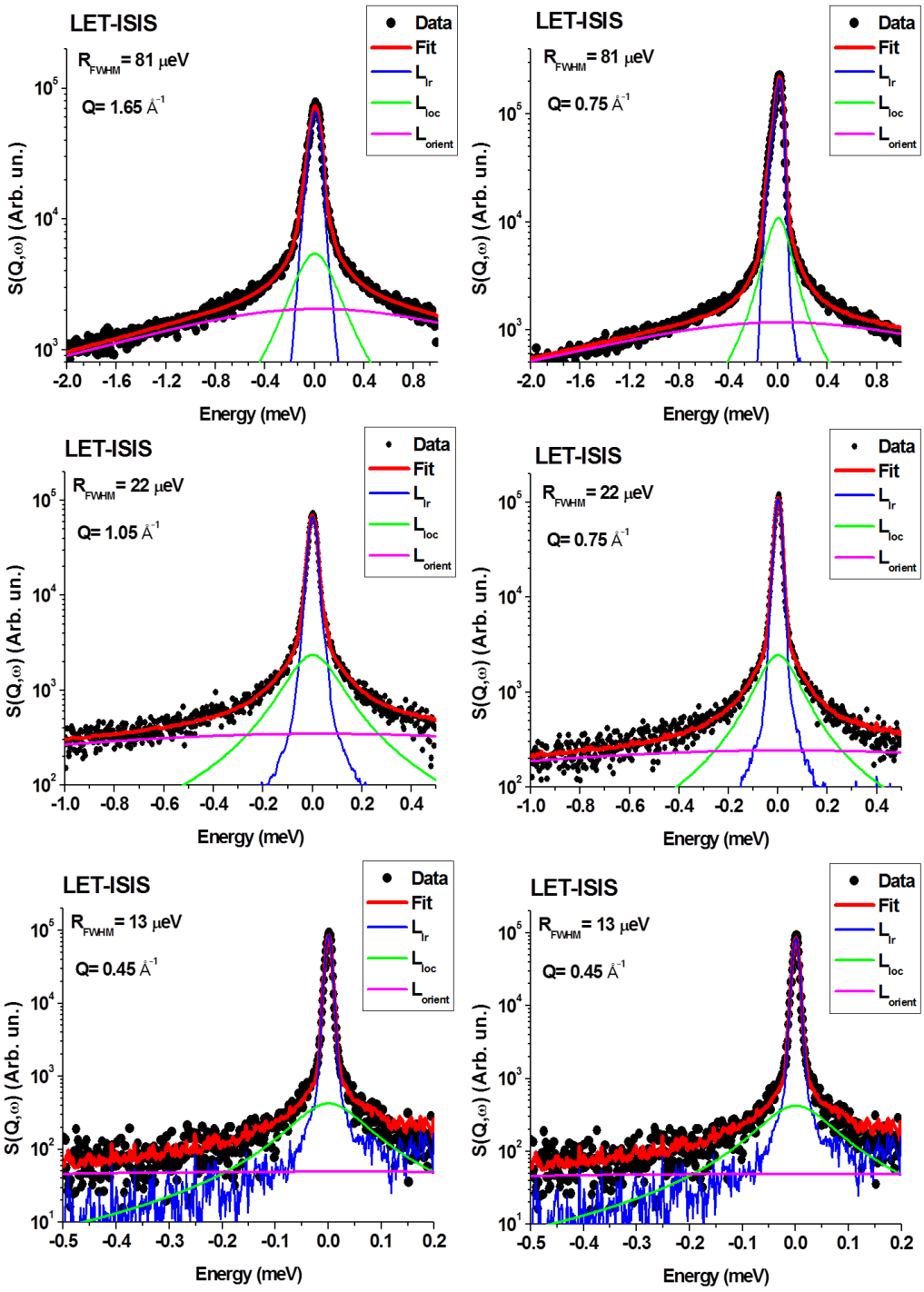

Figure 1.28: OMIM-BF_4 ToF spectra fit using function 1.41.

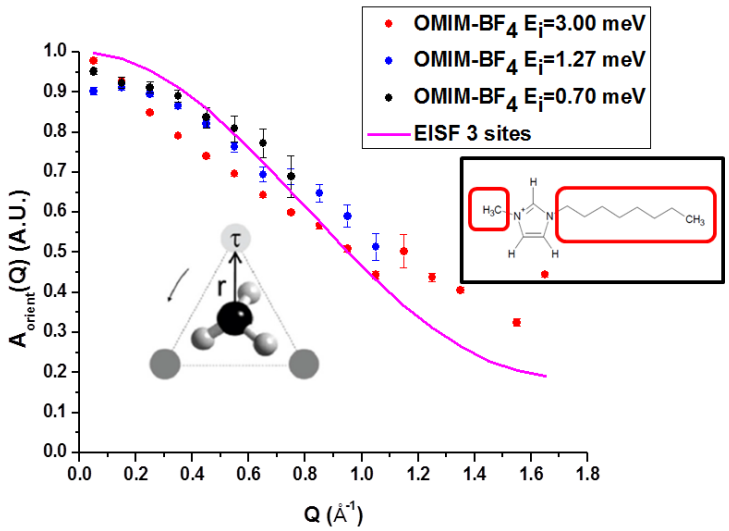

Figure 1.29: EISF deduced by ToF fit due to cationic re-orientation dynamics. We solid curve is the fit calculated using the function 1.50 which represents a rotational dynamics on three equivalent sites. This means that with our model we observed mainly the rotation of the methyl groups. Inset: Cation molecule where they are shown the hydrogen nuclei participating to the re-orientation dynamics.

$$EISF_{3-sites}\left(\mathbf{Q}\right) = \frac{1}{3}\left(1 + 2j_0\left(\sqrt{3}Qr\right)\right) \tag{1.50}$$

where j_0 is the 0^{th} order spherical Bessel function of the first kind while r is the distance between each site and the center of circumference where the sites are placed. From the fit we find a value of r equal to 1.5 Å.

From this result we can conclude that, with the approximation of the molecular re-orientation to an unique relaxation, we can observe mainly the rotation of the two methyl groups placed on the charged imidazole head and at the end of the alkyl-chain.

From the value of Γ_{orient}, we could find the characteristic mean residence time of an hydrogen on one site. In the case of a rotation on three equivalent sites i is given by the equation [1]:

$$\tau_{3-sites} = \frac{3\hbar}{\Gamma} \tag{1.51}$$

where $\hbar$ is the reduced Planck constant.

From the fit we found $\Gamma_{orient} \approx 1.79$ meV which corresponds to a time of 1.1 ps.

1.3.5.4.2 Diffusion inside the aggregate

In figure 1.30 A we show the trend of Γ_{loc} versus Q obtained by the ToF data fit.

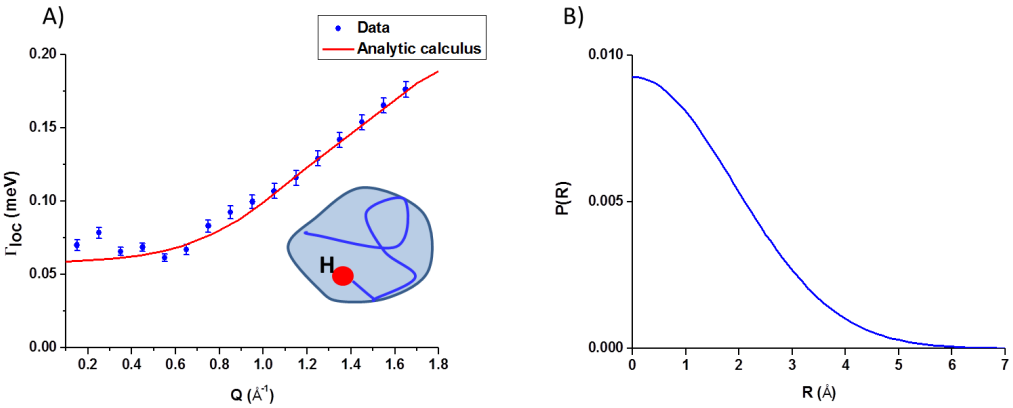

Figure 1.30: A) Trend of Γ_{loc} versus Q due to diffusion of the cation inside the aggregate (shown in the inset). The solid red line is the calculated HWHM of the Lorentzian of the QENS signal (eq. 1.27) using the values showed in table 1.4. B) Hydrogen displacement distribution deduced from the results of the simulation (table 1.4).

We can notice that for Q smaller than 0.75 $Å^{-1}$ we observe that the HWHM has a constant value of 0.06 meV, after that it seems to increase proportionally to Q. For finding the dynamical parameter associated at this diffusion, we simulated the scattering function of the Gaussian model 1.26 varying the values of D_{loc}, σ and τ_{mi}. After that we performed the frequency FFT of the curves and we fitted it QENS signal with a Lorentzian function (law 1.28).

The values for whom the simulation reproduces the experimental data are reported in the table 1.4.

D_{loc} (cm^2/s)	2σ (Å)	τ_{mi} (ps)
2.9 10^{-5}	3.6	1.1

Table 1.4: Values of the parameters of the Gaussian model obtained by the simulation of Γ_{loc} using the Fourier Transform of the function 1.28.

We can see from the table 1.4, that each hydrogen nucleus has a very fast diffusion dynamics inside a confined space of few Å with a waiting time between two jumps of 1 picosecond.

The hydrogen displacement associated to this value is reported in figure 1.30 B. It was calculated using the formula:

$$P(\mathbf{R}) = \frac{1}{(2\pi\sigma^2)^{\frac{3}{2}}} e^{-\frac{R^2}{2\sigma^2}} \tag{1.52}$$

The EISF of this dynamical component was deduced using the relation 1.46. The obtained trend is reported in Figure 1.31. Also in this case we can notice a good agreement between the three ToF resolutions.

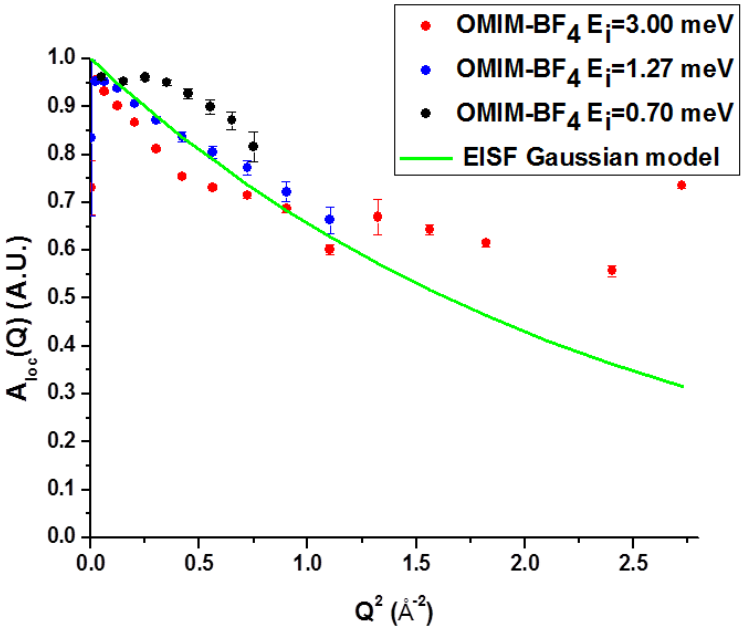

Figure 1.31: Trend of A_{loc} versus Q due to diffusion of the cation inside the aggregate. The solid line is the simulated EISF using σ= 0.65 Å.

We tried to simulate the EISF using the equation 1.30. We can see that the value of σ for which the simulation follows the data trend is for $\sigma = 0.65$ Å, which is in disagreement with the simulation of Γ_{loc}. We can explain this discrepancy with the bigger incertitude of the EISF values that could disturb the fit. We notice also a discrepancy between the fit and the data at high Q. We remind that in that zone in Q there is a peak in the structure factor due to the correlation between the alkyl-chain. We can thus suppose that the data are affected by a coherent contribution for these values of Q.

1.3.5.4.3 Long range diffusion

The value of the self-diffusion coefficient D_{lr} obtained at different Q values is reported in figure 1.32. We can verify that they are all compatible.

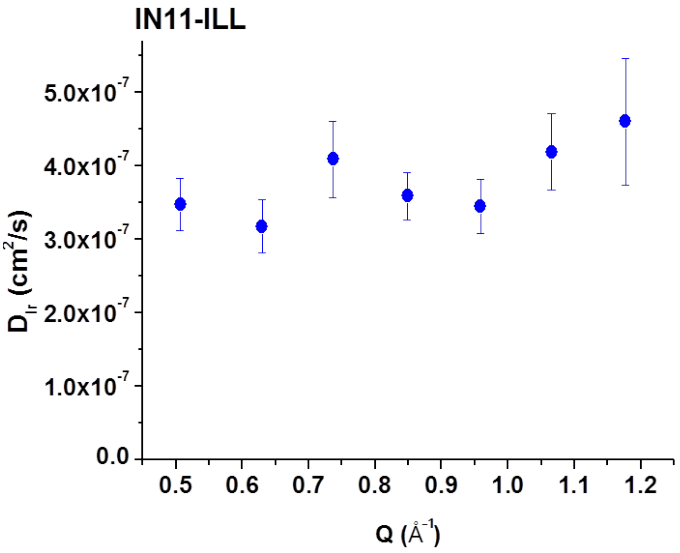

Figure 1.32: Values of D_{lr} obtained by the fit of NSE spectra using the function 1.49.

We calculated the average of them and we obtained the value $D_{lr} = 3.7\ 10^{-7}$ cm^2/s.

In order to verify that the free diffusion reproduces well the cation motion between the aggregates we determined the master curve (MC) of the diffusion at long range. For this purpose we separated the contribution due to this excitation. Using the relation 1.49, we can write the MC as:

$$I^{lr}_{MC}(\mathbf{Q},t) = \frac{I_{exp}(\mathbf{Q},t) - I_2(\mathbf{Q})\, e^{-\frac{t}{\tau_{loc}(\mathbf{Q})}} - I_3(\mathbf{Q})\, e^{-\frac{t}{\tau_{orient}(\mathbf{Q})}}}{I_1(\mathbf{Q})} \tag{1.53}$$

where $I_{exp}(\mathbf{Q},t)$ is the measured intermediate scattering function. The calculated curves are shown in figure 1.33. For underling the validity of the equation 1.33 we plotted the curve in function of the variable tQ^2.

We can observe the all curve are superimposed. We traced also on same plot the theoretical scattering function of the free diffusion process [1]:

$$I^{lr}_{theo}(\mathbf{Q},t) = e^{-D_{lr}Q^2t} \tag{1.54}$$

with D_{lr} equal to 3.7 10^{-7} cm^2/s. We can see that the theoretical curve is in very good agreement with the experimental data. We can conclude that the hypothesis of a free diffusion for the modelling the diffusional motion at long range is correct.

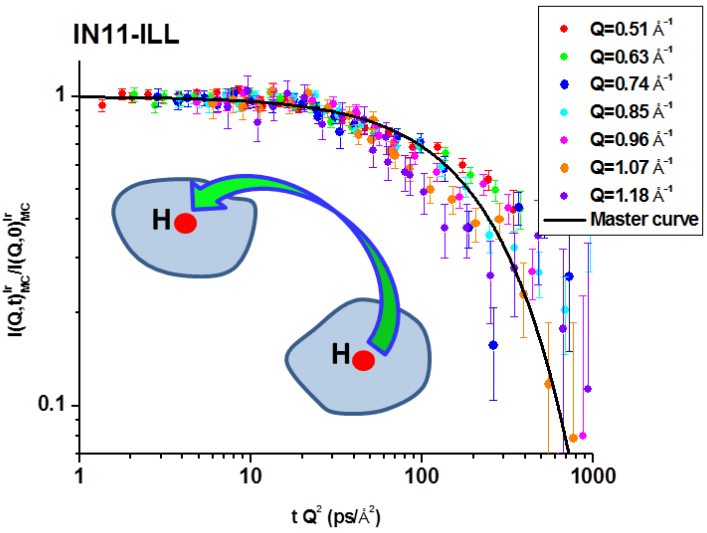

Figure 1.33: Master curve due to lr diffusion calculated using the relation 1.53. The solid line is master curve defined by the relation 1.54 with $D_{lr} = 3.7\ 10^{-7}$ cm^2/s.

1.3.6 Test of model robustness with the selective deuteration: the case of the BMIM-TFSI

The results obtained on the OMIM-BF_4 with the model shown in the section 1.3.5.2 seem to be very promising. We wanted thus test the robustness of model studying the dynamics of the selectively deuterated cation. This is a classic method used in the study of the protonated systems dynamics which consists in studying the change of quasi-elastic signal where some parts of the sample are selectively deuterated. The deuterium incoherent scattering cross section is about forty times smaller than that of the hydrogen ($\sigma_{inc}\,(^1D)$= 2.1 barns while $\sigma_{inc}\,(^1H)$= 80.3 barns) [44], so the contribution of the deuterated parts are essentially negligible. This means that the deuteration "hides" the dynamic modes of the deuterated moiety. This strategy allows thus to extract the different dynamical modes of the sample and to analyse them separately.

For this purpose we have chosen to focus on the BMIM-TFSI. We selected this liquids for testing also how the model fits the dynamics of less organized system. We remind that the BMIM based ILs show a very broad and bad defined pre-peak cause of their short a-polar chain which doesn't allow a good self-organisation (see section 1.2).

The studied samples are reported in the table 1.5. The deuterated sample has

been synthesised by Dr. Patrick Judeinstein (Laboratoire Léon Brillouin).

Name	Cation	Comment
BMIM-TFSI	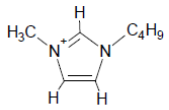	Fully protonated cation
B(d9)MIM-TFSI	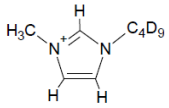	Deuterated alkyl-chain

Table 1.5: Ionic liquids studied in this section.

In this work we studied two liquids. The first one is the ionic liquid completely hydrogenated whereas the second one has its chain deuterated. In this way we hoped to minimize the contribution of the cation re-orientation dynamics that in the second sample is due only to the methyl group bounded to the imidazole.

We analysed the data with the same method used for the OMIM-BF_4. As for this system, we passed the two liquids on the spectrometer LET and IN11 and we performed the analysis procedure explained in the section 1.3.5.3. In this case the fraction of hydrogen atoms concerned in the diffusional and re-orientation dynamics (see equation 1.41) is p=12/15 for the BMIM-TFSI and p=3/6 for B(d9)MIM-TFSI.

We present now the results obtained on each relaxations doing the comparison between the two samples.

1.3.6.1 Re-orientation dynamics

The values of the parameters of re-orientation dynamics are shown in table 1.6.

	Γ_{orient} (meV)	Waiting time (ps)	r (Å)
BMIM-TFSI	1.55	1.3	1.4
B(d9)MIM-TFSI	1.54	1.3	1.7

Table 1.6: Dynamical parameters obtained by the analysis of the re-orientation dynamics. The waiting time and the typical distance r have been deduced by the model of the rotation on three equivalent sites (see section 1.3.5.4.1).

We can notice that the HWHM of the Lorentzian representing the re-orientation excitation has the same value in the two cases. This suggests that the broad component in the quasi-elastic signal is essentially due to the rotation of the methyl groups. This result confirms so that our approximation of this dynamics to an unique relaxation is correct.

The obtained EISFs (eq. 1.47) are shown in figure 1.34.

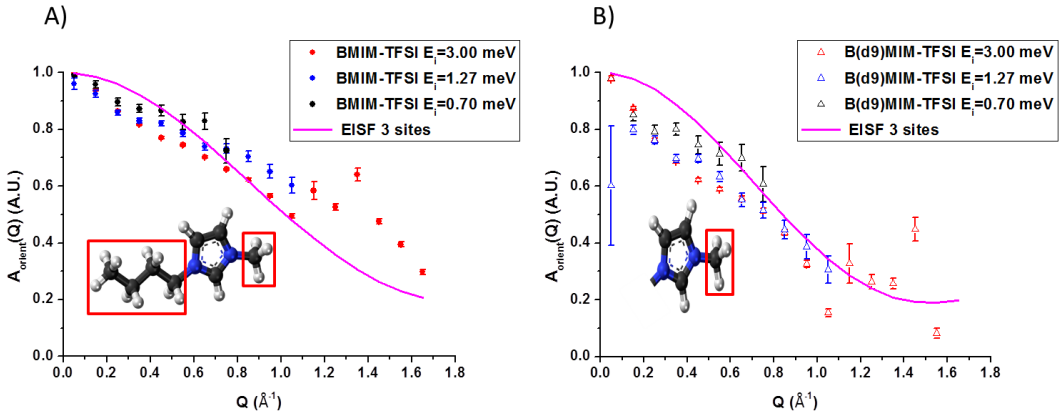

Figure 1.34: EISF of the re-orientation component of the BMIM-TFSI (A) and B(d9)MIM-TFSI (B). The points values have been obtained by the fit of the ToF data, while the solid line is the fit function. The inset of each plot shows the cation hydrogen nuclei seen by the beam during the QENS experiment. The atoms inside the red squares are those concerned by the re-orientation dynamics.

We can observe that the trend in two cases is very similar. We fitted the curves with the EISF of model of the rotation on three equivalent sites (eq. 1.50) and we found that the typical distance in the two liquids differs of the 20%. Also the waiting times of the two ILs are in good agreement between them.

1.3.6.2 Diffusion inside the aggregate

The EISF and HWHM of component due to the localised diffusion are shown in figure 1.35.

If we compare the trend of width of the Lorentzian versus Q in the two liquids, we can notice that for Q$>$ 0.5 Å^{-1} the values of Γ_{loc} are compatible for the two samples. Only for low Qs we can observe that the plateau is shifted to low values in the case of semi-deuterated liquid. We can suppose that this feature is due to a contribution of the coherent scattering (de Gennes narrowing effect [57]), which is amplified for presence of the deuterated parts. We have to remind in that zone there is the coherent contribution of the pre-peak in the structure factor of

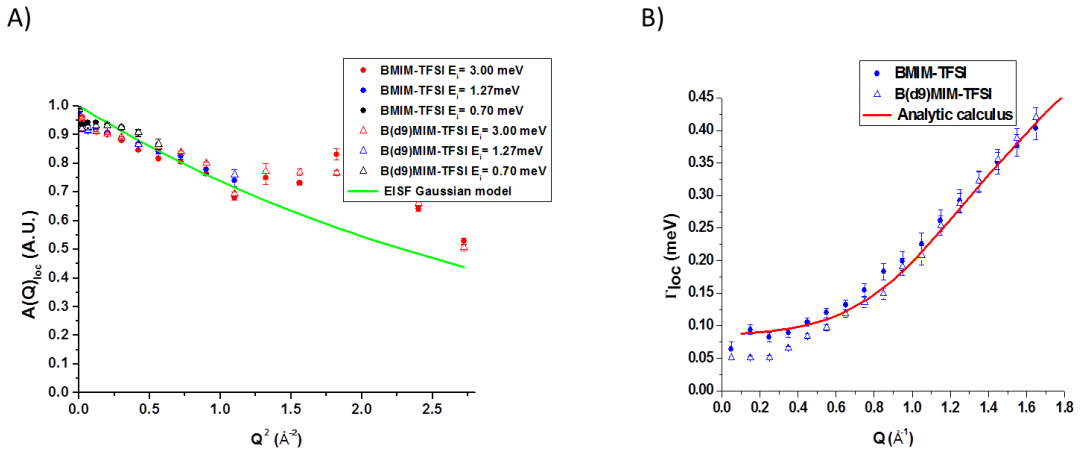

Figure 1.35: A) EISF due to the local diffusion calculated by the equation 1.46. The point values are obtained by the ToF data fit, while the solid curve is fit using the EISF of the Gaussian model (eq. 1.30). B) HWHM of the Lorentzian due to confined diffusion. The solid red line is the analytic model using the Gaussian model with $D_{loc} = 4.8\ 10^{-5}$ cm^2/s, $\sigma = 1.9$ Åand $\tau_{mi} = 0.4$ ps.

the BMIM-TFSI. As for the OMIM-BF_4, we performed the analytical calculation, using the Gaussian model, for finding the dynamical parameters which fit the experimental data (see table 1.7).

D_{loc} (cm^2/s)	2σ (Å)	τ_{mi} (ps)
$4.8\ 10^{-5}$	3.8	0.4

Table 1.7: Values of the parameters of the Gaussian model obtained by the analytic calculation for reproducing the trend of Γ_{loc} (FT of the function 1.28) on the BMIM-TFSI.

We can see that in this case we have a faster cationic dynamics compare to the OMIM, which is constituted by higher self-diffusion coefficient and a smaller waiting time between two jump. This result is consistent with analysis performed on the ionic couple effect on the ILs molecular dynamics (sec. 1.3.3).

If we observe the EISFs of the samples (figure 1.35 A), we can notice that the trend in the two liquids is identical. We tried to fit the curves with the EISF of the Gaussian model defined in the equation 1.30, we found that this model fits well the data at except for the zone at high Q. We have to stress that in that interval in Q there is a peak in the structure factor due to correlation between the alkyl chain [20], that could introduce some detrimental coherent contribution. Also for

this case the fit gives a value of σ of 0.55 which doesn't agree with the results obtained by the analysis of Γ_{loc}.

1.3.6.3 Long range diffusion

The long range diffusion was characterize by the analysis of NSE curves.

We have to underline the analysis of B(d9)MIM-TFSI was particularly delicate because the contribution of the coherent scattering produced a decrease of the beam polarisation (see section 1.3.2.2.4), which affects deeply the statistic of the signal. For this reason we could analyse a very small Q range.

The values of the long range self-diffusion coefficient of the two ILs are shown in table 1.8.

	BMIM-TFSI	B(d9)MIM-TFSI
D_{lr} (cm^2/s)	1.21 10^{-6}	9.2 10^{-7}

Table 1.8: Values of the long range self-diffusion coefficient obtained by the fit of NSE spectra.

We can observe a difference of about 30% between of the values, however we underline that the incertitude of this coefficient is rather high especially concerning the case of the B(d9)MIM-TFSI, for the reason that we have explained. We can conclude then the results are reasonable.

Also for these liquids we determined the master curve due to the long range diffusion diffusion (eq 1.53) that are shown in figure 1.36.

We sketched on each plot the theoretical curve due to free diffusion scattering function (eq. 1.54) using the values of D_{lr} obtained by the fit of the curve. We can conclude that the model is in a good agreement with the data.

1.3.7 Conclusions and comparison with the previous results

From the results shown in the sections 1.3.5 and 1.3.6, we can conclude that the developed model fits well the experimental data and it is able to reproduce the dynamics of different systems in a very wide time interval which covers three order of magnitude.

This new approach allowed to analyse deeply the dynamical modes of the cation and it brought to light some important properties of the cationic dynamics.

First of all the presence of two diffusional motion occurring at two different time scale. We could observe in fact that the self-diffusion coefficient associated to the localised diffusion is almost 2.5 times bigger than that one of long range

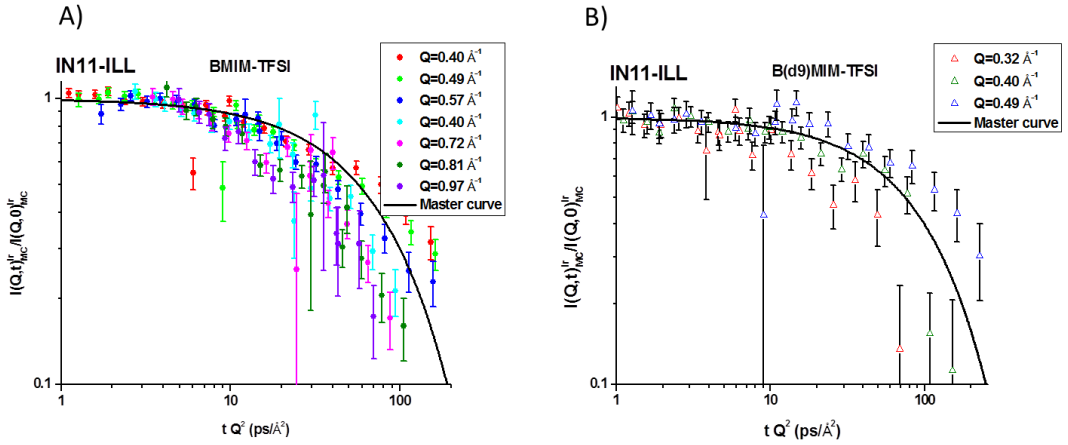

Figure 1.36: Master curves due to the long range diffusion obtained using the relation 1.54 on the NSE data of BMIM-TFSI (A) and B(d9)MIM-TFSI (b). The solid curve are the trend of the intermediate scattering function of a free diffusion process (eq.1.54) using as values of self-diffusion coefficient those reported in the table 1.8.

motion. The presence of two diffusional dynamics in different times ranges was observed by other QENS studies on different ILs [34, 37–40], we can then conclude that our results seem consistent with the literature.

Another important aspect revealed by this study is the characterization of the re-orientation dynamics. Indeed the strategy of the selective deuteration of the alkyl-chain has permitted to show that the unique rotational modes observable by QENS is that due to the rotation of methyl groups.

In closing we can compare the results given by our analysis with those ones obtained by other experimental techniques.

We can check the agreement between the results on the dynamics at the local scale and those about the structural properties obtained by SANS. Using the generalized Gaussian model, it is possible to deduce the average distance between two aggregates, called L, which is given by the relation [53]:

$$L = 2\sqrt{-8\sigma^2 \frac{D_{ld}}{D_{loc}}} \tag{1.55}$$

If we insert the values of σ, D_{ld} and D_{loc} obtained in our QENS study in the equation 1.55 we obtain respectively L $\approx$ 2.2 nm for the OMIM-BF_4 and L $\approx$ 2.1 nm for the BMIM-TFSI. We can see that for the case of the first liquid there is a very good agreement with the value of the correlation length the OMIM-BF_4 deduced by position of the pre-peak in structure factor measured by SANS (see

section 1.2), while for the second there is a difference of about 30%. However we want to underline that the BMIM based ILs are a quite borderline case because they don't have a well defined pre-peak of auto-organisation, but a very broad shoulder that is difficult to identify [19,20]. With these considerations we can thus conclude that the results on the dynamics are in a good agreement with the results obtained on the structure.

We can therefore compare the results obtained with the NMR data of the literature, for performing a comparison of the dynamics occurring at different scales. For this purpose we used as reference for the OMIM the self-diffusion coefficient at 293 K reported in the reference [50], while for the BMIM that one of the reference [41]. The value of the different coefficients, with the relative probed dynamical scale are shown in table 1.9.

Technique	$D_{OMIM-BF_4}$ (cm^2/s)	$D_{BMIM-TFSI}$ (cm^2/s)	Time scale (s)	Length scale (m)
ToF	$2.9\ 10^{-5}$	$4.8\ 10^{-5}$	10^{-12}	10^{-10}
NSE	$3.7\ 10^{-7}$	$1.21\ 10^{-6}$	10^{-11}	10^{-9}
NMR	$2.8\ 10^{-8}$ [50]	$2.2\ 10^{-7}$ [41]	10^{-2}	10^{-6}

Table 1.9: Values of different self-diffusion coefficient of cation of OMIM-BF_4 and of BMIM-TFSI at room temperature obtained by different spectroscopic techniques with relative probed dynamical range.

As we can see from the results reported in this table, the two ILs have a quite complex dynamical behaviour, that is unusual for a bulk liquid.

First of all two different diffusional motions are present at the molecular scale. Generally for a classic liquid only a translational dynamics is observable in this dynamical range. If we take, for example, the studies done on the bulk water by QENS, they show that, at the picosecond time scale, the protons have a simple diffusive motion constituted by a jump diffusion behaviour [58]. The feature of two different translational diffusions usually is typical of the confined liquids in tortuous mesoporous materials [56], where there is a complex network of interactions between the confinement matrix and the fluid molecules which modifies deeply the dynamics of the system.

Furthermore we observe a big discrepancy between the dynamics probed on the molecular scale by QENS (Å, ps-ns) and that one probed on the microscopic scale by NMR (μm, 10 ms). In fact the first one is much faster than the second. Also this feature is quite unexpected. In fact if we take another time the example of the bulk water, it was shown that the hydrogen self-diffusion coefficient measured by NMR [59] is compatible with that one deduced by QENS measure [58].

We explain thus these features in the dynamical properties as consequences of the self-organisation of the system. In fact we suppose that the presence of an order at the local level generates a complex interplay of interactions between the different ionic components which generates a system whose it dynamics it is strongly dependent on the probed scale. The effects of the organisation are already visible by the QENS analysis, where we can observe that dynamics at the nanometer scale is much slower than those probed at the Ångström one. We can conclude so that the dynamics undergoes a slowing down because of the self-organisation. This hypothesis seems to be coherent also with previous QENS study performed on imididazolium based IL with a short alkyl-chain (i.e. with no self-organisation) where there no localised diffusion was observed [36].

This braking of the dynamics seems to be even amplified when we pass to probe the dynamics at larger scale with a further diminution of the self-diffusion coefficient showed by NMR measurements. However the dynamical scale probed by this technique is too far from that one probed by QENS for studying more quantitatively the effects of the self-organisation on the microscopic scale. Additional measurements of field cycling NMR relaxometry, which probes an intermediate scale, could be useful for this purpose.

In conclusion by this multi-scale approach we have pointed out how the self-organisation of the system plays a very important role for the dynamical properties of the IL. We have demonstrated in fact that it causes a slowing-down the dynamics at nanometric/microscopic scale. From this conclusion we can finally suppose that a frustration of the self-organisation could be a good method for improving the dynamical properties of these systems.

Chapter 2

Properties of the ionic liquids confined in anodic aluminium oxide membranes

From the results given by the study performed on the bulk ILs properties, we showed the ILs self-organisation plays a key role in the determination of the liquids dynamical properties. We can then suppose that changing the static correlation of these systems we can induce also modification on the ionic dynamics and transport properties. In this context the use of nanoconfinement appears as an interesting strategy to apply to ILs. It is well known that many materials change their physical properties when one or more of their spatial dimensions are subjected to a geometrical restriction. Some recent studies showed that the ILs confined in different materials change some of their physical features such as their thermodynamic properties [60–62], their vibrational excitations [61], or their dynamical and transport properties [9, 63–65].

In this part we will show the study performed on the confined ILs in the porous anodic aluminium oxide (AAO) membranes. After a general introduction about these systems, we will present the main effects induced by the confinement on the ILs features. We will begin showing the observed effects induced on the liquids physics at the macroscopic scale such as the thermodynamical properties. Then we will tackle the confinement effects induced on the microscopical properties, i.e. the self-organisation behaviour and the dynamics, using as point of departure the results observed in the bulk state.

2.1 State of the art on the ILs confinement: the ionogels

The most studied confining matrix for the ILs are certainly the *ionogels*. They are composite materials formed by a solid porous skeleton, entrapping in it cavities the IL (see Figure 2.1 A).

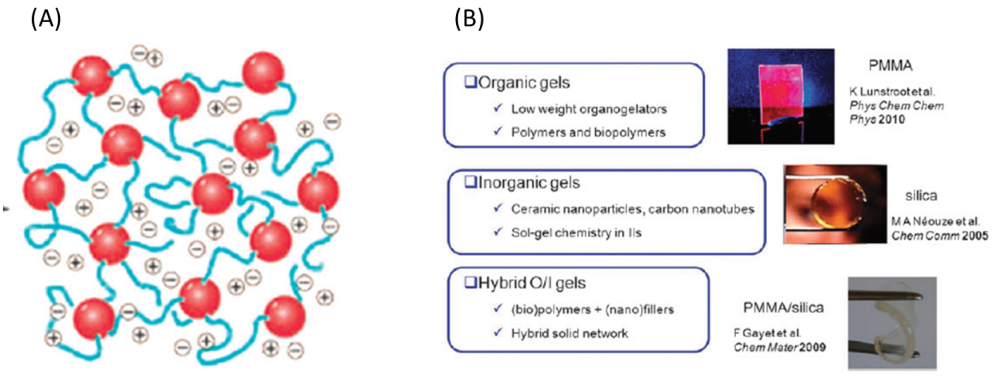

Figure 2.1: (A) Sketch of an organic ionogel composed by an ABA triblock copolymer. The A blocks (red), in contrast with the B (blue), are insoluble in the IL so they self-assemble when they are in solution into liquid, forming the ionogel (the ions are represented by the sign + and −). (B) Different families of ionogels. This figure is taken by the reference [62].

Nowadays many types of ionogels have been discovered and characterized. They can be divided in three main families (Fig.2.1B), as a function of the material forming the solid matrix [62];

- *Organic ionogels*: porous systems composed by an organic material, such as low weight organic gelators or polymers,
- *Inorganic ionogels*: matrices composed by inorganic compounds (carbon nanotubes, silica particles etc.) or by sol-gel process inside the liquid.
- *hybrid organic-inorganic ionogels*: complex systems composed by mixture of organic and inorganic compounds (e.g. silica+polymer).

These systems represent the most important reference when we are interested in the ILs confinement.

2.2 The porous anodic aluminium oxide membranes

The AAO membranes are nanostructured porous materials which have been intensively used as confining matrix for studying the confinement effects on the properties of different systems such as liquid crystals [66, 67] or polymers [68–70]. The goal of this chapter is to illustrate the main properties of this porous material.

2.2.1 The AAO synthesis

A porous oxide layer could be produced by an anodizing process on aluminium plate. The metal is placed as anode in a electrochemical cell whose electrolyte can dissolve partially the aluminium oxide. When a voltage is applied to this system, we can observe an electric current flowing between the electrodes whose intensity as a function of time follows the trend shown in figure 2.2.

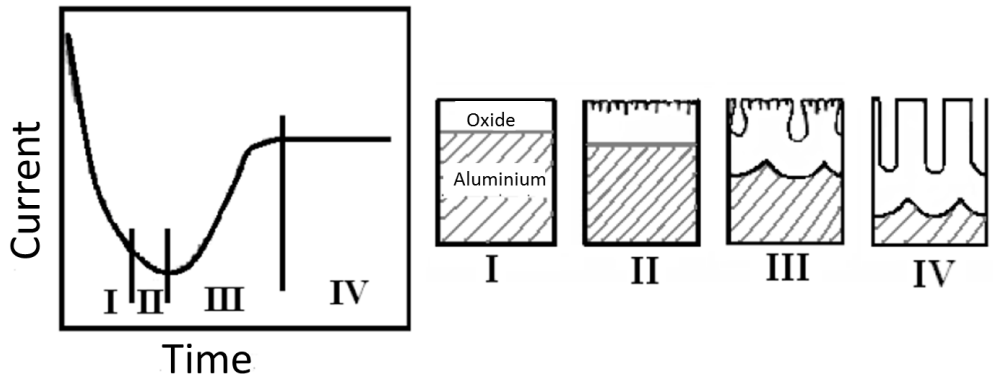

Figure 2.2: On the left: trend of the current between the electrodes as a function of the time during the anodization process. On the right the sketch of the different steps of oxide porous layer formation: I) Formation of alumina layer at interface metal/electrolyte, II) defects produced by the dissolution of the oxide in the electrolyte, III) formation of the porous structure due to the interplay between the oxidation and the dissolution process, IV) equilibrium achievement between the two chemical reactions. From reference [71].

We can explain this complicate trend as a succession of different steps [71]. Initially there is a significant decrease of the current (I) due to a fast corrosion process which produces an oxide barrier at the metal/electrolyte interface. After that the shut down of the intensity slows down due to the formation of small defects generated by the alumina dissolution in the electrolyte (II). Thereafter an interplay between the oxide dissolution and the metal oxidation produces the formation of

the pores with an increase of current intensity (III) which finally reaches a stable value when the equilibrium between the two reactions is achieved (IV).

This method produces thus a porous oxide layer where the pores dimension, the inter-pore distance and the oxide thickness could be controlled by the experimental parameters (e.g. the nature of the electrolyte, the anodization duration, the voltage) used during the process [72]. It was observed that the pores produced by this technique show a quasi perfect honeycomb arrangement at the metal/oxide interface which is partially lost at the interface between the electrolyte and oxide [73, 74].

This limitation has been overcame by the two-step anodizing process proposed by Masuda et al. [75]. This is one of the most used method for fabricating AAO membranes nowadays. The main steps of the membrane formation are shown in figure 2.3.

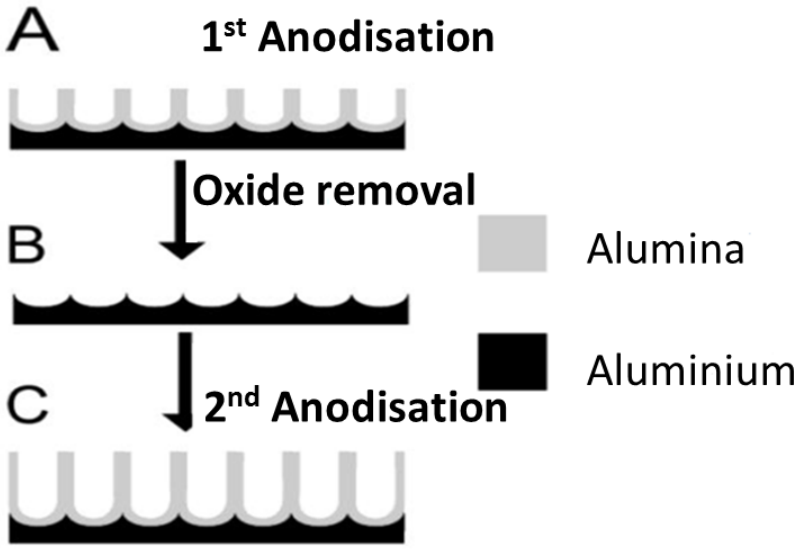

Figure 2.3: Main steps of the AAO production by a double anodization steps proposed by Masuda et al. [75]. A) First anodising process (see Fig.2.2). B) Oxide removal by acid attack which leaves an aluminium substrate with a patterned surface. C) Second anodising process. This method produces AAO membranes whose pores have a quasi-hexagonal (honeycomb) arrangement. This figure is taken by the reference [72].

After a preliminary degreasing and electropolishing operation the aluminium is submitted to a first anodization process (Fig.2.3A). This produces a porous alumina layer which is removed by an acid attack. After this step the system is just an aluminium layer whose surface is textured by a pattern of concave holes

(Fig.2.3B). Thereafter the metal is subjected to a second anodizing process similar to the first (Fig.2.3C).

After the oxide formation the system in subjected to a post-anodisation process where the aluminium substrate and the oxide barrier at the metal/oxide interface are removed by an acid attack [72]. This produces an oxide membrane whose pores are open at both sides.

An example of the system obtained by this method is shown in figure 2.4.

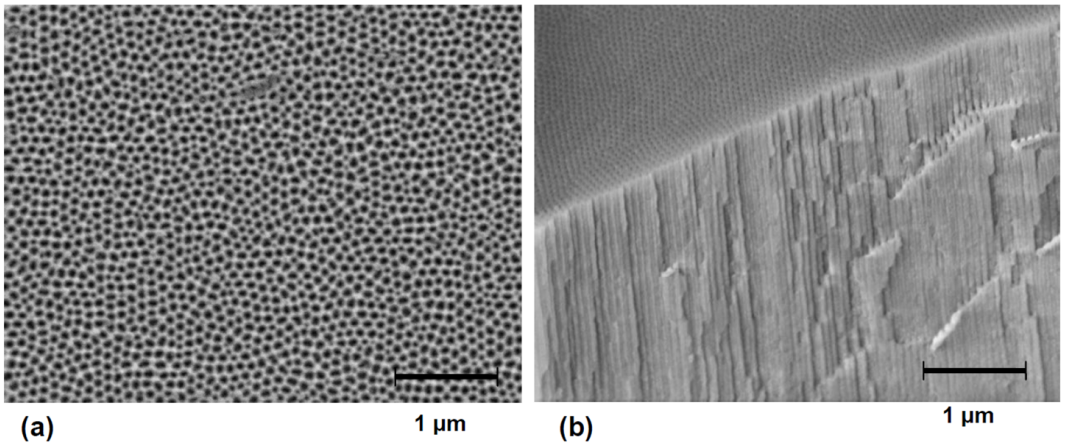

Figure 2.4: Scanning electron microscopy pictures of the AAO membranes produced by the double anodisation method following the experimental protocol described in the reference [76]. A) Surface of the membrane. B) 3D image which shows the macroscopic alignment of the pores. After the reference [72].

2.2.2 The AAO morphology

The morphology of the AAO membranes produced by this method has been intensively studied with different experimental techniques. A combination of microscopy and SANS measurements have extrapolated the geometrical shape of the pores and their arrangement inside the membranes [68, 72]. It was shown that the pores have a cylindrical shape and their radius follows a Gaussian distribution with a standard deviation of few nanometers [72]. It was also demonstrated that the geometrical arrangement of the pores conserves its hexagonal arrangement showing a structure factor which could be approximated to that of honeycomb lattice [72].

Another very particular feature of these membranes is the quasi-perfect macroscopic alignment of the pores. SANS measurements have demonstrated the AAO are strongly anisotropic systems. It was shown that few tenths of degree between the neutron beam and the membrane surface suffice for obtaining an anisotropic signal at small angles as it is shown in figure 2.5.

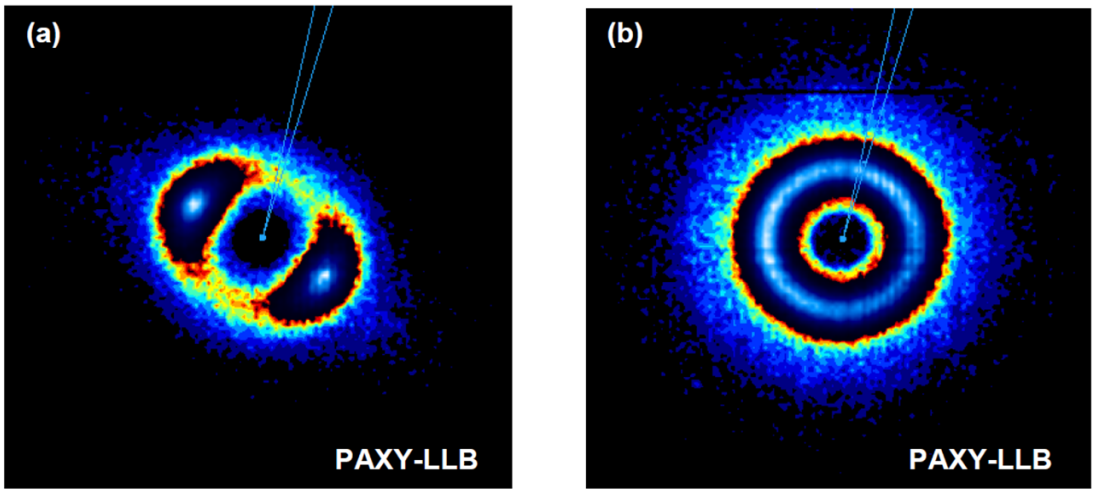

Figure 2.5: AAO SANS spectra (after [72]) acquired on the spectrometer PAXY (LLB-France) the Q scale is between 8 10^{-3} $Å^{-1}$ and 7 10^{-2} $Å^{-1}$. A) The pores are tilted in comparison to the beam; this produces a small angle signal which is strongly anisotropic. B) The axis of pores is perfectly oriented parallel to the beam.

This high sensitivity to the membrane orientation suggests a strong orientation a the macroscopic scale which has been confirmed by the SEM microscopy (Fig.2.4).

Form this brief presentation we can now understand the interest of using the AAO as confining matrix for the ILs. Indeed this systems show multiple vantages.

Firstly the fair monodispersity of the pores dimension, together to the accessibility of a wide range of pores diameter (from 25 nm to 400 nm), enable a study of confinement effects in function the confinement size.

Furthermore we can also imagine to exploit the strong anisotropy of the AAOs. We can suppose in fact that this feature could oblige the ionic dynamics toward a preferential direction parallel to the pores axis. This could be a very useful properties for the possible application in the electrochemical system development such as the batteries separators.

2.2.3 Choice and preparation of the sample

For this study we have chosen to use the AAO membranes produced by the company smartmembrane [77]. We focus our attention on three specific diameters of pores: 25, 60 and 160 nm. We picked these values in order to span the largest range of confinement size. The dimension of each membrane was 10x10x0.1 mm^3.

We have studied confinement effects on two specific ILs: the OMIM-BF_4 and

the BMIM-TFSI. The first liquid has been chosen for analysing the changes of the ILs properties at the local scale. In fact we have shown in the chapter 1 of this thesis that this liquid has a well defined pre-peak that highlights a strong nanoscopic self-organisation. This feature makes this system as very good model for studying the confinement effect on the self-organisation and on the dynamics at the molecular scale. On the other hand we were also interested in studying the effect of confinement on the ILs macroscopic properties such as their thermal phase transition features (e.g. melting point, glass transition etc,). Since the OMIM-BF_4 does not crystallize and hence it has no melting point [5], we choose the BMIM-TFSI, which shows several first order and second order phase transitions [78], for analysing the confinement effect on the ILs thermal properties.

The preparation of the samples was the same for the two liquids.

Before to fill the membranes with the ILs they were subjected to a pre-treating process. On the pore walls are present hydroxyl groups which are extremely hydrophilic. They can thus develop easily hydrogen bonds with water molecules in the atmosphere trapping them inside the pores. For removing the residual water we put the membranes at 100° C under the vacuum (using a secondary vacuum system) for 24 hours.

There after the membranes were imbibed with ILs by submerging them in the liquid for 24 hours.

Finally the excess of IL on the membranes surface was removed by absorption of a paper tissue.

The membranes were weighted before and after the filling procedure. In the table 2.1 we show the measured porosity calculated as $(m_{filled} - m_{empty})/m_{filled}$ compared to that given by the supply company [79]. We can notice a good agreement between the measured and the tabulated values.

Sample	Measured porosity (%)	Given porosity (%)
AAO $\oslash$ = 160 nm	11	11
AAO $\oslash$ = 60 nm	24	29
AAO $\oslash$ = 25 nm	10	13

Table 2.1: Measured porosity of the AAO samples compared to the values given by the supply company. We can notice a good agreement with the two series of values.

2.2.4 Check of the IL confinement by contrast variation

Before dealing with the physics of IL in restricted geometry, a crucial step is to estimate the degree of confinement.

Contrast matching in SANS is the perfect tool to assess such an issue [69,80,81].

For centro-symmetric objects the scattered intensity, $I(Q)$, is described by the general relation:

$$I(\mathbf{Q}) = \Delta\rho^2 P(\mathbf{Q}) S(\mathbf{Q}) \tag{2.1}$$

$P(\mathbf{Q})$ and $S(\mathbf{Q})$, the *form* and *structure factors* are respectively related to the shape of a single pore and to the spatial arrangement of their centers. Beside the specific structure of the porous network itself, the scattered intensity is controlled by the so-called *contrast factor* term: $\Delta\rho^2$. In neutron scattering, the fundamental process leading to the scattering of the incident neutrons by the target nuclei is a nuclear interaction resulting in a coherent scattering length b_{coh}, which is strongly dependent on the isotope under consideration. In practice in Small and Ultra Small Angle Neutron Scattering (SANS/USANS), the scattering of a pure component is characterized by its coherent Scattering Length Density (SLD), ρ, which is defined as the ratio of the coherent scattering length of an elementary block of the material (atoms/molecules) over it molar volume:

$$\rho = \frac{N_A \rho_m}{M} b_{coh} \tag{2.2}$$

where N_A is the Avogadro's number, ρ_m its volumetric mass (g/cm^3), M its molar mass (g/mol). This quantity has thus the dimension of the inverse of a length and it is generally expressed in cm^{-1}.

The SANS/USANS signal is caused by the fluctuations of the scattering length density of the sample. In the field of confinement ρ and ρ_0 are the SLDs of the confining matrix and of the confined material.

If we suppose that the matrix is filled *completely* and *homogeneously*, the geometry of the sample is not modified. This implies that the only parameter that changes in the relation 2.1 is the contrast factor. So, considering the case of the IL confined in the AAO, if we perform the ratio between the SANS signal of the filled membrane and that of the empty one, we have to obtain:

$$R = \frac{I_{AAO+IL}(\mathbf{Q})}{I_{AAO}(\mathbf{Q})} = \left(\frac{\rho_{AAO} - \rho_{IL}}{\rho_{AAO} - \rho_0}\right)^2 \tag{2.3}$$

where ρ_0 is the SLD of the air (or of the vacuum) which is $\rho_0 \approx 0$.

So in the case of complete and homogeneous filling the spectra ratio must be a Q independent quantity equal to the squared ratio of the contrast factor.

In this work we performed the check of AAO filling in the case of OMIM-BF_4. For this purpose we performed SANS measurements on the spectrometer SANS-1 (MLZ Germany) [82]. The SLDs of the considered materials are respectively

$\rho_{AAO} = 4.22\ 10^{10}$ cm^{-2} [72] and $\rho_{OMIM-BF_4} = 9.65\ 10^{9}$ cm^{2}. This implies that theoretical ratio of the squared contrast factor (eq.2.3) is $R_{theo} = 0.59$.

An example of the acquired spectra is reported in figure 2.6A. In this case the AAO membrane with pores of 60 nm is shown. The presence of a fully hydrogenated confined IL is clearly detected at high Q as the liquid incoherent contribution induces an higher intensity than in the case of the neat AAO. For smaller Q values, we can notice that the spectra of the empty and the filled membrane have a very similar shapes.

We can observe a first peak near to $7\ 10^{-3}$ Å^{-1} that is due to inter-pore distance, while a second one, in the region of 10^{-2} Å^{-1} is related to pore dimension [72]. Finally in the part at high Q the intensity follows a power law (Porod law) whose prefactor is the membrane specific surface [72]. We can observe that generally the scattered intensity of the filled membrane is smaller than that of the empty one.

The ratios of the spectra of between the filled and the empty AAO, for the

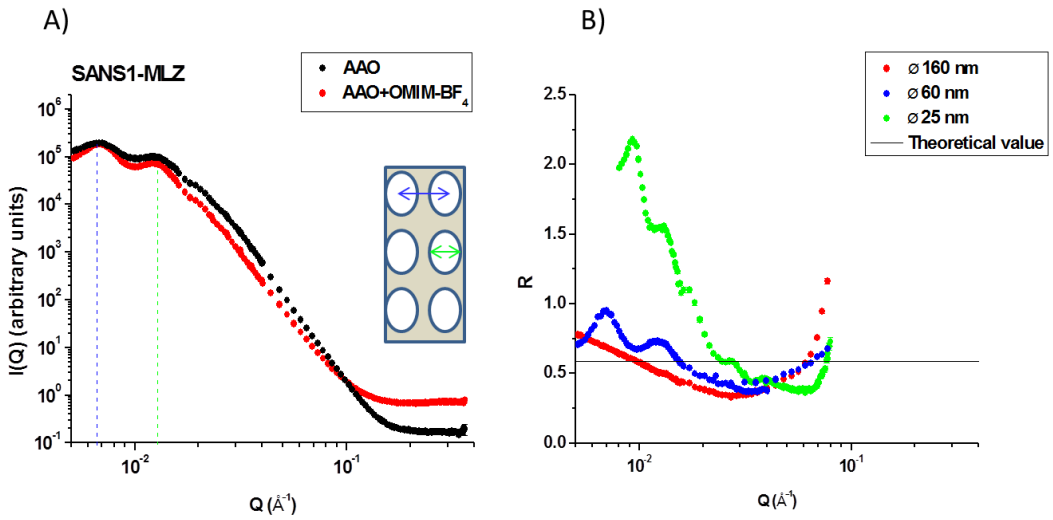

Figure 2.6: A) SANS spectra measured on SANS-1 (MlZ-Germany) of the empty AAO ($\oslash$ = 60 nm), in black, and of AAO with the same pores diameter filled by OMIM-BF_4, in red. We can distinguish two peak due to inter-pores distance and the pores dimension. The dashed line are just guide-eye for specifying the peaks position. Near to the plot there is an AAO sketch. The arrows indicate the characteristic distances in the system. The peak at small lower Q is related by the distance between two pores center, while that at larger Q is related to the pores dimension. B) Ratio between filled AAO and the empty one (eq.2.3) for pores of 25 nm (green), 60 nm (blue) and 160 nm (red). We notice that in all cases the ratio oscillates around to the theoretical value $R_{theo} = 0.59$.

three pore sizes, are shown in figure 2.6B. From this plot we can notice that the ratio is not Q independent as one would expect in the case of a perfect full and homogeneous confinement, but instead it oscillates around the theoretical value 0.59. Since the bulk liquid has a flat structure factor at small Q, such ratio trend has to be due to the IL confinement inside the pores. We can conclude then that while it is possible to confine the IL within the AAO network (we detected the incoherent signal due to the confined IL), the confinement is not homogeneous. We can invoke different scenarios to explain such an imperfect confinement (see Fig. 2.7).

Figure 2.7: Possible scenarios which can describe the IL confinement in the AAO. a) Concave meniscus formation generated by the tension surface between the liquids and pores walls b) IL drops not interconnected between each others (or equivalently bubbles in the liquids). c) IL film formation on pores surface.

Among the different structuration situation shown in figure 2.7, the case b) seems unlikely, we suppose then that the imperfect match can be a combination of the scenario a) and c). However we could not characterize more properly the liquid confinement condition as we observed an IL layer formation between the membrane and the sample cell during the measurements. This suggests the presence of a kinetic process, which induces an expulsion of the confined liquid as a function of the time. The IL perfect and homogeneous confinement is a metastable situation i.e. after several hours we observe a desegregation of the liquid that results in the formation of a liquid layer on the top of the membrane.

By removing the expelled liquid quantity from the membrane and measuring the mass variation, we can estimate the "leaking" is of the order of 30% of the total mass of the initially confined liquid (1 mg on the 3.2 mg initially confined).

2.3 ILs under confinement: thermodynamical aspects

2.3.1 A brief introduction about the ILs thermodynamical properties

2.3.1.1 Bulk IL phase diagram

As we have already pointed out in the section 1.1, ILs show a mp at much lower temperature than the classic inorganic salts. This particular feature is caused by the use of a bigger organic cation. The increasing of the cation size seems indeed to cause a mp depression below the room temperature [11].

In figure 2.8 we show the phase diagram, determined by differential scanning calorimetry (DSC), of the ILs series C_n-MIM-BF_4 with $0 \leq n \leq 18$ measured by Holbrey et al. [5].

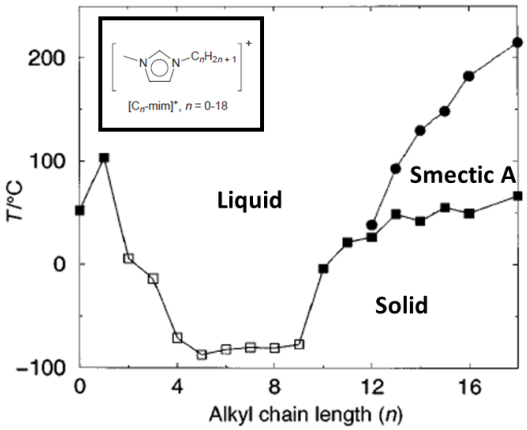

Figure 2.8: Phase diagram, determined by DSC, of the ILs series C_n-MIM-BF_4 showing the melting point (close squares), the glass transition (open square) and the clearing point (close circles). In the inset the cation structure of the ILs. This figure is taken from the reference [5].

From this plot we can distinguish three main behaviours as a function of the alkyl-chain length. For short chains (n≤1) the salt has a crystalline phase with a mp at relatively high temperature. For intermediate lengths (2≤n≤9), on the other hand, the system passes directly from the liquid to the glass state, with a T_g below the room temperature, without showing an ordered phase. Finally for long chains (n>9) the system shows again a crystalline phase, but with a mp below room temperature. Moreover for extremely long chains (n≥12) the system shows another phase transition from liquid to a smectic A phase for high temperature.

However the chain length is not the unique parameter which defines the thermodynamic properties of ILs. For example another possible parameter which could reduce further the IL mp is the cation symmetry. It seems in fact that ILs with the asymmetrical cations have lower mp than ILs with symmetrical one [11].

In closing also the anions seems to have some importance in the IL phase diagram. If we consider, for example, the BMIM-TFSI, it was shown that, heating the system, this salt passes from the glass to the crystalline phase by a cold crystallization, showing thus a different thermophysical behaviour of the BMIM-BF_4 which never crystallizes [5].

2.3.1.2 Confinement effects on the ILs phase transition

It was shown that nanoconfinement has particularly evident effects on the ILs thermal phase transitions. The reduction of dimensionality can change the temperature where the phase transitions, of first or second order, occur.

The nature of these effects is varied and it seems to depend by different parameters such as the material of the matrix, the liquid or the anion size [83].

The most common effect in this field is the depression of the melting point to low temperature [60, 61, 83], which is often proportional to the inverse of the confinement pores (see Fig. 2.9). Many models have been developed for explaining this phenomenon e.g. thermodynamic ones based on the crystal dimension (Gibbs-Thomson effect) [84], or mean field theory based of the coordination number of each molecule in the fluid [60].

In addition to the melting point depression, other secondary effects such as the modification of the crystallization and glass transition temperature have been observed [60, 83, 85].

2.3.2 The case of the confined BMIM-TFSI: a DSC study

The first step of the analysis of the ILs confinement inside the AAO concerned their thermal properties. As we explained in the chapter 2.2.3, in this study we focused on the BMIM-TFSI because this system shows several phase transitions. For this work we used the differential scanning calorimetry (DSC). The DSC measurements were performed on the apparatus TA instrument DSC Q100. All measurements were done on heating with a rate of 10 K/min in the temperature range between 175 and 300 K.

A typical bulk liquid DSC scan, is shown in figure 2.10.

We can observe three phase transitions in the interval between 175 and 300 K. We notice:

1. a glass transition as C_p jump as 188.6 K (see the zoom in Fig. 2.10B);

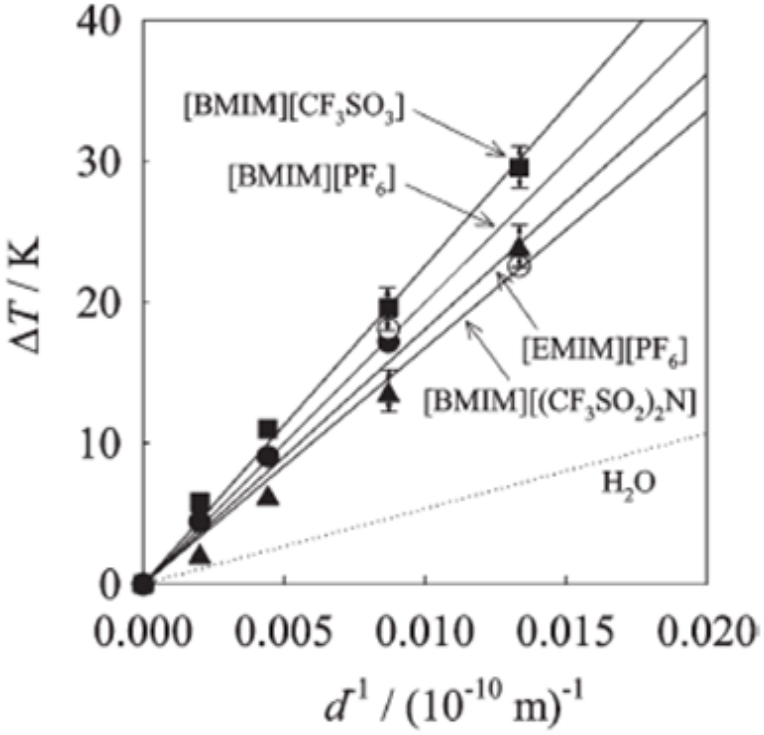

Figure 2.9: Melting point depression of some ILs as a function the inverse pore diameter the dashed line represents the mp depressions of water, while the solid lines are linear fit of the experimental data points. This figure is taken by the reference [84].

2. a cold crystallization detected as an exothermic peak at 228.2 K;

3. a melting transition (endothermic peak) at 270.6 K.

These transitions are coherent with those present in the literature [78].

In this chapter we will show that all these transitions are influenced by the nanoconfinement in the AAO membranes. For this study we considered three pores sizes: 160, 60 and 25 nm. Each membrane was broken in several pieces and stacked inside the DSC cell in order to guarantee a better thermal contact. Each sample was measured with the same protocol as the bulk liquid. In figure 2.11 we show the thermogram measured of the bulk liquid compared to the that of the IL confined in the pores of 160 nm. We can notice that we are able to distinguish the three phase transitions observed in the bulk IL, which present some differences than the bulk transitions. The presence of these latter has been observed in all samples.

We divided this chapter in three sections, each of them dedicated to a specific

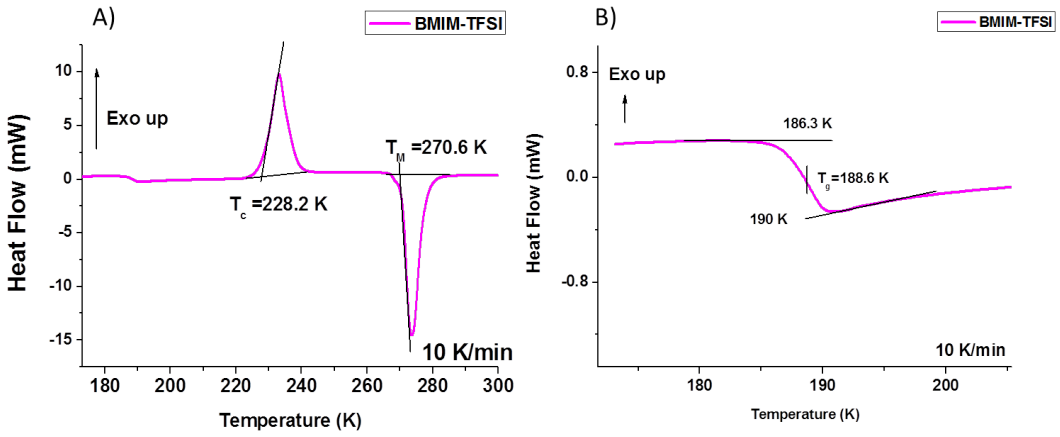

Figure 2.10: A) DSC scan measured on the BMIM-TFSI bulk, on heating, with a rate of 10 K/min. We can notice three phase transitions: a glass transition at 188.6 K, followed by a cold crystallization at 228.2 K and a melting point at 270.6 K B) Zoom on the transition from the glass to the subcooled state.

IL phase transition. From this analysis we will demonstrate how the surface effects are important in the confinement state, and how it is possible to find their signature in all IL thermodynamic transitions.

2.3.2.1 A double glass transition in the confined state

Here we will show that, in the confined state, the system shows two different glass transitions, which are radius dependent.

We show an example of this double transition in figure 2.12A, where the measured DSC thermogram of the IL confined in the AAO $\oslash = 25$ nm is plotted.

From this plot we can distinguish two glass transitions: one, that we call T_{g1}, occurring at lower temperature ($T_{g1} = 182.1$ K) than in the bulk ($T_{g_{bulk}} = 188.6$ K) and an other, called T_{g2}, taking place at higher temperature ($T_{g_2} = 215.8$ K).

This double transition was observed also in the other confined BMIM-TFSI samples considered in this work.

In figure 2.12B we show the trend of the two T_gs as a function of the inverse of the pores diameter. We can notice that T_{g1} is higher for larger pores and it decreases proportionally with the pores size. On the other hand T_{g2} shows a different trend increasing with the diminution of the confinement size.

A similar behaviour was observed by Park and McKenna on their study of polystyrene/o-terphenyl solutions confined in nanometric pores [86]. In this work the authors observed, by DSC measurements, the presence of two T_gs in the con-

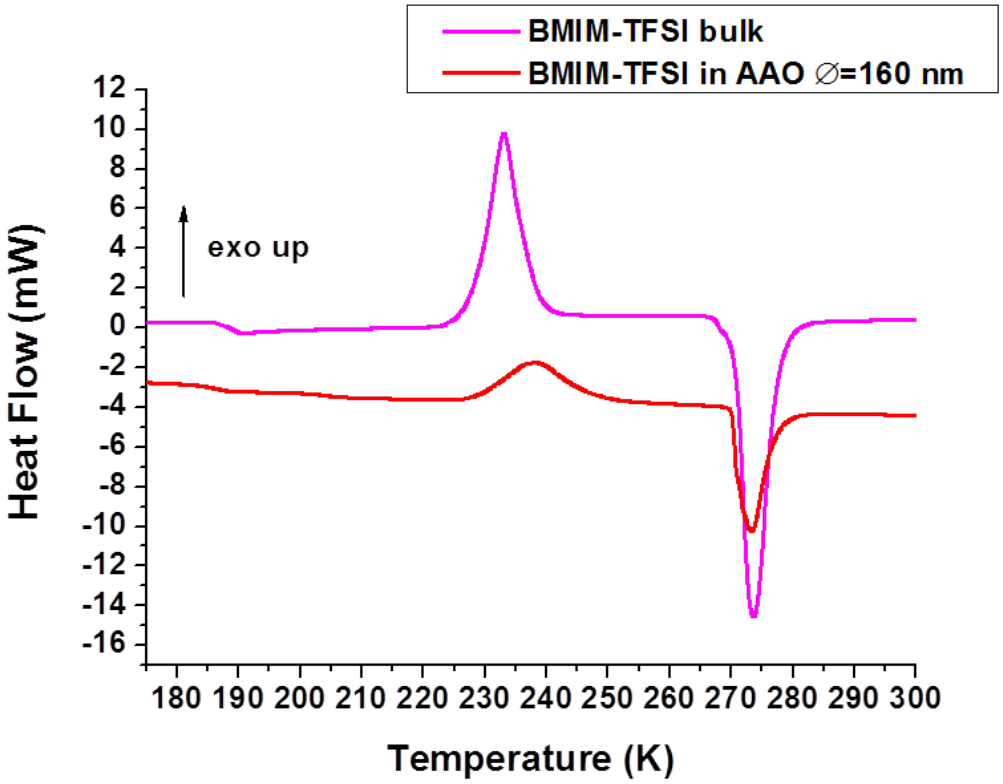

Figure 2.11: DSC signal measured on the bulk BMIM-TFSI (black) and BMIM-TFSI confined in AAO $\oslash = 160$ nm (red). We can notice that three phase transitions observed in the bulk liquid are still present in the confined one.

fined state: one lower and the other one higher than bulk T_g. As in the BMIM-TFSI case, the lower glass-transition temperature decreases with decreasing of the pores size while the higher temperature one seems to increase with the diminution of the pores diameter (in the case of pure o-terphenyl). The authors associate the higher temperature T_g to a liquid layer in the vicinity of the pores surface, while the lower one to the inner liquid, which is not sensitive to the liquid-solid interface. Despite the two liquids have different natures, we can propose an analogous explanation of our sample. We thus suppose that in the confined ILs there is a formation of core-shell system, where the ions near to the walls form a layer which interacts with the alumina, while those in the central part have not interactions with the matrix. This conclusions seems to be coherent with previous NMR studies performed on the same IL confined in the AAO, where it was observed a slowing down of the

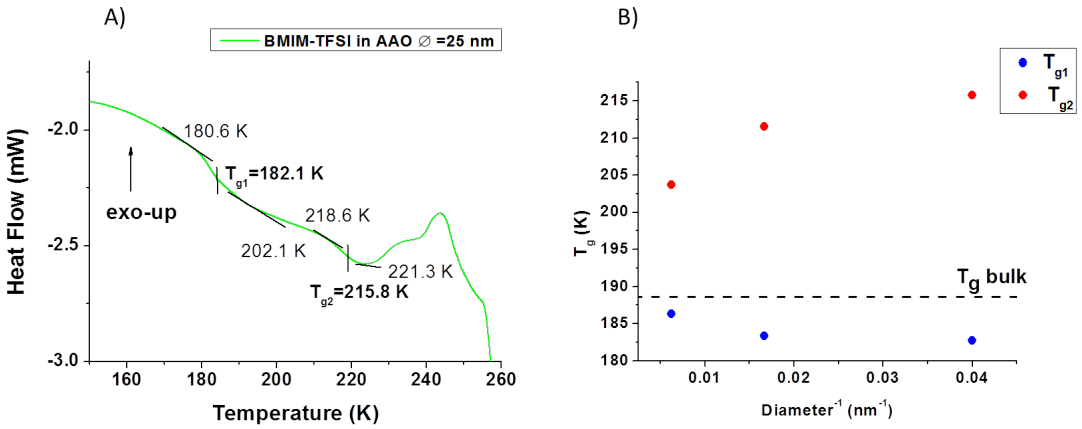

Figure 2.12: A) Example of DSC scan on the BMIM-TFSI in AAO $\oslash = 25$ nm. We can distinguish two different T_gs in the range between 160 and 200 K. B) Trend of the two T_gs as a function of the inverse of pores diameter. We can notice the T_{g1} is lower than bulk T_g and it seems to decrease with the pores size decreasing. On the other hand T_{g2} is higher than bulk transition temperature and it increases with diminution of pores size.

cationic dynamics, associated to the presence of immobile ionic shell interacting with pores surface [65].

2.3.2.2 Crystallisation temperature

In figure 2.13 we show how the exothermic peak, due to the liquid cold crystallization, changes as a function of the pores size.

Compared to the bulk, we can also observe that for large pores the crystallization peak seems to broaden and for the small ones we can distinguish clearly that this bump is composed by the superposition of two peaks. Especially analysing the plot in figure 2.13B, we can understand that two crystallization process occur in the systems: one at the same place than the bulk liquid and the other at higher temperature. Similarly to the discussion made for the glass transition temperature, we associate the peak at low temperature to the liquid placed at the center of the pore, while the second to the crystallization of the liquid layer at the interface with pores wall.

We couldn't separate the two contributions to crystallization temperature T_C as a function of the pore dimension, however we can estimate roughly an increasing of the crystallization temperature which is inversely proportional to the pores size. This effect has been also observed in a silica ionogels using different ILs [85]. We can suppose that this increase of T_C is a consequence of the interaction

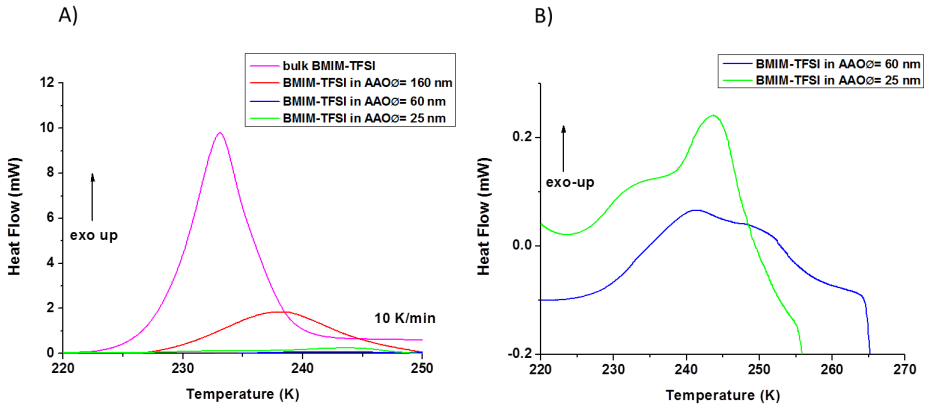

Figure 2.13: A)Comparison of the exothermic crystallization peak in the bulk liquid (magenta) and confined in AAO membranes with pores of 160 (red), 60 (blue) and 25 nm (green). We can notice that the peak shifts to higher temperature. The associated enthalpy decreases proportionally to diminution of pores size. B) Zoom on the DSC scan for the AAO with pores of 60 and 25 nm. In this case we can distinguish the presence of two peaks: one due to liquid the near to the pores walls of the AAO and the other due to the that in the inner part of the pores.

between the ions and the pores walls. This hypothesis seems to be coherent with observation of a crystallization temperature increase proportional to the sample ratio surface/volume.

2.3.2.3 Melting point depression

An example of confinement effect on the melting transition is shown in figure 2.14A. The plot represent the DSC scan acquired for the IL confined in AAO with pores of 60 nm.

We can notice the presence of two endothermic melting peaks. One of them is at the same temperature as the bulk liquid, $T_{M_{bulk}}$=270.6 K, (see Fig.2.10A), whereas the second is near to 265 K. Considering the different intensity of the two peaks we can attribute the intense one to the melting of the confined IL, while the second is due to the trace of bulk system remained on the AAO surface after the membrane filling. We observe then that, when the liquid is confined, there is a melting point shift to lower temperature. An analogous depression was observed also for two other pores sizes. In figure 2.14B we show the quantity $\Delta T_M = T_{M_{bulk}} - T_{M_{confined}}$ measured on the different samples on a function of the inverse of the pore radius.

We can notice that the depression shows an inverse proportionality with the pores size. In the introduction we have shown that, in several cases, the confined

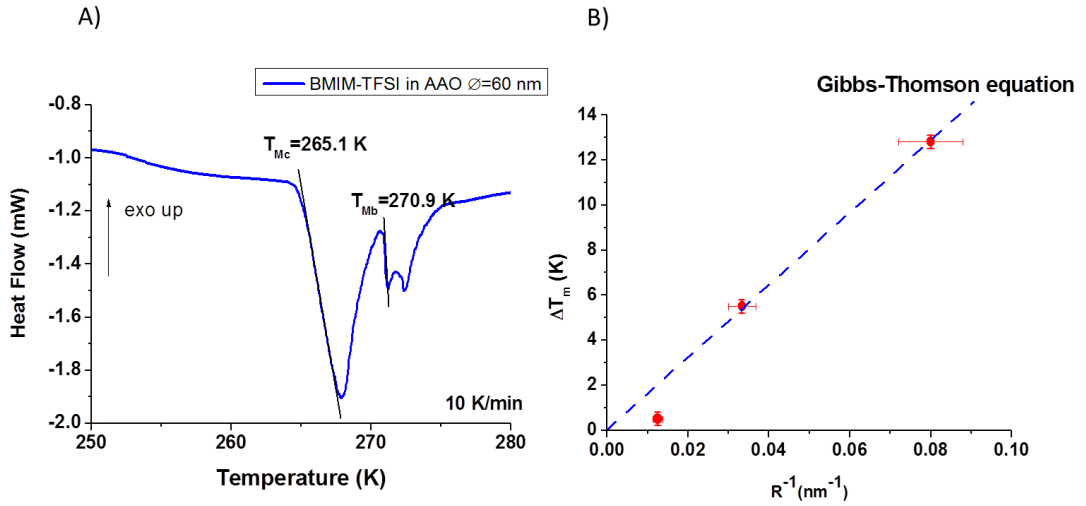

Figure 2.14: A) DSC scan measured on the BMIM-TFSI bulk confined in AAO with pores of 60 nm, with a rate of 10 K/min. We can notice a big endothermic peak at 265 K due to the confined liquid melting, showing a melting point depression of 6 K. We can observe another small endothermic peak due to the melting of the trace of bulk liquid remained on the membrane surface.B) Melting point depression trend as a function of the inverse of pores radius measured on three samples considered in this work. The dashed line represent the ideal trend of the Gibbs-Thomson equation (eq.2.4). The deviation observed from the ideal trend could be due the presence of the surface effects, which are not considered in the relation 2.4.

IL melting point depression follows the so called *Gibbs-Thomson equation* (GB), which, for liquid confined in cylindrical pores at the thermodynamic equilibrium, is [87]:

$$\Delta T_M = T_{M_{bulk}} \frac{2\sigma_{sl} V}{dH_F} \tag{2.4}$$

where σ_{sl} is the surface energy of the solid-liquid interface, V is the system molar volume, H_F is it fusion enthalpy and d is the confinement diameter. However from the figure 2.14 B, we notice that for large pore size the trend is no more linear. A similar behaviour has been observed also for the cyclohexane confined in mesoporous materials [88]. In this case the deviation from the GB law was explained as the effect of the pores surface. We have to highlight, in fact, that the equation 2.4, explains the melting point depression as a consequence of the diminution of the crystallite dimension due to the reduced confinement space, i.e. it considers just the thermodynamic state of the system. This approximation is

valid if the interactions between the matrix walls and the liquid are negligible. As we have already mentioned in the chapter 2.2.3, we know that the pores can interact with the liquid ions forming H-bonds. We can suppose then that surface effects are not negligible for this kind of systems. This hypothesis could explain so the observed deviation of ΔT_M from the Gibbs-Thomson equation.

2.4 Confinement effect on the IL self-organisation behaviour by WAXS

An important part of the study of the confinement effects on the ILs properties was committed to analyse how these systems organisation changes when they are confined inside the AAO membranes. A radical modification of the molecular structure induced by the confinement is a well known phenomenon in the confined liquid physics. Generally it is due to the so called *excluded-volume effect*, which is just a geometrical consequence to the fact that the liquid in the confined state can't occupy all the space [89]. The excluded-volume effect has been observed for several molecular liquids such as water, methanol, benzene etc. [90–94]. Particularly visible consequences, related to this effect, were detected on the those liquids, which have a pre-peak due to a supramolecular assemblies. In this case it was demonstrated that the confined systems show a less intense and broader pre-peak, which means a suppression of the self-organisation [92–94]. We can expect then to observe an analogous effect in the case of confined ILs. The goal of this section is thus to illustrate our study performed on the confinement effects on the IL pre-peak properties. At the end of our analysis we will demonstrate the ILs don't act as the molecular liquids, i.e. their self-organisation is not suppressed by the confinement, but, actually, it seems amplified by the dimensionality reduction of the system.

This chapter is divided in four sections. The first one describes the experimental part of this study. In this part we will explain which experimental technique we chose and how the sample were prepared for optimizing the measured signal. The second part is dedicated to the used method for determining the contribution of the matrix in the case of confined liquid. The third one will explain the used approach for studying the changes of the pre-peak characteristics in the confined state, while the last will show the conclusions obtained by our approach.

2.4.1 Introduction: Surface effects

Several measurements, based on microscopy [95–97] and spectrometry [98,99] techniques, showed that ILs ions, in presence of a solid substrate, organise themselves

in layers at the liquid-solid interface. In particular it was demonstrated that this structuration depends by several factors such as the temperature, the ions species, the nature and the electrical charge of the substrate.

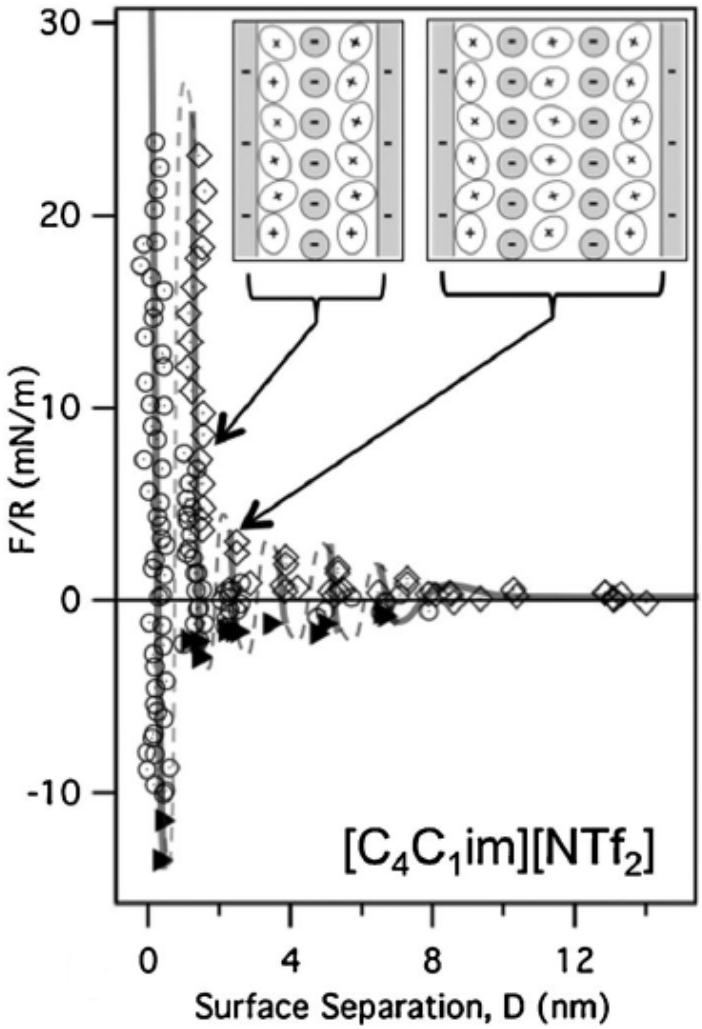

Figure 2.15: Force, F_N, between two mica surface separated by a BMIM-TFSI film versus the thickness of this latter measured by a surface force balance. Open diamond are the data points measured during the approach of the two surface, the open circles those ones acquired during their retraction. The filled triangles are the points measured from the jump-apart of the surface from the stable minima. The line is eye-guide for highlighting the oscillating trend of the curve due to the IL layering. The inset is a sketch which represents various points of the curve. This figure is taken by the reference [100].

This surface organisation becomes important when we consider confined IL. In the bulk state this latter is negligible because the ratio surface/volume of the sample is much smaller than one. However in the confined condition the system volume is extremely reduced, so this approximation is no more valid, thus the effects occurring at the interface become relevant. A layering was recently observed for the ILs confined between flat surfaces by surface force apparatus measurements [101, 102] (see Fig.2.15), which highlighted the importance of a residual charge for the layer formation [102]. An analogous layering at the surface was observed also by MD simulation on cylindrical geometries such as silica pores or carbon mesopores [103, 104], which confirm that the nature of the surface plays a fundamental role in the layer formation. In conclusion for very small confinement size (i.e. CNTs), MD studies show a geometry dependent extension of the ions layering also through the center of pores [105–107], suggesting an ion re-organisation of the ions, in the case of very small pores, which seems be confirmed also by experimental works [108].

2.4.2 Experimental part

As in the bulk case, for studying the feature of the liquid self-organisation in the confined state, we had to observe the IL pre-peak.

As we showed in the chapter 1 of this manuscript, the OMIM-BF_4 pre-peak lies in the Q region between 0.1 and 0.3 $Å^{-1}$. At the end of section 1.2 we have pointed out that the SANS techniques have a too low resolution in that wave vector region ($\frac{\delta Q}{Q} \approx 15$ %), which doesn't allow to analyse finely the pre-peak features. For this reason we have chosen to use the Wide-Angle X-Rays Scattering (WAXS), which shows a higher resolution in this Q interval.

The measurements were performed on the spectrometer MOMAC (CEA-LPS-France) [109]. This instrument is a SAXS-WAXS spectrometer is at the "Laboratoire de Physique des Solides" (LPS) of the Paris Sud University. The measurements were performed with the collaboration of Dr. Doru Constantin. The particular feature of this set-up is the use of a molybdenum X-rays source, which produces a beam with a much higher penetration length than X-rays generated by a classic copper source.

We have selected an instrumental configuration using a wavelength of 0.709 Å and a detector distance of 72.85 cm. This set-up allowed to measure the Q interval between 0.2 and 3 $Å^{-1}$.

The samples considered in this part, along with the relative acquisition times, are reported in table 2.2. We measured the liquid in the bulk state and confined in three different pore sizes: 25, 60 and 160 nm. In order to subtract the contribution of the empty matrix to the filled AAOs signal we measured also the spectra of the empty membranes for the three pores diameters.

Sample	Acquisition time (min)
bulk OMIM-BF_4	30
OMIM-BF_4 in AAO $\oslash$ = 160 nm	90
OMIM-BF_4 in AAO $\oslash$ = 60 nm	90
OMIM-BF_4 in AAO $\oslash$ = 25 nm	90
Empty AAO $\oslash$ = 160 nm	90
Empty AAO $\oslash$ = 60 nm	90
Empty AAO $\oslash$ = 25 nm	90

Table 2.2: Samples measured on MOMAC in this work, with the respective acquisition times. In the case of duration longer than 30 minutes the sample acquisition were divided in multiple acquisition of 30 minutes each.

In the case of the membrane samples, the pores axis were aligned parallel to the incident beam. This means that is probed the structural organisation of the sample in the plane perpendicular to pores axis.

In this study two different sample holder were used.

The bulk liquid was put in a classic quartz capillary tube of thickness of 2 mm (produced by Glas).

On the other hand, for the empty and the filled AAOs, it was necessary to develop a proper flat sample cell. Usually the windows composing the flat sample holder in a small/wide angle X-rays scattering experiments are made of Kapton. Unfortunately for these measurements it was not possible to use this polymer because it shows a broad diffraction peak in the same Q interval as the IL pre-peak [110]. For this reason we opted for use mica windows because this mineral has no peak in this Q interval and, furthermore, it produces a much lower parasitic scattering than the other typical materials used as windows in X-rays scattering experiments [110–112].

We constructed thus home-made X-ray scattering cells composed by two mica foils of thickness of 25 μm (produced by Good Fellow) separated by a steel washer. In this case each membrane has been broken in several parts and all of them have been stacked inside the cell in order to have the maximum quantity of sample inside the beam. Owing to the low IL quantity inside the membrane ($m_{IL} < 10$ mg), we used an acquisition time much longer than for the bulk liquid. For the same reason we have chosen the same acquisition time for the empty AAO since we need a good signal for the subtraction of the empty membrane contribution.

Finally, together with the samples listed in table 2.2, we measured also the empty cells and a reference lupolen sample in order to transform the signal to absolute units.

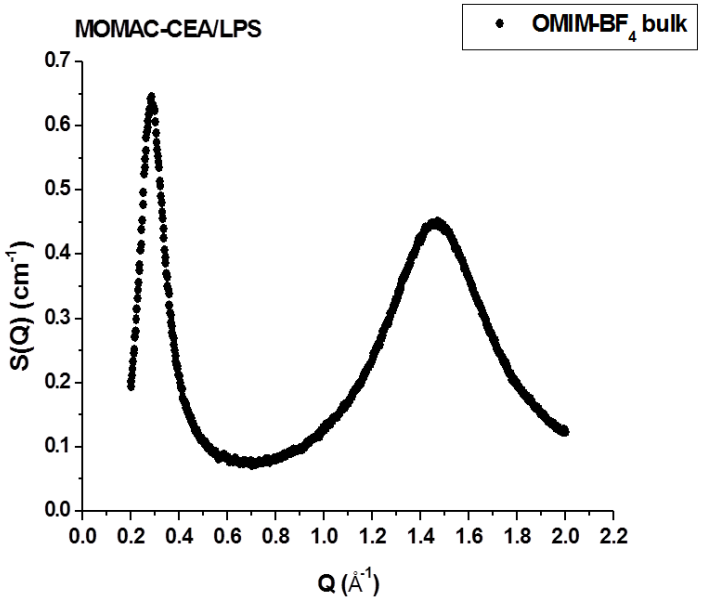

Figure 2.16: OMIM-BF_4 structure factor measured by MOMAC (CEA). We can distinguish two different diffraction peaks: the first near to 0.3 $Å^{-1}$, the pre-peak due to system self-organisation [4] and second near to to 1.5 $Å^{-1}$, is due to the correlations like anions, adjacent alkyl-chains and chain-anion correlations [20].

2.4.3 The liquid structure factor determination

The data treatment for passing from to the raw 2D spectra to the sample scattering intensity versus Q is described in the reference [113]. The result of this procedure on the bulk liquid is shown in figure 2.16.

We can notice that for this system we can observe two diffraction peaks: one in the zone of 0.3 $Å^{-1}$ and the other near to 1.5 $Å^{-1}$. According to the literature [4], and the previous SANS measures, the low Q peak is due to the IL self-organisation, while the other is generated by neighbouring ionic solvatation shells and several intermolecular correlation (such as anion pairs, adjacent tails etc.) [20].

In order to be able to subtract the signal of the neat membrane, it is crucial to reach a correct estimation of the sample quantity for the systems AAO+IL and the empty membranes. If we consider the bulk liquid diffraction peak at high Q, the correlation length associated at the position of this latter is relatively small (L= $2\pi/Q \approx 4.2$ Å). We can thus suppose that the pores dimension, considered in this work, are too large for affecting this kind of correlation, so the peak properties shouldn't be affected when the liquid is confined. This implies that the intensity of the broad peak at high Q of the system AAO+IL is the weighted sum of the two contributions:

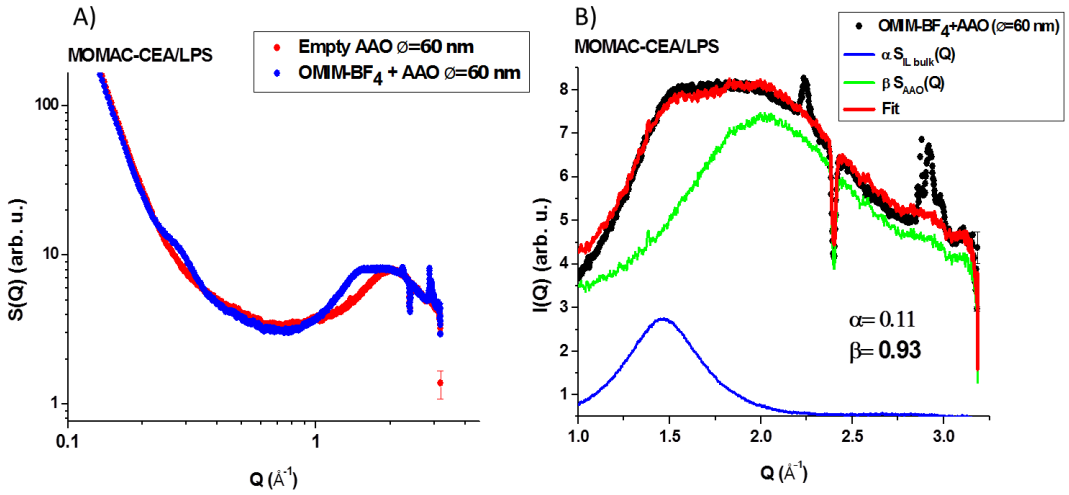

Figure 2.17: A) Scattered intensity of the sample AAO($\oslash$ = 60 nm)+OMIM-BF_4 (blue) and empty AAO($\oslash$ = 60 nm) (red) measured on MOMAC. B) Fit of the broad peak at high Q of the AAO($\oslash$ =60 nm)+OMIM-BF_4 using the equation 2.5. The black circles are the experimental data point, the solid red line is the fit function, while the solid green and blue line are respectively the sub-functions $\alpha S_{IL_{bulk}}(\mathbf{Q})$ and $\beta S_{AAO}(\mathbf{Q})$

$$S_{AAO+IL}(\mathbf{Q}) = \alpha S_{IL_{bulk}}(\mathbf{Q}) + \beta S_{AAO}(\mathbf{Q}) \tag{2.5}$$

where α (β) is the quantity of liquid (AAO) present in the sample whereas $S_{IL_{bulk}}(\mathbf{Q})$ and $S_{AAO}(\mathbf{Q})$ are respectively the signal of the bulk IL and the empty AAO.

The broad peak for three filled AAOs has been fitted using the equation 2.5 in order to determine the quantity of the two materials inside the beam. An example of the fit is reported in figure 2.17. As we can see from the plot in figure 2.17B, the function 2.5 fits well the experimental data.

After that we subtracted the quantity $\beta S_{AAO}(\mathbf{Q})$ to the signal and we used the value of α for determining the effective thickness of the liquid necessary for the conversion to absolute unities. The signals obtained at the end of this procedure are reported in figure 2.18.

We can notice that finally we recovered the same spectrum shape observed in the bulk liquid.

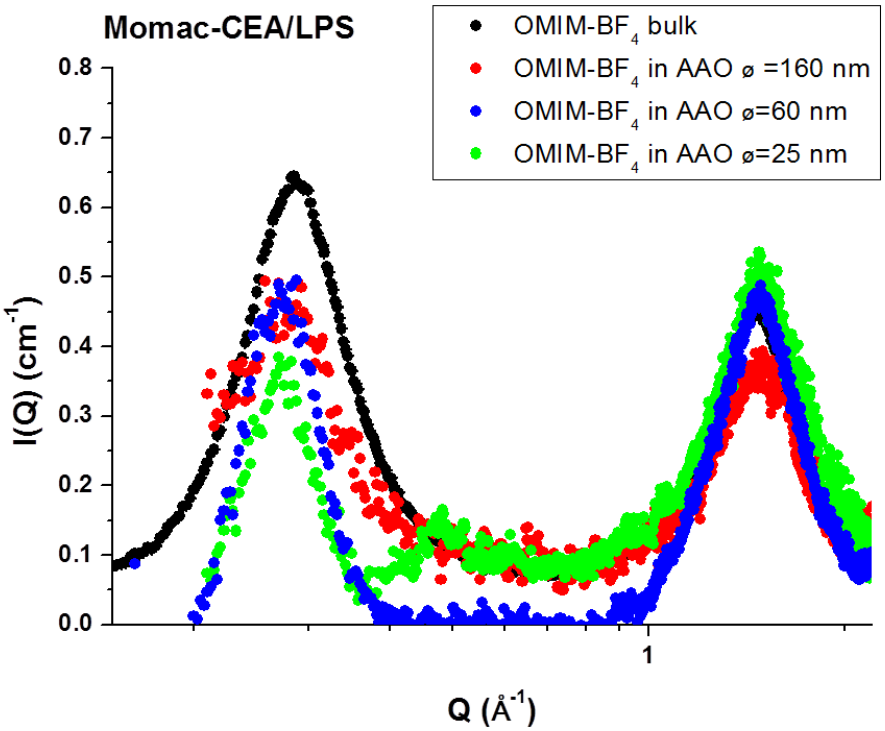

Figure 2.18: Diffraction patter of the bulk OMIM-BF_4 (black) and confined in AAO membranes with pores of 25 (green), 60 (red) and 160 nm (blue) measured on Momac.

2.4.4 Phenomenological analysis

After the subtraction of the empty membrane contribution we can analyse quantitatively the changes induced by the confinement on the pre-peak features. For this purpose we used the same phenomenological approach adopted by many authors in the literature [20, 28, 29]. The pre-peak is fitted with the Lorentzian function:

$$I\left(Q\right) = \frac{I_0}{\pi} \frac{\Gamma}{\Gamma^2 + \left(Q - Q_P\right)^2} \tag{2.6}$$

where I_0 is the integrated intensity of the peak, Q_P is the maximum position and Γ is the HWHM of the bump. In this model the strength of the self-organisation is expressed by the Lorentzian intensity I_0. On the other hand the position peak is related to the value of the correlation length L_{corr} by the relation:

$$L_{corr} = \frac{2\pi}{Q_P} \tag{2.7}$$

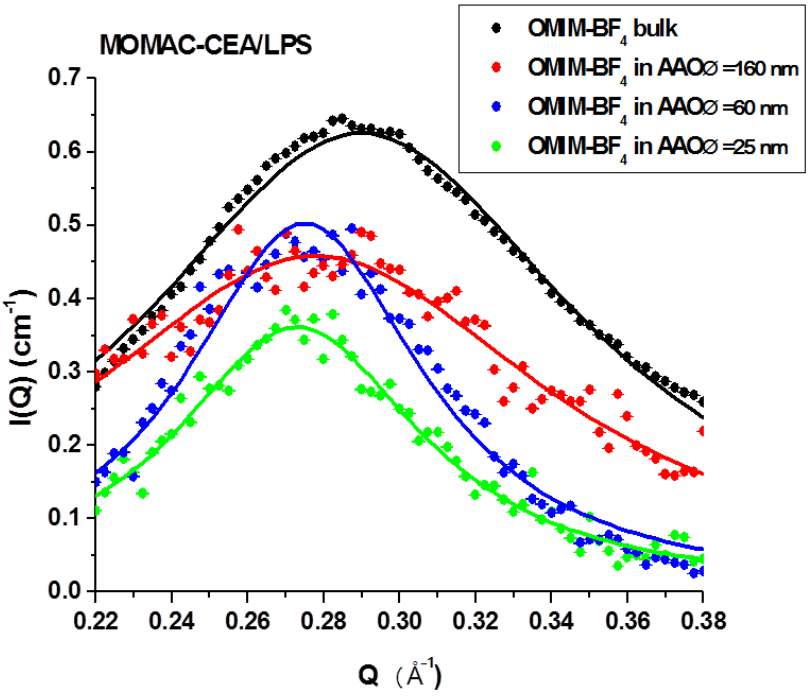

Figure 2.19: Fit of the pre-peak, using the equation 2.6 on the bulk OMIM-BF_4 (black) and confined in AAO membranes with pores of 25 (green), 60 (red) and 160 nm (blue). The full symbols are the experimental data whereas the full lines are the fit functions.

while the dispersion of this length, D_L, is related to the Lorentzian HWHM:

$$D_L = \frac{2\pi}{\Gamma} \tag{2.8}$$

Since we observe the presence of a new bump, in case of the liquid confined in small pores, near to 0.5 $Å^{-1}$, we limited the fit in interval between 0.22 and 0.38 $Å^{-1}$. The fit are shown in figure 2.19, while the obtained fit parameters values are reported in table 2.3.

The relative values of the correlation length and dispersion for the four samples can be estimated using the equations 2.7 and 2.8.

We report in figure 2.20 the trend of I_0, L_{corr} and D_L as a function of the confinement size D.

We can notice that three parameters follow different evolution as a function of the diameter of the AAOs pores.

The intensity of the pre-peak seems to have a linear relation with the pores size (Fig.2.20A). This quantity is proportional to the sample density, however,

Sample	$I_0(cm^{-1})$	Q_P (Å^{-1})	Γ(Å^{-1})
bulk OMIM-BF_4	0.139±0.002	0.2899±0.0004	0.0707±0.0008
OMIM-BF_4 in AAO ⊘ = 160 nm	0.108±0.005	0.278±0.001	0.075±0.003
OMIM-BF_4 in AAO ⊘ = 60 nm	0.060±0.002	0.2750±0.0008	0.038±0.001
OMIM-BF_4 in AAO ⊘ = 25 nm	0.0454±0.0008	0.2731±0.0008	0.040±0.001

Table 2.3: Parameters values obtained by the fit of pre-peak using the equation 2.6.

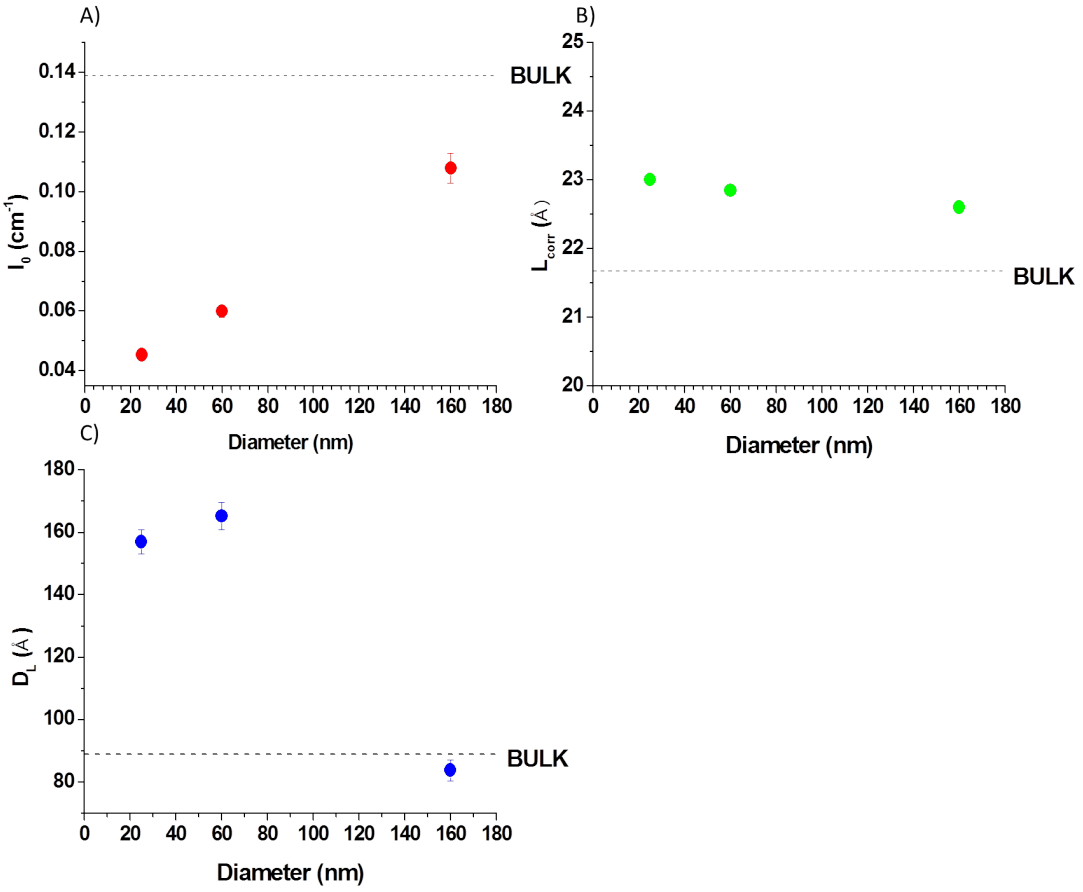

Figure 2.20: Trend of the parameter I_0 (A), L_{corr}, eq.2.7, (B) and D_C, eq.2.8 (C) as a function of the confinement size. The dashed lines show the value obtained on bulk liquid.

concerning this analysis, the used model is too simplified for extracting the realistic information about this quantity. For determining the real trend of this it would

necessary fitting the whole structure factor, procedure that wasn't performed in this work.

On other hand the correlation length tends to increase when the liquid is confined (see Fig.2.20B). Already for the big pores size ($\oslash$ = 160 nm), this quantity shows an increase of 5%. The variance from the bulk value seems to increase again when the pores diameter decreases. Since the correlation length represents the distance of the two cations head separated by an apolar domain [25], we can conclude that the dimension of the tails aggregates increases when the liquid is confined.

Finally if we consider the dispersion (Fig.2.20C), we observe a strange variation in function of the confinement size. For big pores this quantity seems to have a value close to the one of the bulk liquid. When the pores size decreases we observe a large and sudden increase of around 76%. For better characterizing the trend of this quantity it would be necessary to perform other measurements with intermediate pores dimension between 60 and 160 nm. However we can conclude that D_L increases when the pores diameters decreases. Being the dispersion the variance of the aggregates size from the mean values given by the peak position, an augmentation of this parameter suggests additional structuration of the systems.

2.4.5 Conclusion

From the X-Rays data shown in this section, as the pre-peak is always detected, we can conclude that the confinement of the IL in the AAOs does not suppress the liquid nanostructuration. A slight shift of the pre-peak to small Q suggests that confinement induces an increase of the correlation length characteristic of the IL domains. The narrowing of peak seems to show that the confinement induces a better organisation within the IL domains.

We want also underline the formation of new peak near to 0.5 $Å^{-1}$, which becomes sharper when the pores diameter decreases (see Fig.2.18). We ascribe this peak formation to a surface effect because the bump becomes clearer with the increase of ratio pores surface/volume. We suppose so that this new bump is due of layering of the ILs near to the pores walls. It was demonstrated that some traces of electrolyte could remain on the AAO after the anodizing process [72]. We can suppose that a small residual electric charge could remain on the pores surface, which can induce an ions layering as the mica case shown in literature [100] (see Fig.2.15). Moreover also the hydroxyl groups present on the pore walls could be the origin of this further organisation, since they can develop hydrogen bonds with ions. We notice that the correlation length related of this new peak is around 1 nm, which is compatible with the cation dimension.

So in the end, we can conclude that the ILs confinement inside the AAOs doesn't contrast the domains formation, but, actually, it increases the self-organisation

inducing a pre-peak narrowing and shift. We want however highlight the limit given by the used confinement matrix. The AAOs don't allow to climb down the tens of nanometers as pores size, which is around tens times bigger than the correlation length in the bulk state. This relatively big confinement size, is, maybe, not enough for suppressing the self-organisation behaviour. From the results given in this study, we can't thus exclude that smaller pores could frustrate the system structuration.

2.5 Confinement effect on the ILs dynamics at molecular level

A large part of our study on the confinement effects on the IL properties concerns liquid dynamical behaviour. In this thesis we focussed our attention on the analysis of the dynamical properties at the molecular level using QENS techniques. Owing to the large incoherent neutron scattering cross-section of the ^1H nucleus and the abundance of this element in IL, incoherent inelastic neutron scattering measurements are able to give a global view of the IL dynamics as sensed via the averaged individual motions of its hydrogen atoms. The dynamics accessible by inelastic neutron spectroscopy will depend on the scattering vector, Q, and energy range, ω, accessible by a specific neutron spectrometer.

The goal of this section is to explain the work done concerning this topic. We will show that the AAO confinement has only secondary effect on the ILs dynamics generating only a slight slowing down of the cationic diffusion at the local level.

This part is divided in three sections. The first one explains the experimental part of the work. The second shows the characterization of the different cation relaxations at the molecular level, and it follows the same structuration shown for the study of the bulk liquid. The last one summarizes the conclusion obtained by this study doing a comparison with the obtained results on the bulk liquid and with other works present in the literature.

2.5.1 Confinement effects on the ILs dynamics in the literature

Confinement effects occurring at the microscopical scale can be also observed measuring the dynamical properties of the confined ILs. In this context the most used technique is the NMR. However there are some other examples of experimental techniques, such as conductivity or QENS measurements, which have been used in this field.

By magic angle spinning (MAS) NMR it was demonstrated, for example, that in

silica moderate ionogels ILs show a liquid-like mobility, but the cation dynamics undergoes a soft slowing down that is emphasized with the diminution of the confinement size [114]. This tendency has been confirmed also by gradient field NMR on the IL confined in porous anodized alumina oxide membranes [65].

Moreover it was shown that ILs interactions with the matrix surface influences also the dynamical properties of these systems. It seems that the ions inside the liquids could be divided in two populations: one, near to walls, which has a slower dynamics, while a second, situated at the center of the pores, which shows faster motions [115]. It was shown that the cations belonging to the slower population have two diffusion regimes [116]. The different influence of the matrix surface on the ions dynamics has been also confirmed by MD simulations, which divide the ions inside the pores in two or more layers with different dynamics [103, 104].

For the dynamics at the microscopical scale (Å, ps/ns) some studies have be done [117]. The "cage effect" seen in bulk state (see section 1.3.1.1), was observed, by MD, in ILs confined in CNTs. However in this case it was measured a slower dynamics than the bulk state.

Also some experimental works has been performed in this context. Mamontov and co-workers measured by QENS two diffusional processes due to the cation, which are faster in the confined than in the bulk states [118, 119].

In conclusion some works have been done about the confinement effects on ILs conductivity. Using patch clamp technique, measurements have shown that pores of 20 nm can enhance the ionic conductivity of one order of magnitude in comparison to the bulk state [9]. Parallel work shows that it is also possible to use a single pore of nanometric dimension for obtaining a current rectification choosing properly the pores shapes and the wall surface properties [120]. A very recent study of Iacob et al. has shown, furthermore, that the ILs confinement in silica porous matrix (pores diameter between 7 and 10 nm), induces a change of ionic conductivity temperature behaviour from a VFT to an Arrehnius like trend provoking a conductivity enhancement of two orders of magnitude [64].

2.5.2 Experimental part

The experimental approach used in this study was the same as the one explained in the chapter 1.3 for the bulk liquids. We used different neutron techniques (ToF, NSE and BS) in order to probe a wide dynamical range between 1 and 1000 ps.

For this analysis we used the spectrometer LET (ISIS-UK) for the ToF measurements, while for the NSE we used the instrument IN11 (ILL-France). The set-up configurations were the same ones chosen for the bulk liquid (see sec.1.3.2.2).

For probing the ILs dynamics at long times ($t > 500$ ps) we performed also some BS measurements using the spectrometer IN16B [121] (ILL-France). We decided to use two techniques to observe the dynamics at long times for several motivations.

First of all, as we explained in the section 1.3.2.2.4, the NSE is sensitive also to the coherent scattering. This means that in the system IL+AAO we have to consider the coherent and incoherent contribution coming from the alumina and the liquid, which could be not trivial. Furthermore cause of the low quantity of the IL inside the beam, the NSE needs very long acquisitions (around 24 hours) for achieving an acceptable signal/noise ratio. On the other hand we have shown that the parts of liquid comes out from the membranes during the measurement (see chapter 2.2.4). The leaked sample produces an additional signal that is averaged with the confined liquid one during the measure. This implies that more the acquisition is long and more this detrimental signal can distort the global information, imposing a further uncertainty on the experimental results. Moreover the incident flux of IN16 in high enough to obtain a sufficient signal statistic with shorter acquisitions (less of two hours) than IN11, minimizing so the signal distortion induced by the liquid leak.

The BS measurements were performed at 293 K using a spectrometer configuration with a wavelength of 6.27 Å. This allowed to scan an energy range included between -30 and 30 μeV, with an experimental resolution of 1 μeV, and Q range between 0.44 and 1.07 $Å^{-1}$.

For this study we focus on the OMIM-BF_4 confined in two pores size: 25 and 160 nm.

For the measurements we used always rectangular aluminium cell filled by ten membranes ($m_{IL} \approx 20$ mg) in order to maximize the quantity of the sample in the beam without introducing signal distortion due to the multiple scattering contribution.

The pores orientation towards the beam was the same that the WAXS measurements with the pores axis parallel to the incident beam.

2.5.3 Characterization of the confined IL dynamical behaviour

For analysing the data we used the same approach and model developed for the bulk liquids (see section 1.3.5).

We will show now the confinement effects on three dynamical relaxations present at the molecular level. We have dedicated at each of them a separate section.

2.5.3.1 Long range diffusion

We have seen in the chapter 1 of this thesis, that, in the ILs, the cation has a diffusional motion between two structural aggregates with a characteristic time which is of order of tens of picoseconds. To characterize this kind of dynamics we used the data coming from the NSE and BS measurements.

We have divided this section in two parts. In the first one we will show that these two experimental techniques give two contrasting results about the cation diffusion between the aggregates in the confined IL. We will conclude showing the method used for discerning which scenario is consistent with the total set of the QENS data. The second part, on the other hand, summarizes the results obtained about this kind of dynamics.

2.5.3.1.1 NSE vs BS scenarios

Let's begin to consider the NSE results. For fitting the data we used the following function:

$$I_{inc}^{AAO+IL}(\mathbf{Q},t) = I_{inc}^{cation}(\mathbf{Q},t) + C_{AAO}(\mathbf{Q}) \tag{2.9}$$

where $I_{inc}^{cation}(\mathbf{Q},t)$ is the cationic intermediate scattering function defined by the equation 1.49, while $C_{AAO}(\mathbf{Q})$ is a constant time factor which represents the AAO elastic contribution. Some example of curves fit are shown in figure 2.21.

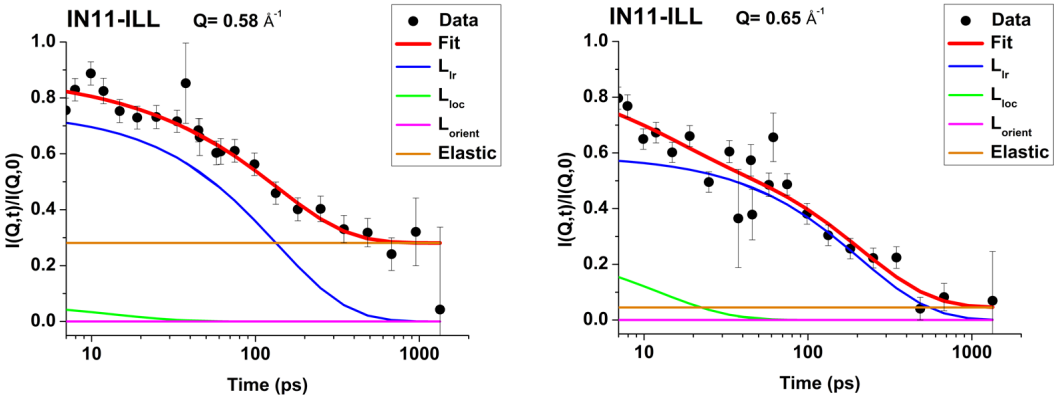

Figure 2.21: OMIM-BF_4 confined in AAO $\oslash = 160$ nm NSE spectra fit using the function 2.9.

The long range self-diffusion coefficient (D_{lr}) values obtained by the NSE data fit, in the case of OMIM-BF_4 confined in AAO ($\oslash = 160$ nm), are shown in figure 2.22.

We can notice that the values measured at the different wave vectors are compatible between them. As in the bulk case, we averaged them and we obtained a $D_{lr} = 1.4 \pm 0.3\ 10^{-6}\ cm^2/s$. We can conclude then that from NSE we observe a considerable dynamics acceleration, with an increasing of self diffusion coefficient of a factor 3-4 compared to the bulk ($D_{lr_{bulk}} = 3.7\ 10^{-7}\ cm^2/s$).

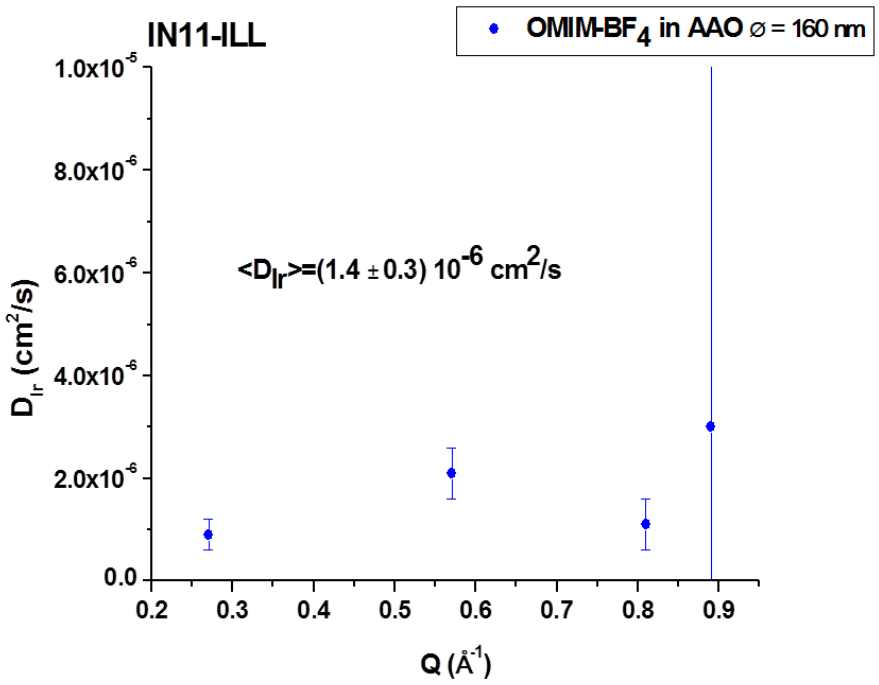

Figure 2.22: D_{lr} values obtained by the fit of NSE data on the OMIM-BF_4 confined AAO ($\oslash = 160$ nm) using the function 2.9. The average value obtained by the fit procedure is shown over the data points.

In the BS case the probed energy interval is very narrow (see Fig.2.23). We could so simplify the model function 1.41 representing the IL dynamics with:

$$S\left(\mathbf{Q},\omega\right)_{inc}^{cation} \approx I_1\left(\mathbf{Q}\right) L_{lr}\left(\mathbf{Q},\omega\right) + bkg \tag{2.10}$$

where the parameter $I_1\left(\mathbf{Q}\right)$ is defined by the equation 1.42, $L_{lr}\left(\mathbf{Q},\omega\right)$ is a Lorentzian function with HWHM $\Gamma_{lr} = D_{lr}Q^2$ and bkg is just a flat term representing the other system relaxations which are much broader to appear as a flat background in the BS spectrum.

These measurements have been performed on an overnight test, so the statistics was not good enough to be able to subtract the AAO elastic contribution to the signal. Our model has been modified as:

$$S\left(\mathbf{Q},\omega\right)_{inc}^{AAO+IL} = S_{AAO}\left(\mathbf{Q}\right)\delta\left(\omega\right) + S\left(\mathbf{Q},\omega\right)_{inc}^{cation} \tag{2.11}$$

where we have added an elastic peak due to membrane contribution.

We could determine the value of the parameter $S_{AAO}\left(\mathbf{Q}\right)$ using the spectrum measured on a sample composed by empty AAOs and renormalizing it to the mass

of the membranes present in the system AAO+IL.

Furthermore cause of the low statistic we couldn't fit properly the data of the confined liquid. However, the signal quality was sufficient for performing some qualitative test in order to confirm the NSE results.

An example of a BS spectrum measured on the system AAO $\oslash = 160$ nm+OMIM-BF_4 at Q=0.57 Å^{-1} is shown in figure 2.23.

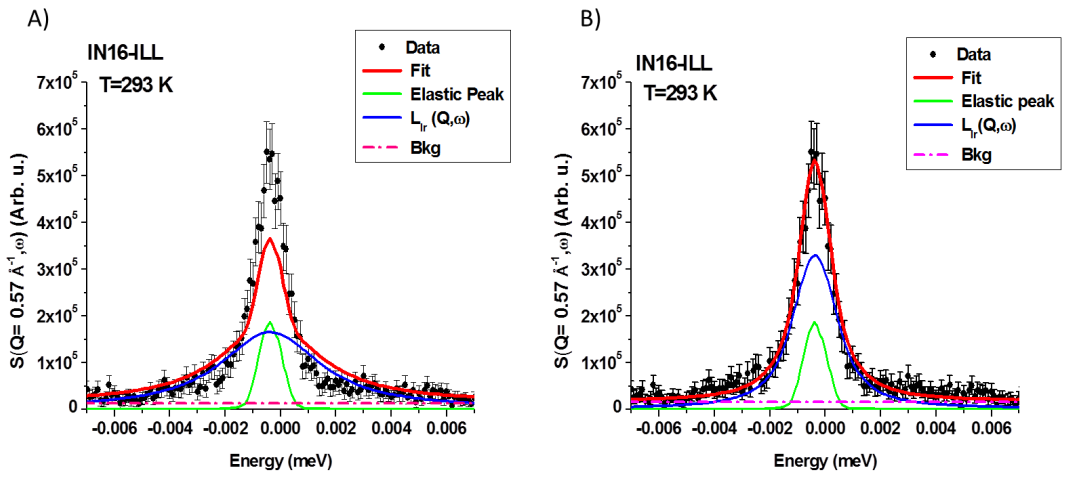

Figure 2.23: Both plots show the BS spectrum of the sample OMIM-BF_4 confined in AAO $\oslash = 160$ measured at 293 K Q=0.57 Å^{-1} with spectrometer IN16B (ILL-Grenoble). A) Data fit using the function 2.11. In this case the elastic contribution was fixed and also the HWHM of the Lorentzian is imposed using $D_{lr} = 3D_{lr_{bulk}}$. B) Fit using the same model of the case A, but imposing $D_{lr} = D_{lr_{bulk}}$. We can notice that the hypothesis of a faster dynamics in the confined case can't reproduce well the experimental data trend.

The part A of this figure shows a data fit using the function 2.10. In this case we imposed as fixed parameters the elastic intensity and the Lorentzian HWHM using a $D_{lr} = 3D_{lr_{bulk}}$, while we used as fit parameters the Lorentzian intensity $I_1(\mathbf{Q})$ and the flat background. We can notice that the fit function doesn't reproduce well the experimental data because the Lorentzian function is too broad for following the data trend at small energies. On the other hand, when we perform the same fit using a self-diffusion coefficient equal to the bulk IL (Fig.2.23B), we observe that the model function reproduces well the data. Analogous results were observed on different Q values. We can then conclude that from the BS measurements the long range diffusion between the aggregate doesn't seem to change with the confinement.

For discerning which of the two scenarios is more reliable we performed also another test on the ToF data.

We considered the data series acquired at the better resolution ($R_E \approx 13\mu eV$), and we tried to fit the data imposing $D_{lr} = 3D_{lr_{bulk}}$. Concerning these data, the statistic was good enough for subtracting the AAO contribution, so we could fit using the equation 1.41. For this fit we supposed that the re-orientation dynamics of the cations is too localised to be modified by the confinement and, for the rest, we used the same approach developed for the bulk. An example of this fit for Q= 0.75 $Å^{-1}$ is shown in figure 2.24.

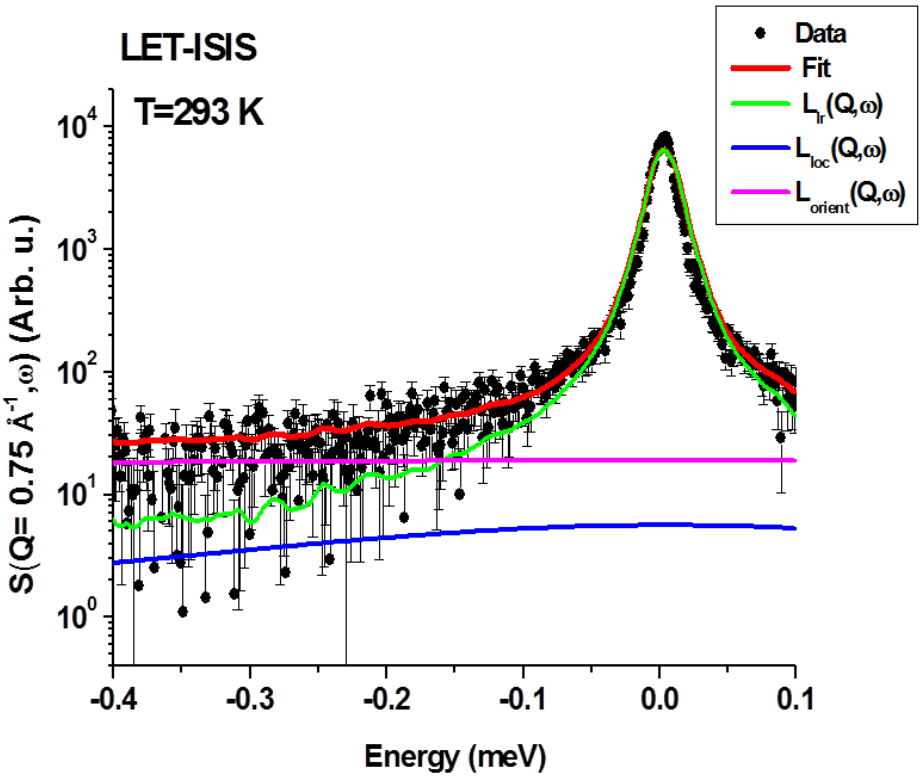

Figure 2.24: Fit of the ToF spectrum of the sample OMIM-BF_4 confined in AAO $\oslash$ = 160 measured at 293 Q=0.75 $Å^{-1}$ with the spectrometer LET (ISIS-UK). The used fit function is the relation 1.41 (the AAO contribution was subtracted before the data fit). In this case we suppose that re-orientation dynamics doesn't change with the confinement so we used the HWHM founded for $L_{orient}(\mathbf{Q}, \omega)$ in the bulk state. We impose also a $D_{lr} = 3D_{lr_{bulk}}$. We can notice that at low energy the model function doesn't follow well the experimental data.

Also in this case we can see that the part of the model function relative to the long range diffusion is too broad to reproduce well the data. We can conclude then that ToF data are concord with the hypothesis that D_{lr} doesn't change with the

Sample	D_{lr} cm^2/s
bulk OMIM-BF_4	3.7 10^{-7}
OMIM-BF_4 in AAO $\oslash$ = 160 nm	3.7 10^{-7}
OMIM-BF_4 in AAO $\oslash$ = 25 nm	3.7 10^{-7}

Table 2.4: Self-diffusion coefficient due to the cation diffusion at long range deduced by our QENS study.

confinement. We conclude then that scenario proposed by the BS measurements is more reliable.

At our knowledge we don't have a sure explanation about the origin of the discrepancy between the NSE and BS result. As we have already mentioned in the section 2.5.2, this could be due to several causes.

The low quantity of the sample in the beam is certainly a big limitation. This produces a low value of the beam polarisation, which worsen the data quality.

Furthermore the confined IL seems to be unstable inside the membranes pores, so it leaks from the AAO reducing the quantity of confined system inside the beam and introducing a detrimental bulk liquid signal. This makes very difficult observing small changes in the liquid dynamics. For this problem it would be necessary to develop a method which prevents the liquid leak during the measure. Concerning this topic a possible solution will be explained at the end of this chapter.

2.5.3.1.2 Results

The discrepancy shown for the case of the OMIM-BF_4 confined in AAO $\oslash$ = 160 nm has been observed also in the case of the pores of 25 nm. The same methods shown in the previous section was used and it has been demonstrated that for all pores dimension the dynamics due to the diffusion of the cation between the aggregates doesn't change with confinement.

These results are summarized in the table 2.4.

2.5.3.2 Diffusion inside the aggregate

The cationic diffusion inside the aggregates was determined by the fit of ToF data using the function 1.41 imposing as D_{lr} and Γ_{orient} the same of the bulk (we are supposing then that the confinement doesn't influence the re-orientation dynamics). Some fit examples are shown in figure 2.25. In the case of the OMIM-BF_4 confined in AAO $\oslash$ = 25 nm sample we couldn't analyse the data at the better resolution (E_i = 0.7 meV) because the spectra statistic was not good enough to perform a fit procedure.

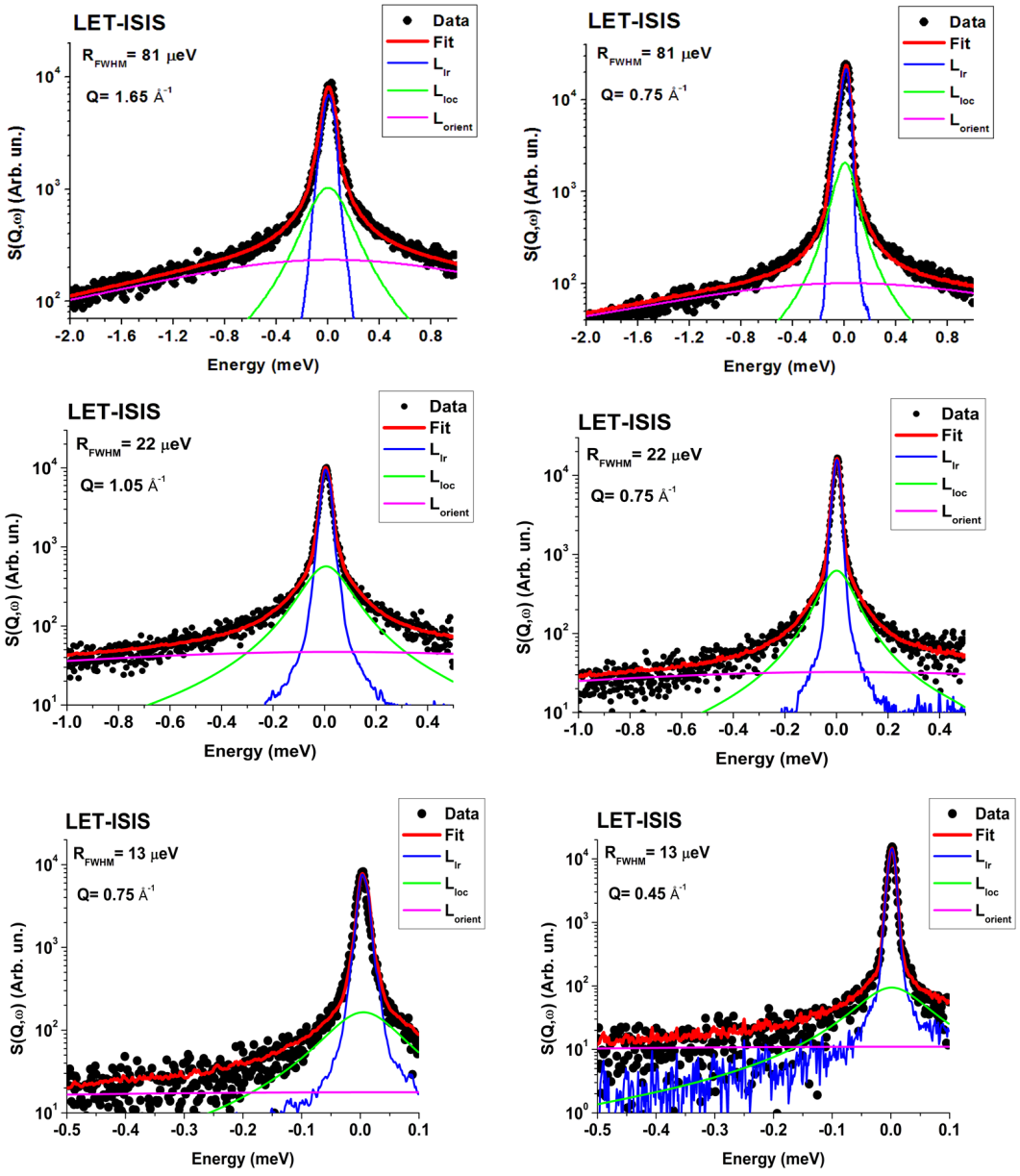

Figure 2.25: OMIM-BF_4 in AAO ⊘= 160 nm ToF spectra fit using the function 1.41. The neat AAO contribution has been subtracted.

The EISF and HWHM of this dynamical component, for the both pores sizes, are shown in figure 2.26.

We can notice that the typical plateau due to the diffusion within a confined space is observable for both pores diameters. As in the bulk liquid we did the

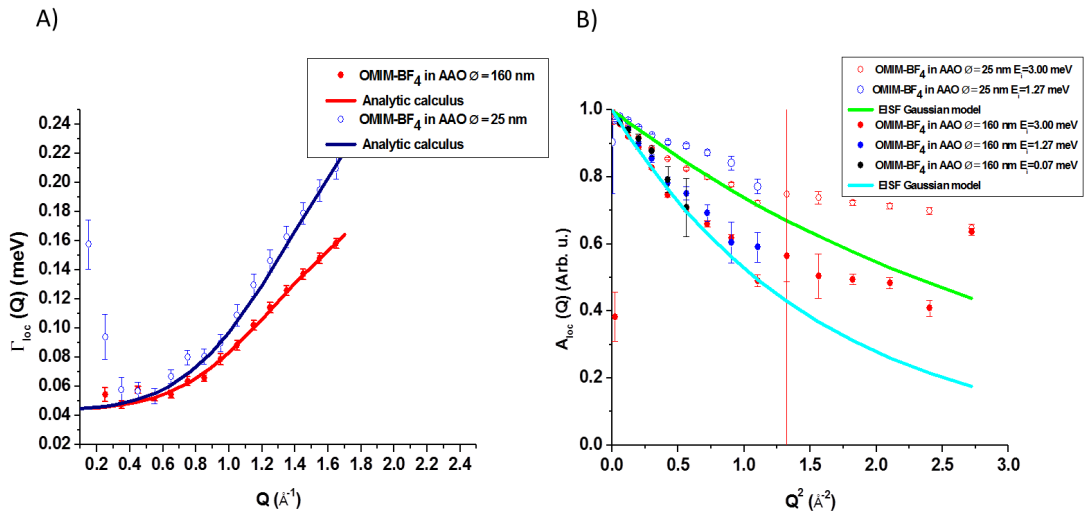

Figure 2.26: A) Γ_{loc} trend versus Q observed for the liquid confined in pores of 160 nm (red full lines) and for that confined in pores of 25 nm (empty blue points). The solid lines are the analytic calculations performed using the Gaussian model equation (FT of the function 1.28), in order to extract the relative dynamical parameters reported in table 2.5. We can notice that for both cases the calculation reproduces well the data trend. B) A_{loc} trend due to diffusion inside the aggregates for the liquid inside the 160 nm pores (full points) and for that in 25 nm pores (empty points). The solid lines are the curves fit using the EISF defined by the Gaussian model (eq.1.30).

analytic calculation, using the Gaussian model in order to extract the dynamical parameters which reproduce well the HWHM trend. The values of these latter are reported in table 2.5 together with those found for the bulk liquid (section 1.3.5).

	D_{loc} (cm^2/s)	2σ (Å)	τ_{mi} (ps)
bulk OMIM-BF_4	2.9 10^{-5}	3.6	1.1
OMIM-BF_4 in AAO $\oslash$ = 160 nm	2.2 10^{-5}	3.6	1.1
OMIM-BF_4 in AAO $\oslash$ = 25 nm	2.2 10^{-5}	3.6	0.6

Table 2.5: Values of the parameters of the Gaussian model obtained by the analytic calculation for reproducing the trend of Γ_{loc} (FT of the function 1.28) on the confined OMIM-BF_4. For more clarity we reported in the same table the values obtained for the bulk liquid (see section 1.3.5).

From the values reported in this table we can affirm that these parameters react in different way to confinement.

We can observe that in both pores sizes the self-diffusion coefficient D_{loc} decreases by the 24% from the bulk state, implying thus a slowing down of the dynamics at the local level.

On other hand the confined space explored by the hydrogen nuclei, 2σ, doesn't change with the confinement. We have to notice that this quantity is much smaller than pores size, so it seems coherent that it is not concerned by the dimensionality reduction of the systems.

Finally the waiting time τ_{mi} is not influenced for bigger pores, while it seems to decreases much for the small ones. We can suppose that this parameter could be linked in some way to the dispersion of the domain size (see sec. 2.4.4), because it seems to follow the same trend of this latter as a function of the pores size. In order to verify this supposition, however, further QENS and WAXS measurements on intermediate pores diameters between 25 and 160 nm are required.

Concerning the EISFs of the two confined cases (figure 2.26B), we can affirm that the trend in the two samples is similar. For the IL confined in the smallest pore, we can observe a bump in the zone near to 0.5 $Å^{-1}$. We can suppose that this is due to coherent contribution of structure factor peak observed in the case IL confined in small pores (see chapter 2.4). We observe, moreover, another peak at high Q in the EISF, that was detected also in the bulk liquid, and it was attributed to coherent contribution of structure factor peak at 1.5$Å^{-1}$. We tried to fit the curves with the EISF function of the Gaussian model defined in the equation 1.30. We found that this function fits well the data except for the zone at high Q, where there is the coherent contribution of the structure factor. Also for the confined case this procedure gives a value of 0.8 (0.55) Å for pores of 160 (25) nm which doesn't agree with the results obtained by the analysis done on the Lorentzian HWHM. We have no a real explanation for this discrepancy. We have to underline that for all the QENS analysis we used a Gaussian model, which supposes an isotropic confinement space. However we are not sure if this supposition is correct already in the case of the bulk, where we can't determine properly the aggregates morphology (see section 1.2.1.2). We can imagine the reduction of dimensionality in the case AAO pores could induce a different organisation along the pores axis the plane perpendicular of them. This supposition would imply another degree of anisotropy, which our model doesn't consider. Also in this case several diffraction measurements are required for verifying this hypothesis.

2.5.3.3 The re-orientation dynamics

As we have already mentioned before, for analysing the QENS data of the IL in the confined state we supposed that the characteristic time associated with this relaxation doesn't change with the confinement because it concerns motions which occur at length much smaller than the confinement size. So the characteristic time

associated at this excitation, in the confined liquid, is 1.1 ps (sec.1.3.5.4.1).

On the other hand we could calculate the EISF relative to this excitation using the equation 1.47. The results for the both samples are shown in figure 2.27.

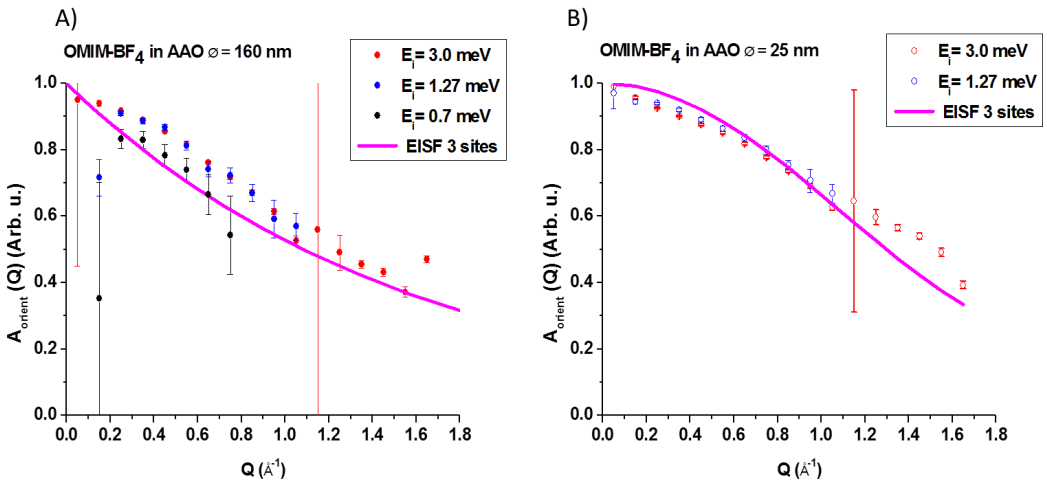

Figure 2.27: A) EISF deduced by ToF due to cationic re-orientation in OMIM-BF_4 confined in pores of 160 nm. B) EISF deduced by ToF due to cationic re-orientation in OMIM-BF_4 confined in pores of 25 nm. The solid line in the two plot is the EISF calculated using the model of a rotation on three equivalent sites (eq.1.50).

We can observe that also in this case we notice a relatively good agreement between the different resolutions. As in the bulk case, we used for analysing the data trend the EISF of a rotation on three equivalent sites (eq.1.50). The obtained curve is shown in figure 2.27 as solid line. We can notice that this model reproduces well the experimental data. We reported finally the values of the dynamical parameters due to this excitation in table 2.6.

	Γ_{orient} (meV)	Waiting time (ps)	r (Å)
bulk OMIM-BF_4	1.79	1.1	1.5
OMIM-BF_4 in AAO $\oslash$ = 160 nm	1.79	1.1	1.3
OMIM-BF_4 in AAO $\oslash$ = 25 nm	1.79	1.1	1.1

Table 2.6: Dynamical parameters obtained by the analysis of the re-orientation dynamics for the different pores size. For clarity we added also the values founded for the bulk liquids in the section 1.3.5. The waiting time and the typical distance r has been deduced by the model of the rotation on three equivalent sites (see sec.1.3.5.4.1.)

We can notice that the there is a little divergence between the bulk sample and the confined ones. For the large pores this is very small (around 13%), so we can say that the value of the distance r is compatible with the that of the bulk. On other hand for small pores this variance is bigger ($\approx 27\%$). However we don't think that this diminution is due to the confinement. In fact the signal acquired on this sample shows a worst statistic, so we think that this could have influenced the fit calculation introducing a big incertitude in the value estimation.

2.5.4 Conclusions

From the analysis shown in the previous section, we conclude that the model developed for the bulk liquid fits well also the data concerning the confined systems.

From the point of view of the dynamics, we can affirm that the confinement in the AAOs has only secondary effects on the cationic dynamics at the local level. Only the local diffusion inside the aggregates seems to be subjected to a low slowing down.

If we calculate the distance travelled for the cation c.o.m. during its long range diffusion (eq.1.55), we found a value around of 2.1 nm which is compatible with that one found in the bulk OMIM-BF_4.

Furthermore the results obtained in this section seem to confirm the supposition that the dynamics is slowed down by the system self-organisation (see the end of chapter 1). In the chapter 2.4 we have shown in fact that the structuration of the system survives in the confined state and it seems amplified by the reduction of the dimensionality. In parallel to the growth of the self-organisation we observed by other techniques that the confinement slows down slightly the ions dynamics at the molecular scale. This seems to confirm the link between the ILs self-organisation and the their particular dynamical behaviour.

All together, if we compare our results with previous reports present in literature, we can notice that in the case of the AAOs we don't observe the dynamics acceleration seen by Mamontov and co-workers [118, 119]. However we have to stress that the confinement matrix used by these authors was a mesoporous carbon with pores diameter of 9 nm. So, being the confinement size and the liquid-surface interactions extremely different, it is difficult to perform a true comparison of these two studies.

So in conclusion we can affirm that, on average, the confinement in AAOs slows down the ILs dynamics at the local level. The origins of the slowing down are not however well explained. Probably they could be justified as a consequence of the surface effects. However more measurements are required for confirming this hypothesis.

2.6 The IL leaks: a NMR 1D tomography study

In the previous chapters we have stressed on the problem of the liquid leaks from the membranes during the measurements on the confined liquid.

Table 2.7 shows the measured mass of OMIM-BF_4 inside the AAOs before and after the ToF measure on LET (the time difference between these two successive experiments is twenty-four hours).

	m_{IL} (mg) before	m_{IL} (mg) after	loss (%)
OMIM-BF_4 in AAO $\oslash = 160$ nm	32	21.8	32
OMIM-BF_4 in AAO $\oslash = 25$ nm	16	26	38

Table 2.7: Measurements of the IL mass inside the membranes before and after the ToF measurements on LET. The time difference between these two successive experiments is twenty-four hours.

We can notice that a significant part of the liquid leaks out during the measurements. Therefore the most important goal to achieve, in order to improve the study of the IL confinement in the AAOs, is preventing the liquid loss.

In this part we will illustrate some first tests that we developed in order to fix this problem.

The origin of this leak is not clear. Studying the physical causes which generate this phenomenon is out of the purpose of this work. The objective of this analysis is just finding a practical solution to prevent the liquid loss. In this section we will demonstrate that we can exploit the surface interactions for frustrating the sample leak.

2.6.1 The NMR 1-D tomography

In order to characterize the liquid loss we have chosen the NMR 1D tomography (Stray-Field Imaging (STRAFI)). This technique holds several advantages. Firstly, its spatial resolution is high enough ($R_s \approx 13\ \mu m$) to measure our samples profile which is one hundred micrometers long. Furthermore, the IL quantity contained in a membrane is sufficient to observe a sample profile in tens of minutes, allowing for a very short acquisition time.

2.6.1.1 The basis of the NMR tomography

From the electro-magnetism, we know that when a physic system, with a magnetic momentum μ (e.g. a nucleus) is placed in a magnetic field $\mathbf{B}$, it momentum μ

experiences a precession with a frequency called *Larmor frequency*, ω_L, which is given by the relation:

$$\omega_L = \gamma B \tag{2.12}$$

where γ is the gyromagnetic ratio of the considered isotope.

Let's consider a sample composed by an unique isotope (i.e. it has a unique gyromagnetic ratio). If the magnetic field is inhomogeneous, it will trigger a distribution of the precession frequencies $g(\omega_L(B))$, which will depend on the atomic positions within the magnetic field only. If then we measure the sample frequency response $I(\omega)$, this will be related to the distribution of the Larmor frequencies of the system:

$$I(\omega) = g(\omega_L(B)) \tag{2.13}$$

If we know the spatial magnetic field dependence, we can use the equation 2.12 in order to associate each Larmor frequency to an atomic position within the field and then reconstruct the quantity:

$$I(\mathbf{x}) = g(\mathbf{x}) \tag{2.14}$$

This is the system's response as a function of position $\mathbf{x}$, i.e. it provides a spatial profile of the sample.

2.6.1.2 The instrument and its calibration

The measurements were performed at the "Laboratoire Structure et Dynamique par Résonance Magnétique" (LSDRM) using an open NMR tomograph.

The magnetic part of this instrument is made up of an assembly of NdFeB permanent magnets. These magnets are disposed in such a manner that they create a controlled magnetic field gradient of 3.3 T/m in the direction perpendicular to the magnet surface, but they maintain an uniform magnetic strength on the surfaces perpendicular to the gradient direction (see sketch in figure 2.28A) [122].

The field strength is defined by the function:

$$B(z) = -grad(B)z \tag{2.15}$$

Where $grad(B)$ is the field gradient and z is the position perpendicular to the magnet surface.

Resuming the formalism defined in the subsection 2.6.1.1, the position response of the sample will defined as:

$$I(z) = -\gamma grad(B)z \tag{2.16}$$

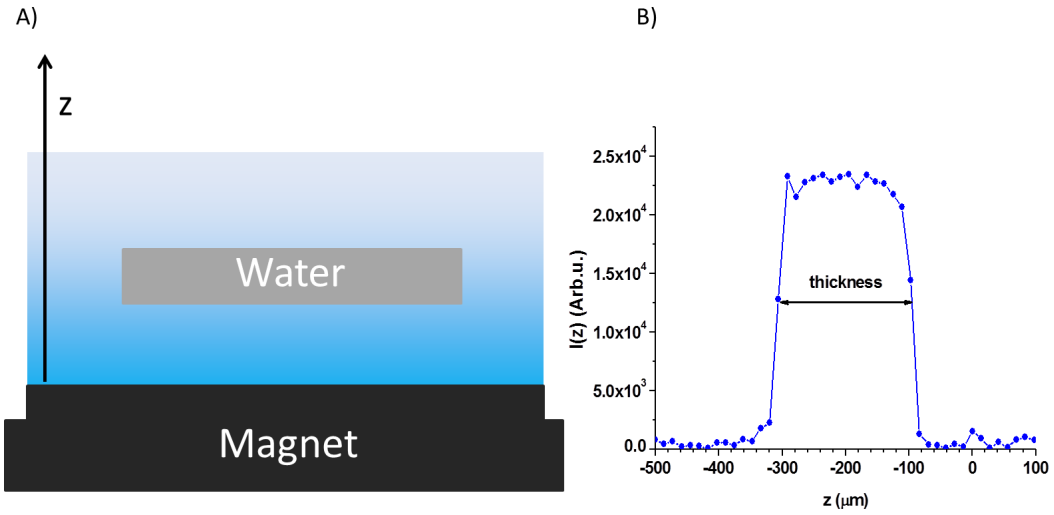

Figure 2.28: A) A sketch of NMR tomograph used in this work. The blue rectangle represents the magnetic field gradient intensity, while the gray rectangle is the sample. The sample is oriented with the pores perfectly parallel to field direction. B) Profile measurement of a water layer of 200 μm in a rectangular cell. The sharp rectangular shape of the profile shows a good orientation of the sample in comparison with field direction.

In our measurements we probe the Hydrogen ($\gamma_{^1H} = 42.576 MHzT^{-1}$).

For an accurate measurement, it is necessary to finely orientate the sample surface so that it is perfectly perpendicular to the magnetic field (Fig.2.28A). For this end we used a reference sample of water contained in a flat quartz cell of 200 μm thick. The profile obtained after the sample orientation is shown in figure 2.28B.

We notice that the profile has a sharp rectangular shape which confirms a good orientation with respect to the field. If we calculate the distance between the two points at half of the profile, which define it width along z, we found a distance of 210 μm which is compatible with the thickness of the cell. Moreover we could also estimate the spatial experimental resolution ,R_{exp}, by doing the ratio of thickness for the number of points which define the profile, which gives $R_{exp} \approx 13$ μm.

2.6.2 Results

Figure 2.29A shows the time evolution of the profile of a single AAO membrane ($\oslash$ = 160 nm) placed between two flat quartz windows. The AAO pores are parallel to the magnetic field.

From this plot we can observe that the liquid seems to move towards the

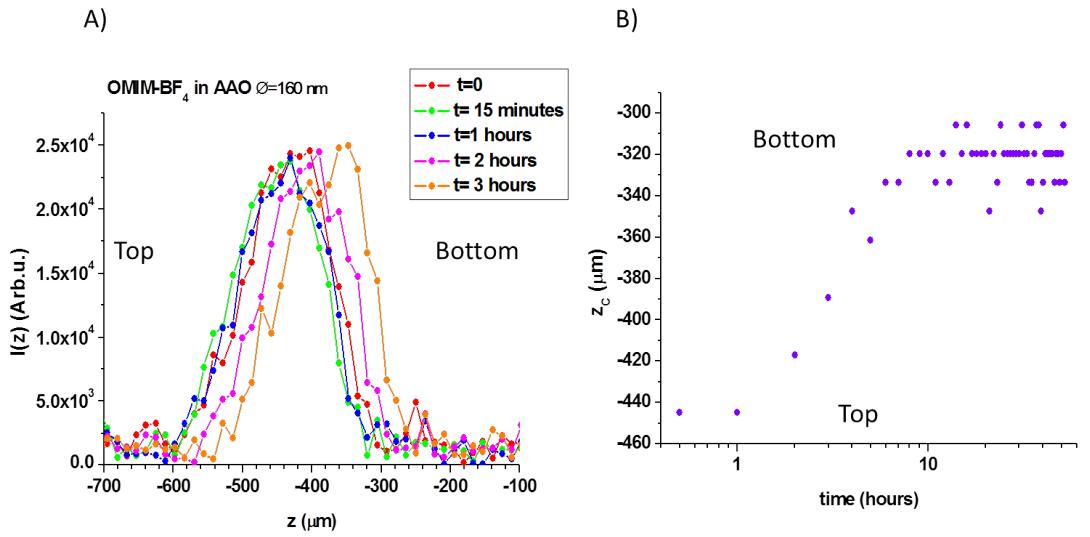

Figure 2.29: A) Time evolution of the hydrogen profiles of the sample OMIM-BF_4 confined in a membrane of AAO $\oslash$ = 160 nm. We can observe that the profile shifts over the time. B) Position of the profile center as function of the time. We can notice that the complete emptying of the membranes (i.e. a displacement of around 100 μm) occurs in eight hours.

bottom of the cell. In the figure 2.29B we plot the position of the center of the profile measured a different time. We can notice that after eight hours the center has shifted by around 120 μm, which is roughly the membrane thickness. Since the environment temperature was maintained constant, we can conclude that this shift is due to the physical leak of the liquid which is coming out through the bottom of the membrane.

We carried out then another measurement by placing between each AAO-window interface a layer Polytetrafluoroethylene (teflon). This polymer has, as opposed to OMIM-BF_4, an hydrophobic behaviour. We can suppose that, in this case, the liquid minimizes it interactions with this material by staying in the pores. The example of two profiles measured at distance of 24 hours are shown in figure 2.30A.

We can see that in this case the liquid profile doesn't change as a function of the time. The evolution of the profile center is shown in figure 2.30B. We can observe that it doesn't change as a function of the time and the small variations are compatible with the experimental resolution.

We can then conclude that the use of a hydrophobic material, in the case of OMIM-BF_4, can prevent the liquid leak from the membranes. This first test opens then new possibilities to improve the experimental conditions for future studies.

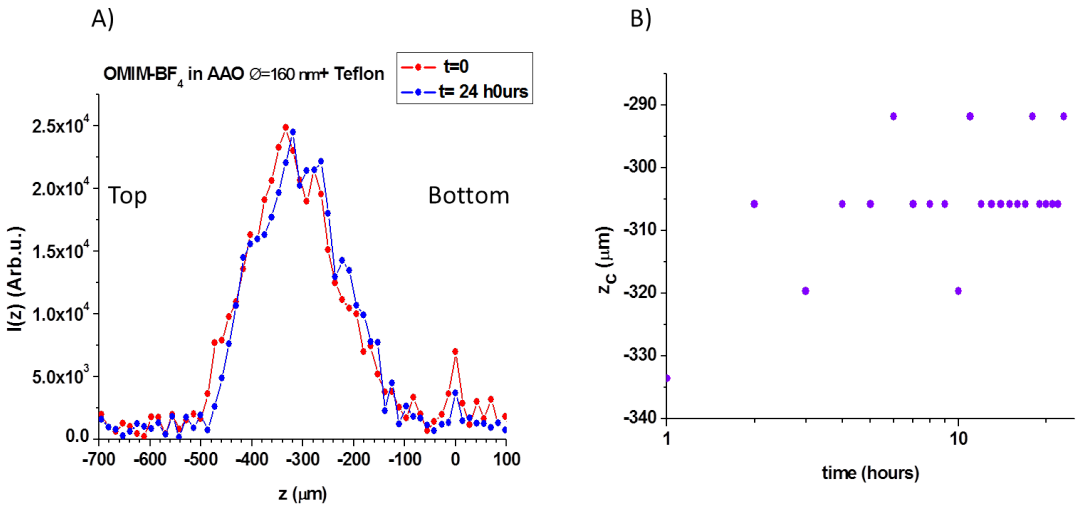

Figure 2.30: A)Hydrogen profiles time evolution of the sample OMIM-BF_4 confined in a membrane of AAO $\oslash = 160$ nm where two layers of teflon placed between the AAO and the windows. B) Position of the profile center as a function of the time. We can observe that it is stable in the time.

Chapter 3

Properties of the ionic liquids confined in carbon nanotubes membranes

In the previous chapter, the study on the ILs confined in the AAO membranes has pointed out that it is possible to observe some confinement effects on the properties of these systems. However, these matrices show some limitations. First of all the surface effects are not negligible. This feature complicates further the analysis because it can induce the formation of two ion populations which behave differently. Moreover the minimum pores size available in these membranes is around 10 nm. Since the pores' diameter is much bigger than the ions size, it is not possible to obtain a quasi 1D pipeline.

These limits could be overtaken using the carbon nanotubes (CNTs). The diameter of this nanostructure is in the nm range, and, therefore, it is comparable to ionic dimension. We can then hope to achieve a more consistent confinement than in the case of the AAO.

Furthermore, the graphene-like structure of the CNTs pores results in a very "smooth" surface potential. So, in this case, we can consider that the interaction of IL with walls could be negligible or, at least, extremely reduced.

For these reasons we dedicate a part of this work to the analysis of the properties of the confined ILs inside the CNTs. The study shown in this chapter represents just an initial approach to this subject. The first problem concerning this topic was the creation of one-dimensional anisotropic matrix composed by the CNTs. A first section describes the protocol for the membrane synthesis. A second section provides the results on the confinement effects.

3.1 Sample preparation

3.1.1 What are carbon nanotubes?

Carbon nanotube (CNTs) are cylindrical nanostructures composed by one or more rolled up carbon atomic layers, called graphene (see Fig. 3.1A).

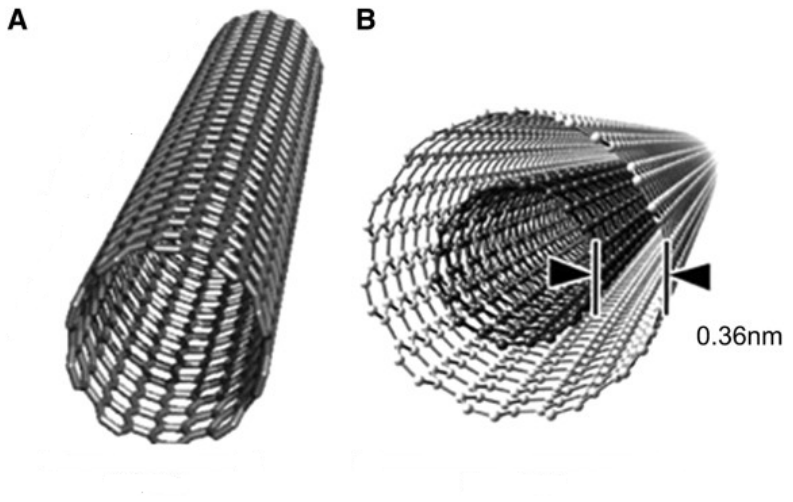

Figure 3.1: (A) Single-walled carbon nanotube (SWCNT) (B) Multi-walled carbon nanotube (MWCNT).

In nature we can observe many kinds of CNTs structure. They can be composed by just a single graphene layer (single-walled nanotube (SWNT)) or by two or more walls (multi-walled nanotube (MWNT)) (see Fig. 3.1 B).

The CNTs seem to be a very promising confinement matrix. They have very small diameters (less than 10 nm), which can ensure a very tight confinement space. Furthermore, they show a very smooth surface where the friction between the walls and confined liquid is negligible.

The CNTs have been already tested as confinement medium in the case of water and it has been shown that they induce surprising effects on the physics of this liquid [7].

Recent studies have also demonstrated that these nanostructures have a very good properties for the mass [8, 123] and charges [124] transport, so they became good candidates for different kinds of applications.

3.1.2 Experimental protocol for the CNTs membranes production

The experimental protocol for the CNTs membranes production, followed in this work is summarised on the figure 3.2.

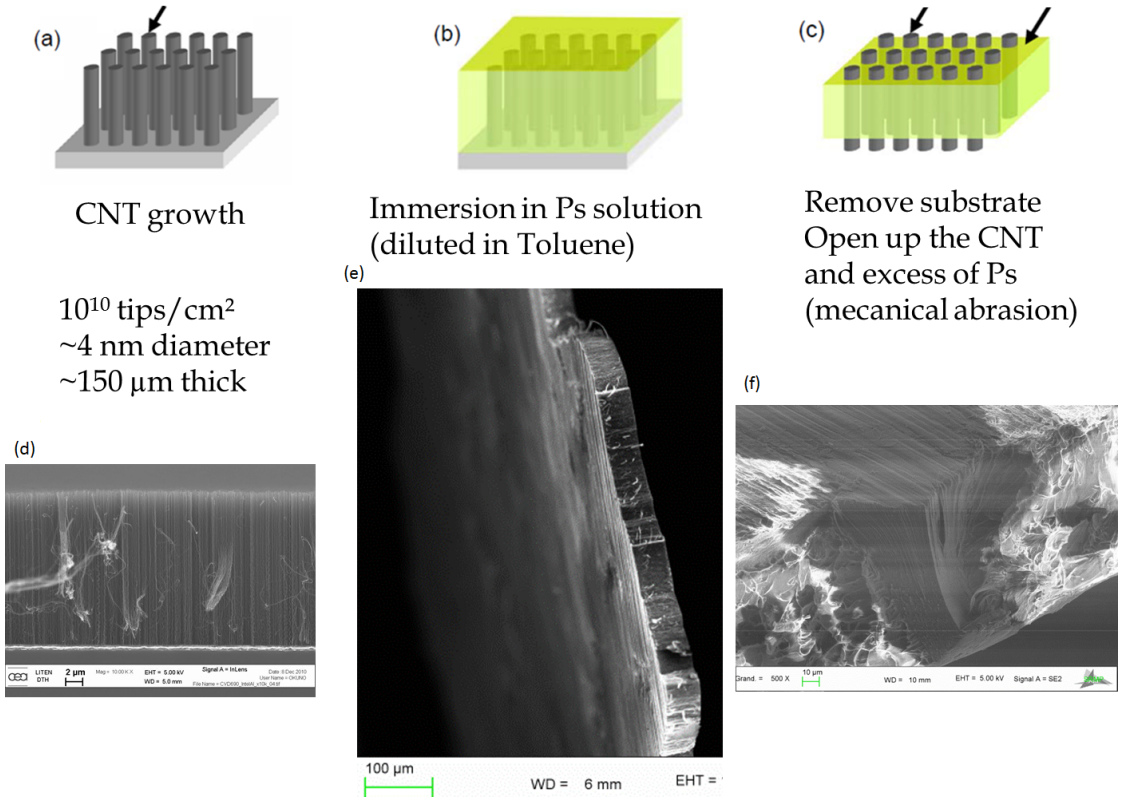

Figure 3.2: The three main steps of the experimental protocol followed for the CNTs based membrane production. a) CNTs carpet synthesis by CCVD. d) a Scanning Electron Microscope (SEM) picture of the carpet produced from this process. We can observe that CNTs grow all parallel in the direction perpendicular to the substrate. The tubes at this step are closed. b) Polymer infiltration of the space inter-tubes. The polymer was introduced by the immersion of the CNTs carpet in a polystyrene and toluene solution. The solvent has been left to evaporate at room temperature. e) a SEM image after the polymer impregnation (courtesy of Patrick Bonnaillie). c) Tube opening by the substrate removal, from one side, and by mechanical abrasion from the other. f) a SEM picture of the finished membrane (courtesy of Patrick Bonnaillie).

As we can observe from the figure, the process is based on three steps, which consist in: *(i)* CNTs synthesis, *(ii)* membranes formation by polymer infiltration,

(iii) pores opening.

The goal of this section is thus to show the different steps of this protocol.

3.1.2.1 Carbon nanotubes synthesis

The CNTs were synthesised at the "Laboratoire d'Innovation pour les Technologies des Energies Nouvelles et les nanomatériaux" (LITEN) at the CEA in Grenoble by Jean-Dijon groups.

The synthesis was done by a Catalytic Chemical Vapour Deposition (CCVD) [125], using a layer of iron as catalyst, deposed on a silicon substrate. This method consists in a production of a solid material at the surface of the catalyst layer from a gas precursor. In particular, for the CNTs synthesis, this process can be divided in the following steps:

- The substrate is placed in an atmosphere, at room temperature, composed by a gas mixture of 20 Standard Cubic Centimeters per Minute (sccm) of C_2H_2, 50 sscm of H_2 and 110 sscm of He at a pressure of 1.2 mbar.
- the system is then warmed up at 400°C by Joule effect by using a power of 800 W.
- This temperature is kept for several minutes after to bring back the system at room temperature.

The catalysis reactions produces then a CNTs carpet of thickness of around 150 μm, where the tubes grow in the direction perpendicular to the catalyst layer (see figure 3.2A).

The CNTs morphologies was then characterized at LITEN by Transmission Electron Microscopy (TEM). It has been then pointed out that tubes produced in this process are generally double or triple-walled, with an average inner diameter of 4 nm and a pore density of 3 10^{11} cm^2/s.

3.1.2.2 The membrane formation

The second step consisted in the filling the inter-tubes volume. For this purpose we performed a polymer impregnation of the CNTs carpet. For this operation we choose to use polystyrene (PS) (M_w= 350000 g/mol), because *(i)* it was shown that it wets well the CNTs [126], *(ii)* it is below T_g at room temperature and *(iii)* it is easily available in deuterated form .

The carpet was immersed in a solution of deuterated PS dissolved in deuterated toluene (wt_{PS}=20%). We chose to use deuterated compounds in order to hide their dynamical contribution during the study of the confined ILs dynamics. The

solvent was evaporated at room temperature. We did not warm the system at high temperatures in order to prevent bubbles formation. After the complete solvent evaporation the membrane was left under vacuum in order to remove the last toluene traces which were remained trapped in the PS.

At the end of this step all the space between the tubes was totally filled by PS. A Scanning Electron Microscopy picture of results of the PS infiltration is shown in figure (see figure 3.2e).

3.1.2.3 The membrane opening

The last step of the membrane synthesis was the tube opening. For one of the sides removing the carpet substrate was sufficient, while for the second side we performed a mechanical abrasion which removed the polymer excess and it opened the CNTs.

In the end of this part a membrane with tubes open on both sides has been obtained (see Fig.3.2f)

3.1.3 Membrane filling

The membranes were filled in the same way as the AAO, by submerging the membrane in the OMIM-BF_4. The IL excess on the membrane surface is removed with a tissue.

In figure 3.3 we show a test of the actual filling of the membrane by Energy Dispersive X-ray (EDX) analysis on the fluorine atoms. To this end, we performed a further mechanical abrasion of membrane, in order to remove few microns from the surface of the CNT membrane. In the SEM picture the black part correspond to the CNTs whereas the white spots are PS. When observing the EDX picture, we can notice that the Fluorine signal (red part) covers all the parts occupied by the CNTs. We can then conclude that the liquid penetrates inside the tubes.

3.2 Dynamical effect of the confinement

The goal of this section is to show the effects of the confinement observed in these systems. These studies have to be interpreted as a first approach to this topic. So they don't represent a detailed study, as the case of the IL confinement in the AAO, but they are rather a starting point for works (e.g. MD simulation (see Fig.3.4)).

This section is divided in three main subsections. In each of them we treat the results obtained by a different technique. Firstly we show the study of the dynamics at the molecular scale by QENS. Then we present the spectacular confinement

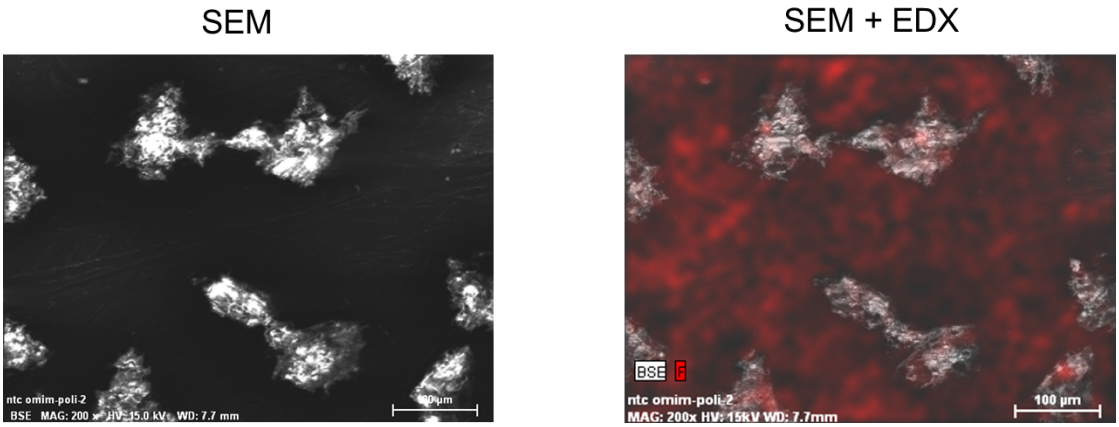

Figure 3.3: On the left SEM picture of a CNTs membrane. In this case the membrane was left several hours in the liquid and was subjected to a further mechanical abrasion in order to penetrate inside of it. The black spots are the CNTs, while the white ones are the PS parts. On the right the same sample picture obtained by the EDX spectroscopy. The red parts represent the Fluorine presence. We can see that it is present in all the surface occupied by the CNTs, confirming the actual membrane filling.

effect observed on the IL dynamics at microscopic scale by impedance spectroscopy and NMR.

3.2.1 Cationic dynamics at molecular scale probed by QENS

The first step of this study, was the analysis of the pores anisotropy on the ILs dynamics the molecular scale. For this purpose we performed QENS measurements on the filled CNTs membranes.

The measurements were done on the spectrometer IN5 (ILL-Grenoble) at a temperature of 293 K. We used a wavelength of 8 Å, which allowed to have an experimental resolution or 20 μeV and to probe a Q range between 0.25 and 0.78 $Å^{-1}$.

The synthesis of the sample considered in this study was done by using deuterated PS and toluene in order to minimize the contribution of the incoherent scattering from these materials.

In this work two orientations of the sample were used (see sketch in figure 3.5): the first one with the tube axis perpendicular to the beam (Fig.3.5A), in order to probe the ionic dynamics along the radial direction, and the second one with the tube parallel to incident beam (Fig.3.5B) in order to observe the dynamical behaviour along the axial direction.

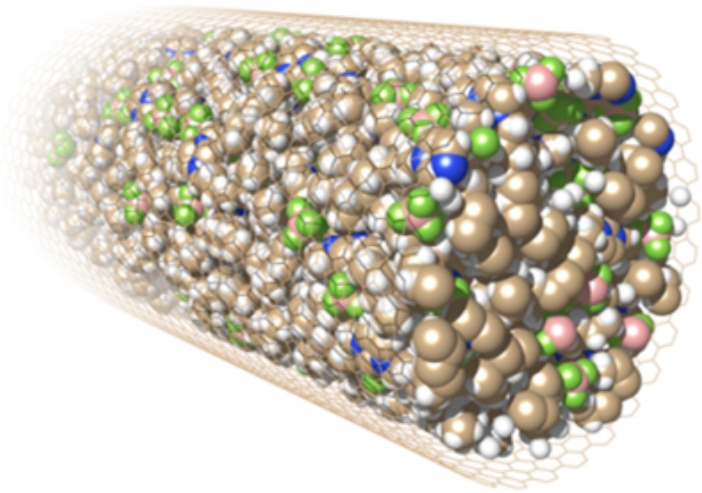

Figure 3.4: Molecular dynamics snapshot showing the OMIM-BF_4 confined inside a CNT by courtesy of Patrick Judeinstein and Benoit Coasne. We can notice that in these systems the diameter ($\oslash = 4$ nm) is much smaller than the AAO pores one and that the tube can contain only few couple of ions.

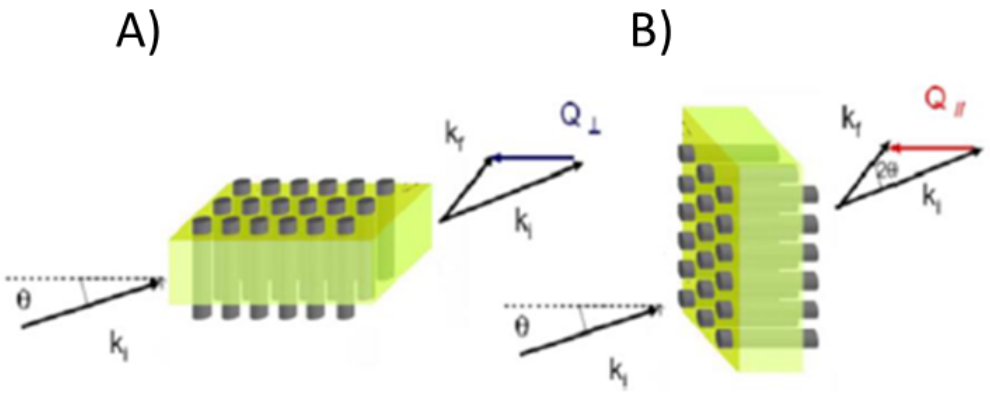

Figure 3.5: Sketch of the two sample orientations used in the QENS measurements. A) tubes perpendicular to the beam, in this case we can observe that the wave vector is perpendicular to the tube axis. In this way we probe the dynamics along the cross section of the tubes. B) tubes parallel to the beam. With this orientation we have access to wave vectors to tube axis in order to observe the ions diffusion along the axial direction.

We initially measured the empty membranes in order to quantify the signal coming from the matrix. We show an example of the measured spectra in figure 3.6. We can notice that the signal coming from the membrane is purely elastic, i.e. the deuteration of the polymer completely hides the dynamical contribution of this component.

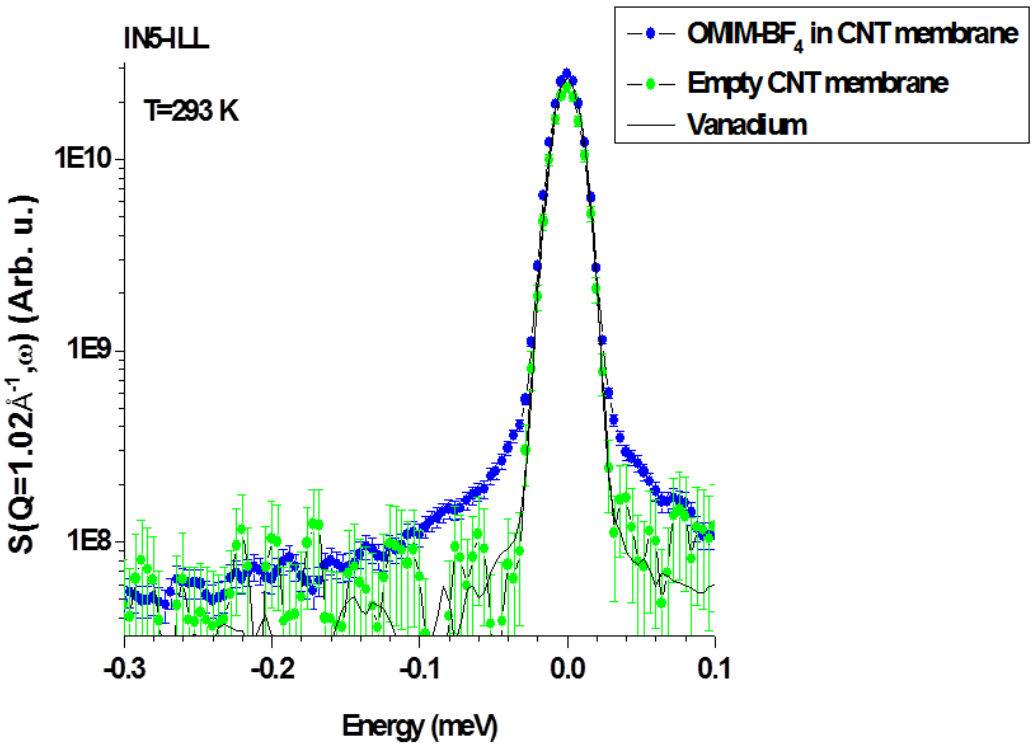

Figure 3.6: QENS spectra measured on IN5 at Q= 1.02 $Å^{-1}$ T= 293 K of the system membrane+IL (tubes parallel to the beam), in blue, the empty membranes (tubes parallel to the beam), in green, and the vanadium, used to show the experimental resolution, in black. We can notice that the membrane contribution is exclusively elastic,showing that the PS deuteration hides the polymer dynamical contributions

After that we measured the same membrane filled by the OMIM-BF_4 in both orientations. We want highlight that in this case the amount of the liquid in the beam is around 2 mg, which is much lower than in the AAO case (around 20-30 mg). However from the example shown in figure 3.6 we can distinguish a signal coming from the IL.

Because of the presence of the IL QENS signal, we tried to check if it is possible to observe a difference between the dynamics along the axial and the radial direction.

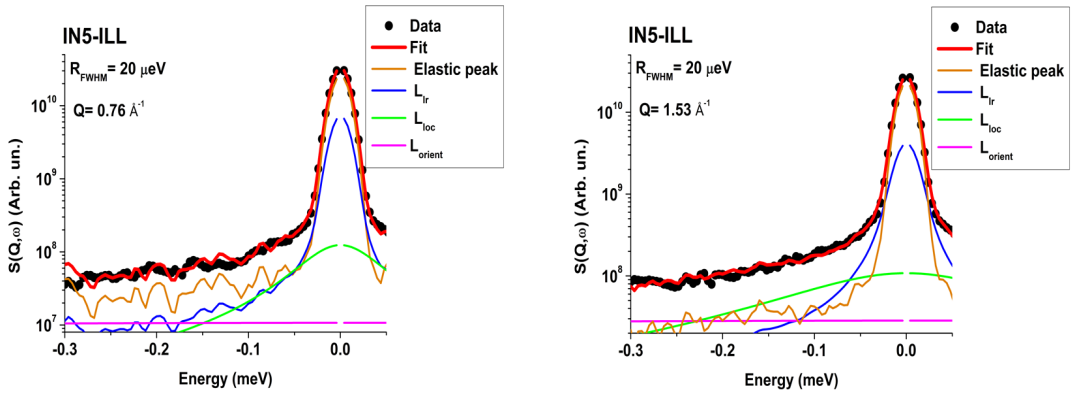

Figure 3.7: OMIM-BF_4 confined in CNTs membranes ToF spectra fit using function 1.41.

To analyse these data, we tried to use the same model developed for bulk liquid (eq.1.41). In this study we didn't have access to the other experimental techniques necessary to determine properly the dynamics in a wide range, so we had to do some approximations. For example since the pore size is still bigger than bulk liquid correlation length ($L_{corr} \approx 2$ nm), we suppose that the long range self-diffusion coefficient D_{lr} is the same as the one of bulk state ($D_{lr} = 3.7\ 10^{-7}$ cm^2/s). Moreover we imposed that the re-orientation dynamics doesn't change with the confinement (i.e. the HWHM of the relative Lorentzian is equal to the bulk one). In conclusion we use the three Lorentzian intensities and the HWHM of the $L_{loc}(\mathbf{Q}, \omega)$ as fit parameters. Some examples of fit are shown in figure 3.7. The trend of Γ_{loc} as a function of Q is shown in figure 3.8.

As we can notice from this plot, the errors bars on the values concerning the confined liquid are too big to discern a difference between the two directions and, even from the bulk.

This great indeterminacy is due to the very low quantity of liquid inside the sample which can't enable a statistic good enough for performing a good fit. So, at the moment, any conclusion could be done for the dynamics at the molecular scale.

For overcoming this problem a bigger quantity of liquid is required in the beam. For this purpose it would be necessary modify the protocol of the CNTs synthesis in order to achieve a higher tube density.

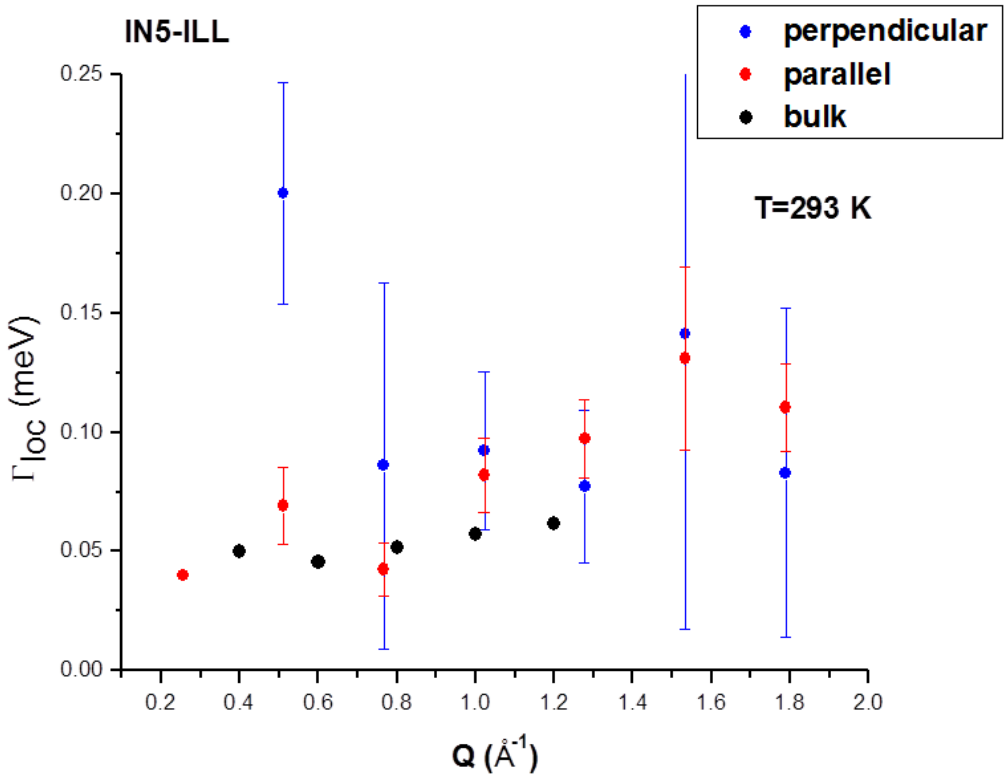

Figure 3.8: Trend of Γ_{loc} versus Q obtained by the fit of the bulk (black) and confined (red parallel orientation and in blue perpendicular one) liquid spectra using the function 1.41. We can notice that incertitude of values is too big to distinguish some differences in the dynamical behaviour as a function of confinement and the tubes orientation.

3.2.2 Ionic conductivity probed by impedance spectroscopy

After the study of the confined IL at the molecular scale, we passed to analyse the confinement effect at the larger scale. For this purpose we started to probe the transport properties of ILs confined in the CNTs. We will show that, in this case, the conductivity of the liquids shows a notable improvement due to the confinement.

For this purpose we performed impedance spectroscopy measurements, with the collaboration of Dr. Quentin Berrod (LLB). This technique enabled us to probe the charges motion at μm length scale.

In this study we used Novocontrol impedance spectrometer (with an Alpha-A

analyser), which allowed to probe the frequencies range between 1 Hz and 10 MHz. For the measurements we used very low voltages (less than 0.2 V) in order to avoid the activation of the electrochemical reaction at the interface electrodes-IL.

To measure the conductivity in the confined state, we developed a specific sample cell. The membrane surface are not perfectly flat and regular, so the flat electrodes don't ensure a good electric contact. To improve it, we have developed a cell where the membrane is placed between two reservoirs of bulk ionic liquid, which are in contact with the electrodes (see sketch in figure 3.9A).

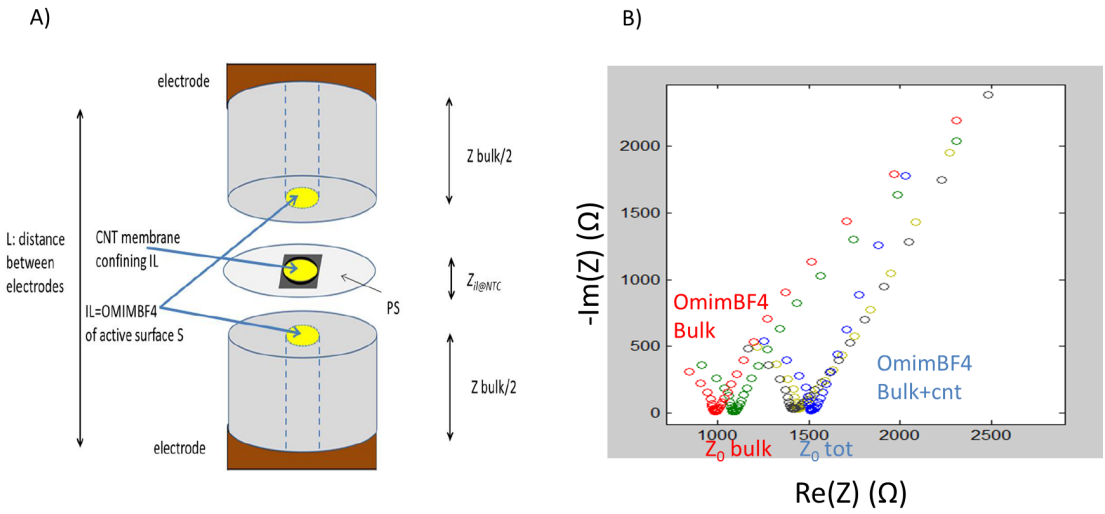

Figure 3.9: A) sketch of the used sample cell during the impedance spectroscopy measures. The membranes is placed between two IL reservoirs in order to allow a good electric contact with the electrodes. B) Cole-Cole plot representing the contribution of liquid reservoirs (in red and green) and the system membrane+reservoirs (in grey, yellow and blue). Several curves of the same sample are represented in order to show the measurements reproducibility. The point where there is a change of curve trend are related to the ionic conductivity (they are marked as Z_0).

This implies that in the case of the confined state, the total impedance measured in the cell is equal to:

$$Z = Z_{bulk} + Z_{IL@CNT} \tag{3.1}$$

where Z_{bulk} is the total impedance of the IL contained in the reservoirs and $Z_{IL@CNT}$ the impedance of the confined IL within the CNTs.

So to determine the contribution of the IL inside the CNTs, first of all it was necessary to measure the response of the bulk liquid in the reservoirs. In figure 3.9A we show an example of the measured impedance of this latter at 298 K (red

and green curves). In this figure we use the so called $Cole - Cole$ representation. We can notice that, in this representation, the data forms a half-circle followed by a monotonic increase. The value of the real part of the impedance, where we observe this change of trend is related to system conductivity. If we call this quantity Z_0, the conductivity of the liquid is defined as:

$$\sigma = \frac{1}{Z_0}\frac{L}{S} \tag{3.2}$$

where L is the distance between the electrode, while S is their surface.

So, in the case of bulk liquid, where $t = 5$ mm and $\oslash_{electrode} = 8$ mm, we found a value of Z_0 equal to 1400 Ω, which corresponds to an ionic conductivity of 0.071 S/m which is compatible (under the 20%) to the value given by the literature [127].

When we insert the membrane in the cell we can notice that the Cole-Cole plot of the system shifted to high impedances. By subtracting the contribution bulk we found a $Z_{0_{bulk}} = 530$ Ω. We could then calculate the conductivity by the relation 3.2 using as distance the membrane thickness (150 μm) and as surface the effective area of the porous space $S = \pi r_{pores}^2 \rho_{pores}$ where r_{pores} is the pores radius (2 nm) and ρ_{pores} is the pores density (3 10^{11} pores/cm^2). This resulted in a conductivity of $Z_{0_{IL@CNT}}$ =0.22 S/m, which points out an enhancement of the transport properties by a factor 3±1.

We conclude that the impedance spectroscopy shows a remarkable enhancement of ionic conductivity due to the liquid confinement. However, we have to highlight the limits of this technique. First of all the reproducibility of measures: as we can notice from experimental data shown in figure 3.9B, there is a difference of around 10% for the Z_0 values measured on the same sample. This increases the uncertainty on the enhancement factor of the ionic conductivity. Furthermore, as both the cation and anion have an electric charge, we can't distinguish if the dynamics improvement is due to only to a specific ionic specie or both. So, in conclusion, by carrying impedance spectroscopy measurements, we can observe an increase of ionic dynamics, but, on other hand, it is necessary to use another experimental technique which could discern the two ions dynamics in order to better characterize this confinement effect.

3.2.3 Ions dynamics probed by NMR spectroscopy

A complementary information to the impedance spectroscopy analysis can be obtained by the pulse filed gradient NMR (PFG-NMR). This technique allows to probe the sample dynamics at the microscopic scale (i.e. 0.1 μm as length scale 10 ms as time scale) and it can choose the atomic specie to probe. These features enable to study separately the cation and anion dynamics, which was not possible with the impedance spectroscopy.

Furthermore, by orientating in different way the membranes towards the magnetic field, it is possible to probe the dynamics along the axial and radial direction in order to test the effect due the anisotropy.

The goal of this study was thus the determination of the cation and anion self-diffusion coefficient.

The measurements were done on the PFG-NMR spectrometer at the "Laboratoire d'Electrochimie et de Physicochimie des Matériaux et des Interfaces" (LEPMI) of the Grenoble university with collaboration of Dr. Quentin Berrod (LLB), Dr. Patrick Judeinstein of the Laboratoire Léon Brillouin (LLB) and Dr. Cristina Iojoiu (LEPMI).

The sample considered in this work was the OMIM-BF_4 confined in the CNT membranes.

The membranes used in this work were broken in several parts and stacked all parallel in a NMR tube, in order to maximize the liquid quantity in the magnetic fields.

We show a first measurements of the anion dynamics in figure 3.10. Here we plot the normalised measured intensity in function of the quantity $X = G\gamma^2\delta^2(\Delta - \delta/3)$, where G is the field gradient, γ the gyromagnetic ratio of the probed nucleus, δ the duration of the gradient pulse and Δ the delay between two pulse. The intensity normalised I_n intensity in function of the variable X can be written as [128]:

$$ln(I_n) = -D_t G\gamma^2\delta^2(\Delta - \delta/3) \tag{3.3}$$

where D_t is the ion self-diffusion coefficient.

We fitted the data using the equation 3.3 to obtain the self-diffusion coefficient of the fluorine and we found respectively (4.4±0.3) 10^{-8} cm^2/s for the bulk liquid and (1.3±0.2) 10^{-7} cm^2/s for the confined one. We observed then an increase on the anion dynamics by a factor 3.0±0.5.

After these first results, we performed another set of measurements probing the cation and anion dynamics on a similar sample. In this set we also tested the confinement effects on the axial and radial direction. For this purpose we used two sample orientations: with the CNT long axis parallel to field and with the the CNT long axis tilted of 90° in comparison to the field direction.

This last analysis was performed only for the cation dynamics.

The cationic dynamics was determined from the signal of the hydrogen nucleus (^{1}H), while the anionic motion by the fluorine (^{19}F) one.

In the case of the motion along the tube axis, the dynamics of the cation and the anion seems to be accelerated with an increase of the self-diffusion coefficient of factor 2-3, as it is shown in table 3.1. On the other hand, in the case of the dynamics along the radial direction of the tube, we found a cationic self-diffusion coefficient 4 10^{-8} cm^2/s, which is similar to the bulk liquid one. We have to

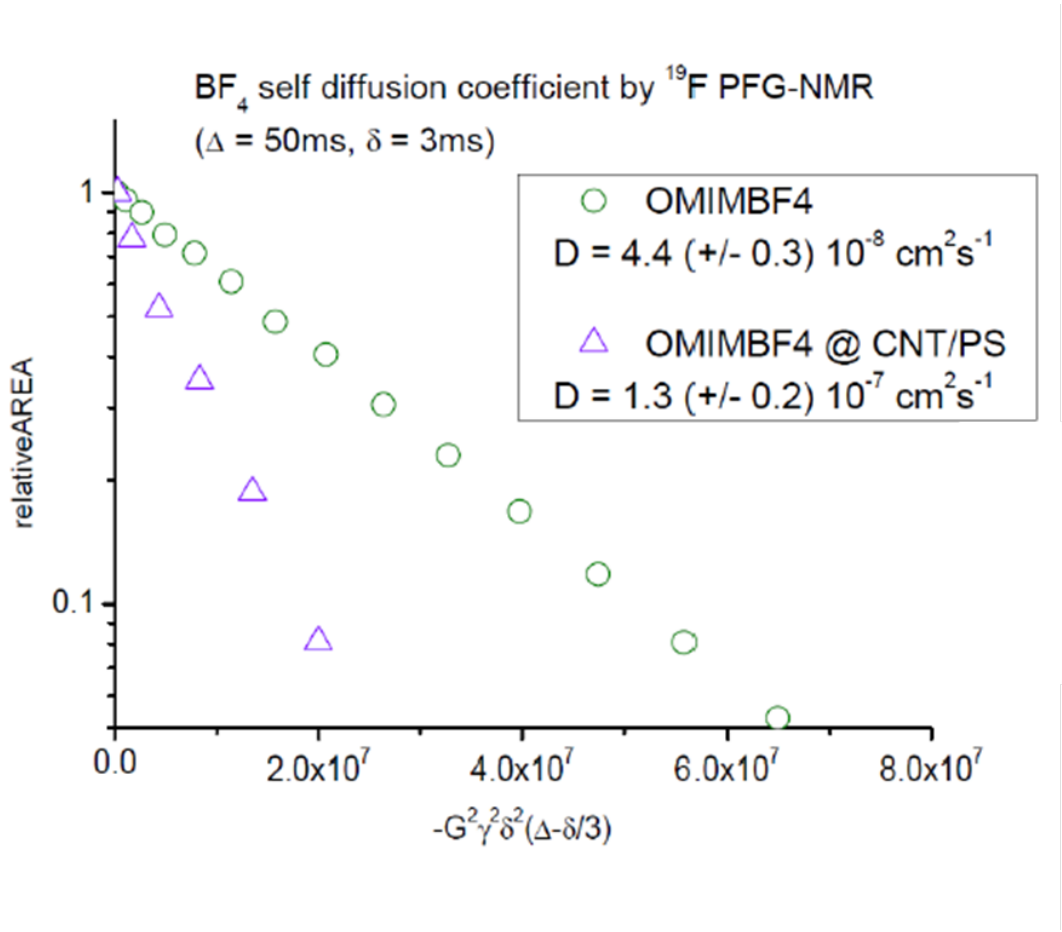

Figure 3.10: NMR signal, using as probe the nucleus ^{19}F, in function of field gradient for bulk liquid (in green) and for the confined one (in purple). The slope of the curves is related to the ion self-diffusion coefficient. The latter was determined by the linear fit of the experimental curve. We can notice a remarkable enhancement of the anionic diffusion in the case of the confined liquids.

underline that in these systems the porous size is extremely small ($\oslash = 4$ nm). The NMR apparatus doesn't have enough spatial resolution to observe the dynamics in the radial direction of the pores. We can conclude that the measured signal due the dynamics in this latter direction is coming from a part of liquid which is not confined in the tubes. As in the AAOs case, we can suppose that a layer of bulk liquids remains on the membrane surface despite the drying operation. We can imagine that it is thin enough that we can observe it dynamical contribution only when we probe a translational directional parallel to the membranes area.

On other hand, for the direction along the tube axis, we can state that we

	$D_{^1H}$ (cm^2/s)	$D_{^{19}F}$ (cm^2/s)
Bulk	$3.67\ 10^{-8}$	$4.4\ 10^{-8}$
Confined $\parallel$	$9.3\ 10^{-8}$	$13\ 10^{-8}$

Table 3.1: Cationic and anionic self-diffusion coefficient or the OMIM-BF_4 confined in the CNTs membranes and in the bulk state.

observe a confinement effect, which enhances the ionic dynamics at microscopic scale. The origins of this phenomenon are, at the moment, still uncertain. We think that it is due to multiple factors. One of them could be the reduction of dimensionality from three to quasi-one dimensional space. If we consider the ionic motion as pure Fickian (diffusive) process, when the IL is in the bulk state, the ion can move in three possible spatial directions, so their MSD, $< R^2 >$, in function of the time, t, is given by the relation [129]:

$$< R^2 >= 6Dt \tag{3.4}$$

where D is the ions self-diffusion coefficient.

If we suppose, then, that the system is placed from the bulk state to an, ideal, 1D space, their MSD become [129]:

$$< R^2 >= 2Dt \tag{3.5}$$

So the reduction of dimensionality could explain an enhance of the dynamics by a factor three. However the CNT diameter is not small enough to produce a single file of ions, so, in the considered sample, we can estimate that the factor due the dimension reduction has to be less than three.

In addition to these geometrical considerations, we have to consider the presence of a possible reduction of the self-organisation, due to the extremely small dimension of the pores and, the (secondary) surface effects between the graphene and ions which could contribute to the diffusion enhancement.

From this first approach we can conclude that an acceleration of the dynamics is observed in the case of the IL confined inside the CNTs based membranes. However several measures, combining different techniques, like WAXS and DSC, are required to make light on the different possible origins of this phenomenon.

Conclusions and perspectives

This PhD thesis is a contribution to a global worldwide effort to improve the performances of electrochemical systems so they can become competitive alternatives to fossil fuels in the field of transportation systems. While one can note constant progress for decades, improvements of batteries are of incremental nature with regular gains of few percents on all the elements of the battery (electrolyte, electrode...). To complement these important but classical technological and applied research efforts, we have proposed a Basic Science approach with, in particular, the ambition to significantly improve the instant power of batteries. The idea is the use of one dimensional nanometric confinement to boost the transport properties of the electrolyte.

Because of their electrochemical and physical/chemical stability they have been identified as promising electrolytes, we have focused our efforts on a particular class of electrolytes: Ionic Liquids (ILs). The competition between electrostatic and Van der Waals interactions of the charged and a-polar alkyl side-chain(s) moieties of their cations drive a specificity of (ILs): a nanometric structuration. This rather original feature for a pure liquid, induces strong density fluctuations within the liquid with detrimental consequences on the viscosity and hence the ionic conductivity. So, despite their stability, this spontaneous nanometric self-assembly property is a severe drawback to the use of IL as electrolytes. We identify confinement as a way to circumvent the nanostructuration and hence turn the IL to a homogeneous liquid (with no density fluctuation) showing improved transport properties. The IL nanostructuration is evidenced by a so-called pre-peak on the diffraction structure factor in the [0.1 $Å^{-1}$-0.5 $Å^{-1}$] range. For the class of imidazolium IL, the intensity and position of this pre-peak are controlled by the length of their alkyl side-chains. As it shows a pronounced pre-peak, for us a good observable to quantify the influence of the confinement, we have focused a significant part of this work on the study of a cation with a rather long (8 carbons) side-chain: OMIM-BF_4 (octyl-3-methylimidazolium). For reference, an analogue with a shorter chain (4 carbons) has also been investigated: BMIM-TFSI (1-butyl-3-methylimidazolium bis(trifluoromethanesulfonyl)imide).

To maximize the transport properties and hence the ionic conduction in be-

tween the electrodes of a battery, the tortuosity of the confining material should be minimized. We have confined ILs in two distinct porous systems: *i)* porous alumina then *ii)* carbon nanotube membranes. These materials share a topological common ground: the macroscopic orientation of their cylindrical pore network but show complementary physico-chemical properties: AAO are hydrophilic while CNT are hydrophobic. Nanometric confinement over macroscopic distances (the spacing in between the electrodes is of the order of a micrometer) implies dealing with characteristic sizes different by orders of magnitude. We have therefore naturally developed a spatial and temporal multi-scale approach of the IL dynamics.

For clarity, in the lines below, we summarize in separate sections the main developments and related conclusion of the three parts of this manuscript.

Ionic Liquids in bulk: Owing to the large incoherent neutron cross-section of the ^{1}H nucleus and the abundance of this element in IL, incoherent Quasi-Elastic Neutron Scattering (QENS) measurements are able to give a global view of the IL dynamics as sensed via the averaged individual motions of its hydrogen atoms. The sample is probed on a local scale (few Å) so that, in a case of a complex molecules (with side-chains) in solution, the dynamical structure factor, S(Q,ω), is an average of the dynamics (both correlation times and geometry of the movements (EISF)) of the different side-chains along with the translational global motion (center of mass) of the whole molecule. A long range translational diffusion coefficient D_{lr} is associated with this contribution. To describe the specific case of the IL, we add to this classical description a contribution to take into account the transient localization within nanometric aggregates. We associate to this contribution, D_{loc}, a local diffusion coefficient within the aggregate. We have probed, by QENS (time-of-flight and neutron spin-echo), the cation dynamics of two imidazolium based Ionic Liquids, BMIM-TFSI and OMIM-BF_4. We have introduced a new physical appealing model taking all the dynamical contributions above and have taken advantage of specific deuteration of the side chains to show that the modelization is robust enough to describe the QENS data over an unprecedented extended Q ([0.15 Å^{-1} - 2.5 Å^{-1}]) and time ([0.5 ps - 2000 ps]) ranges.

• Diffusion within the aggregates: the Q dependence of the correlation times associated with the diffusion within the aggregate (D_{loc}) shows a plateau at small Q (Fig. 1.30 and 1.35). This behaviour is characteristic of a diffusion in a confined volume. Within the Gaussian model proposed by Volino, we extract the characteristic size of an aggregate: it is of the order of 20 Å. Interestingly, this size is comparable to the correlation length deduced from the position of the pre-peak ($2.\pi/0.3 = 21$ Å).

• Long range diffusion: we introduce the contributions of the local diffusion and of the side chains easily measured by time-of-flight in the ps time-scale, in the NSE data to extract D_{lr} the long range translational diffusion coefficient of the center of mass of the IL cation. We show that the NSE correlation times associated with D_{lr} obeys the so-called $D.Q^2$ law (Fig. 1.33 and 1.36). This is a strong evidence that D_{lr} is related to a genuine translational long range motion.
As they are single component liquids, the density fluctuations within the system remain extremely weak so that, due to the absence of contrast, the direct experimental assessment of the nanometric structuration by small angle scattering techniques (neutron or X-ray) is impossible. In a somehow unexpected way since they are rather indirect methods to determine structures, we show that, through dynamical quantities resulting from Quasi-Elastic Neutron Scattering (QENS) experiments, we are able to evidence the nanometric organization of the system (the characteristic size associated to D_{loc} and D_{lr}).

As it rules the electrical transport properties (through the Nernst-Einstein relation), the long range translational diffusivity of IL is a key quantity to settle the hot debate between the groups of Israelachvili [130] and Perkin [131] about the exact nature of (ILs): despite the average strong concentration of charges, does massive ion-pairing within neutral nanometric aggregates makes IL weakly dissociated electrolytes or instead are they strongly dissociated solutions? In our view, the aggregates that we characterize should be neutral (otherwise what is the mechanism of formation of the aggregate?). Therefore the concentration of free charges (disassociated anion+cation) in the liquid should be low. We nevertheless think that, at the present stage, a key question remains: are the charges placed in the interior of an aggregate or at its surface? It seems to us that only MD simulations can settle the debate.

IL under AAO confinement: Since their pores diameter can be finely customized in the 700 nm to 10 nm range, our strategy has been to confine $OMIMBF_4$ in porous AAO membranes. A goal of this thesis was, on decreasing the pore diameter, to expect to detect a shallow transition where the prepeak would vanish and therefore *i)* to be able to estimate the characteristic size of the nanometric domains so as *ii)* to undertake a full characterization of the confined "de-segregated" $OMIMBF_4$ transport properties. It turns out that even on confinement within AAO with the smallest pores available for this work (25 nm), the prepeak is still detected by diffraction (Fig. 2.18), meaning that the nanostructuration is not frustrated. Nevertheless AAO confinement seems to affect the biphasic behaviour of ionic liquids: WAXS data suggest a better organization within the domains (narrowing of the prepeak) and a slight increase of their size (shift of the prepeak to smaller Q) (Fig. 2.20).

Compared to the bulk situation, DSC detects an additive glass transition (Fig. 2.12) and an additive peak is detected by diffraction (Fig. 2.18). We interpret these observations, as a strong interactions of a fraction of the confined IL with the AAO pores walls. We note indeed, that such surface effects are rather usual when dealing with material under confinement.
The model developed to assess the IL local dynamics in bulk, is also able to describe the dynamics under AAO confinement. We nevertheless detect no significant influence of confinement on the IL dynamics.
At this point, we need to stress a strong caveat that moderates the conclusion above: the IL imbibition within AAO membranes has shown an unexpected behaviour. While the confinement of the IL is possible, the confined state seems to be metastable: if IL in excess at the AAO membrane surface is wiped out, after few hours, a significant fraction (30% after few hours) of the IL is expelled from the AAO matrix. Even if a full study of this phenomenon is beyond of the scope of this thesis, this suggest interesting surface tensions issues of the alumina+IL systems. We suspect that the very low vapour pressure of the IL could play an important role in this phenomenon. We have used NMR tomography to finely quantify and propose an experimental solution (Teflon lining of the AAO surface) to prevent this detrimental effect (Fig. 2.30). The fact that this tomography work has come in a late stage of this work explains why the core of the study on AAO confinement has been conducted despite this problem of IL desegregates from the AAO pores.

Confinement of IL within CNT membrane: A confinement effect is effective when the size of confinement is smaller than the characteristic fluctuations of the system in bulk. The ultimate goal when dealing with confinement is indeed to observe *pure volume* effect. Unfortunately, as in this work with AAO confinement, most of the confining materials induce detrimental *surface effects*. Among different interesting properties, CNTs are appealing systems because of the graphenic structure of their pores strongly limits interactions with the confined materials. This study of IL confinement within CNT membranes is still preliminary, but seems promising. Again, no strong dynamical effects of confinement have been detected at the molecular scale (ps-ns) both for the radial and longitudinal dynamics. Beyond statistics issue of the QENS experiments of this sample, a possible explanation is the too light confinement effect: the CNT internal diameter (4 nm) is probably still too large to induce a strong influence at the molecular scale. But we have been able to show that at the microscopic (PFG-NMR), Fig. 3.10, and macroscopic scales (impedance spectroscopy), Fig.3.9, we can obtain the effect that we have been seeking in developing this research program: a noticeable enhancement (by a factor 3) of the transport properties in a 1D situation. A patent has been

filed in March 2015 on the use of CNT membranes as a possible solution to boost the transport properties and hence the specific power of lithium batteries.

Perspectives: At the end of this study, we can identify interesting perspectives at both the fundamental and technological levels.

During this PhD, next to the QENS experiments, we have probed the IL, on the mesoscopic (μm and μs) scale, by Pulsed Field Gradient NMR (PFG-NMR). We have noted that the QENS and NMR long range diffusion coefficient measured by the two techniques are one (or more) order of magnitude different. Such a discrepancy between QENS and NMR data is rather classical when dealing with systems under confinement showing a strong tortuosity. It is easily understood if one consider the very different characteristic lengths probed by the two techniques: at the local scale and short time probed by QENS, a confined particle can still have to diffuse before being influenced by the confining volume, while at the larger scale and time probed by PFG-NMR the tortuous structure of the confining material can impose a labyrinthic trajectory resulting in a very low apparent diffusion coefficient. In the case of the IL, we can suspect that the presence of the transient aggregates plays a similar role as a porous structure for a ionic liquid molecule not yet trapped in an aggregate. NMR relaxometry would probably be a very relevant tool to bridge the QENS and NMR data in bulk. Moreover, as it is a perfect way to probe wetting properties, this techniques should be very instructive to assess the interaction of ionic liquids with the pores walls in the confinement situation.

At the technological level, for relevance to the field of battery systems, it now seems crucial to develop a specific study on CNT membrane confinement of IL charged with lithium salts. Such systems have been well characterized in bulk, but the aspect of confinement is still an opened subject. It will be also important to synthesize CNT forests with narrow pores (1-2 nm in diameter). Working with such narrow pipes seems important to strongly enhance the transport properties: it would also ensure that the gain of 3 obtained so far is more than a directionality effect (1D vs 3D diffusion). The fact that CNT are good electronic conductors could limit the relevance of CNT membranes as battery separators. As such a modification would strongly modify the CNT carbon atoms electronic hybridation, this limitation could be lifted by chemical polymer grafting of the CNT external walls.

Appendix A

The neutron scattering theory (from [1, 2])

A.1 Fundamental quantities in a scattering experiment

Neutron scattering is a central technique to study the condensed matter properties.

Due to the wave-particle duality we can associate to neutrons typical wave quantities such as the wave length λ, the wave vector $\mathbf{k}$ and the frequency ω which are linked by the equation:

$$E = \frac{p^2}{2m} = \frac{\hbar^2 k^2}{2m} = \frac{h^2}{2m\lambda^2} = \hbar\omega \tag{A.1}$$

where p, E and m are respectively the momentum, the kinetic energy and the mass of the neutron, while $\hbar$ is the Planck reduced constant.

The kinetic energies accessible in a neutron source are included between few meV and hundreds of meV, which is the typical intra-molecular energy range of the excitation in the condensed matter phase. This makes neutrons very good candidates for probing the dynamical properties of the condensed systems. Furthermore for these energy values, the associated wavelengths are of few Å (eq.A.1), i.e. they are of the same order as the intermolecular distances. The neutrons are able to analyse also the static properties of the condensed matter. To take some examples, for the study of the vibrational properties of the solid matter neutrons thermalised at 300 K ar generally used, which have an energy of 25 meV and a wave length of 1.8 Å. On the other hand to probe the atomic translational and rotational motions cold neutrons (T $\approx$ 25 K) with a kinetic energy of around 2 meV and a wavelength of 4.7 Å are utilised.

When a neutron beam is sent on a sample these particles interact with it nuclei

and magnetic momentums. Due to this interaction, which has a very short range ($\approx$ 1-10 fm [2]), the neutrons scatter isotropically in space. The scattering process is characterised by a parameter called *scattering length* (b). This is typically a complex quantity, where it imaginary part represents the neutron absorption by the sample which is a function of the incident particle velocity. Usually, in a neutron experiment, the latter is negligible so the scattering length is a real quantity, which depends on the nuclear and isotopic nature of the atoms and on the coupling of the nucleus and the neutron spin [1]. For a specific chemical element, marked by the index i, we can define the coherent, b_{coh}, and incoherent, b_{inc}, scattering length as:

$$b_{coh} = \overline{b_i} \tag{A.2}$$

$$b_{inc} = \sqrt{\overline{b_i^2} - \overline{b_i}^2} \tag{A.3}$$

where the over line represents the average on the spin state and the isotope natural abundance. We can then introduce the relative scattering cross sections:

$$\sigma_{coh} = 4\pi\overline{b_i}^2 \tag{A.4}$$

$$\sigma_{inc} = 4\pi(\overline{b_i^2} - \overline{b_i}^2) \tag{A.5}$$

The origin of the two scattering phenomenons is different. The coherent cross section represents the average nucleus population and spin state of the sample seen by the neutron so this scattering is related to the mean properties of the systems. On the other hand the incoherent cross section is the variance from this mean value and it is the effect generated by the nuclear and spin disorder in the system. The scattering length are empirical and measured quantities, so the relative scattering cross section are tabulated (see table A.1).

A neutron scattering experiment consists in sending a neutron beam on the sample and analysing the energy and momentum transfer occurring in the beam probe after its interaction with the system. Each particle arrives on the sample with a given wave vector $\mathbf{k}_i$ and kinetic energy E_i and after its interaction it scatters in a precise direction acquiring an energy E_f and a wave vector $\mathbf{k}_f$. We define as scattering angle 2θ the angle between $\mathbf{k}_f$ and $\mathbf{k}_i$ (see Fig. A.1).

Owing to the energy and momentum conservation we can write the following equations:

$$\mathbf{Q} = \mathbf{k}_i - \mathbf{k}_f \tag{A.6}$$

$$\hbar\omega = E_i - E_f \tag{A.7}$$

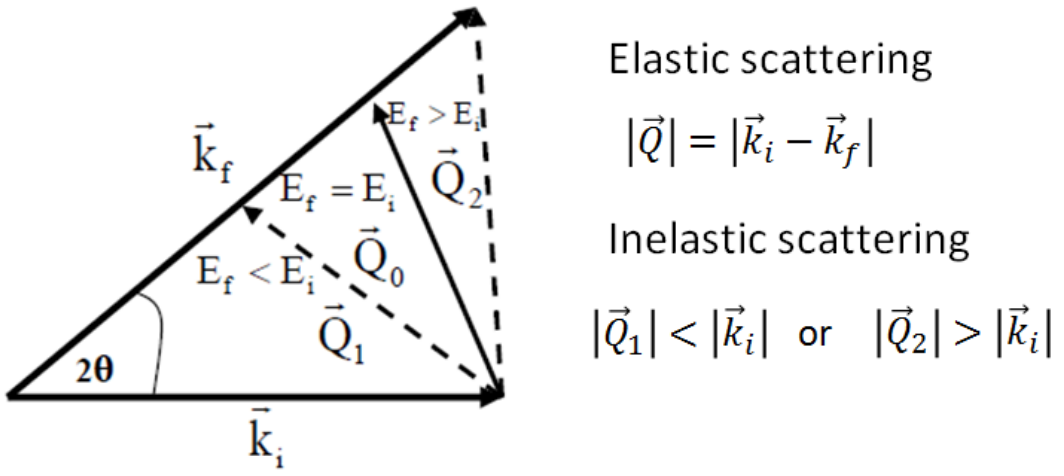

Figure A.1: Sketch of fundamental quantities in a neutron scattering measurement. The wave vector before the scattering event, $\vec{k}_i$, and that one after the scattering event, $\vec{k}_f$, are separated by the angle 2θ called *Scattering angle*. The difference of the two vector is defined as $\vec{Q}$ (eq. A.6). In this figure are represented also the case of elastic scattering (no energy transfer) and inelastic scattering. This figure was adapted by the reference [72].

where $\mathbf{Q}$ is the neutron scattering wave vector while $\hbar\omega$ is the energy gained (or lost) by the neutron in the scattering event.

Experimentally we measure the sample *differential cross section* $d^2\sigma/\mathrm{d}\Omega\mathrm{dE}$, i.e. the number of neutron detected for unity of solid angle $d\Omega$ and for unity of energy dE. Using a quantum approach we express this quantity as [2]:

$$\frac{d^2\sigma}{d\Omega dE} = \frac{k_f}{k_i}\frac{1}{2\pi\hbar}\sum_{jl}^{N}\langle b_j b_l\rangle \int_{-\infty}^{+\infty}\langle e^{-i\mathbf{Q}\cdot\mathbf{R_l}(0)}e^{i\mathbf{Q}\cdot\mathbf{R_j}(t)}\rangle e^{-i\omega t}dt \tag{A.8}$$

where N is the number of scatters, $\mathbf{R_l}\,(0)$ the position of the l^{th} atom at t= 0, $\mathbf{R_j}\,(t)$ the position of the j^{th} atom at the generic instant t and b_l (b_j) is the scattering lengths of the $\mathrm{l(j)}^{th}$ atom.

From the previous equation we can define the quantity called *Intermediate Scattering Function* $I\,(\mathbf{Q},t)$ as:

$$I\,(\mathbf{Q},t) = \frac{1}{N}\sum_{lj}^{N}\langle e^{-i\mathbf{Q}\cdot\mathbf{R_l}(0)}e^{i\mathbf{Q}\cdot\mathbf{R_j}(t)}\rangle \tag{A.9}$$

In the equation A.8 the development of the term $\langle b_j b_l\rangle$ allows to explicit the

differential cross section in two terms:

$$\begin{aligned}\frac{d^2\sigma}{d\Omega dE} &= \frac{k_f}{k_i}\frac{1}{2\pi\hbar}\frac{1}{4\pi}\sigma_{inc}\sum_j^N\int_{-\infty}^{+\infty}\langle e^{-i\mathbf{Q}\cdot\mathbf{R_j}(0)}e^{i\mathbf{Q}\cdot\mathbf{R_j}(t)}\rangle e^{-i\omega t}dt \\ &+ \frac{k_f}{k_i}\frac{1}{2\pi\hbar}\frac{1}{4\pi}\sigma_{coh}\sum_{lj}^N\int_{-\infty}^{+\infty}\langle e^{-i\mathbf{Q}\cdot\mathbf{R_l}(0)}e^{i\mathbf{Q}\cdot\mathbf{R_j}(t)}\rangle e^{-i\omega t}dt \\ &= \frac{k_f}{k_i}\frac{1}{2\pi\hbar}\frac{1}{4\pi}\sigma_{inc}I_{inc}\left(\mathbf{Q},t\right) + \frac{k_f}{k_i}\frac{1}{2\pi\hbar}\frac{1}{4\pi}\sigma_{coh}I_{coh}\left(\mathbf{Q},t\right) \end{aligned} \tag{A.10}$$

where $I_{inc}\left(\mathbf{Q},t\right)$ is the incoherent part of the intermediate scattering function:

$$I_{inc}\left(\mathbf{Q},t\right) = \frac{1}{N}\sum_j^N\langle e^{-i\mathbf{Q}\cdot\mathbf{R_j}(0)}e^{i\mathbf{Q}\cdot\mathbf{R_j}(t)}\rangle \tag{A.11}$$

We can then define the *dynamical structure factor* as the Fourier transform in time of the intermediate scattering function:

$$S\left(\mathbf{Q},\omega\right) = \frac{1}{2\pi\hbar}\int_{-\infty}^{+\infty} I\left(\mathbf{Q},t\right)e^{-i\omega t}dt \tag{A.12}$$

$$S_{inc}\left(\mathbf{Q},\omega\right) = \frac{1}{2\pi\hbar}\int_{-\infty}^{+\infty} I_{inc}\left(\mathbf{Q},t\right)e^{-i\omega t}dt \tag{A.13}$$

So we can rewrite the equation A.10 as:

$$\begin{aligned}\frac{d^2\sigma}{d\Omega dE} &= \frac{k_f}{k_i}\frac{1}{2\pi\hbar}\frac{1}{4\pi}\left(\sigma_{inc}S_{inc}\left(\mathbf{Q},\omega\right) + \sigma_{coh}S\left(\mathbf{Q},\omega\right)\right) \\ &= \left(\frac{d^2\sigma}{d\Omega dE}\right)_{incoh} + \left(\frac{d^2\sigma}{d\Omega dE}\right)_{coh}\end{aligned} \tag{A.14}$$

The coherent and incoherent dynamical structure factors give different information about the dynamics occurring inside the sample as it will be shown in the section A.2. The first difference between these two functions is their integral in energy:

$$\int_{-\infty}^{+\infty} S_{inc}\left(\mathbf{Q},\omega\right)_{inc}d\omega = 1 \tag{A.15}$$

$$\int_{-\infty}^{+\infty} S\left(\mathbf{Q},\omega\right)d\omega = S\left(\mathbf{Q}\right) \tag{A.16}$$

Form the relation A.16 we can observe that the integral in energy of the coherent dynamical structure factor is equal to the statical structure factor, so it is related to the structural correlation of sample (Bragg peaks etc.). On the other hand we can notice from the equation A.15 that the integral in energy of the incoherent part has no dependences by **Q**. For this reason the incoherent scattering contribution is considered as a flat noise in a diffraction experiment, as it can't give any information about the structure properties of sample. However we will show in this appendix how this quantity is rich of information concerning the sample dynamics.

A.2 Van Hove formalism

As we mentioned previously the dynamical structure factor is linked to the sample properties. The goal of this section is to demonstrate how this function is related to sample microscopic features.

Let's consider a systems of N particles. We can define the *microscopic density of particle* $\rho(\mathbf{r},t)$ which can be written as:

$$\rho(\mathbf{r},t) = \sum_{j}^{N} \delta\left(\mathbf{r} - \mathbf{R_j}(t)\right) \tag{A.17}$$

where $\mathbf{R}_j(t)$ is the position of jth particle at the instant t.

This quantity has the specific property that its integral over the system volume is equal to the total number of particles:

$$\int \rho(\mathbf{r},t)d\mathbf{r} = N \tag{A.18}$$

Given then a particle P which is in the position $\mathbf{r} = 0$ at the instant t=0, we can define the function G$(\mathbf{r},t)$ which represents the probability to find a particle P_1 in the position $\mathbf{r}$ at the instant t. This will be given by the correlation function of the particle density [132]:

$$\begin{aligned} G\left(\mathbf{r},t\right) &= \langle \frac{1}{N} \int \rho\left(\mathbf{r^I}+\mathbf{r},t\right)\rho\left(\mathbf{r^I},0\right)d\mathbf{r^I}\rangle \\ &= \langle \frac{1}{N} \int \sum_{jl}^{N} \delta\left(\mathbf{r^I}+\mathbf{r}-\mathbf{R_j}(t)\right)\delta\left(\mathbf{r^I}-\mathbf{R_l}(0)\right)d\mathbf{r^I}\rangle \end{aligned} \tag{A.19}$$

where $\langle ... \rangle$ represents the thermal average.

If now we perform the spatial FT of the correlation function, we obtain:

$$TF(G(\mathbf{r},t)) = \int G(\mathbf{r},t)\, e^{-i\mathbf{Q}\cdot\mathbf{r}} d\mathbf{r}$$
$$= \frac{1}{N}\sum_{j}^{N} \langle e^{-i\mathbf{Q}\cdot\mathbf{R_j}(0)} e^{i\mathbf{Q}\cdot\mathbf{R_j}(t)} \rangle = I(\mathbf{Q},t) \tag{A.20}$$

Then from the relations A.12 and A.13 we can conclude:

$$S(\mathbf{Q},\omega) = \frac{1}{2\pi}\int G(\mathbf{r},t)\, e^{-i(\omega t - \mathbf{Q}\cdot\mathbf{r})} d\mathbf{r} dt \tag{A.21}$$

So from this last equation we understand that the dynamical structure factor is deeply related to the microscopical properties of the sample, as it represents the spectrum of the spontaneous fluctuations of the system density.

Furthermore we can demonstrate that the incoherent and coherent parts of this function are linked to specific kind of dynamics.

If we return to relation A.19, we can then separate the sum in two terms:

$$G(\mathbf{r},t) = \langle \frac{1}{N}\int \sum_{j}^{N} \delta\left(\mathbf{r^I} + \mathbf{r} - \mathbf{R_j}(t)\right) \delta\left(\mathbf{r^I} - \mathbf{R_j}(0)\right) d\mathbf{r^I} \rangle$$
$$+ \langle \frac{1}{N}\int \sum_{j\neq l}^{N} \delta\left(\mathbf{r^I} + \mathbf{r} - \mathbf{R_j}(t)\right) \delta\left(\mathbf{r^I} - \mathbf{R_l}(0)\right) d\mathbf{r^I} \rangle$$
$$= G_s(\mathbf{r},t) + G_d(\mathbf{r},t) \tag{A.22}$$

where $G_s(\mathbf{r},t)$ is the "self" part (sum with $j = l$). Provided a particle P placed at the position $\mathbf{r} = 0$ at $t = 0$, $G_s(\mathbf{r},t)$ gives the probability to find the particle P in the position $\mathbf{r}$ at the instant t (autocorrelation function). On other hand the second term is the "distinct" part (sum with $j \neq l$) that represents the probability to find a particle $P_1 \neq P$ in that position and time.

So, from equation A.21, we can conclude that:

$$S(\mathbf{Q},\omega) = \frac{1}{2\pi}\int G(\mathbf{r},t)\, e^{-i(\omega t - \mathbf{Q}\cdot\mathbf{r})} d\mathbf{r} dt \tag{A.23}$$
$$S_{inc}(\mathbf{Q},\omega) = \frac{1}{2\pi}\int G_s(\mathbf{r},t)\, e^{-i(\omega t - \mathbf{Q}\cdot\mathbf{r})} d\mathbf{r} dt \tag{A.24}$$

The coherent dynamic structure factor is linked to the distinct and self part of the correlation function. So we can obtain information about the collective

dynamics of the system (e.g. phonon dynamics). This is confirmed by the integral of the coherent dynamics structure factor:

$$S(\mathbf{Q}) = \int_{-\infty}^{+\infty} S(\mathbf{Q}, \omega)\, d\omega = G(\mathbf{r}, t = 0) \tag{A.25}$$

On the other hand the incoherent part is linked only to the self-part of the correlation function, so it gives on information about the individual dynamics of the particle and it isn't able to give information about the structure the systems.

The two kinds of scattering are simultaneously observed during an experiment. As we can observe from the equation A.10, each term is weighted by the coherent and incoherent cross sections of the element of the system. So the measured contribution of each kind of scattering strongly depends on the chemical element in the sample. To take an example we show the different coherent and incoherent cross section of the chemical elements contained in the sample studied in this work.

Element	σ_{coh} (barn)	σ_{inc} (barn)
H	1.76	80.27
D	5.59	2.05
B	3.55	1.70
C	5.55	0.001
N	11.01	0.50
O	4.23	0.00
F	4.02	0.00
Al	1.50	0.01
S	1.02	0.001

Table A.1: Neutron coherent and incoherent scattering cross section (1 barn= 10^{-24} cm^2) of the elements present in the samples studied in this work. [44]

A.3 Single particle dynamics probed by incoherent quasi-elastic scattering

From the previous section we have demonstrated that the incoherent scattering is related to the single particle motion. The interpretation of this phenomenon is based on two hypothesis: i) the decoupling of the atomic and molecular modes in function of the energy transfer ii) the classic approximation for the energy and momentum transfer, i.e. $\hbar\omega \ll \frac{1}{2}k_bT$ and $\frac{\hbar Q^2}{2m} \ll \frac{1}{2}k_bT$ where $\frac{1}{2}k_bT$ is thermal energy per degree of freedom of the scattering atom.

Considering the relative time scale of the atomic dynamical relaxation in the condensed matter (translation: 10^{-10}-10^{-9} s, rotation: 10^{-11}-10^{-12} s, vibration: 10^{-12}-10^{-13} s), it seems that the assumption i) is reasonable.

The information about the sample dynamics is contained in the energy distribution of the scattered neutron at a specific scattering angle. The dynamical excitation in the sample atoms are responsible for an energy transfer in the neutron beam. In particular, the translation and the rotation produce a quasi-elastic neutron signal (neutrons having a small energy transfer $\hbar\omega \leq 1$ meV), while the vibration produces an inelastic neutron intensity (neutrons having a big energy transfer $\hbar\omega > 1$ meV).

If we return to the definition of the incoherent intermediate scattering function and if we apply the decoupling modes approximation, we can factorize the contributions of the different atomic motions as:

$$\begin{aligned} I_{inc}(\mathbf{Q},t) &= \frac{1}{N}\sum_j \langle e^{i\mathbf{Q}\cdot\mathbf{R_j^{trans}}(t)} e^{-i\mathbf{Q}\cdot\mathbf{R_j^{trans}}(0)}\rangle \langle e^{i\mathbf{Q}\cdot\mathbf{R_j^{rot}}(t)} e^{-i\mathbf{Q}\cdot\mathbf{R_j^{rot}}(0)}\rangle \langle e^{i\mathbf{Q}\cdot\mathbf{R_j^{vibr}}(t)} e^{-i\mathbf{Q}\cdot\mathbf{R_j^{vibr}}(0)}\rangle \\ &= I_{inc}^{trans}(\mathbf{Q},t)\, I_{inc}^{rot}(\mathbf{Q},t)\, I_{inc}^{vibr}(\mathbf{Q},t) \end{aligned} \tag{A.26}$$

Following this factorization, for the convolution theorem, the incoherent dynamic structure factor becomes:

$$S_{inc}(\mathbf{Q},\omega) = S_{inc}^{trans}(\mathbf{Q},\omega) \otimes S_{inc}^{rot}(\mathbf{Q},\omega) \otimes S_{inc}^{vibr}(\mathbf{Q},\omega) \tag{A.27}$$

In the quasi-elastic zone the vibrational contribution is a Gaussian function of the wave vector [45], thus:

$$I_{inc}^{qel}(\mathbf{Q},t) = I_{inc}^{trans}(\mathbf{Q},t)\, I_{inc}^{rot}(\mathbf{Q},t)\, e^{-<u^2>Q^2/3} \tag{A.28}$$

$$S_{inc}^{qel}(\mathbf{Q},\omega) = \left[S_{inc}^{trans}(\mathbf{Q},\omega) \otimes S_{inc}^{rot}(\mathbf{Q},\omega)\right] e^{-<u^2>Q^2/3} \tag{A.29}$$

The factor $e^{-<u^2>Q^2/3}$ is called *Debye-Waller Factor* and the parameter u is the mean square displacement of the vibrational motion [1].

On the other hand the terms related to the rotational and translational excitations in the equations A.28 and A.29 are more complicated since they depend on Q and ω. We need a specific model for explaining them, which will be shown in the next section.

Concerning the classical approximation, this implies a uniform population of the sample energetic level. It is generally valid for high temperature. In this case the dynamical structure factor can be considered as a symmetric function $S(-\mathbf{Q},-\omega) = S(\mathbf{Q},\omega)$. At low temperature, on the other hand, the sample energetic levels are no more uniformly populated. The probability of a nenergy gain

for neutron is reduced owing to the low population of the scatter energy levels, so the symmetry in ω breaks. In this case the scattering function of the system could be approximated as the symmetric dynamic structure factor multiplied by the Boltzmann factor $e^{-\hbar\omega/k_bT}$ in order to satisfy the detailed balance principle [2,133].

A.4 Quasi-elastic neutron scattering analysis: model for the atomic motion

In this section we write some models to explain the term relative to translational and rotational motion in the equations A.28 and A.29.

Before presenting the model we introduce the concept of *Elastic Incoherent Structure Factor* (EISF), which will be used after in this part.

The self dynamics of the system atoms is defined by the van Hove correlation function, which at t=0 is:

$$G_s(\mathbf{r}, 0) = \delta(\mathbf{r}) \tag{A.30}$$

Let's suppose we are studying a system subjected to a perturbation a t=0. When it reaches it equilibrium state there is no correlation between the scatter position at t=0 and t=∞. We can write the self (or incoherent) intermediate scattering function as:

$$\begin{aligned} I_s(\mathbf{Q}, t=\infty) &= \langle e^{-i\mathbf{Q}\cdot\mathbf{r}(t=0)} e^{i\mathbf{Q}\cdot\mathbf{r}(t=\infty)} \rangle \\ &= \langle e^{-i\mathbf{Q}\cdot\mathbf{r}(t=0)} \rangle \langle e^{i\mathbf{Q}\cdot\mathbf{r}(t=\infty)} \rangle \\ &= \langle e^{-i\mathbf{Q}\cdot\mathbf{r}(t=\infty)} \rangle \langle e^{i\mathbf{Q}\cdot\mathbf{r}(t=\infty)} \rangle \\ &= |\langle e^{i\mathbf{Q}\cdot\mathbf{r}(t=\infty)} \rangle|^2 \\ &= \int G_s(\mathbf{r}, t=\infty)\, e^{i\mathbf{Q}\cdot\mathbf{r}} \end{aligned} \tag{A.31}$$

The quantity $I_s(\mathbf{Q}, t=\infty)$ is then the form factor of the space accessible to the atom during its dynamics. This depends strongly on the dynamics type of the scatter. For example for particles which can move freely in the space this quantity is $I_s(\mathbf{Q}, t=\infty)$ =1/V, which tends to zero for sufficiently large sample volume V.

By the equation A.31, we can write the scattering function as:

$$S_{inc}(\mathbf{Q}, \omega) = I_s(\mathbf{Q}, t=\infty)\, \delta(\omega) + S_{inc}^{qel}(\mathbf{Q}, \omega) \tag{A.32}$$

where $S_{inc}^{qel}(\mathbf{Q}, \omega)$ is the quasi-elastic intensity of the scattering function.

We define thus the EISF as the intensity of the elastic peak in the equation A.32, or, more precisely, owing to the property of the incoherent scattering function (eq.A.32), as the elastic fraction of the scattered intensity in the elastic and quasi-elastic way. So, for a precise Q values, we can measure the EISF as result of the ratio [45]:

$$EISF(Q) = \frac{I^{el}(Q)}{I^{el}(Q) + I^{qel}(Q)} \tag{A.33}$$

where $I^{el}(Q)$ and $I^{qel}(Q)$ are respectively the elastic and quasi-elastic intensity determined by a numerical fit of the neutron spectra. The comparison of the experimental quantity expressed in the equation A.33 with a theoretical EISF defined by a specific model allows to distinguish the geometrical properties of the atomic motion.

A.4.1 Translational motion model

A.4.1.1 Free diffusion model (Fick's law)

If we observe the particle diffusion at long range (i.e. at length and time scale much longer than the single particle atomic path), the van Hove function has to satisfy the Fick law which describes the macroscopic system diffusion due the concentration gradient. This latter can be written as:

$$\frac{\partial G_S(\mathbf{r}, t)}{\partial t} = D_t \nabla^2 G_S(\mathbf{r}, t) \tag{A.34}$$

where the D_t is the particle self-diffusion coefficient.

The solution of the differential equation A.34, using the boundary conditions $G_S(\mathbf{r}, 0) = \delta(\mathbf{r})$ and $G_S(\mathbf{r}, t = \infty) = 0$ is:

$$G_S(\mathbf{r}, t) = \frac{1}{(4\pi D_t t)^{\frac{3}{2}}} e^{\frac{r^2}{4D_t t}} \tag{A.35}$$

The relative intermediate scattering function and the dynamical structure factor are thus:

$$I_{inc}(\mathbf{Q}, t) = e^{-D_t Q^2 t} \tag{A.36}$$

$$S_{inc}(\mathbf{Q}, \omega) = \frac{1}{\pi} \frac{D_t Q^2}{(D_t Q^2)^2 + \omega^2} \tag{A.37}$$

So the incoherent dynamic structure factor is a Lorentzian function of the intensity 1 ($\int_{-\infty}^{+\infty} S_{inc}(\mathbf{Q}, \omega) d\omega = 1$) with Half Width at Half Maximum (HWHM) equal to $D_t Q^2$ (see Fig.A.2).

We can notice that in this case there is no elastic peak in the equation A.37. The particle can move freely inside the sample, so the form factor of the explored space of particle ($I_s(\mathbf{Q}, t = \infty)$) is zero.

A.4.1.2 Jump diffusion model

When we reduce the length and time scale, the particle diffusion is no more a continuous translational motion so the Fick law (eq.A.34) is no more valid. This is the case when we observe large wave vectors in a neutron scattering experiment. In such conditions we can distinguish the elementary step of the diffusion. The particle motion is constituted by elementary jumps spaced out by a waiting time τ_0.

In this model we can demonstrate that the dynamical structure factor which represents this motion is still a Lorentzian function:

$$S_{inc}(\mathbf{Q}, \omega) = \frac{1}{\pi} \frac{\Gamma(Q)}{\Gamma(Q)^2 + \omega^2} \tag{A.38}$$

where it HWHM is a function of the wave vector:

$$\Gamma(Q) = \frac{D_t Q^2}{1 + D_t Q^2 \tau_0} \tag{A.39}$$

An example of the plot of the Lorentzian HWHM versus Q is shown in figure A.2. We can notice that for small Q it follows the "$D_t Q^2$ law" as the free diffusion model (we are probing much longer lengths than the particle jump length), while for higher wave vector we observe that it moves away from the linear trend and it the tends to the asymptotic value equal to $1/\tau_0$.

As in the free diffusion case no elastic peak is observed because the particle can explore all the space.

A.4.2 Rotation motion models

A.4.2.1 Jump model between two equivalent sites

Let's consider a particle P which can jump on equivalent sites defined respectively by the position $\mathbf{r_1}$ and $\mathbf{r_2}$. The rate equations, which defines the particle motion in one specific site are:

$$\frac{dp_1(t)}{dt} = -\frac{1}{\tau} p_1(t) + \frac{1}{\tau} p_2(t) \tag{A.40}$$

$$\frac{dp_2(t)}{dt} = -\frac{1}{\tau} p_2(t) + \frac{1}{\tau} p_1(t) \tag{A.41}$$

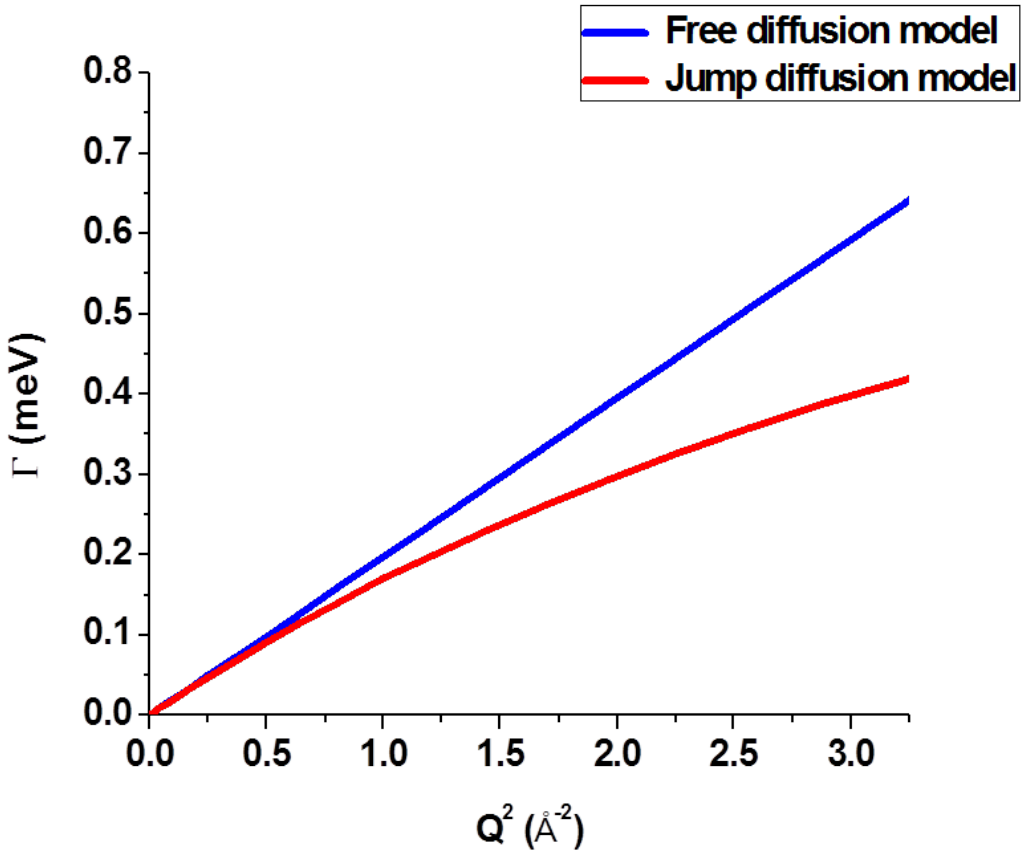

Figure A.2: Trend of HWHM of the Lorentzian scattering function versus Q^2 for the free diffusion model (D= 3 10^{-5} cm^2/s) in blue and for the jump diffusion model (D= 3 10^{-5} cm^2/s τ= 0.8 ps) in red.

where $p_1(t)$ ($p_2(t)$) is the probability that a particular atom is at site 1(2) at time t and τ is the time between the jumps.

The system of the equations A.40 and A.41 with the boundary conditions that $p_1(t=0)=1$ and $p_2(t=0)=0$, has as solutions:

$$p_1(t) = -\frac{1}{2}\left[1+e^{-\frac{2t}{\tau}}\right] \quad \text{(A.42)}$$

$$p_2(t) = -\frac{1}{2}\left[1-e^{-\frac{2t}{\tau}}\right] \quad \text{(A.43)}$$

If we suppose that the site 1 is the position $\mathbf{r}=0$, whereas the other is at $\mathbf{r}=\mathbf{R}$, the van Hove correlation function of the system is:

$$G_S(\mathbf{r},t) = p_1(t)\delta(\mathbf{r}) + p_2(t)\delta(\mathbf{r}-\mathbf{R}) \tag{A.44}$$

If we perform the spatial and temporal FT of the van Hove correlation function we obtain the following incoherent dynamic structure factor [1]:

$$S_{inc}(Q,\omega) = \frac{1}{2}\left(1 + j_0\left(QR\right)\right) + \frac{1}{2}\left(1 - j_0\left(QR\right)\right)\frac{1}{\pi}\frac{2\tau}{4+\omega^2\tau^2} \tag{A.45}$$

where $j_0\left(QR\right)$ is the spherical Bessel function of order 0.

In this case we can notice that the quasi-elastic contribution has a Lorentzian shape, but its HWHM is constant in Q and it is equal to $1/2\tau$.

Furthermore in this model the particle can not explore all space, but it is bounded to the two site. This confinement of the particle dynamics induces a elastic peak in the scattering function. Using the equation A.33 we can calculate the EISF in this model:

$$EISF_{2equivalentsites} = \frac{1}{2}\left(1 + j_0\left(QR\right)\right) \tag{A.46}$$

This is an oscillating function in Q with asymptotic value at 1/2 (see example in Fig.A.3).

A.4.2.2 Jump model between three equivalent sites

The model developed for a jump between two equivalent sites can be generalised for n sites [1].

In this case the rates equation becomes:

$$\frac{dp_j(t)}{dt} = -\frac{1}{\tau}p_j(t) + \frac{1}{\tau}\sum_{l\neq j} p_j(t) \tag{A.47}$$

For the case of three equivalent sites performing the same method shown in the previous part we obtain the incoherent scattering function:

$$S_{inc}(Q,\omega) = A_0(Q)\delta(\omega) + (1 - A_0(Q))\frac{1}{\pi}\frac{3\tau}{9+\omega^2\tau^2} \tag{A.48}$$

where $A_0(Q)$ is the EISF which is given by the relation:

$$A_0(Q) = \frac{1}{3}\left(1 + 2j_0\left(QR\sqrt{3}\right)\right) \tag{A.49}$$

So, also in this case, the incoherent scattering function is composed by a Lorentzian shape quasi-elastic components with a HWHM constant in Q (equal to $3/\tau$), and an EISF oscillating in Q with asymptotic value at 1/3 (see example on Fig.A.3).

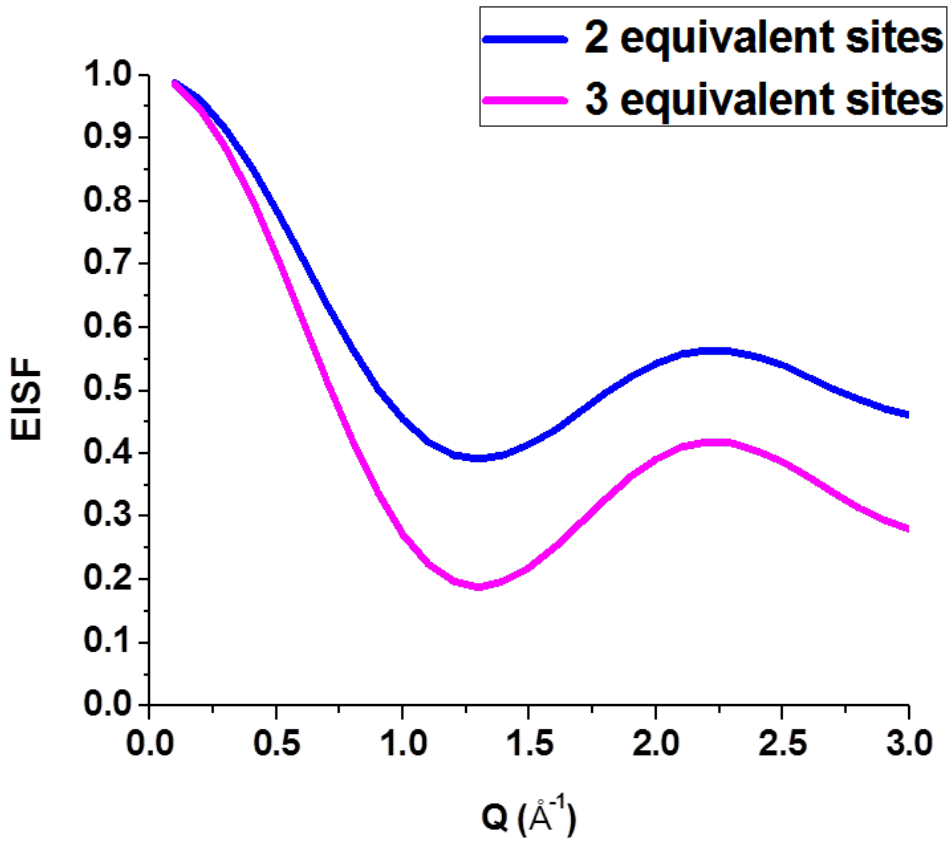

Figure A.3: Trend of the EISF versus Q for a jump model between two equivalent sites in blue and for a jump model between three equivalent sites in red.

Appendix B

Time of flight technique

B.1 ToF spectrometer

Time of Flight (ToF) is a classic technique for performing neutron quasi-elastic or inelastic experiments. It allows to measure the energy transfer range between 10-10^5 μeV, which corresponds to the time interval between 10^{-2}-10^2 ps. So it represents a very good technique for characterizing the dynamical modes occurring in the condensed matter systems.

The ToF spectroscopy measures the van Hove sample function in the Fourier space ($\mathbf{Q}$,ω), this means that, with this techniques, we observe the dynamic structure factor of the sample $S(\mathbf{Q}, \omega)$.

A ToF spectrometer can divided in two main parts: the primary spectrometer (placed before the sample) and the secondary spectrometer (placed after the sample). The technology composing these two parts changes according to the typology of spectrometer.

ToF spectrometers can be divided in two classes: **(i)** the direct geometry spectrometers and **(ii)** the indirect (inverted) geometry spectrometers.

The differences between the two typology are summarised in figure B.1.

In the direct geometry the incident beam is composed by a unique kinetic energy (or wavelength) selected by a crystal or a chopper, while the final kinetic energy is measured by the neutron time-of-flight.

On the contrary in the inverted geometry the sample is illuminated by a quasi white beam (i.e. containing several wavelengths). In this case the final energy is selected by Bragg diffraction where the initial one by the beam time of flight.

As in this thesis our ToF measurements were performed using direct geometry spectrometers, this appendix will focus only on this type of apparatus.

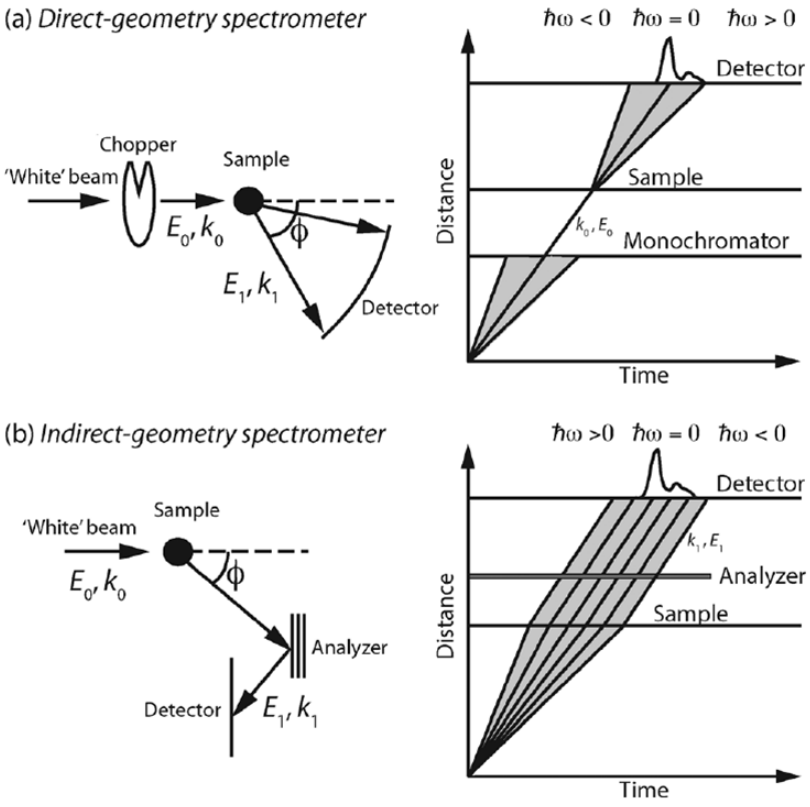

Figure B.1: Sketch of the direct (a) and indirected (b) geometry ToF spectrometers (after). together with the Distance-Time diagram for a single neutron pulse. This figure is taken by reference [134].

B.2 Direct geometry ToF spectrometer

In the direct geometry spectrometers the kinetic energy of incident neutron is fixed by a beam monochromatisation and the neutron final energy is measured by the time of flight of the scattered neutrons.

A schematic representation of a ToF spectrometer is shown in figure B.2.

The primary spectrometer produces a monochromatic beam. This can be realised by a set of 6 choppers (absorbing discs with a slit).

The explication of the monochromatisation process is represented in figure B.3.

The choppers are divided in three groups. In each couple the rotation sense of two disc is opposite in order to reduce the pulse duration and to improve the temporal resolution [136].

The incoming beam passes through a first group (pulsing choppers P), which

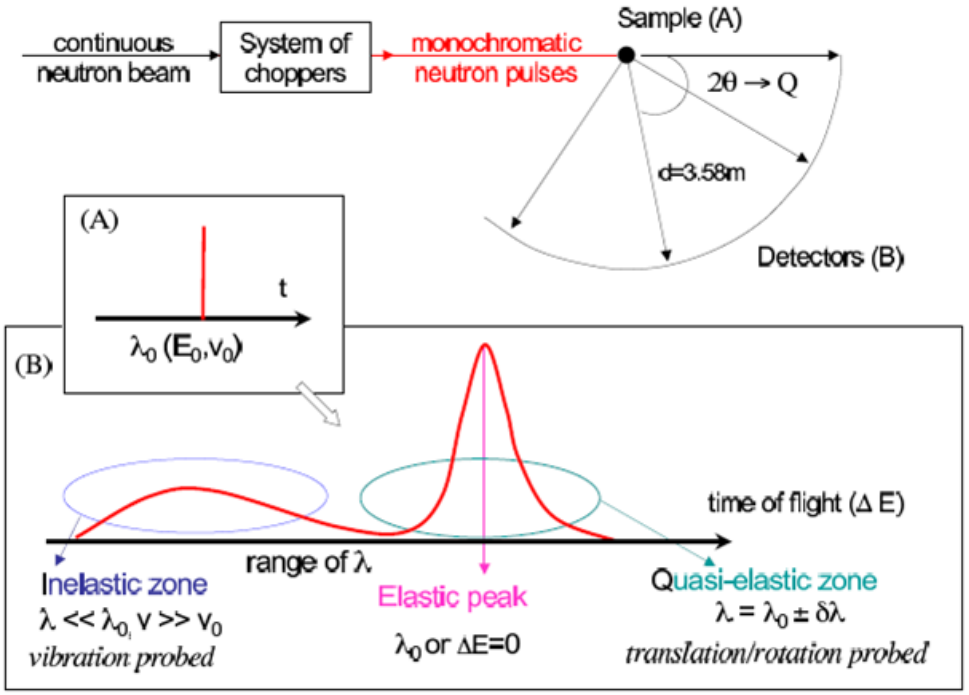

Figure B.2: Schematic representation of a direct geometry ToF spectrometer (after [135].). A monochromatic beam (A) is produced by the primary spectrometer (set of choppers) and sent to the sample. The scattered neutrons are detected simultaneously in a wide interval of scattering angle in the secondary spectrometer. Each detector measures the wavelength (or velocity) neutron dispersion in function of the time (B). By changing the probed energy transfer different sample dynamical modes are observed, passing from translational/rotational (small energy transfer) to vibrational ones (bigger energy transfer).

produces the pulses of short duration containing a Maxwellian distribution of wavelengths. The wavelength is selected by another choppers couple (monochromatisation choppers M), which is placed at a distance L_{PM}. The value of the wavelength is determined by the temporal phase difference between the P and M choppers.

Two successive pulses produced by the P choppers overlap during their path toward the spectrometer: the faster neutron of N+1 pulse lap the slower ones of the N pulse. In order to prevent this effect another couple of choppers (frame overlap choppers *FOCO*) is placed between the pulsing and the monochromatisation ones. These latter rotates with a slower rotation speed assuring a bigger separation between the pulses.

The ToF measurement consists in the counting of the scattered neutrons in

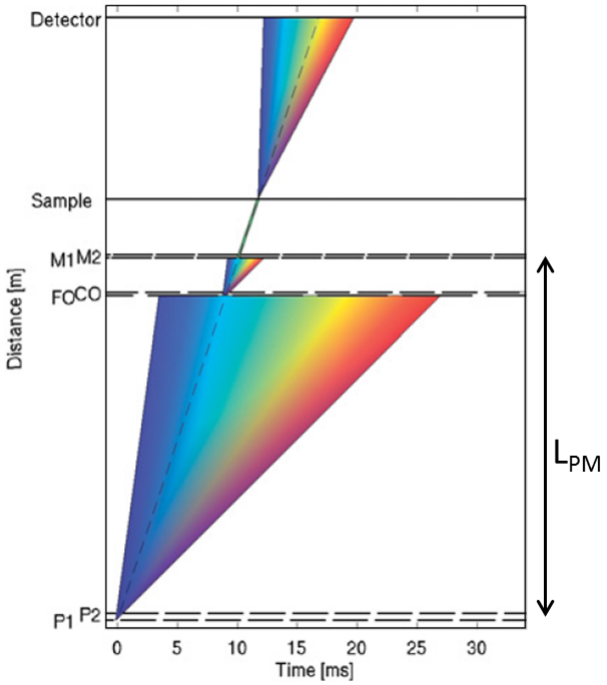

Figure B.3: Time-distance diagram (after [136]) showing the monochromatisation process occurring a direct geometry ToF spectrometer.

function of their scattering angles 2θ and the time of flight t_{ToF}.

The raw data can be converted in the (Q,ω) domain using the relations:

$$Q = \frac{4\pi}{\lambda_0} sin(\theta) \tag{B.1}$$

$$\hbar\omega = \frac{1}{2} m l^2 \left(\frac{-\Delta t_{tof}}{t_0^2 + t_0 \Delta t_{tof}} \right)^2 \tag{B.2}$$

where λ_0 is the wavelength on the incident beam, m the neutron mass, l the distance between the sample and the detectors, t_0 the time of flight of the elastically scattered neutrons and Δt_{tof} the time of flight difference between the quasi and elastically scattered neutron. Then combining the relations of the momentum and energy transfer (eq. A.6 and A.7) the following equation is obtained:

$$\frac{\hbar^2 Q^2}{2m} = 2E_i - \hbar\omega - 2cos(2\theta)\sqrt{E_i^2 - E_i \hbar\omega} \tag{B.3}$$

The signal detected at a given scattering angle 2θ corresponds to a cut in space (Q,ω) (see Fig. B.4).

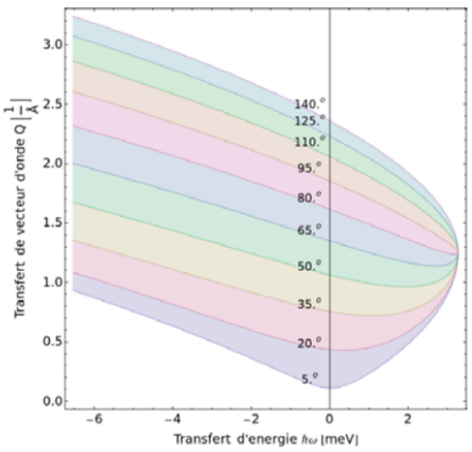

Figure B.4: (Q,ω) trajectories calculated for $\lambda_i = 5.2$ Å (after [136]).

In a rigorous data treatment the dynamic structure factor S(Q,ω) must be reconstructed from a series of cuts at constant Q of the surface S(Q,ω) [1].

The main factors which define the spectrometer energy resolution are: *(i)* the neutron wavelength and *(ii)* the degree of monochromaticity of the beam. Longer wavelengths are preferable for a ToF experiment as for longer wavelengths correspond lower energies that are more clearly dispersed in function of the time. Furthermore the other main factor influencing the spectrometer resolution is the beam monochromaticity, which is related to the incident pulse duration. To shorter pulses correspond narrower wavelength distributions, but, at the same time, this implies a weaker incident flux. This coupling between the resolution and the flux represents the biggest limitation of ToF technique, that is absent for the spin-echo spectroscopy (see appendix C).

The experimental resolution is generally determined by measuring the signal of a vanadium sample (incoherent scatter) at all the wavelengths used. The measured scattering function is sample the "real" S(Q,ω) (i.e. that measured by an instrument with an infinite resolution) convoluted by the experimental resolution. This means that for the data analysis, the used theoretical model is convoluted to the measured resolution before to be compared to the experimental data.

Appendix C

Neutron spin-echo spectroscopy (from [3])

The neutron spin-echo (NSE) spectroscopy was developed by Mezei in 1972 [137]. This technique represents a complementary tool for the study of the neutron quasielastic scattering. In fact this spectroscopy has an extreme small energy resolution ($\delta E_{NSE} \simeq 1\ neV$), which is three order of magnitude smaller than the back scattering (BS) spectroscopy one ($\delta E_{BS} \simeq 1\ \mu eV$). This allows to broaden the observed dynamical window in the time range between 0.01 and 10 nanosecond, that typically is not accessible with the classic neutron Time of Flight (ToF) based techniques.

This gain in resolution is possible because the scattering function is determined indirectly by measuring the scattered neutrons polarisation change after their interaction with the sample. This approach avoids, moreover, too strict constrains on the incident beam monochromatisation ($\frac{\Delta\lambda}{\lambda} \approx 15\%$), allowing to obtain an high incident flux.

Another particularity of NSE technique is that we measure directly the intermediate scattering function $I(\mathbf{Q}, t)$, which is the time Fourier transform of dynamic structure factor $S(\mathbf{Q}, \omega)$.

This chapter will be divide in five sections. In the first we will review briefly the fundamental laws of the spin dynamics in a magnetic field. In the second part we will illustrate the basic principle of the spin-echo and how we can observe this phenomenon with a NSE spectrometer. In the third section we will introduce the concept of polarisation of neutron beam and how this quantity influences the transmission of the scattered beam though a polariser. In the fourth we will show how we can determine the polarisation from a spin-echo measure, while in the last one we will explain the methods for extracting the sample intermediate scattering function from the polarisation in a quasielastic experiment.

C.1 The spin dynamics in a magnetic field

For understanding the basic principles of NSE technique, it is necessary to review briefly the fundamental equations which rule the dynamics of a spin a in magnetic field.

Let's start considering a neutron with mass m and spin **S** in a space occupied by a magnetic field **H**. The spin evolution in time is given by the equation:

$$\frac{d\mathbf{S}}{dt} = \gamma \mathbf{S} \times \mathbf{H} \tag{C.1}$$

where γ is the neutron gyromagnetic ratio ($\gamma \approx -2\pi\ 2916.4\ G^{-1}s^{-1}$). The torque caused by the magnetic field generates a spin precession around the **H** direction whose frequency is the Larmor one:

$$\omega_L = |\gamma| H \tag{C.2}$$

Therefore the spin will acquire a precession angle Φ, which will be linear to the time spent by the neutron in the space where $\mathbf{H} \neq \mathbf{0}$. This latter is equal to the ratio between the particle flight path l and it speed v. With these considerations, the precession angle will be given by the relation:

$$\Phi = \omega_L \frac{l}{v} = |\gamma| H \frac{l}{v} \tag{C.3}$$

We have to consider also the quantum nature of the particle. The neutron has a wavelength λ_0 which is linked to its kinetic energy by the equation:

$$\frac{1}{2} m v^2 = \frac{h^2}{2m\lambda_0} \tag{C.4}$$

where h is the Planck constant. Putting the equation C.4 into the C.3 one, we obtain finally the relation for the precession angle:

$$\Phi = \frac{|\gamma| \lambda_0 m}{h} H l \tag{C.5}$$

C.2 The spin-echo principle

With the introduction discussed in the previous section, we can explain what the spin-echo principle is and how we can observe it with a NSE spectrometer.

For the moment we consider an ideal instrument without any sample inside and with a monochromatic incident beam. We can find a sketch of NSE set up in Fig.C.1A.

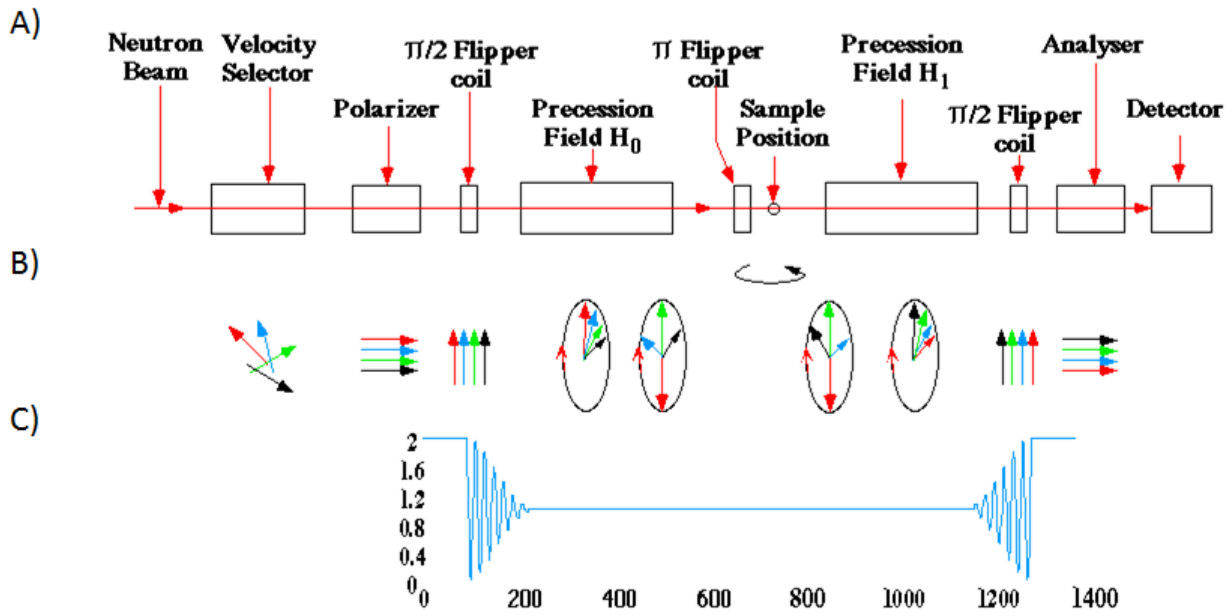

Figure C.1: A) Schematic sketch of NSE spectrometer. B) Neutrons spin state in the different part of apparatus (the different colors correspond to neutrons with different wavelength.) C) Spin polarisation at the different point of the apparatus (for more explanations see the section C.4). This picture was taken from the reference [49].

As we can observe from the Fig.C.1B, the neutrons have to pass a first preparation stage, where their spins are firstly polarised along the direction of their motion and successively rotated of 90° by a $\frac{\pi}{2}coil$. Then they pass through a first solenoid (called precession coil), where inside there is a magnetic field $\mathbf{H_0}$ parallel to the neutrons speed. This field generates a spin precession motion. Using the relation C.5, we can calculate the acquired precession angle Φ_1 for each neutron spin:

$$\Phi_1 = \frac{|\gamma|\lambda_0 m}{h} \int_{L_1} H_0 \, dz \tag{C.6}$$

where L_1 is the solenoid length and z is the neutron direction. At the exit of the coil, the beam is submitted to a spin rotation of 180° induced by π coil. After this the beam passes through a second precession coil, identical to the first one, where there is another magnetic field $\mathbf{H_1}$ parallel to $\mathbf{H_0}$. Because of the spin inversion by the π coil, in this arm the spins rotate in the opposite sense compared with the one in the first solenoid. The precession angle Φ_2 acquired in this arm is:

$$\Phi_2 = -\frac{|\gamma|\lambda_0 m}{h}\int_{L_2} H_1\, dz \tag{C.7}$$

where the minus in the relation C.7 takes into account the inverted spin rotation sense. So at the end of second coil the total precession angle acquired by every neutron is:

$$\Phi_{TOT} = \Phi_1 + \Phi_2 = \frac{|\gamma|\lambda_0 m}{h}(\int_{L_1} H_0\, dz - \int_{L_2} H_1\, dz) \tag{C.8}$$

After that the beam passes through another $\frac{\pi}{2}$*coil*, which induces another spin rotation of 90°, and thought a polariser, called analyser. The latter lets through only those neutrons with a spin state parallel to their speed. Finally a detector counts the neutrons which have survived to the analyser selection.

We can note that in order to have a signal different to zero, the total precession angle acquired by each neutron has to be null. In this way the spins have the same turns number (in inverse sense) in the two arms and the neutrons arrive to the analyser without modifying their initial spin polarisation. This condition is called *spin-echo point* (see Fig.C.1.C). Using the relation C.8, we can observe this condition is verified only if the two field integrals are equal. This means, being the two coils identical, the field has to be the same in two solenoids.

The spin-echo principle is the base for understanding the NSE experiments. In order to explain how we can obtain information about the sample, we now have to talk about the beam polarisation and it influence on the analyser neutrons counting.

C.3 The transmission of a analyser

From the section C.2, we have seen that the analyser plays a very important role in a NSE spectrometer. This element lets through the neutrons with a determinate spin state only, changing therefore the intensity of the scattered beam seen by the detector.

It is essential now to quantify the transmission of the analyser in function of a generic spin state and to understand how it changes in relation to the beam polarization.

In this case we are obliged to develop our considerations using a quanto-mechanical approach. It is well known that the neutron is a particle with spin S equal to $\frac{1}{2}$. Considering a specific direction, the neutron spin could have only two possible states [138]: one parallel to this direction ($|+\rangle$) and another one antiparallel ($|-\rangle$).

If we consider analyser allowed direction as reference, in a system of spherical coordinates, we can express the generic neutron spin state $|S\rangle$ as linear combination of $|+\rangle$ and $|-\rangle$:

$$|S\rangle = e^{i\phi}cos(\frac{\theta}{2})|+\rangle + e^{-i\phi}sin(\frac{\theta}{2})|-\rangle \tag{C.9}$$

where θ and ϕ are the angles that define the orientation between the spin and the reference direction. From the equation C.9, we can note the neutron has a probability to be in state $|+\rangle$ or $|-\rangle$, which is function of the angle θ. If we define as N_+ (N_-) the probability that the spin is in the state $|+\rangle$ ($|-\rangle$), this will be equal to $N_+ = cos^2(\frac{\theta}{2})$ ($N_- = sin^2(\frac{\theta}{2})$).

Let's consider now a neutron where its orientation angle θ follows a normalized population $F(\theta)$. We suppose, e.g., the analyser lets pass only the spin in the state $|+\rangle$. With these assumptions we can calculate the transmission T as:

$$T = \frac{N_+}{N_+ + N_-} = \frac{1}{2}(1 + \int F(\theta)cos\theta d\theta) = \frac{1}{2}(1 + \langle cos\theta\rangle) \tag{C.10}$$

If we consider the polarisation of neutron beam P, this will be given by the classic definition $P = \frac{N_+ - N_-}{N_+ + N_-}$ [138]. Using the quantities defined above we can easily demonstrate:

$$P = \frac{\int F(\theta)(cos^2(\frac{\theta}{2}) - sin^2(\frac{\theta}{2})d\theta}{\int F(\theta)d\theta} = \langle cos\theta\rangle \tag{C.11}$$

Finally from the equations C.10 and C.11, we observe the polarisation and the transmission are strictly linked by the relation:

$$T = \frac{1}{2}(1 + P) \tag{C.12}$$

From the relation C.12, we can note that the polarisation could deeply influence the analyser transmission. This is a key-concept to understand the following section which explains how we can extract the polarisation of the beam from the measure the spin-echo.

C.4 Determination of the beam polarisation from a spin-echo measure

We consider now a neutron scattering measurement on a purely elastic scatter sample using the NSE apparatus shown in Fig.C.1A . In this case the neutrons don't change their energy (i.e. their wavelength) after the scattering event. So the

precession angle Φ_{TOT} (eq. C.8) depends on the neutrons incident wavelength and on the spectrometer configuration only.

We consider also a more realistic case, where the beam is submitted to a partial monochromatisation, by a velocity selector, that gives a resolution of $\frac{\Delta\lambda}{\lambda} \approx 15\%$. We can approximate the incident wavelength distribution $f(\lambda)$ as Gaussian:

$$f(\lambda) = \frac{1}{\sqrt{2\pi}\sigma} e^{\frac{(\lambda-\lambda_0)^2}{2\sigma^2}} \tag{C.13}$$

where λ_0 is the expected value of the distribution and σ it deviation. Given that Φ_{TOT} depends by λ, using the eq. C.11, we calculate the polarisation as:

$$P = \langle cos\theta \rangle = \int_0^{+\infty} f(\lambda) cos(\Phi_{TOT}(\lambda))\, d\lambda = \int_0^{+\infty} f(\lambda) cos(\alpha\lambda)\, d\lambda \tag{C.14}$$

where $\alpha = \frac{|\gamma|m}{h}(\int_{L_1} H_0\, dz - \int_{L_2} H_1\, dz)$ is a parameter independent from the neutron wavelength. It has been demonstrated that the integral in the relation C.14 could be resolved by analytical methods [3]. Following this reference we obtain the relation:

$$P = \int_0^{+\infty} f(\lambda) cos(\alpha\lambda)\, d\lambda = cos(\alpha\lambda_0) e^{\frac{-\alpha^2\sigma^2}{2}} \tag{C.15}$$

Thus, by the equation C.12, the analyser transmission is:

$$T = \frac{1}{2}(1 + cos(\alpha\lambda_0) e^{\frac{-\alpha^2\sigma^2}{2}}) \tag{C.16}$$

Now let's imagine to fix a current value i_0 in the first precession coil, while imposing a current i_1 in the second, which is tunable. These currents generate the magnetic fields $H_0 = \mu_0 N_t i_0$ and $H_1 = \mu_0 N_t i_1$, where μ_0 is the magnetic permittivity in the free space and N_t is the number of solenoids turns (which is the same in the two coils). This implies that we can change the number of the turns done by a neutrons in the two coils changing the value i_1. So the number $n(i_1)$ of the counted neutrons by the detector as a function of the second solenoid current will be given by the relation:

$$n(i_1) = NT(i_1) = \frac{N}{2}[1 + Pcos(\beta(i_0 - i_1)\lambda_0) e^{-\frac{\beta^2(i_0-i_1)^2\sigma^2}{2}}] \tag{C.17}$$

where N is the number of the incident neutrons, P the scattered beam polarisation and $\beta = \frac{|\gamma|\mu_0.N_t m}{h}$.

From equation C.17, we can observe that the number of the counted neutrons is the sum of an oscillating function, proportional to polarisation, damped by a Gaussian envelope function and a constant ($\frac{N}{2}$).

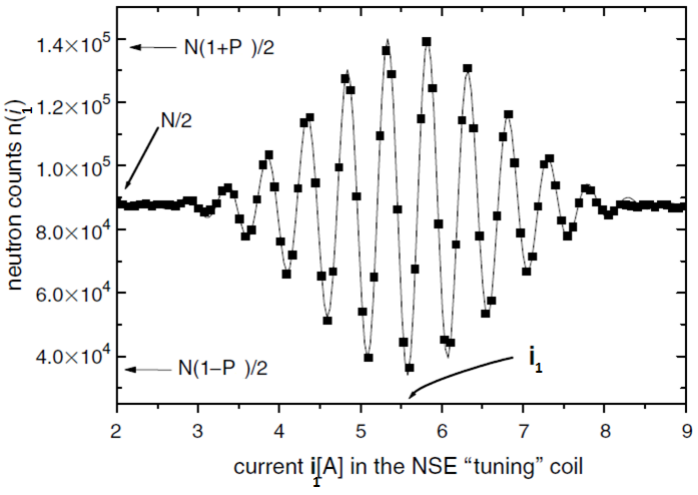

Figure C.2: Fully-measured echo the on spectrometer MUSES (LLB Saclay). The full squares are the experimental points, while the continuous line is the obtained fit using the relation C.17. This figure is adapted from the reference [3].

As we can see from the example shown in figure C.2, the maximum and minimum value of the $n(i_1)$ are respectively equal to $\frac{N}{2}(1+P)$ and $\frac{N}{2}(1-P)$ and they are observed near to echo point $(i_0 = i_1)$ where $e^{-\frac{\beta^2 {i_{TC}}^2 \sigma^2}{2}} \approx 1$.

In conclusion from the measure of the number of the counted neutrons as a function of the second coil current, we can extract the beam polarisation value using the relation C.17. This value is essential to determine the intermediate scattering function as it will be shown in the following section.

C.5 The case of quasi-elastic neutron scattering measure

In this section we consider a NSE measurement on a sample where we observe quasi-elastic scattering.

In this case the neutrons could have an energy change $\hbar\omega$ after the scattering, this implies a change of wavelength from λ_0 to $\lambda_0 + \delta\lambda$. Being the scattering quasi-elastic, the condition $\delta\lambda \ll \lambda$ is verified. With this assumption we can write the energy exchange as:

$$\hbar\omega = \frac{\hbar^2(2\pi)^2}{2m}\left(\frac{1}{{\lambda_0}^2} - \frac{1}{(\lambda_0 + \delta\lambda)^2}\right) \approx -\frac{h^2}{2m}\frac{\delta\lambda}{\lambda^3} \tag{C.18}$$

From the equation C.18, we can then rewrite $\delta\lambda$ as:

$$\delta\lambda = \frac{m(\lambda_0\omega)^3}{2\pi h} \tag{C.19}$$

In this case the measured polarisation of the scattered beam will depend also on the sample dynamics. We can thus generalize the relation C.15 for the average polarisation in the following way [3]:

$$\langle P\rangle = \int_0^{+\infty} f(\lambda_0)\, d\lambda_0 \int_{-\lambda_0}^{+\infty} p(\lambda_0,\delta\lambda) cos(\Phi_{TOT}(\lambda_0,\delta\lambda))\, d(\delta\lambda) \tag{C.20}$$

where the quantity $p(\lambda_0,\delta\lambda)$ is the probability of the event where a neutron, with incident wavelength λ_0, has the wavelength change $\delta\lambda$ after its scattering with the sample. Using the relation C.8, we can write the total precession angle as:

$$\Phi_{TOT}(\lambda_0,\delta\lambda) = \frac{|\gamma|m}{h}(\lambda_0 \int_{L_1} H_0\, dz - (\lambda_0+\delta\lambda)\int_{L_2} H_1\, dz) \tag{C.21}$$

If we set the spectrometer at the echo-point ($\mathbf{H_0} = \mathbf{H_1}$), we can simplify the previous relation:

$$\Phi_{TOT}(\lambda_0,\delta\lambda) = -\frac{|\gamma|m}{h}\delta\lambda \int_{L_2} H_1\, dz = -\frac{|\gamma|m^2}{2\pi h^2}\omega{\lambda_0}^3 \int_{L_2} H_1\, dz \tag{C.22}$$

where in the last term of the equation C.22 we have used the relation C.19.

If we pass now from the wavelength change $\delta\lambda$ to energy change $\hbar\omega$, we notice that the probability $p(\lambda_0,\delta\lambda)$ is the dynamic structure factor $S(\mathbf{Q},\omega)$. Thus, with this last consideration and with the relation C.22, we can write the equation for the polarisation as:

$$\langle P\rangle \approx \int_0^{+\infty} f(\lambda_0)\, d\lambda_0 \int_{-\infty}^{+\infty} S(\mathbf{Q},\omega) cos(\omega\tau_{NSE})\, d(\omega) \tag{C.23}$$

with

$$\tau_{NSE} = \frac{|\gamma|m^2}{2\pi h^2}{\lambda_0}^3 \int_{L_2} H_1\, dz \tag{C.24}$$

We can observe that the second integral in the equation C.23 is the real part of the time Fourier transform of dynamic structure factor. The spin-echo time τ_{NSE} approximates the Fourier time t, so we can finally write the equation C.23 as:

$$\langle P\rangle \approx I(\mathbf{Q},t) \tag{C.25}$$

We have however to bear in mind that the average polarization approximates the intermediate scattering function only if $S(\mathbf{Q},\omega)$ is a symmetric function of ω. This condition is generally verified for quasi-elastic experiments because the energy change in the scattering event is low, so the asymmetry imposed by the detailed balance factor is negligible [2].

In practice in a real NSE experiment we measure, for given $\mathbf{Q}$ values, the intermediate scattering function at different time probed by changing the magnetic field in two precession coils. Generally we are interested in the normalized value:

$$\frac{I(\mathbf{Q},t)}{I(\mathbf{Q},0)} = \frac{\int_{-\infty}^{+\infty} S(\mathbf{Q},\omega) cos(\omega\tau_{NSE})\, d(\omega)}{\int_{-\infty}^{+\infty} S(\mathbf{Q},\omega)\, d(\omega)} \tag{C.26}$$

so we divide each measured scattering function for its value at $\mathbf{H} = 0$.

Furthermore, in a real experiment we have not an ideal spectrometer. Thus to obtain the real value of the sample scattering function, we have to correct the data for the instrumental resolution function $R(\mathbf{Q},t)$. The latter is determined by the polarisation measure on a purely elastic sample of reference (i.e. quartz or graphite). The sample scattering function is finally calculated by dividing the normalized polarisation measured on the sample for that measured on the reference one.

$$I(\mathbf{Q},t) = \frac{P_{sample}(\mathbf{Q},t)}{P_{sample}(\mathbf{Q},0)} \frac{P_{ref}(\mathbf{Q},0)}{P_{ref}(\mathbf{Q},t)} \tag{C.27}$$

Appendix D

Ion pairs and the concept of ionicity

As it was already pointed out by Walden, when he discovered the ILs, the ions in the liquid phase are not totally dissociated, but part of them forms some neutral ion couples [10]. This feature has a very important impact on the electrical transport properties of the system, because it implies that not all ions can participate to the charge transport phenomenon.

This concept was recalled and deepened by Tokuda et al. [41–43, 139], who measured the molar ionic conductivity Λ of several ILs and they compared it with the one calculated from the diffusion properties. From the self-diffusion coefficient of the cation (D_+) and the anion (D_-), it is possible to determine the molar conductivity of the IL by the Nernst-Einstein (N-E) equation:

$$\Lambda_{NE} = \frac{N_A e^2}{k_B T} (D_+ + D_-) \tag{D.1}$$

where N_A is the Avogadro's number, e is the electronic charge, k_B is the Boltzmann and T is the temperature of the system.

The relation is valid only in the case of completely dissociated ions. A deviation from the values defined by the N-E equation means that part of charges still forms electric neutral groups in the system. Tokuda and co-workers showed that in the case of ILs the measured molar conductivity (Λ_M) and the conductivity defined by the N-E equation are not the same, but Λ_M shows smaller values than Λ_{NE} (see examples figure D.1):

$$\Lambda_M = (1 - \Delta)\, \Lambda_{NE} \qquad with \qquad \Delta > 0 \tag{D.2}$$

The discrepancy between Λ_M and Λ_{NE}, introduced by the presence of the positive parameter Δ in the equation D.2, pushes Tokuda et al. to define a new property of ILs called *ionicity*, which represents how much the salts nature is ionic i.e. how much the ions are dissociated in the systems.

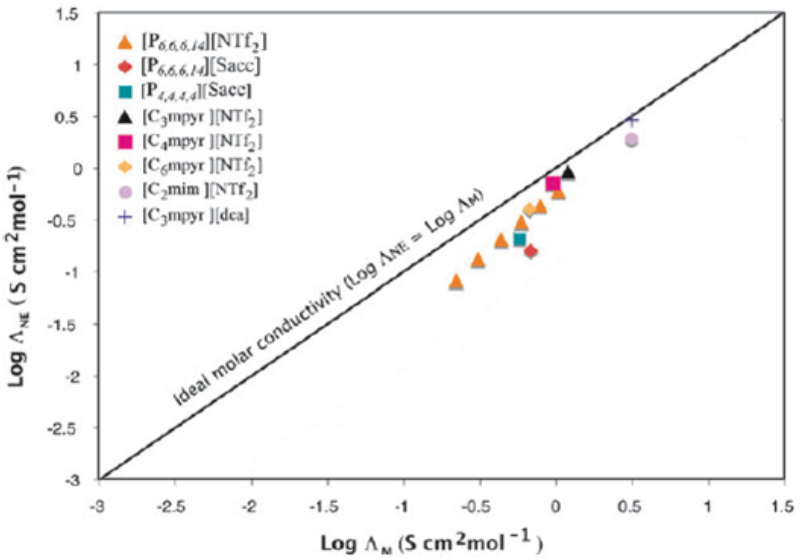

Figure D.1: Molar conductivity determined by N-E equation (eq.D.1) in function of the measure ionic conductivity for different ILs. The solid line is the ideal molar conductivity trend for a completely dissociated salt ($\Lambda_M = \Lambda_{NE}$). We can notice that for all ILs we can observe a discrepancy from the ideal trend suggesting the formation of neutral ions groups (pairs o bigger clusters). This figure is taken by the reference [140].

The properties of the ionicity and its dependence by the other ILs features were later studied by MacFarlane et al. [140]. From this analysis the authors pointed out that the ions coupling is not a long-lived aggregation, but it has a very short life ($t_{coupling} \approx 2\ 10^{-13}$ s), which is not detectable by the classic spectroscopy techniques.

In their discussion the authors underline that ions pairing is a possible correlation to form electric neutral groups of particles, however there is no proof that denies the existence of bigger aggregates which involve more than two ions.

Despite this ionic association the authors of this study estimated that ILs behave as "high dissociated electrolytes" with a percentage of free ions of around 50-90% .

This estimation has been recently called into question. A recent work of the Israelachvili's groups denies the high ionic dissociation claiming that the estimation, based on diffusivity and conductivity measurements, is influenced on kinetic effects which are not directly related to the static equilibrium association of the ions [130]. They show in fact that, with equilibrium force measurements, the percentage of dissociate ions is extremely low ($\approx 0.003\%$).

This new assumption, however, is not shared by the whole scientific community. So nowadays the debate about the ion aggregation is still open, as we can see from the various example in literature on this topic. [131, 141].

Appendix E

ILs applications

Despite the goals of this thesis are rather based on the ILs physical properties, we dedicate this section to the main applications of these liquids. The goal of this part is to show that these systems are not only interesting from the point view of the fundamental research, but that they can also be exploited in many application fields.

We want to underline that this part is just a hint of the possible ILs applications. For more details we invite the reader to see specific reviews [11, 142–146] .

As we have already mentioned in the section 1.1, nowadays the number of available ILs is enormous. The wide set of ionic couple design allows then to tune the molten salt physico-chemical properties (such as hydrophobicity/hydrophilicity, viscosity etc.) as a function of the desired use of the liquid. In the last decades the number of paper and patent concerning the ILs has exponentially grown (see Fig.1.1), showing that the ILs features can be exploited in a wide range of application fields.

In this part we will focus on two main ILs possible utilisation: as solvent and in the energy management.

E.1 ILs as green solvents

A big branch of ILs applications concerns the so called *Green Chemistry*.

In figure E.1 the main properties of ILs and the Organic Molecular Solvents (OMSs) generally used in the industrial applications, are compared.

If we focus on the first lines of this tables we can easily realize the great potential of this class of compounds. Beyond the larger amount of available ILs, the simultaneous presence of a polar and an a-polar part in the ionic structure gives to ILs the ability to solubilize at the same time polar and a-polar compounds, which

Property	Organic solvents	Ionic liquids
Number of solvents	>1000	>1,000,000
Applicability	Single function	Multifunction
Catalytic ability	Rare	Common and tuneable
Chirality	Rare	Common and tuneable
Vapour pressure	Obeys the Clausius–Clapeyron equation	Negligible vapour pressure under normal conditions
Flammability	Usually flammable	Usually nonflammable
Solvation	Weakly solvating	Strongly solvating
Polarity	Conventional polarity concepts apply	Polarity concept questionable
Tuneability	Limited range of solvents available	Virtually unlimited range means "designer solvents"
Cost	Normally cheap	Typically between 2 and 100 times the cost of organic solvents
Recyclability	Green imperative	Economic imperative
Viscosity/cP	0.2–100	22–40,000
Density/g cm^{-3}	0.6–1.7	0.8–3.3
Refractive index	1.3–1.6	1.5–2.2

[a] The data summarised in this Table are not comprehensive, nor do they represent outliers; they are meant to give a brief visual comparison of typical values. Detailed values can be found elsewhere.[70]

Figure E.1: Summary of the main properties of ILs and OMSs as solvent. This figure is taken by the reference [11].

is not possible with the classic molecular solvents. Furthermore the chirality and the catalytic ability are common properties in this class of systems, in contrast with the OMSs where these features are rather rare.

After that the presence of a strong electrostatic interaction between the ions gives to the ILs a very low volatility amd flammability. Due to these particular features many authors call ILs *green solvents* in contrast to the conventional OMSs which are usually volatile and flammable and, thus, less safe for the environment safety. However we must notice that the term "green" is somewhat misleading because it doesn't refer to the toxicity of the ILs [11].

The most known ILs application in the green chemistry field is probably the utilisation of the ILs for cellulose dissolution. This bio-polymer, in fact, is not soluble in water and in the common organic solvents and most of the technologies employed nowadays in the cellulose processing are non-green. As we said in the section 1.1, at beginning of the 20^{th} century it was shown that ILs can dissolve easily this material [11]. At that time this process was not intensively exploited because it was necessary to work at high temperature for having a molten salt. With the RTILs arrivals, however, this method was restarted and today there are many groups which are studying how to improve this type of process [147, 148].

Beyond this most known example, there are other many applications fields using ILs as solvents. Among them we remember liquid/liquid extraction of fission products [143, 145], metal ions [143] and biological molecules [143, 145], desulfurization processes [143, 145], gas separation [142, 143, 145] and the catalysis reactions [143].

E.2 Energy management by electrochemical devices

Another very promising application field for ILs is the energy storage and management.

It is well known the disastrous impact of fossil fuels on the climate changes, which is, nowadays, a very actual topic. The environmental safety has raised the issue of developing some alternative methods of energy production. For this reason, there has been an increasing effort to find some more sustainable long term energy sources such as the solar or aeolian one. The limit of these power sources is their intermittence. This limitation has generated the parallel necessity of increasing the capacity to deliver and to store the produced power. In this environment the electrochemical devices development has acquired an increasing importance, because these systems allow to store energy that can be used later on. For these reasons the improvement of these devices has been intensively studied in the last years. In this context the ILs have raised a big interest: in addition to their low volatility and their conductive nature, they show also a very high electrochemical stability. These features make these salts very good candidates as electrolyte.

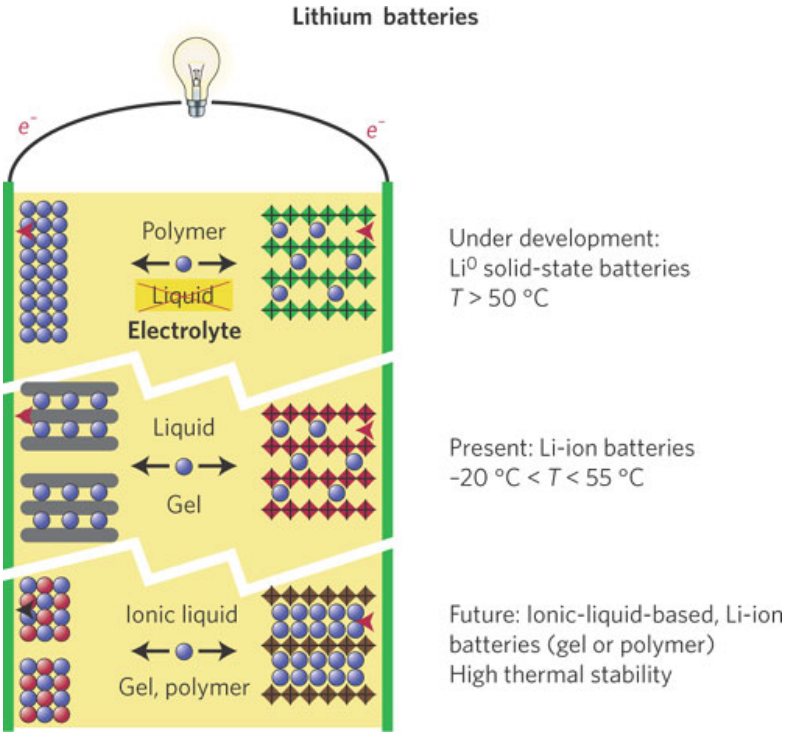

Figure E.2: Sketch of the possible lithium batteries. From the top: battery with solid electrolyte, Li battery with organic electrolyte, Li battery with IL as electrolyte. This figure is taken from the reference [144].

One of the most widely used electrochemical devices in consumer-electronic market is the lithium battery. This system consists in two electrodes separated by a solution of lithium salt in an organic solvent trapped in a gel (see fig.E.2). The charge transfer is obtained by cycling the lithium ions from one electrode to the other. The phenomena that occur during the electrochemical reaction are not completely controlled: some unwanted processes such as short circuits, or exothermic reactions can take place during the utilisation of this device, and they can damage the system causing fire or explosion. For these reasons some alternative solutions are being evaluated. One of them is the use of a solid electrolyte (such as electrolyte polymers [72]). However it has been proven that this kind of system can work only at high temperature (T$>$ 50° C) [72, 144]. Another solution could be the utilisation of ILs as electrolyte. These salts are not flammable and they show a very wide electrochemical window, so they seem to be very promising for this kind of application. Nowadays there are thus many works dedicated to the study of the behaviour of the lithium batteries using ILs [144–146].

However the lithium accumulator is not the only electrochemical system where ILs are tested in order to produce improvements. Among them we remember the works performed to modify the humidity sensitivity of the fuel cells [144] and the preliminary studies to use ILs in the supercapacitors [144, 146].

Appendix F

Résumé en français

Cette thèse de doctorat est une contribution à l'effort global pour améliorer les performances des systèmes électrochimiques afin qu'ils puissent devenir une alternative compétitive aux combustibles fossiles dans le domaine des transports. Bien qu'on puisse noter un constant avancement pendant les dernières décennies, les améliorations des batteries sont de nature incrémentale avec des gains de quelques pour cent sur chacun des éléments de la pile (électrolyte, électrode etc.). Pour compléter cette approche technologique, nous proposons ici une approche fondamentale. Notre ambition est d'augmenter considérablement la puissance des batteries. L'idée à la base de ce projet est l'usage du confinement nanométrique unidimensionnel pour exalter les propriétés de transport de l'électrolyte.

Nous avons concentré nos efforts sur une classe particulière d'électrolytes : les Liquides Ioniques (LI) qui en raison de leur stabilité électrochimique, physique et chimique ont été identifiés comme électrolytes prometteurs. La compétition entre les interactions électrostatiques des parties chargées et les forces de Van der Waals des chaînes alkyles apolaires de leurs cations génèrent une spécificité des LI: une structuration nanométrique. Cette caractéristique plutôt originale pour un liquide pur, induit de fortes fluctuations de densité au sein du liquide avec des conséquences nuisibles sur la viscosité et donc sur la conductivité ionique. Ainsi, malgré leur stabilité, cette propriété d'auto-assemblage nanométrique spontanée est un inconvénient majeur pour l'utilisation des LI comme électrolytes. Nous identifions le confinement comme un moyen de frustrer la nanostructuration et donc de transformer le LI en un liquide homogène (sans fluctuations de densité) montrant des propriétés de transport (coefficient de diffusion translationnel) améliorées. La nanostructuration du LI est caractérisée par un pré-pic dans le facteur de structure de diffraction dans la gamme [0,1 $Å^{-1}$ - 0,5 $Å^{-1}$]. Pour la classe de LI de type l'imidazolium, l'intensité et la position de ce pré-pic sont contrôlées par la longueur de leur chaîne alkyle. Comme ils montrent un pré-pic prononcé, qui est pour nous une bonne observable permettant de quantifier l'influence du confinement, nous

avons concentré une partie importante de ce travail sur l'étude d'un cation avec une chaîne latérale assez longue (8 atomes de carbone) : OMIM-BF_4(octyl-3-méthylimidazolium). Pour référence, un analogue avec une chaîne plus courte (4 carbones) a également été étudié : BMIM-TFSI (1-butyl-3-méthylimidazolium bis (trifluorométhanesulfonyl) imide).

Afin d'optimiser les propriétés de transport et, par conséquent, la conduction ionique entre les électrodes d'une batterie, la tortuosité du matériau de confinement doit être minimisée. Nous avons confiné les LI dans deux systèmes poreux différents: *i)* des alumines poreuses (Anodic Aluminum Oxyde, AAO) et *ii)* des membranes de nanotubes de carbone (NTC). Ces matériaux partagent une topologie commune: l'orientation macroscopique de leur réseau de pores cylindriques, mais montrent des propriétés physico-chimiques complémentaires: les AAO sont hydrophiles tandis NTC sont hydrophobes. Le confinement nanométrique sur des distances macroscopiques (l'espacement entre les électrodes est de l'ordre du micromètre) conduit naturellement à considérer des tailles caractéristiques différant de plusieurs ordres de grandeur. Nous avons donc naturellement développé une approche spatiale et temporelle multi-échelle pour étudier la dynamique des LI.

Pour plus de clarté, dans les lignes ci-dessous, nous résumons dans des sections séparées les principaux développements et conclusion des trois parties de ce manuscrit.

Liquides ioniques en volume: En raison de la grande section de diffusion incohérente des protons et de l'abondance de cet élément dans les LI, la diffusion incohérente quasi-élastique de neutrons (QENS) est une technique très appropriée pour accéder à une vue globale de la dynamique des LI via la dynamique individuelle moyenne de ses atomes d'hydrogène. L'échantillon est sondé sur une échelle locale (quelques Å). Ainsi, dans le cas d'une molécule complexe (avec des chaînes latérales) en solution, le facteur de structure dynamique, S (Q, ω), est une moyenne de la dynamique (corrélation temporelle et géométrie des mouvements (EISF)) des différentes chaînes latérales ainsi que du mouvement global de translation (centre de masse) de la molécule entière. Un coefficient de diffusion translationnel à longue distance D_{lr} est associé à cette contribution. Pour décrire le cas spécifique du LI, nous ajoutons à cette description classique, une contribution pour tenir compte de la localisation transitoire dans les agrégats nanométriques. Nous associons à cette contribution, D_{loc}, un coefficient de diffusion local dans un agrégat de LI. Nous avons sondé, par QENS (diffusion de neutrons par temps de vol et diffusion de neutrons à écho de spin (NSE)), la dynamique de cations de deux liquides ioniques à cation imidazolium, le BMIM-TFSI et l'OMIM-BF $_4$. Nous avons introduit un nouveau modèle physique décrivant toutes les contributions dynamiques ci-dessus et nous avons profité de la deutériation spécifique des chaînes latérales pour mon-

trer que la modélisation est assez robuste pour décrire les données QENS sur une gamme en Q ([0,15 Åde $^{-1}$ - 2,5 Å^{-1}]) et en temps ([0,5 ps - 2000 ps]) très large.

• Diffusion dans les agrégats : la dépendance en Q des temps de corrélation associés à la diffusion au sein de l'agrégat (D_{loc}) présente un plateau à petit Q (Fig. 1.30 et 1.35). Ce comportement est caractéristique d'une diffusion dans un volume confiné. Suivant le modèle gaussien proposé par Volino [53, 54], nous extrayons la taille caractéristique d'un agrégat: il est de l'ordre de 20 Å. Fait intéressant, cette taille est comparable à la longueur de corrélation déduite de la position du pré-pic ($2\ \pi/0.3 = 21$ Å).

• Diffusion à longue distance: nous introduisons les contributions de la diffusion locale et des chaînes latérales facilement mesurées par le temps de vol dans l'échelle de temps de ps, des données de diffusion des neutrons par écho de spin nous pouvons extraire D_{lr} la coefficient de diffusion à longue distance dû à la translation du centre de masse du cation. Nous montrons que les temps de corrélation, mesurés par NSE, associés à D_{lr} obéit à la soi-disant «loi DQ^2» (Fig. 1.33 et 1.36). Ceci est une preuve solide que D_{lr} est lié à un véritable mouvement de translation à longue distance.
Comme les LI sont des liquides purs, les fluctuations de densité au sein du système restent extrêmement faibles de sorte que, en raison de l'absence de contraste, l'analyse expérimentale directe de la structuration nanométrique par diffusion à petites angles (de neutrons ou de rayons X) est impossible. D'une manière en quelque sorte inattendue, puisque ce sont des méthodes plutôt indirectes pour déterminer des structures, nous montrons que, par les quantités dynamiques résultant de mesures de diffusion quasi-élastique de neutrons (QENS) nous sommes capables de mettre en évidence l'organisation nanométrique du système (la taille caractéristique associée à D_{loc} et D_{lr}).

Comme il règle sur les propriétés de transport électrique (par la relation de Nernst-Einstein), la diffusivité translationnelle à longue distance du LI est une quantité clé pour trancher le débat très actuel entre les groupes de Israelachvili [130] et celui de Perkin [131] sur la nature exacte des LI : malgré la forte concentration moyenne de charges, l'appariement entre les ions au sein d'agrégats nanométriques globalement neutres rendent-ils les LI un électrolyte faiblement dissocié ou, à l'inverse, constituent-ils une solution d'ions fortement dissociés? À notre avis, les agrégats devraient être neutres (sinon, quel est leur mécanisme de formation?). Par conséquent, la concentration de charges libres (cations et anions dissociés) dans le liquide doit être faible. Nous pensons néanmoins que, au stade actuel, la question clé reste: les charges sont-elles situées à l'intérieur des agrégats ou à leur surface? Il nous semble que seulement les simulations par dynamique

moléculaire peuvent répondre à cette question.

LI confinés dans les AAO: Le diamètre de leurs pores pouvant être finement adapté dans la gamme de 700 nm à 10 nm, notre stratégie est de confiner OMIM-BF_4 dans les membranes poreuses AAO. Un objectif de cette thèse était, en réduisant le diamètre des pores, de détecter une transition où le pré-pic disparaîtrait et donc i) être en mesure d'estimer la taille caractéristique des domaines nanométriques afin ii) de procéder à une caractérisation complète des propriétés de transport de l'OMIM-BF_4 confiné et « désagrégé ». Nous avons montré que même sur sous confinement au sein d'AAO présentant les plus petits pores disponibles pour ce travail (25 nm), le pré-pic est toujours détecté par diffraction (Fig. 2.18), ce qui signifie que la nanostructuration n'est pas frustrée. Néanmoins le confinement au sein des AAO semble affecter le comportement biphasique de liquides ioniques: les données WAXS suggèrent une meilleure organisation des domaines (rétrécissement de pré-pic) et une légère augmentation de leur taille (décalage du pré-pic vers les petits Q) (Fig. 2.20).
Par rapport à la situation en volume, la DSC détecte une transition vitreuse (Fig. 2.12) supplémentaire et un nouveau pic est détectée par diffraction (Fig. 2.18). On interprète ces observations, comme une forte interaction d'une fraction du LI confiné avec les parois des pores des AAO. Nous notons que ces effets de surface sont plutôt communs pour un matériau sous confinement.
Le modèle mis au point pour évaluer la dynamique locale des LI en volume, est également capable de décrire la dynamique des liquides confinés dans les AAO. Nous ne détectons cependant pas d'influence significative du confinement sur la dynamique du LI.
A ce stade, nous devons insister sur une mise en garde qui modère la conclusion ci-dessus: l'imbibition du LI dans des membranes d'AAO a montré un comportement inattendu. Alors que le confinement du LI est possible, l'état confiné semble être métastable: après quelques heures, une fraction significative (30 % après quelques heures) de liquide est expulsée de la matrice. Même si une étude complète de ce phénomène dépasse les objectifs de cette thèse, cela suggère des questions intéressantes quand à la tension de surface du système alumine+LI. Nous soupçonnons que la pression de vapeur très faible du LI peut jouer un rôle important dans ce phénomène. Nous avons utilisé la tomographie RMN pour quantifier finement la fuite de liquide et pour proposer une solution expérimentale (doublure en téflon de la surface d'AAO) pour éviter cet effet gênant (Fig. 2.30). Le fait que ce travail de tomographie soit venu dans un stade tardif de ce travail explique pourquoi la partie centrale de l'étude sur le confinement dans les AAO a été menée malgré ce problème.

LI confines dans les membranes de nanotubes de carbone : Un effet de confinement est effectif lorsque la taille de confinement est plus petite que les fluctuations caractéristiques du système en volume. Le but ultime lorsqu'on parle de confinement est en effet d'observer un *effet de volume*. Malheureusement, comme dans ce travail sur le confinement dans les AAO, la plupart des matériaux de confinement induisent des textit effets de surface parasites. Parmi les différentes propriétés intéressantes, les NanoTubes de Carbone NTC sont des systèmes très attrayants en raison de leur structure graphénique interne qui limite fortement les interactions avec les matériaux confinés. Cette étude du confinement des LI dans les membranes de NTC en est encore à un stade préliminaire, mais semble prometteuse. A nouveau, on ne détecte pas de forts effet de confinement à l'échelle moléculaire (ps-ns) en termes de dynamique radiale ainsi que longitudinale au sein des tubes de NTC. Au-delà des problèmes de statistique dans les expériences de QENS sur cet échantillon, une explication possible est l'effet de confinement trop léger: le diamètre interne des NTC (4 nm) est sans doute encore trop grand pour induire une forte influence à l'échelle moléculaire. Mais nous avons été en mesure de montrer qu'à l'échelle microscopique (PFG-RMN), Fig. 3.10, macroscopique (spectroscopie d'impédance), Fig.3.9, nous pouvons obtenir l'effet que nous avons cherché en développant ce programme de recherche: une amélioration notable (par un facteur 3) des propriétés de transport dans une situation 1D. Un brevet a été déposé en mars 2015 sur l'utilisation de membranes NTC comme une solution possible pour stimuler les propriétés de transport et donc la puissance spécifique de batteries au lithium.

Perspectives: À la fin de cette étude, nous pouvons identifier des perspectives intéressantes aux niveaux fondamentaux et technologiques.

Au cours de cette thèse, à côté des expériences QENS, nous avons sondé le LI, à l'échelle mésoscopique (μm et mus), par RMN à gradient pulsé (PFG-RMN). Nous avons noté que les coefficients de diffusion à longue distance mesuré par QENS et RMN sont différents d'un (ou plus) ordre de grandeur. Un tel écart entre les données QENS et RMN est assez classique lorsqu'ils traitent des systèmes sous confinement montrant une forte tortuosité. Il est facile à comprendre si on considère les longueurs caractéristiques très différentes sondées par les deux techniques: à l'échelle locale et à temps court sondés par QENS, une particule confinée peut encore avoir à diffuser avant d'être influencée par le volume de confinement, par contre à plus grande échelle et temps plus long sondés par PFG-RMN la structure tortueuse du matériau de confinement peut imposer une trajectoire labyrinthique qui entraîne une très faible coefficient de diffusion apparent. Dans le cas des LI, on

peut penser que la présence d'agrégats joue un rôle similaire à celui d'une structure poreuse pour une molécule de liquide ionique non encore pris au piège dans un agrégat. La relaxométrie RMN serait probablement un outil très pertinent pour compléter les informations obtenues par les données QENS et RMN sur le liquide en volume. En outre, comme il est un moyen idéal pour sonder les propriétés de mouillage, cette technique devrait être très instructive pour évaluer l'interaction de liquides ioniques avec les murs des pores dans le cas du liquide confiné.

Au niveau technologique, pour une réelle pertinence dans le domaine des batteries, il semble maintenant crucial de développer une étude spécifique sur les LI chargés de sels de lithium confinés dans les membranes de NTC. Ces systèmes ont été bien caractérisés en volume, mais l'aspect concernant le confinement est encore un sujet ouvert. Il sera également important de synthétiser des forêts NTC avec des pores étroits (1-2 nm de diamètre). Travailler avec de tels canaux étroits semble important pour améliorer fortement les propriétés de transport. Une telle étude pourrait en effet garantir que le gain de 3 obtenu jusqu'à présent est plus qu'un effet de dimensionnalité (diffusion en 1D vs diffusion en 3D). Le fait que les NTC constituent de bons conducteurs électroniques pourrait limiter la pertinence des membranes NTC comme séparateurs de batteries. Comme une telle modification affecterait fortement l'hybridation électronique des atomes de carbone des NTC, cette limitation pourrait être levée par greffage de polymère chimique des parois extérieures des NTC.

Bibliography

[1] M. Bée. Quasielastic Neutron Scattering: Principles and Applications in Solid State Chemistry, Biology and Materials Science, 1988.

[2] S. W. Lovesey. *Theory of Neutron Scattering from Condensed Matter. Vol. 1: Nuclear Scattering.* Oxford, 1984.

[3] R. E. Lechner and S. Longeville. *Neutron Scattering in Biology Techniques and Applications.* Springer, 2006.

[4] A. Triolo, O. Russina, H.-J. Bleif, and E. Di Cola. Nanoscale segregation in room temperature ionic liquids. *Journal of Physical Chemistry B*, 111(18):4641–4644, 2007.

[5] J. D. Holbrey and K. R. Seddon. The phase behaviour of 1-alkyl-3-methylimidazolium tetrafluoroborates; ionic liquids and ionic liquid crystals. *Journal of the Chemical Society-Dalton Transactions*, (13):2133–2139, 1999.

[6] J. N. Canongia Lopes and A. A.H. Pádua. Nanostructural organization in ionic liquids. *Journal of Physical Chemistry B*, 110(7):3330–3335, 2006.

[7] A. I. Kolesnikov, J.-M. Zanotti, C.-K. Loong, P. Thiyagarajan, A. P. Moravsky, R. O. Loutfy, and C. J Burnham. Anomalously soft dynamics of water in a nanotube: a revelation of nanoscale confinement. *Physical review letters*, 93(3):035503, 2004.

[8] J. K. Holt, H. G. Park, Y. Wang, M. Stadermann, A. B. Artyukhin, C. P. Grigoropoulos, A. Noy, and O. Bakajin. Fast mass transport through sub-2-nanometer carbon nanotubes. *Science*, 312(5776):1034–1037, 2006.

[9] C. Tasserit, A. Koutsioubas, D. Lairez, G. Zalczer, and M.-C. Clochard. Pink noise of ionic conductance through single artificial nanopores revisited. *Physical review letters*, 105(26):260602, 2010.

[10] P. Walden. Molecular weights and electrical conductivity of several fused salts . *Bull. Acad. Imp. Sci. St.-Petersbourg*, 8:405–422, 1914.

[11] N. V. Plechkova and K. R. Seddon. Applications of ionic liquids in the chemical industry. *Chemical Society Reviews*, 37(1):123–150, 2008.

[12] F. H. Hurley and T. P. Wier. Electrodeposition of metals from fused quaternary ammonium salts. *Journal of The Electrochemical Society*, 98(5):203–206, 1951.

[13] A. A. Fannin Jr, D. A. Floreani, L. A. King, J. S. Landers, B. J. Piersma, D. J. Stech, R. L. Vaughn, J. S. Wilkes, and L. Williams John. Properties of 1, 3-dialkylimidazolium chloride-aluminum chloride ionic liquids. 2. phase transitions, densities, electrical conductivities, and viscosities. *The Journal of Physical Chemistry*, 88(12):2614–2621, 1984.

[14] J. S. Wilkes and M. J. Zaworotko. Air and water stable 1-ethyl-3-methylimidazolium based ionic liquids. *J. Chem. Soc., Chem. Commun.*, (13):965–967, 1992.

[15] C. Hardacre, S.E. J. McMath, M. Nieuwenhuyzen, D. T. Bowron, and A. K. Soper. Liquid structure of 1, 3-dimethylimidazolium salts. *Journal of Physics-Condensed Matter*, 15(1):S159–S166, 2003.

[16] C. Hardacre, J. D. Holbrey, S.E. J. McMath, D. T. Bowron, and A. K Soper. Structure of molten 1,3-dimethylimidazolium chloride using neutron diffraction. *Journal of Chemical Physics*, 118(1):273–278, 2003.

[17] M. Deetlefs, C. Hardacre, M. Nieuwenhuyzen, A. A.H. Padua, O. Sheppard, and A. K. Soper. Liquid structure of the ionic liquid 1, 3-dimethylimidazolium bis {(trifluoromethyl) sulfonyl} amide. *The Journal of Physical Chemistry B*, 110(24):12055–12061, 2006.

[18] A. Triolo, O. Russina, B. Fazio, R. Triolo, and E. Di Cola. Morphology of 1-alkyl-3-methylimidazolium hexafluorophosphate room temperature ionic liquids. *Chemical Physics Letters*, 457(4-6):362–365, 2008.

[19] O. Russina, A. Triolo, L. Gontrani, R. Caminiti, D. Xiao, L. G. Hines Jr, R. A. Bartsch, E. L. Quitevis, N. Plechkova, and K. R. Seddon. Morphology and intermolecular dynamics of 1-alkyl-3-methylimidazolium bis{(trifluoromethane)sulfonyl}amide ionic liquids: structural and dynamic evidence of nanoscale segregation. *Journal of Physics-Condensed Matter*, 21(42), 2009.

[20] A. Martinelli, M. Maréchal, Å Östlund, and J. Cambedouzou. Insights into the interplay between molecular structure and diffusional motion in 1-alkyl-3-methylimidazolium ionic liquids: a combined PFG NMR and X-ray scattering study. *Physical Chemistry Chemical Physics*, 15(15):5510–5517, 2013.

[21] X. Song, H. Hamano, B. Minofar, R. Kanzaki, K. Fujii, Y. Kameda, S. Kohara, M. Watanabe, S.-I. Ishiguro, and Y. Umebayashi. Structural heterogeneity and unique distorted hydrogen bonding in primary ammonium nitrate ionic liquids studied by high-energy x-ray diffraction experiments and md simulations. *The Journal of Physical Chemistry B*, 116(9):2801–2813, 2012.

[22] A.E. Bradley, C. Hardacre, J.D. Holbrey, S. Johnston, S.E.J. McMath, and M. Nieuwenhuyzen. Small-angle x-ray scattering studies of liquid crystalline 1-alkyl-3-methylimidazolium salts. *Chemistry of materials*, 14(2):629–635, 2002.

[23] W. Zheng, A. Mohammed, L. G. Hines Jr, D. Xiao, O. J. Martinez, R. A. Bartsch, S. L. Simon, O. Russina, A. Triolo, and E. L.Pink noise of ionic conductance through single artificial nanopores revisited Quitevis. Effect of Cation Symmetry on the Morphology and Physicochemical Properties of Imidazolium Ionic Liquids. *Journal of Physical Chemistry B*, 115(20):6572–6584, 2011.

[24] B. L. Bhargava, R. Devane, M. L. Klein, and S. Balasubramanian. Nanoscale organization in room temperature ionic liquids: a coarse grained molecular dynamics simulation study. *Soft Matter*, 3(11):1395–1400, 2007.

[25] H. V.R. Annapureddy, H. K. Kashyap, P. M. De Biase, and C. J. Margulis. What is the origin of the prepeak in the x-ray scattering of imidazolium-based room-temperature ionic liquids? *The Journal of Physical Chemistry B*, 114(50):16838–16846, 2010.

[26] K. Shimizu, C. E.S. Bernardes, and J. N. Canongia Lopes. Structure and aggregation in the 1-alkyl-3-methylimidazolium bis (trifluoromethylsulfonyl) imide ionic liquid homologous series. *The Journal of Physical Chemistry B*, 118(2):567–576, 2014.

[27] C. Hardacre, J. D. Holbrey, C. L. Mullan, T. G.A. Youngs, and D. T. Bowron. Small angle neutron scattering from 1-alkyl-3-methylimidazolium hexafluorophosphate ionic liquids (C(n)mim PF6 , n=4, 6, and 8). *Journal of Chemical Physics*, 133(7), 2010.

[28] M. Kofu, M. Nagao, T. Ueki, Y. Kitazawa, Y. Nakamura, S. Sawamura, M. Watanabe, and O. Yamamuro. Heterogeneous Slow Dynamics of Imidazolium-Based Ionic Liquids Studied by Neutron Spin Echo. *Journal of Physical Chemistry B*, 117(9):2773–2781, 2013.

[29] O. Yamamuro, T. Yamada, M. Kofu, M. Nakakoshi, and M. Nagao. Hierarchical structure and dynamics of an ionic liquid 1-octyl-3-methylimidazolium chloride. *Journal of Chemical Physics*, 135(5), 2011.

[30] `http://www-llb.cea.fr/spectros/pdf/paxy-llb.pdf`.

[31] H. Weingaertner. Understanding ionic liquids at the molecular level: Facts, problems, and controversies. *Angewandte Chemie-International Edition*, 47(4):654–670, 2008.

[32] A. Triolo, O. Russina, V. Arrighi, F. Juranyi, S. Janssen, and C. M. Gordon. Quasielastic neutron scattering characterization of the relaxation processes in a room temperature ionic liquid. *Journal of Chemical Physics*, 119(16):8549–8557, 2003.

[33] A. Triolo, O. Russina, C. Hardacre, M. Nieuwenhuyzen, M. A. Gonzalez, and H. Grimm. Relaxation processes in room temperature ionic liquids: The case of 1-butyl-3-methyl imidazolium hexafluorophosphate. *Journal of Physical Chemistry B*, 109(46):22061–22066, 2005.

[34] T. Burankova, E. Reichert, V. Fossog, R. Hempelmann, and J. P. Embs. The dynamics of cations in pyridinium-based ionic liquids by means of quasielastic- and inelastic neutron scattering. *Journal of Molecular Liquids*, 192(0):199–207, 2014.

[35] Z. Hu and C. J. Margulis. Heterogeneity in a room-temperature ionic liquid: Persistent local environments and the red-edge effect. *Proceedings of the National Academy of Sciences of the United States of America*, 103(4):831–836, 2006.

[36] B. Aoun, M. A. González, J. Ollivier, M. Russina, Z. Izaola, D. L. Price, and M.-L. Saboungi. Translational and Reorientational Dynamics of an Imidazolium-Based Ionic Liquid. *Journal of Physical Chemistry Letters*, 1(17):2503–2507, 2010.

[37] E. Mamontov, G. A. Baker, H. Luo, and S. Dai. Microscopic diffusion dynamics of silver complex-based room-temperature ionic liquids probed by quasielastic neutron scattering. *ChemPhysChem*, 12(5):944–950, 2011.

[38] J. P. Embs, T. Burankova, E. Reichert, and R. Hempelmann. Cation Dynamics in the Pyridinium Based Ionic Liquid 1-N-Butylpyridinium Bis((trifluoromethyl)sulfonyl) As Seen by Quasielastic Neutron Scattering. *Journal of Physical Chemistry B*, 116(44):13265–13271, 2012.

[39] J. P. Embs, T. Burankova, E. Reichert, V. Fossog, and R. Hempelmann. QENS Study of Diffusive and Localized Cation Motions of Pyridinium-based Ionic Liquids. *Journal of the Physical Society of Japan*, 82, 2013.

[40] T. Burankova, R. Hempelmann, A. Wildes, and J. P. Embs. Collective ion diffusion and localized single particle dynamics in pyridinium-based ionic liquids. *The Journal of Physical Chemistry B*, 118(49):14452–14460, 2014.

[41] H. Tokuda, K. Hayamizu, K. Ishii, M. A. B. H. Susan, and M. Watanabe. Physicochemical properties and structures of room temperature ionic liquids. 1. Variation of anionic species. *Journal of Physical Chemistry B*, 108(42):16593–16600, 2004.

[42] H. Tokuda, K. Hayamizu, K. Ishii, M. A. B. H. Susan, and M. Watanabe. Physicochemical properties and structures of room temperature ionic liquids. 2. Variation of alkyl chain length in imidazolium cation. *Journal of Physical Chemistry B*, 109(13):6103–6110, 2005.

[43] H. Tokuda, K. Ishii, M. A. B. H. Susan, S. Tsuzuki, K. Hayamizu, and M. Watanabe. Physicochemical properties and structures of room-temperature ionic liquids. 3. Variation of cationic structures 10.1021/jpO53396f. *Journal of Physical Chemistry B*, 110(6):2833–2839, 2006.

[44] A.-J. Dianoux and G.H. Lander. *Neutron data booklet*. Old City Philadelphia, 2003.

[45] J.-M. Zanotti. Vibrations et relaxations dans les molécules biologiques. Apports de la diffusion incohérente inélastique de neutrons. *Journal de Physique IV*, 130:87–113, 2005.

[46] `http://www.ill.eu/instruments-support/instruments-groups/instruments/in5/characteristics/`.

[47] `http://www.isis.stfc.ac.uk/instruments/let/science/let-science-6442.html`.

[48] `http://www.isis.stfc.ac.uk/instruments/iris/iris4691.html`.

[49] `http://www.ill.eu/instruments-support/instruments-groups/instruments/in11/characteristics/`.

[50] K. R. Harris, M. Kanakubo, N. Tsuchihashi, K. Ibuki, and M. Ueno. Effect of pressure on the transport properties of ionic liquids: 1-alkyl-3-methylimidazolium salts. *Journal of Physical Chemistry B*, 112(32):9830–9840, 2008.

[51] J.-M. Zanotti, M.-C. Bellissent-Funel, and S.-H. Chen. Relaxational dynamics of supercooled water in porous glass. *Physical Review E*, 59(3):3084–3093, 1999.

[52] A. Arbe, J. Colmenero, M. Monkenbusch, and D. Richter. Dynamics of glass-forming polymers: "Homogeneous" versus "heterogeneous" scenario. *Physical Review Letters*, 81(3):590–593, 1998.

[53] F. Volino, J.-C. Perrin, and S. Lyonnard. Gaussian model for localized translational motion: Application to incoherent neutron scattering. *Journal of Physical Chemistry B*, 110(23):11217–11223, 2006.

[54] J.-C. Perrin, S. Lyonnard, F. Volino, and A. Guillermo. Gaussian model for localized translational motion. Application to water dynamics in Nafion (R) studied by quasi-elastic neutron scattering. *European Physical Journal-Special Topics*, 141:57–60, 2007.

[55] F. Volino and A.-J. Dianoux. Neutron incoherent scattering law for diffusion in a potential of spherical symmetry: general formalism and application to diffusion inside a sphere. *Molecular Physics*, 41(2):271–279, 1980.

[56] Q. Berrod. *Relation structure - transport dans des membranes et matériaux modèles pour pile à combustible* . PhD thesis, Grenoble, 2013.

[57] P.-G. De Gennes. Liquid dynamics and inelastic scattering of neutrons. *Physica*, 25(7):825–839, 1959.

[58] J. Teixeira, M.-C. Bellissent-Funel, S.-H. Chen, and A.-J. Dianoux. Experimental determination of the nature of diffusive motions of water molecules at low temperatures. *Physical Review A*, 31(3):1913, 1985.

[59] M. Holz and H. Weingartner. Calibration in accurate spin-echo self-diffusion measurements using 1 h and less-common nuclei. *Journal of Magnetic Resonance (1969)*, 92(1):115–125, 1991.

[60] M.-A. Neouze, J. Le Bideau, P. Gaveau, S. Bellayer, and A. Vioux. Ionogels, new materials arising from the confinement of ionic liquids within silica-derived networks. *Chemistry of Materials*, 18(17):3931–3936, 2006.

[61] M. P. Singh, R. K. Singh, and S. Chandra. Properties of Ionic Liquid Confined in Porous Silica Matrix. *Chemphyschem*, 11(9):2036–2043, 2010.

[62] J. Le Bideau, L. Viau, and A. Vioux. Ionogels, ionic liquid based hybrid materials. *Chemical Society Reviews*, 40(2):907–925, 2011.

[63] C. Iacob, J. R. Sangoro, P. Papadopoulos, T. Schubert, S. Naumov, R. Valiullin, J. Karger, and F. Kremer. Charge transport and diffusion of ionic liquids in nanoporous silica membranes. *Physical Chemistry Chemical Physics*, 12(41):13798–13803, 2010.

[64] C. Iacob, J.R. Sangoro, W.K. Kipnusu, R. Valiullin, J. Kärger, and F. Kremer. Enhanced charge transport in nano-confined ionic liquids. *Soft Matter*, 8(2):289–293, 2012.

[65] K. S. Panesar, C. Hugon, G. Aubert, P. Judeinstein, J.-M. Zanotti, and D. Sakellariou. Measurement of self-diffusion in thin samples using a novel one-sided NMR magnet. *Microporous and Mesoporous Materials*, 178:79–83, 2013.

[66] D. Lefort R. Béziel W. Guendouz M. Noirez L. Henschel A. Guégan, R. Morineau and P. Huber. Guégan, régis and morineau, denis and lefort, ronan and béziel, wilfried and guendouz, mohammed and noirez, laurence and henschel, anke and huber, patrick. *The European Physical Journal E*, 26(3):261–273, 2008.

[67] C. V. Cerclier, M. Ndao, R. Busselez, R. Lefort, E. Grelet, P. Huber, A. .V Kityk, L. Noirez, A. Schönhals, and D. Morineau. Structure and phase behavior of a discotic columnar liquid crystal confined in nanochannels. *The Journal of Physical Chemistry C*, 116(35):18990–18998, 2012.

[68] K. Lagrene and J.-M. Zanotti. Anodic aluminium oxide: Concurrent sem and sans characterisation. influence of aao confinement on peo mean-square displacement. *The European Physical Journal Special Topics*, 141(1):261–265, 2007.

[69] K. Lagrené, J.-M. Zanotti, M. Daoud, B. Farago, and P. Judeinstein. Large-scale dynamics of a single polymer chain under severe confinement. *Physical Review E*, 81(6):060801, 2010.

[70] K. Lagrené, J.-M. Zanotti, M. Daoud, B. Farago, and P. Judeinstein. Dynamical behavior of a single polymer chain under nanometric confinement. *The European Physical Journal Special Topics*, 189(1):231–237, 2010.

[71] V.P. Parkhutik and V.I. Shershulsky. Theoretical modelling of porous oxide growth on aluminium. *Journal of Physics D: Applied Physics*, 25(8):1258, 1992.

[72] K. Lagrené. *Étude dynamique de polymères sous confinement quasi-uniaxial.* PhD thesis, Paris, 2008.

[73] H. Masuda and K. Fukuda. Ordered metal nanohole arrays made by a two-step replication of honeycomb structures of anodic alumina. *Science*, 268(5216):1466–1468, 1995.

[74] H. Masuda, F. Hasegwa, and S. Ono. Self-ordering of cell arrangement of anodic porous alumina formed in sulfuric acid solution. *Journal of the electrochemical society*, 144(5):L127–L130, 1997.

[75] H. Masuda and M. Satoh. Fabrication of gold nanodot array using anodic porous alumina as an evaporation mask. *Japanese Journal of Applied Physics*, 35(1B):L126, 1996.

[76] T.L. Wade and J.-E. Wegrowe. Template synthesis of nanomaterials. *The European Physical Journal Applied Physics*, 29(01):3–22, 2005.

[77] `http://www.smartmembranes.de/en/products/nanoporous-alumina/`.

[78] C. P. Fredlake, J. M. Crosthwaite, D. G. Hert, S.N.V.K. Aki, and J. F. Brennecke. Thermophysical properties of imidazolium-based ionic liquids. *Journal of Chemical and Engineering Data*, 49(4):954–964, 2004.

[79] Private comunication.

[80] K. L. Stefanopoulos, G. E. Romanos, O. C. Vangeli, K. Mergia, N. K. Kanellopoulos, A. Koutsioubas, and D. Lairez. Investigation of confined ionic liquid in nanostructured materials by a combination of sans, contrast-matching sans, and nitrogen adsorption. *Langmuir*, 27(13):7980–7985, 2011.

[81] J.-M. Zanotti, K. Lagrené, N. Malikova, P. Judeinstein, K. Panesar, J. Ollivier, S. Rols, M. Mayne-L'Hermite, M. Pinault, and P. Boulanger. Nanometric confinement: Toward new physical properties and technological developments. *The European Physical Journal Special Topics*, 213(1):129–148, 2012.

[82] `http://www.mlz-garching.de/sans-1`.

[83] M. P. Singh, R. K. Singh, and S. Chandra. Ionic liquids confined in porous matrices: Physicochemical properties and applications. *Progress in Materials Science*, 64:73–120, 2014.

[84] M. Kanakubo, Y. Hiejima, K. Minami, T. Aizawa, and H. Nanjo. Melting point depression of ionic liquids confined in nanospaces. *Chem. Commun.*, (17):1828–1830, 2006.

[85] A. K. Gupta, M. P. Singh, R. K. Singh, and S. Chandra. Low density ionogels obtained by rapid gellification of tetraethyl orthosilane assisted by ionic liquids. *Dalton Transactions*, 41(20):6263–6271, 2012.

[86] J.-Y. Park and G. B. McKenna. Size and confinement effects on the glass transition behavior of polystyrene/o-terphenyl polymer solutions. *Physical Review B*, 61(10):6667, 2000.

[87] H. K. Christenson. Confinement effects on freezing and melting. *Journal of Physics-Condensed Matter*, 13(11):R95–R133, 2001.

[88] G. Dosseh, Y. Xia, and C. Alba-Simionesco. Cyclohexane and benzene confined in mcm-41 and sba-15: confinement effects on freezing and melting. *The Journal of Physical Chemistry B*, 107(26):6445–6453, 2003.

[89] A. K. Soper. The excluded volume effect in confined fluids and liquid mixtures. *Journal of Physics-Condensed Matter*, 9(11):2399–2410, 1997.

[90] F. Bruni, M.-A. Ricci, and A. K. Soper. Water confined in Vycor glass. I. A neutron diffraction study. *Journal of Chemical Physics*, 109(4):1478–1485, 1998.

[91] A. K. Soper, F. Bruni, and M.-A. Ricci. Water confined in Vycor glass. II. Excluded volume effects on the radial distribution functions. *Journal of Chemical Physics*, 109(4):1486–1494, 1998.

[92] D. Morineau and C. Alba-Simionesco. Liquids in confined geometry: How to connect changes in the structure factor to modifications of local order. *Journal of Chemical Physics*, 118(20):9389–9400, 2003.

[93] D. Morineau, R. Guegan, Y. D. Xia, and C. Alba-Simionesco. Structure of liquid and glassy methanol confined in cylindrical pores. *Journal of Chemical Physics*, 121(3):1466–1473, 2004.

[94] D. Morineau and C. Alba-Simionesco. Does Molecular Self-Association Survive in Nanochannels? *Journal of Physical Chemistry Letters*, 1(7):1155–1159, 2010.

[95] R. Atkin and G. G. Warr. Structure in confined room-temperature ionic liquids. *Journal of Physical Chemistry C*, 111(13):5162–5168, 2007.

[96] R. Hayes, S. Z. El Abedin, and R. Atkin. Pronounced structure in confined aprotic room-temperature ionic liquids. *The Journal of Physical Chemistry B*, 113(20):7049–7052, 2009.

[97] R. Hayes, N. Borisenko, M. K. Tam, P. C. Howlett, F. Endres, and R. Atkin. Double layer structure of ionic liquids at the au (111) electrode interface: an atomic force microscopy investigation. *The Journal of Physical Chemistry C*, 115(14):6855–6863, 2011.

[98] J. Bowers, M. C. Vergara-Gutierrez, and J. R.P. Webster. Surface ordering of amphiphilic ionic liquids. *Langmuir*, 20(2):309–312, 2004.

[99] E. Sloutskin, B. M. Ocko, L. Tamam, I. Kuzmenko, T. Gog, and M. Deutsch. Surface layering in ionic liquids: an x-ray reflectivity study. *Journal of the American Chemical Society*, 127(21):7796–7804, 2005.

[100] S. Perkin. Ionic liquids in confined geometries. *Physical Chemistry Chemical Physics*, 14(15):5052–5062, 2012.

[101] S. Perkin, T. Albrecht, and J. Klein. Layering and shear properties of an ionic liquid, 1-ethyl-3-methylimidazolium ethylsulfate, confined to nano-films between mica surfaces. *Physical chemistry chemical physics*, 12(6):1243–1247, 2010.

[102] I. Bou-Malham and L. Bureau. Nanoconfined ionic liquids: effect of surface charges on flow and molecular layering. *Soft Matter*, 6(17):4062–4065, 2010.

[103] B. Coasne, L. Viau, and A. Vioux. Loading-controlled stiffening in nanoconfined ionic liquids. *The Journal of Physical Chemistry Letters*, 2(10):1150–1154, 2011.

[104] S. Li, K. S. Han, G. Feng, E. W. Hagaman, L. Vlcek, and P. T. Cummings. Dynamic and structural properties of room-temperature ionic liquids near silica and carbon surfaces. *Langmuir*, 29(31):9744–9749, 2013.

[105] K. Dong, G. Zhou, X. Liu, X. Yao, S. Zhang, and A. Lyubartsev. Structural evidence for the ordered crystallites of ionic liquid in confined carbon nanotubes. *The Journal of Physical Chemistry C*, 113(23):10013–10020, 2009.

[106] M. P. Singh, R. K. Singh, and S. Chandra. Thermal stability of ionic liquid in confined geometry. *Journal of Physics D-Applied Physics*, 43(9), 2010.

[107] S. Aparicio and M. Atilhan. Molecular dynamics study of carbon nanostructures in n-methylpiperazinium lactate ionic liquid. *The Journal of Physical Chemistry C*, 117(42):22046–22059, 2013.

[108] S. Chen, K. Kobayashi, Y. Miyata, N. Imazu, T. Saito, R. Kitaura, and H. Shinohara. Morphology and melting behavior of ionic liquids inside single-walled carbon nanotubes. *Journal of the American Chemical Society*, 131(41):14850–14856, 2009.

[109] `http://iramis.cea.fr/Images/astImg/1987/MOMAC_SAXS2012.pdf`.

[110] T. Zemb, O. Tache, F. Ne, and O. Spalla. Improving sensitivity of a small angle x-ray scattering camera with pinhole collimation using separated optical elements. *Review of Scientific Instruments*, 74(4):2456–2462, 2003.

[111] S.J. Henderson. Comparison of parasitic scattering from window materials used for small-angle x-ray scattering: a better beryllium window. *Journal of applied crystallography*, 28(6):820–826, 1995.

[112] L. Lurio, N. Mulders, M. Paetkau, P. R. Jemian, S. Narayanan, and A. Sandy. Windows for small-angle x-ray scattering cryostats. *Journal of synchrotron radiation*, 14(6):527–531, 2007.

[113] P. Calmettes. Diffusion des neutrons aux petits angles : choix de l'échantillon et traitement des données. *Journal de Physique IV*, 9:83–93, 1999.

[114] J. Le Bideau, P. Gaveau, S. Bellayer, M. A. Neouze, and A. Vioux. Effect of confinement on ionic liquids dynamics in monolithic silica ionogels: H-1 NMR study. *Physical Chemistry Chemical Physics*, 9(40):5419–5422, 2007.

[115] K. S. Han, X. Wang, S. Dai, and E. W. Hagaman. Distribution of 1-butyl-3-methylimidazolium bistrifluoromethylsulfonimide in mesoporous silica as a function of pore filling. *The Journal of Physical Chemistry C*, 117(30):15754–15762, 2013.

[116] D. Petit, J.-P. Korb, P. Levitz, J. Le Bideau, and D. Brevet. Multiscale dynamics of 1 h and 19 f in confined ionogels for lithium batteries. *Comptes Rendus Chimie*, 13(4):409–411, 2010.

[117] R. Singh, J. Monk, and F. R Hung. A computational study of the behavior of the ionic liquid [bmim+][pf6-] confined inside multiwalled carbon nanotubes. *The Journal of Physical Chemistry C*, 114(36):15478–15485, 2010.

[118] E. Mamontov, D. J. Wesolowski, P. F. Fulvio, and S. Dai. Fast diffusion in a room-temperature ionic liquid confined in mesoporous carbon. *European Physics Letters*, 97(6), 2012.

[119] E. Mamontov, P. F. Fulvio, X. Wang, et al. An unusual slowdown of fast diffusion in a room temperature. *European Physics Letters*, 102(02955075), 2013.

[120] M. Davenport, A. Rodriguez, K. J. Shea, and Z. S. Siwy. Squeezing ionic liquids through nanopores. *Nano letters*, 9(5):2125–2128, 2009.

[121] `http://www.ill.eu/instruments-support/instruments-groups/instruments/in16b/more/old-in16/characteristics/`.

[122] C. Hugon, G. Aubert, and D. Sakellariou. An expansion of the field modulus suitable for the description of strong field gradients in axisymmetric magnetic fields: Application to single-sided magnet design, field mapping and STRAFI. *Journal of Magnetic Resonance*, 214:124–134, 2012.

[123] H. Verweij, M. C. Schillo, and J. Li. Fast mass transport through carbon nanotube membranes. *small*, 3(12):1996–2004, 2007.

[124] J. Wu, K. Gerstandt, H. Zhang, J. Liu, and B. J. Hinds. Electrophoretically induced aqueous flow through single-walled carbon nanotube membranes. *Nature nanotechnology*, 7(2):133–139, 2012.

[125] V. Jourdain and C. Bichara. Current understanding of the growth of carbon nanotubes in catalytic chemical vapour deposition. *Carbon*, 58:2–39, 2013.

[126] S. Boncel, K. K. K. Koziol, K. Z. Walczak, A. H. Windle, and M. S. P. Shaffer. Infiltration of highly aligned carbon nanotube arrays with molten polystyrene. *Materials Letters*, 65(14):2299–2303, 2011.

[127] `http://www.sigmaaldrich.com/catalog/product/aldrich/96324?lang=fr&region=FR`.

[128] T. D.W. Claridge. *High-resolution NMR techniques in organic chemistry*, volume 27. Newnes, 2008.

[129] A. Einstein. On the movement of small particles suspended in stationary liquids required by the molecular-kinetic theory of heat. *Annales der Physik*, 17:549–560, 1905.

[130] M. A. Gebbie, M. Valtiner, X. Banquy, E. T. Fox, W. A. Henderson, and J. N. Israelachvili. Ionic liquids behave as dilute electrolyte solutions. *Proceedings of the National Academy of Sciences of the United States of America*, 110(24):9674–9679, 2013.

[131] S. Perkin, M. Salanne, P. Madden, and R. Lynden-Bell. Is a stern and diffuse layer model appropriate to ionic liquids at surfaces? *Proceedings of the National Academy of Sciences of the United States of America*, 110(44):E4121–E4121, 2013.

[132] L. Van Hove. Correlations in space and time and born approximation scattering in systems of interacting particles. *Physical Review*, 95(1):249, 1954.

[133] M. Bée. La diffusion quasiélastique des neutrons; introduction et principes généraux. *Le Journal de Physique IV*, 10(PR1):Pr1–1, 2000.

[134] M. Karlsson. Proton dynamics in oxides: insight into the mechanics of proton conduction from quasielastic neutron scattering. *Physical Chemistry Chemical Physics*, 17(1):26–38, 2015.

[135] N. Malikova. *Dynamics of water and ions in montmorillonite clays by microscopic simulation and quasi-elastic neutron scattering*. PhD thesis, 2008.

[136] J. Ollivier and J.-M. Zanotti. Diffusion inélastique de neutrons par temps de vol. *École thématique de la Société Française de la Neutronique*, 10:379–423, 2010.

[137] F. Mezei. Neutron spin echo: a new concept in polarized thermal neutron techniques. *Zeitschrift für Physik*, 255(2):146–160, 1972.

[138] J. J. Sakurai and J. Napolitano. *Modern quantum mechanics*. Addison-Wesley, 2011.

[139] H. Tokuda, S. Tsuzuki, M. Susan, K. Hayamizu, and M. Watanabe. How ionic are room-temperature ionic liquids? An indicator of the physicochemical properties. *Journal of Physical Chemistry B*, 110(39):19593–19600, 2006.

[140] D. R. MacFarlane, M. Forsyth, E. I. Izgorodina, A. P. Abbott, G. Annat, and K. Fraser. On the concept of ionicity in ionic liquids. *Physical Chemistry Chemical Physics*, 11(25):4962–4967, 2009.

[141] M. Banquy X. Henderson W. A. Gebbie, M. A. Valtiner and J. N. Israelachvili. Reply to perkin et al.: Experimental observations demonstrate

that ionic liquids form both bound (stern) and diffuse electric double layers. *Proceedings of the National Academy of Sciences of the United States of America*, 110(44):E4122–E4122, 2013.

[142] J. F. Brennecke and E. J. Maginn. Ionic liquids: Innovative fluids for chemical processing. *Aiche Journal*, 47(11):2384–2389, 2001.

[143] H. Zhao, S. Xia, and P. Ma. Use of ionic liquids as 'green'solvents for extractions. *Journal of chemical technology and biotechnology*, 80(10):1089–1096, 2005.

[144] M. Armand, F. Endres, D. R. MacFarlane, H. Ohno, and B. Scrosati. Ionic-liquid materials for the electrochemical challenges of the future. *Nature Materials*, 8(8):621–629, 2009.

[145] J. F. Wishart. Energy applications of ionic liquids. *Energy & Environmental Science*, 2(9):956–961, 2009.

[146] D. R. MacFarlane, N. Tachikawa, M. Forsyth, J. M. Pringle, P. C. Howlett, G. D. Elliott, J. H. Davis, M. Watanabe, P. Simon, and C. A. Angell. Energy applications of ionic liquids. *Energy & Environmental Science*, 7(1):232–250, 2014.

[147] R. P. Swatloski, S. K. Spear, J. D. Holbrey, and R. D. Rogers. Dissolution of cellose with ionic liquids. *Journal of the American Chemical Society*, 124(18):4974–4975, 2002.

[148] D. A. Fort, R. C. Remsing, R. P. Swatloski, P. Moyna, G. Moyna, and R. D. Rogers. Can ionic liquids dissolve wood? Processing and analysis of lignocellulosic materials with 1-n-butyl-3-methylimidazolium chloride. *Green Chemistry*, 9(1):63–69, 2007.

Filippo FERDEGHINI **20 octobre 2015**

Liquides ioniques sous confinement nanométrique unidimensionnel

Résumé : L'idée à la base de ce projet est de mettre à profit le confinement nanométrique unidimensionnel pour décupler la conduction ionique des électrolytes et donc la puissance des accumulateurs au lithium. Nous avons concentré nos efforts sur une classe particulière d'électrolytes qui, en raison de leurs stabilités physique et électrochimique, ont été identifiés comme prometteurs : les Liquides Ioniques (LI). Nous avons confiné les LI dans deux systèmes poreux présentant une topologie commune (pores cylindriques macroscopiquement orientés) mais aux propriétés physico-chimiques complémentaires : i) des alumines poreuses (AAO, interface hydrophile, diamètre des pores de 25 à 160 nm) et ii) des membranes de NanoTubes de Carbone (NTC, interface hydrophobe, diamètre des pores 4 nm). Nous avons développé un modèle microscopique multi-échelle original, prenant en compte la dynamique complexe des cations des LI : combinaison *i)* de la dynamique de réorientation rapide des chaînes latérales alkyle, *ii)* de la diffusion de la molécule au sein des agrégats nanométriques spontanément formés par les LI, puis *iii)* de la diffusion entre ces agrégats. Ce modèle reproduit de façon remarquablement robuste les données de diffusion quasi-élastique de neutrons sur une gamme étendue de vecteurs de diffusion (0,1 à 2,5 $Å^{-1}$) et de temps (10^{-1} à 2.10^3 ps). A cette échelle locale, nous ne détectons pas d'influence du confinement sur la dynamique du LI confiné au sein des AAO et des CNT. Nous montrons cependant qu'à l'échelle microscopique (PFG-NMR) et macroscopique (spectroscopie d'impédance) le confinement des LI au sein des NTC permet d'obtenir un gain de conductivité d'un facteur 3. Un brevet est déposé.

Mots clés : Liquide ionique, confinement, dynamique, neutrons, poreux, nanotube de carbone

Ionic liquids under one-dimensional nanometric confinement

Abstract : This PhD thesis is a contribution to a global worldwide effort to improve the performances of electrochemical systems so they can become competitive alternatives to fossil fuels in the field of transportation systems. As due to their electrochemical and physical/chemical stability they have been identified as promising electrolytes, we have focused our efforts on a particular class of electrolytes: Ionic Liquids (ILs). The competition between electrostatic and van der Waals interactions of the charged and a-polar alkyl side-chain(s) moieties of their cations drive a specificity of IL: a nanometric structuration. We identify confinement as a way to circumvent the nanostructuracion and hence turn the IL to a homogeneous liquid (with no density fluctuation) showing improved transport properties. We have confined imidazolium based ILs in two distinct porous systems: *i)* porous alumina (AAO) and *ii)* carbon nanotube membranes (CNTs). These materials share a topological common ground: the macroscopic orientation of their cylindrical pore network, but show complementary physico-chemical properties: AAO are hydrophilic while CNT are hydrophobic.
Owing to the large incoherent neutron scattering cross-section of the hydrogen atom and the abundance of this element in IL, incoherent Quasi-Elastic Neutron Scattering (QENS) measurements are able to provide a global view of the IL dynamics as sensed via the averaged individual motions of its protons. We have introduced a new physical appealing model taking into account all the dynamical contributions of the ionic liquid cations : the dynamics of the side-chains, the diffusion of the cation as a whole both within an IL aggregate and at long range. We have taken advantage of specific deuteration of the IL cation side chains to show that the modelization is robust enough to describe the QENS data over an unprecedented extended Q ([0.15 $Å^{-1}$ - 2.5 $Å^{-1}$]) and time ([0.5 ps - 2000 ps]) ranges. We discuss the connection between our model and the generalized Gaussian model. The model we propose to assess the IL local dynamics in bulk, is able to also describe the dynamics under AAO confinement. When confined within the AAO pores (25, 60 and 160 nm) we identify, by DSC ans diffraction, a strong interactions of a fraction of the confined IL with the AAO pores walls. We nevertheless detect no significant influence of confinement on the IL dynamics. By QENS, no strong dynamical effect of confinement has been detected at the molecular scale (ps-ns) both for the radial and longitudinal dynamics of IL confined in 4 nm pore diameter CNT. But we have been able to show that at the microscopic (by Pulsed Field Gradient NMR) and macroscopic scale (by impedance spectroscopy), we can obtain the effect that we have been seeking in developing this research program: a noticeable enhancement (by a factor 3) of the transport properties in a 1D situation. A patent has been filed on the use of CNT membranes as a possible solution to boost the transport properties and hence the specific power of lithium batteries.

Keywords : Ionic liquid, confinement, dynamics, porous, carbon nanotube, AAO, neutron, NMR.